NMR Spectroscopic studies of calmodulin plasticity in calcium signalling

Ph.D. Thesis

In partial fulfillment of the requirements
for the degree “Doctor of Philosophy (Ph.D.)”
in the Molecular Biology Program
at the Georg August University Göttingen,
Faculty of Biology

submitted by

Fernando Rodríguez Castañeda

born in

Guatemala City

2007

Herewith I declare, that this thesis represents my original work and all the concepts and material that I did not create have been cited.

Göttingen, 29 of September of 2007,

Fernando Rodríguez Castañeda

Aknowledgements

The work presented here has been accomplished in the NMR-Based Structural Biology Department of the Max-Planck Institute for Biophysical Chemistry within the frame of the International Molecular Biology Program, Max-Planck Research Schools and University of Göttingen. I acknowledge these Institutions and people involved in its creation and management.

I thank my Ph.D. supervisor and Director of the NMR-Based Structural Biology Department, Prof. Christian Griesinger for his guidance and trust in the scientific endeavours I have undertaken.

I would like to acknowledge Dr. Teresa Carlomagno for her contribution in the NMR studies of calmodulin interaction with Munc13. Dr. Laurent Verdier, Dr. Christophe Fàres and Dr. Vinesh Vijayan for introduction to the use of the NMR spectrometer and their assistance when problems were encountered.

I acknowledge Dr. Andrei Leonov who provided the paramagnetic tags used in this work and also for giving me advices how to use them.

I acknowledge Dr. Steffan Becker and Karin Giller for their contribution in various aspects of the sample preparation in this work.

I acknowledge Dr. Volker Klaukien, Kerstin Overkamp and Gerhard Wolff for peptide synthesis and HPLC purification.

I acknowledge Dr. Pierre Montaville for stimulating scientific discussions and practical advices on the sample preparation.

I acknowledge Dr. Nicolas Coudeville and Jegannath Korukottu for their assistance in the structure calculation part of this work

I acknowledge Pinar Karpinar for her help in Dynamic Light Scattering measurements.

I acknowledge Prof. Thomas Jovin, Director of the Department of Molecular Biology at the Max-Planck Insitute for Biophysical Chemistry for giving me the opportunity to do some fluorescence studies.

I acknowledge Prof. Nils Brose, Director of the Molecular Neurobiology Department at the Max-Planck Institute for Experimental Medicine for giving me the opportunity to collaborate on the interaction of calmodulin and Munc13. I also thank Dr. Harald Junge, Dr.Olaf Jahn, Kalina Dimova and Noa Lippstein who are also part of this joint effort.

I would like to thank all the members of the NMR-Structural Biology Department for the collegial working atmosphere.

I dedicate this work to my family who gave me their unconditional support during these five years abroad. I thank my friends in Göttingen who always gave me a helping hand when I needed it.

List of publications

Rodríguez-Castañeda, F., Haberz, P., Leonov, A., Griesinger, C. (2006) Paramagnetic tagging of diamagnetic proteins for solution NMR. Magnetic Resonance in Chemistry. 44, S10-S16.

Haberz, P., Rodríguez-Castañeda, F., Junker, J., Becker, S., Leonov, A., Griesinger, C. (2006) Two new chiral EDTA-Based metal chelates for weak alignment of proteins in solution. Organic Letters. 8, 1275-1278.

Leonov, A., Voigt, B., Rodríguez-Castañeda, F., Sakhaii, P., Griesinger, C. (2005) Convenient syntheses of multifunctional EDTA-Based chiral metal chelates substituted with an S-mesylcysteine. Chemistry- a European Journal. 11, 1-8.

Rodríguez-Castañeda, F., Brose, N., Carlomagno, T., Griesinger, C. Resonance assignment of the Calmodulin-Munc13-1 peptide complex. J. Biomol. Assignments. To be submitted.

Abstract

The present work focused both in structural and dynamic studies on the ubiquitous Ca^{2+} signaling protein calmodulin. Calmodulin has been extensively studied both for its biological importance in the regulation of its interaction partners which are key regulators in various processes like protein phosphorylation, dephosphorylation and regulation of gene transcription and as a two-domain model protein, binding the signaling calcium ion in a cooperative fashion. Pioneering high-resolution structural studies both by X-ray crystallography (Babu *et al*., 1988) and NMR (Ikura *et al*., 1992; Barbato *et al*., 1992) done on calmodulin revealed that its two domains are linked by a flexible linker giving a large degree of conformational freedom. Thus, its two domains can adopt various orientations to recognize and activate its targets. Upon calcium binding, the EF-hand motifs in CaM undergo a large conformational change exposing hydrophobic side-chains to the surface, which engage in hydrophobic interactions with its targets. Among this hydrophobic side chains, methionines play a prominent role in CaM plastic interactions (Siivari *et al*., 1995).

The dynamic part of the investigation made use of anisotropic NMR restraints that sample protein motions up to the submillisecond time-scale. In solution-state NMR, anisotropic interactions average to zero due to molecular tumbling. For this reason, these anisotropic interactions are observable (and measurable) just under special sample conditions. In this work, the use of lanthanide-binding EDTA-based paramagnetic tags attached to cysteine mutants in CaM served this purpose; since the unpaired electron in the paramagnetic lanthanide ion provides strong magnetic susceptibility anisotropy, aligning the macromolecule in solution. Using this methodology, it was possible to establish a difference in the CaM dynamics in three different activated sates. First, the paramagnetic alignment of the CaMS17C mutant established a difference in the dynamic behavior of apoCaM and holoCaM on the basis of pseudocontact shifts measured in the linker region of CaM. Second, the measurement of residual dipolar couplings from the paramagnetic alignment of the CaMT146C mutant in the free state and in complex to the C20W peptide belonging to the plasma membrane Ca^{2+}-pump, established a difference in the dynamics between these two activated states. Bertini *et al*. 2004, reported a reduced alignment for the C-terminal domain of CaM (around 10% of the alignment was retained) mutant by direct lanthanide binding to the metal binding site in the N-terminal domain of holoCaM. In this work, a consistent reduced alignment in three independent measurements of ~25% in the N-terminal domain of CaM in complex with the C20W peptide is reported. In contrast, for the holoCaM case, a residual alignment of the N-terminal domain of CaM could not be measured because of the weak alignment impaired by the paramagnetic tag (up to 8Hz at 900 MHz) yielding rDC within the error range of the measurements.

The structural part of the investigation focused in the interaction of CaM with the diacylglycerol-binding protein Munc13-1, an essential protein involved in the priming process of vesicles in neurotransmitter release. Junge *et al*., 2004 found that CaM binds to a conserved region in Munc13-1 and regulates neurotransmitter release in response to residual calcium signals. The complete sequential resonance assignment and determination of the NMR solution structure of the CaM/Munc13-1 (458-492) peptide complex is reported. The ^{1}H, ^{15}N, and ^{13}C resonance assignment list has been deposited to the biological magnetic resonance data bank (BMRB): deposition number 15470. The structure describes a new binding motif for CaM, where CaM interacts with Munc13-1 in a bipartite mode. The C-terminal domain of CaM interacts with the N-terminal amphiphilic α-helix (1-5-8) hydrophobic motif of the Munc13-1 peptide and the N-terminal domain of CaM builds a hydrophobic interaction with a LW motif at the C-terminus of the peptide. Other singular properties of this protein-peptide complex include residual interdomain dynamics in the submillisecond time scale probed by

paramagnetically-derived residual dipolar couplings; and monomer-dimer equilibrium to a (2:2) complex favored at larger salt concentrations.

Electrophisiology studies done on primary neuron cultures of the CaM insensitive (W464R) and the phorbol ester insensitive (H567K) mutants (Junge *et al*., 2004; Rhee *et al*., 2002) of Munc13-1 have revealed striking similarities in their vesicle priming properties. This motivated the study of the interaction of CaM with a fragment of Munc13-1 containing both the CaM-binding and the diacylglycerol/phorbol ester-C_1 binding domains of Munc13-1. The ^{15}N-labeled NMR sample for this protein-protein complex could be prepared using a co-expression approach and allowed its spectroscopic investigation. Although the sequential backbone resonance assignment for this CaM/Munc13-1(447-631) protein complex was not undertaken, the similarity to the HSQC of the CaM/Munc13-1 (458-492) peptide complex allowed the description of several novel properties of this protein-protein interaction. First, the monomer(1:1)-dimer (2:2) equilibrium described for the CaM/Munc13-1(458-492) peptide complex is also described in this larger complex, but with an increased binding affinity. Therefore, the monomeric and dimeric complex species could be separated by size-exclusion chromatography and studied independently. The analysis of the HSQC spectra of the monomeric complex species of the wild type, W489A and W588A mutant complexes suggest that the N-terminal domain of CaM switches between two hydrophobic motifs in Munc13-1: the LW motif revealed in the NMR structure and a second motif within the C_1 domain of Munc13-1. The rigorous proof of a direct interaction between the N-terminal domain of CaM and the C_1 domain of Munc13-1 is not provided, but ongoing studies is addressing this possibility that would give a structural correlate to the physiological studies mentioned before.

The studies on the dimeric (2:2) CaM/Munc13-1(447-631) protein complex also suggest a conformational exchange equilibrium mediated by the N-terminal domain of CaM and the C_1 domain of Munc13-1. Moreover, there is preliminary evidence that the C_1 domain agonist PDBu might activate Munc13-1 by shifting the equilibrium towards the monomeric state of the complex, possibly relieving an auto-inhibited state. The homodimerization of the C_2A domain of Munc13-1 has been described in the studies by Lu *et al*., 2006. For this reason, further studies on the relationship of the oligomerization state of Munc13-1 and its priming activity are highly encouraged to better understand how the variable N-terminal region of Munc13 proteins with its numerous interaction partners like RIM1 and Rab3A (Dubulova *et al*., 2005) remodels the highly conserved C-terminal MUN catalytic domain in this family of proteins to fine-tune the priming of vesicles in the active zone of neurons and more importantly how these different protein-protein interactions shape the short-term synaptic plasticity processes in the brain.

Zusammenfassung

Dieser Arbeit befasst sich mit den strukturellen und dynamischen Aspekten der Kalzium Signal Transduktion von Calmodulin (CaM). Dieses Protein ist intensiv erforscht worden, da es eine Vielzahl von Interaktionspartnern reguliert und in Schlüsselprozessen, wie Proteinphosphorylierung, -dephosphorylierung und Transkription involviert ist. Darüber hinaus ist ein Model eines Zwei-Domänen-Proteins, welches Kalzium kooperativ bindet. Die strukturelle Pionierarbeit, sowohl kristallographisch (Babu *et al*., 1988), als auch NMR-spektroskopisch (Ikura *et al*., 1992; Barbato *et al*., 1992) hat gezeigt, dass beide Calmodulindomänen durch einen flexibler Linker verbunden sind, was ein hohes Maß an konformativer Freiheit zulässt. Bedingt dadurch können beide Domänen unterschiedliche Orientierungen einnehmen, um ihre Interaktionspartner zu erkennen und zu aktivieren. Nach der Kalziumbindung erfahren die EF-Hand-Motive eine umfangreiche Konformationsänderung, wodurch hydrophobe Seitenketten auf der Oberfläche präsentiert werden und eine hydrophobe Wechselwirkung mit ihren Partnern eingehen. Hierbei spielen besonders Methioninseitenketten eine wichtige Rolle (Siivari *et al*., 1995).

Der Teil, der sich mit der Dynamik von CaM befasst, nutzt anisotrope NMR Bedingungen, um Bewegungsvorgänge im bis zum Millisekundenbereich „abzutasten“. In Lösung belaufen sich solche anisotropen Interaktionen, bedingt durch die Molekularbewegung, im Durchschnitt auf Null. Daher lassen sie sich nur unter speziellen Probenbedingungen beobachten (und messen). Im Rahmen dieser Arbeit wurden Lanthanoid-komplexierte, auf EDTA-basierende, paramagnetische Tags verwendet, die über Cysteinseitenketten an CaM gebunden sind. Das allein stehende ungepaarte Elektron des paramagnetischen Lanthanoid-Ions bewirkt eine starke anisotropische magnetische Suszeptibilität, die das Makromolekül im Magnetfeld ausrichtet. Mit dieser Methode war es möglich, Unterschiede zwischen drei aktivierten Zuständen von CaM zu untersuchen (apoCaM, holoCaM und CaM-C20W-Peptid-Komplex). Dabei zeigte die paramagnetische Anordnung der CaM-S17C Mutante einen Unterschied im dynamischen Verhalten zwischen apoCaM und holoCaM anhand von, in der Linker-Region gemessener, Pseudokontaktverschiebungen. Durch die Messung dipolarer Kopplungen der CaM-T146C Mutante im freien und komplexierten Zustand mit dem Peptid (C20W) der membrangebundenen Ca^{2+}-ATPase-Pumpe, konnten ebenfalls Unterschiede im dynamischen Verhalten beobachtet werden. Bertini *et al*. (2004) beschrieb eine verbliebene Ausrichtung der C-terminalen Domäne von rund 10%, wenn ein Lanthanoid-Ion direkt N-terminal von holoCaM gebunden wird. In dieser Arbeit konnte, übereinstimmend in drei unabhängigen Messungen, eine verbliebene N-terminale Ausrichtung von 25% im Komplex mit C20W beobachtet werden. Im Gegensatz dazu wurde für den N-Terminus von holoCaM keine verbliebene Orientierung gemessen, da das Alignment des paramagnetischen tags (bis zu 8 Hz dipolare Kopplungen am 900 MHz Spektrometer) zu schwach ist und die Ergebnisse in der Grössenordnung des Fehlerbereiches liegen.

Der strukturelle Teil der Arbeit befasst sich mit der Interaktion von CaM mit dem Diacylglycerol-bindinden Protein Munc13-1, welches eine wichtige Rolle hinsichtlich Neurotransmitterfreisetzung spielt. Junge *et al*., (2004) fand heraus, dass CaM an eine konservierte Region von Munc13-1 bindet und als Antwort auf Kalziumsignale die Freisetzung solcher Neurotransmitter reguliert. Die vollständige sequenzielle Zuordnung der chemischen Verschiebungen und die gelöste NMR-Struktur des CaM/Munc13-1 (458-492) Peptid Komplexes wird in dieser Arbeit beschrieben. Die ^{1}H, ^{15}N, und ^{13}C chemischen Verschiebungen wurden auf der Biological Magnetic Resonance Data Bank (BMRB) unter der Nummer 15470 abgelegt. Die Struktur beschreibt ein neues bindendes Motiv für CaM, in dem es mit Munc13-1 in zweiteiliger Weise interagiert. Die C-terminale Domäne vom CaM wechselwirkt hierbei mit dem N-terminalen, amphiphilen und α-helikalen (1-5-8) Motiv des

Munc13-1 Peptids und der CaM-N-terminalen Domäne, so dass eine hydrophobe Interaktion durch eine LW Motiv am C-terminus des Peptids aufgebaut wird. Zu den weiteren Eigenschaften dieses Protein-Peptid Komplexes zählt eine verbliebene Inter-Domänen-Dynamik im sub-Millisekundenbereich, die mittels paramagnetischer dipolarer Kopplungen untersucht wurde, sowie die Verschiebung eines Monomer-Dimer Gleichgewichtes in Richtung eines 2:2 Komplexes, unter Verwendung höherer Salzkonzentrationen.

Electrophysiologische Studien an primären Neuronalkulturen von Munc13-1 Mutanten, die eine Unempfindlichkeit gegenüber CaM (W464R) und Phorbolester (H567K) aufweisen, zeigten eine vergleichbare Eigenschaft hinsichtlich der Auflösung von Neurotransmittervesikeln (Junge *et al.*, 2004; Rhee *et al.*, 2002). Dies wiederum regte die Studie der Interaktion zwischen CaM und einem Fragment von Munc13-1 an, welches beide, die CaM- und Diacylglycerol/Phorbolester-C_1 bindende Domäne enthält. Die ^{15}N markierte NMR Probe zur Untersuchung dieses Protein-Protein Komplexes, konnte mittels einer Co-Expression hergestellt und anschließend untersucht werden. Die Ähnlichkeiten zwischen den HSQC-Spektren des CaM/Munc13-1(458-492) Komplexes und des CaM/Munc13-1(447-631) Proteinkomplexes ermöglichten die Beschreibung einiger neuer Eigenschaften dieses Protein-Protein Komplexes, obwohl keine sequentielle Zuordnung des CaM/Munc13-1(447-631) Komplexes vorgenommen wurde. Erstens, das für den CaM/Munc13-1(458-492) Komplex bereits beschriebene Monomer (1:1)- Dimer (2:2)-Gleichgewicht, ist für den größeren Komplex ebenfalls zu beobachten, jedoch mit einer erhöhten Bindungs-Affinität. Daher war es möglich, das Monomer vom Dimer mittels Größenausschlusschromatographie zu trennen, um jede Spezies unabhängig voneinander untersuchen zu können. Die HSQC-Analyse des monomeren Komplexes des Wildtyps, sowie der W489A- und W588A-Mutanten weist darauf hin, dass die N-terminale Domäne von CaM zwischen zwei hydrophoben Motiven in Munc13-1 wechselt: das LW Motiv, gezeigt in der NMR Struktur, und ein zweites Motiv, innerhalb der C_1-Domäne von Munc13-1. Der entscheidende Beweis für die Interaktion zwischen der N-terminalen Domäne vom CaM und der C_1-Domäne vom Munc13-1 konnte nicht erbracht werden, aber laufende Studien untersuchen diese Möglichkeit, die eine Brücke zwischen die strukturellen und den genannten physiologischen Studien schlagen würde.
Die Untersuchungen des CaM/Munc13-1(447-631)-Dimer-(2:2) Komplexes legen einen konformativen Gleichgewichtsaustausch zwischen der N-terminalen Domäne vom CaM und der C_1-Domäne von Munc13-1 nahe. Außerdem gibt es Hinweise darauf, dass der C_1-Domänen-Agonist PDBu von Munc13-1 eine Verschiebung des Gleichgewichts in Richtung des Monomers bewirkt, möglicherweise bedingt durch eine reduzierte Autoinhibition. Die Homodimerisierung der C_2A Domäne von Munc13-1 wurde in den Studien von Lu *et al.* (2006) bereits beschrieben. Daher sind weitere Studien, die das Verhältnis zwischen dem Oligomerisierungszustand von Munc13-1 und der Regulation der Neurotransmitterfreisetzung untersuchen, wichtig, um besser verstehen zu können, wie die hoch konservierte C-terminale MUN-Domäne von Interaktionspartnern, wie RIM1 und Rab3A, von der variablen N-terminalen Region der Munc13-Proteine verändern wird. Dies führt zu einer Feinabstimmung der Neurotransmitterfreisetzung im aktiven Bereich der Neuronen. Darüber hinaus gilt es zu klären, wie diese verschiedenen Protein-Protein-Interaktionen die kurzzeitig plastischen Prozesse im Gehirn bewirken könnten.

Table of Contents

Page

I. INTRODUCTION……. 1

1. Signal transduction and second messengers…… 1

2. Synapses and calcium signaling in neurons…… 2

3. Synaptic vesicles……. 3

4. Brain modulator protein: calmodulin…….. 4

5. The EF-hand superfamily of proteins: calmodulin plasticity……. 5

6. Regulated exocytosis…….. 10

7. Presynaptic plasticity……... 13

8. Active Zones and the presynaptic plasma membrane…….. 15

9. Allosteric modulation of the presynaptic Ca^{2+} sensor for vesicle fusion…… 16

10. Kinetics of the neurotransmitter release…… 17

11. C_1 domain as membrane localization module in Munc13-1……. 17

12. Priming activity of Munc13 proteins…… 19

13. Study of macromolecular structure with nuclear magnetic resonance……. 21

14. Study of macromolecular dynamics with nuclear magnetic resonance…… 26

15. Paramagnetic tagging of diamagnetic proteins……. 37

16. Calmodulin dynamics…… 38

II. MATERIALS AND METHODS……. 42

1. Polymerase chain reaction (PCR) based-cloning of the different Munc13-1 protein expression constructs…….. 42

a. Polymerase chain reaction (PCR)……... 42

b. Restriction digestion of the PCR products……. 43

c. Preparation of the plasmid DNA expression vectors for cloning……... 44

d. Ligation reaction……. 44

e. Transformation of the ligated plasmid DNA…….. 45

f. Plasmid DNA amplification and purification…….. 45

g. Screening, DNA sequencing and transformation of positive clones…….. 45

h. Protein over expression test in LB medium and protein solubility…… 46

2. PCR-mediated Site-directed mutagenesis…… 47

3. Over expression of the different proteins in Minimal Medium for uniform isotope labeling……. 49

4. Purification of the hexahistidine-tagged Munc13-1 proteins…….. 49
5. Purification of the GST-tagged Munc13-1 proteins…… 50
6. Purification of CaM……. 50
7. Purification of the Munc13-1-185aa protein……... 52
8. Electrospray ionization mass spectrometry (ESI-MS)…… 52
9. NMR measurements…… 52
10. Docking and structure calculation approaches for the CaM/Munc13-1(457-492) peptide complex…… 54
11. Data analysis of residual dipolar couplings and pseudocontact shifts…….. 56
III. RESULTS…… 58
1. Cloning, overexpression and purification of CaM and Munc13-1 proteins…… 58
a. Cloning of Munc13-1(457-492) (Munc13-1-36aa)…… 58
b. Cloning of Munc13-1(567-631) C_1 domain (Munc13-1-65aa) ……. 58
c. Cloning of Munc13-1(447-631) (Munc13-1-185aa) ……. 59
d. Site-directed mutagenesis……... 59
e. Overexpression and purification of the Munc13-1(457-492) peptide…… 59
f. Overexpression and purification of the Munc65 protein…… 61
g. Overexpression and purification of the Munc185 protein…….. 63
h. Overexpression and purification of calmodulin……. 65
i. Biochemical separation of Munc185 from calmodulin……... 65
2. Biophysical characterization of CaM and Munc13-1 proteins…… 67
a. NMR studies on the ^{15}N,^{13}C CaM/Munc13-1(459-479) peptide complex…. 67
b. NMR studies on the ^{15}N,^{13}C CaM/Munc13-1(459-492) peptide complex…. 68
c. NMR studies of the ^{13}C,^{15}N Munc13-1(457-492) peptide binding to CaM... 73
d. NMR studies of the CaM binding region and the C_1 domain of Munc13-1 (Munc185)……... 77
e. Tryptophan Nε-Hε1 side chain heterogeneity as evidence of a switch mechanism in the calcium coupling mechanism of CaM and Munc13-1….. 78
f. NMR studies of the C_1 domain of Munc13-1 (Munc65)……. 81
g. NMR studies of ^{15}N CaM/^{15}N Munc13-1(185aa) complex with its agonist: phorbol dibutirate (PDBu)…….. 82
h. Sequential backbone and side-chain resonance assignment for the ^{13}C,^{15}N CaM/Munc13-1 (459-492) peptide complex……... 85
i. Long-range NMR restraints for the structure determination of the

CaM/Munc13-1 (457-492) peptide complex……... 94
j. NMR structure determination of the CaM/Munc13-1 (457-492) peptide complex…… 104
k. Dynamic studies of CaM in its various activated states with paramagnetic alignment……. 111
IV. DISCUSSION…….. 127
1. Dynamic studies on apoCaM……... 127
2. Dynamic studies on holoCaM……. 127
3. Dynamic studies on the CaM/C20W peptide complex…… 128
4. Structural studies on the CaM/Munc13-1 interaction…….. 128
a. apoCaM interaction with Munc13-1 and ubMunc13-2…….. 128
b. [2Ca^{2+}]CaM interaction with Munc13-1……. 128
c. [4Ca^{2+}]CaM interaction with Munc13-1……. 129
d. Solution structure of the CaM/Munc13-1(457-492) peptide complex……... 129
e. Accuracy of the solution structure of the CaM/Munc13-1(457-492) peptide complex…… 129
f. NMR studies on the CaM/Munc13-1(185aa) monomeric (1:1) and dimeric (2:2) complexes……... 130
V. CONCLUSIONS…….. 132
VI. BIBLIOGRAPHY……... 133
VII. APENDIX…….. 141
1.Magnetization pathways in the backbone nuclei of the polypeptide chain…….. 141
2. Pictorial view of the heteronuclear multidimensional NMR pulse sequences…… 142
3. Chemical shift assignments for the CaM/Munc13-1(457-492) peptide complex... 147

List of Figures

No.		Page
1	Anatomy of a typical synapse……...	2
2	Molecular model of CaM X-ray crystallographic structure…….	6
3	Model of the EF-hand motif…….	6
4	CaM peptide recognition motifs……...	8
5	Different activation models for CaM binding partners……	9
6	Domain structure of Munc13-1……	11
7	Neurotransmitter vesicle endo- and exocytotic cycle in a presynaptic neuron…	12
8	Flash photolysis response…….	15
9	^{1}J-Coupling pathways for the nuclei in the polypeptide backbone……..	22
10	Orientation-dependent magnetic field experienced by an amide ^{15}N nucleus due to the directly bonded proton……	32
11	Orientation of the internuclear vector and the magnetic field relative to a molecule fixed frame……	35
12	PCR-based cloning strategy…….	42
13	Pulse sequence for the ^{1}H detected heteronuclear single quantum coherence spectrum (HSQC) experiment……..	53
14	PCR products of the Munc13-1(457-492) DNA insert……	58
15	Positive clones for the pGEX2T-Munc13-1(457-492) construct……	58
16	PCR products of the Munc13-1 C_1 domain (Munc 65aa) DNA insert……	59
17	PCR products of the Munc13-1 (185aa) DNA insert……...	59
18	Over expression and purification from pGEX2T-Munc13-1(457-492) construct……	60
19	Munc13-1 (457-492) peptide purification……	60
20	Overexpression of the MBP- Munc13-1(457-492) fusion protein……...	61
21	Overexpression and purification of the Munc65aa-$(his)_6$ protein……	62
22	Overexpression of the GST-Munc65aa fusion protein…….	62
23	Overexpression of the pET16b-Munc185aa construct…….	63
24	Co-expression of the pET16b-Munc185aa and pET28a CaM constructs……	63
25	Overexpression of the CaM/Munc185aa complex from the pETDuet-1(CaM-Munc185aa) construct……..	64
26	Purification of CaM/Munc185aa……..	64

27 Purification of the CaM/GST-Munc185aa complex…… 65
28 CaM purification……... 66
29 Biochemical separation of Munc185aa…… 66
30 ^{1}H-^{15}N HSQC spectrum of the uniformly labelled ^{15}NCaM/Munc13-1(459-479) peptide complex……... 67
31 Chemical shift perturbation plot for CaM upon binding to the Munc13-1 (459-479) peptide…….. 68
32 ^{15}N-^{1}H HSQC spectra of ^{15}N CaM and ^{15}NCaM/Munc13-1(459-492) peptide complex……. 69
33 Chemical shift perturbation plot for the amide region in CaM upon binding to the Munc13-1 (459-492) peptide…….. 69
34 ^{15}N-^{1}H HSQC spectra for apoCaM and apoCaM/Munc13-1 (459-479) peptide…… 70
35 ^{15}N-^{1}H spectra of apoCaM with increasing amounts of Munc13-1 (459-479) peptide…… 71
36 Saturation binding curve for the Valine 91 NH cross peak of ^{15}N labelled apoCaM upon increasing amounts of Munc13-1 (459-479) peptide……. 71
37 Residues in apoCaM affected by the binding of the Munc13-1 (459-479) and ubMunc13-2 (382-402) peptide……. 72
38 ^{1}H-^{15}N HSQC of the CaM/Munc13-1(459-492) complex at three different activated states……... 72
39 ^{15}N -^{1}H HSQC spectrum of the ^{13}C,^{15}N Munc13-1(457-492) peptide……... 73
40 Strip plots of the 3D-HNN spectrum for three diagonal peaks of the ^{13}C,^{15}N Munc13-1(457-492) peptide…….. 74
41 ^{1}H-^{15}N HSQC of the bound ^{13}C,^{15}N Munc13-1(457-492) peptide to CaM…….... 75
42 Chemical shift perturbation plot of the Munc13-1 (457-492) peptide upon binding to CaM…….. 76
43 Chemical shift difference between the Munc13-1(457-492)/CaM and Munc13-1(457-492)/apoCaM peptide complexes…… 76
44 ^{15}N-^{1}H HSQC spectra of the bound ^{15}N, ^{13}C Munc13-1(457-492) peptide to CaM in H_2O and D_2O…… 77
45 ^{15}N-^{1}H HSQC of the ^{15}N CaM and ^{15}N CaM/^{15}N Munc13-1(185aa) *wt* monomeric (1:1) complex…….. 78
46 ^{15}N-^{1}H HSQC spectra for the ^{15}N CaM/^{15}N Munc13-1(185aa) *wt* monomeric

(1:1) complex and dimeric (2:2) complex……. 79
47 Intensity ratio of the amide cross-peaks between the monomeric (1:1) and dimeric (2:2) ^{15}N CaM/^{15}N Munc13-1(185aa) *wt* complexes……... 79
48 Residues in CaM with line-broadening upon dimerization with Munc13-1 (185aa)…… 80
49 ^{15}N-^{1}H HSQC spectra of the tryptophan Nε-Hε1 side-chain region…….. 80
50 1D-^{1}H spectrum for the amide region of unlabelled Munc13-1 C_1 domain…….. 81
51 ^{15}N-^{1}H HSQC of the C_1 domain of Munc13-1……... 82
52 ^{15}N-^{1}H HSQC spectra for the ^{15}N CaM/^{15}N Munc13-1(185aa) *wt* monomeric (1:1) complex the ^{15}N Munc13-1 C_1 domain……. 82
53 ^{15}N-^{1}H HSQC spectra of the ^{15}N CaM/^{15}N Munc13-1(185aa) *wt* dimeric (2:2) complex in the inactive and active states……... 83
54 ^{15}N-^{1}H HSQC spectra for the ^{15}N CaM/^{15}N Munc13-1(185aa) W489A monomeric (1:1) complex in its inactive and active states…… 83
55 Intensity ratio of the amide cross-peaks for the ^{15}N CaM/^{15}N Munc13-1(185aa) W489A mutant in the absence and presence of its agonist PDBu……. 84
56 Binding curve of the C_1 domain agonist PDBu to the ^{15}N CaM/^{15}N Munc13-1(185aa) W489A monomeric (1:1) complex…… 85
57 Assigned ^{1}H-^{15}N-HSQC spectrum of the ^{13}C,^{15}NCaM/Munc13-1(459-492) peptide complex……. 86
58 Strips extracted from the 3D-CBCA(CO)NH and HNCACB spectra……... 87
59 Strips from the 3D-HNCO and 3D-HN(CA)CO spectra for residues F89 to D93 of CaM……... 88
60 ^{13}C-^{1}H HSQC spectrum of ^{13}C,^{15}N CaM/Munc13-1(459-492) complex……... 89
61 Strips extracted from the 3D-(H)CC(CO)NH-TOCSY spectrum…….. 90
62 Strips extracted from the 3D-H(CC)(CO)NH-TOCSY spectrum…….. 91
63 Strips selected from the 3D-HCCH-TOCSY spectrum to illustrate the side-chain assignment of Valine108 in CaM……. 92
64 2D-HBCB(Caro) spectra for the aromatic side chain proton assignments (Hε and Hδ)……... 93
65 3D-HMBC spectrum for methionine ε-CH_3 assignment……... 94
66 Selected amide cross peaks of the 3D-^{15}N (edited) NOESY-HSQC for ^{13}C,^{15}N CaM/Munc13-1(459-492) peptide complex…….. 95
67 Selected aliphatic cross peaks of the 3D-^{13}C(edited) NOESY-HSQC for ^{13}C,^{15}N

CaM/Munc13-1(459-492) peptide complex…….. 96
68 Selected aliphatic cross-peaks of CaM that show intermolecular NOEs to the Munc13-1(459-492) peptide in the 3D-(^{13}C-filtered)-NOESY-HSQC…….. 97
69 ^{15}N-^{1}H IPAP-HSQC spectra for ^{15}N CaM/Munc13-1(459-492) complex with bacteriophage Pf1 as cosolvent and in isotropic conditions …….. 98
70 Correlation plots for the measured NH residual dipolar couplings of the ^{15}N CaM/Munc13-1(459-492) peptide complex aligned sterically with Pf1……... 99
71 Paramagnetic alignment of the ^{15}N CaM/Munc13-1(459-492) peptide complex with an EDTA-based lanthanide binding tag……. 100
72 Secondary chemical shift for the Hα resonance of CaM in complex with the Munc13-1(459-492) peptide…….. 101
73 Secondary chemical shift for the Hα resonance of the ^{13}C,^{15}N Munc13-1(457-492) bound to CaM…… 102
74 Number of NOE restraints per amino acid residue in CaM and the Munc13-1(457-492) peptide……. 102
75 Contact map for the CaM/Munc13-1(457-492) peptide complex…….. 103
76 Survey of the sequential and medium range ^{1}H-^{1}H NOEs along the primary sequence of CaM and the Munc13-1 peptide (457-492)…… 104
77 Different models for the backbone conformation of the Munc13-1(457-492) peptide…… 105
78 Model of the CaM/Munc13-1 docked structure based on intermolecular NOEs and NH residual dipolar couplings……. 106
79 CaM/Munc13-1(457-492) peptide complex calculated with CYANA using the full-length CaM and peptide restraints…….. 107
80 CaM/Munc13-1 (457-492) peptide complex calculated with the C-terminal domain distance constraints for CaM……. 107
81 Ribbon and surface representation of the C-terminal domain of CaM bound to the N-terminal amphiphilic α-helix of the Munc13-1 (457-492) peptide…….. 108
82 Ribbon and surface representations for the N-terminal domain of CaM bound to the C-terminal part of the Munc13-1 (457-492) peptide…… 108
83 Ramachandran plot of the ensemble of 20 structures of the CaM/Munc13-1(457-492) peptide complex…….. 109
84 Cylinder α-helical representation of CaM for interhelical angle measurements……. 110

85 Overlay of C-terminal domain of CaM/Munc13-1(457-492) peptide complex with the CaM/smMLCK and CaM/CaMKII peptide complex structures…….. 111
86 Overlay of N-terminal domain of the CaM/Munc13-1(457-492) peptide complex with the CaM/CaMKII peptide complex and the CaM N-terminal structures…… 111
87 Molecular structures of pk1 and pk2 paramagnetic tags…… 112
88 Molecular structures of t43L and t43D paramagnetic tags…… 112
89 Titration of the apoCaMS17C-t43D with Tb^{3+}…….. 113
90 Correlation plot of the measured rDCs for the N-terminal domain of apoCaMS17C-T43D-Tb^{3+} and apoCaMS17C-T43L-Tb^{3+}…… 114
91 ^{15}N-^{1}H-HSQC spectra for ^{15}N apoCaMS17C-t43L and ^{15}N apoCaM S17C-t43L-Tb^{3+}…… 115
92 Correlation plot between the measured PCS for apoCaMS17C-t43D-Tb^{3+} and apoCaMS17C-t43L-Tb^{3+} against the back-calculated PCS……... 116
93 Correlation plot between the measured PCS for apoCaMS17C-pk2-Tb^{3+} and the back-calculated PCS……... 117
94 Location of the metal ion (Tb^{3+}) based on the PCS restraints for the N-terminal domain of apoCaMS17C-t43D, apoCaMS17C-t43L and apoCaMS17C-pk2….. 117
95 Relationship of the measured lanthanide ion- amide distances and the observed PCS for apoCaMS17Ct43D-Tb^{3+} and apoCaMS17Ct43L-Tb^{3+}…… 118
96 Histogram for the measured residual dipolar couplings of the C-terminal domain of the CaMT146C-pk2-Tb^{3+}/C20W peptide complex…….. 119
97 Histogram for the measured residual dipolar couplings of the N-terminal domain of the CaMT146C-pk2-Tb^{3+}/C20W peptide complex…….. 119
98 Correlation plots for the measured rDCs for the C-terminal domain and N-terminal domain of the CaMT146C-pk2-Tb^{3+}/C20W peptide complex…… 120
99 ^{15}N-^{1}H HSQC spectra for the holoCaMT146C-t43D aligned with Tb^{3+} and with Tm^{3+}…… 121
100 Correlation plot between the measured rDCs and back-calculated rDCs for the C-terminal domain of CaMT146C-pk2-Tb^{3+}……. 121
101 Distribution for the Axial component of the alignment tensor for the CaMT146C-pk2-Tb^{3+}/C20W peptide complex…….. 122
102 Distribution for the Rhombic component of the alignment tensor for the CaMT146C-pk2-Tb^{3+}/C20W peptide complex…….. 122

103 Mapping of the individual tensor values for the 1000 SVD calculations on a 3D plot for the CaMT146C-pk2-Tb^{3+}/C20W complex…… 122
104 Distribution for the axial component (Da) of the alignment tensor for CaMT146C-pk2-Tb^{3+}……. 123
105 Distribution for the Rhombic component of the alignment tensor for the C-terminal domain of CaMT146C-pk2-Tb^{3+}……. 123
106 Mapping of the individual tensor values for the 1000 SVD calculations on a 3D plot for CaMT146C-pk2-Tb^{3+}…… 124
107 Correlation plot of the measured PCS for the C-terminal domain of CaMT146C-pk2-Tb^{3+} and its complex with the C20W peptide against the back-calculated PCS…… 125
108 Correlation plot between the measured distances between the lanthanide ion and each amide proton and the observed PCS for CaMT146C-pk2-Tb^{3+}…….. 125
109 Correlation plot between the measured distances between the lanthanide ion and each amide proton and the observed PCS for CaMT146C-pk2-Tb^{3+}/C20W peptide complex……. 126

List of Tables

No.		Page
1	Oligonucleotide primers for site-directed mutagenesis……	48
2	NMR spectra acquired for the solution structure determination of the CaM/ Munc13-1(457-492) peptide complex……..	53
3	NMR experiments for the sequential backbone and side chain resonance assignment of the $^{13}C,^{15}N$ Munc13-1 (457-492) peptide…….	75
4	NMR experiments for the sequential resonance assignment of the backbone and side chain atoms in the $^{13}C,^{15}N$ CaM/Munc13-1(459-492) peptide complex…….	86
5	Summary of the structure statistics for the NMR solution structure of the CaM/Munc13-1 (457-492) peptide complex……	109
6	Comparison of the interhelical angles for the CaM/Munc13-1(457-492) peptide complex and previous high resolution CaM structures with different EF-hand states……...	110
7	Axial (Da-HN) and Rhombic(Rhomb.) components (apoCaMS17C) of the alignment tensors and angles between them achieved for the four paramagnetic tags bound to Terbium……..	113
8	Axial (Da-HN) and Rhombic(Rhomb.) components of the alignment tensors and angles between them achieved for the holoCaM samples aligned with Terbium…….	118
9	Axial (Da-HN) and Rhombic(Rhomb.) components of the alignment tensors and angles between them achieved the CaMT146C/C20W complex aligned with Terbium……	120

I. INTRODUCTION

1. Signal transduction and second messengers

Calcium is one of the most important signaling entities in the living cell and its intracellular levels are tightly regulated; at high concentrations calcium is also toxic for cells. Calcium is known as a "second messenger", since its concentration is regulated after a first signal arrives to the cell. Most intracellular Ca^{2+} ions are sequestered in the mitochondria and endoplasmic reticulum (ER) or other vesicles. Cells employ various mechanisms for regulating the concentration of free Ca^{2+} ions in the cytosol, which usually is kept below 0.2 μM. Ca^{2+}-ATPases pump cytosolic Ca^{2+} ions across the plasma membrane to the cell exterior or into the lumens of the endoplasmic reticulum or other intracellular vesicles that store Ca^{2+} ions. (Lodish *et al*., 2000).

The precise spatial control of Ca^{2+} release from intracellular stores also plays an important role in cell physiology. Localized increases in the cytosolic level of free Ca^{2+} are critical to its function as a second messenger. In secretory cells, such as insulin-producing β cells in the pancreatic islets, a rise in Ca^{2+} triggers the exocytosis of secretory vesicles and the release of insulin. (Lodish *et al*., 2000).

Other important cellular second messengers are lipidic in nature; phosphoinositides can be cleaved by the membrane associated enzyme phospholipase C (PLC) to generate second messengers. These cleavage reaction produce 1,2-diacylglycerol (DAG), a lipophilic molecule that remains linked to the membrane, and free phosphorylated inositols, which can diffuse into the cytosol. The main pathway generates DAG and inositol 1,4,5-trisphosphate (IP_3). (Lodish *et al*., 2000).

Since IP_3 is water-soluble it diffuses within the cytosol carrying a hormone signal from the cell surface to the ER surface. IP_3 binds to a Ca^{2+}-channel protein composed of four identical subunits, each containing an IP_3 binding site in the large N-terminal cytosolic domain. IP_3 binding induces opening of the channel allowing Ca^{2+} ions to exit from the ER into the cytosol. The resulting rise in the cytosolic Ca^{2+} level is only transient because of the activity of the Ca^{2+}-ATPase pumps. In addition, within a second of its generation, IP_3 is hydrolyzed to inositol 1,4-bisphosphate, which does not stimulate Ca^{2+} release from the ER. The IP_3 receptor in the ER membranes is regulated in a complex manner, which give rise to rapid oscillations in the cytosolic Ca^{2+} level when the IP_3 pathway in cells is stimulated. (Lodish *et al*., 2000).

After the action of PLC on phosphatidyl-inositol phosphate, the diacylglycerol (DAG) remains associated with the membrane. The principal function of DAG is to activate a family of plasma-membrane protein kinases collectively termed protein kinase C. In the absence of hormone stimulation, protein kinase C is present as a soluble cytosolic protein that is catalytically inactive. A rise in the cytosolic Ca^{2+} level causes protein kinase to bind to the cytosolic leaflet of the plasma membrane, where it can be activated by the membrane-associated DAG. Thus, activation of protein kinase C depends on both Ca^{2+} ions and DAG, suggesting an interaction between the two branches of the inositol-lipid signaling pathway. (Lodish *et al*., 2000).

The activation of protein kinase C in different cells results in a varied array of celluar responses, indicating that it plays a key role in many aspects of cellular growth and metabolism. In liver cells, for instance, protein kinase C helps regulate glycogen

metabolism by phosphorylating glycogen synthase, yielding the inactive form of this enzyme. Protein kinase C also phosphorylates various transcription factors; depending on the cell type, these induce or repress synthesis of certain messenger RNAs. (Lodish *et al*., 2000).

2. Synapses and calcium signaling in neurons

Synapses generally transmit signals in only one direction: an axon terminal from the presynaptic cell sends signals that are picked up by the postsynaptic cell. There are two general types of synapse: the relatively rare electric synapse and the chemical synapse (see Figure 1). In the later type of synapse, the axon terminal of the presynaptic cell contains vesicles filled with a particular neurotransmitter. The postsynaptic cell can be a dendrite or cell body of another neuron, a muscle or gland cell. When an action potential in the presynaptic cell reaches an axon terminal, it induces a localized rise in the level of Ca^{2+} in the cytosol. This, in turn, causes some of the vesicles to fuse with the plasma membrane, releasing their contents in to the synaptic cleft, the narrow space between the cells. The neurotransmitters diffuse across the synaptic cleft; it takes about 0.5 milliseconds (ms) for them to bind to receptors on postsynaptic cells. (Lodish *et al*., 2000).

Binding of the neurotransmitter triggers changes in the ion permeability of the postsynaptic plasma membrane, which, in turn, changes the membrane's electric potential at this point. If the postsynaptic cell is a neuron, this electric disturbance may be sufficient to induce an action potential. In some cases, enzymes attached to the fibrous network connecting the cells destroy the neurotransmitter after it has functioned; in other cases, the signal is terminated when the neurotransmitter diffuses away or is transported back into the presynaptic cell. (Lodish *et al*., 2000).

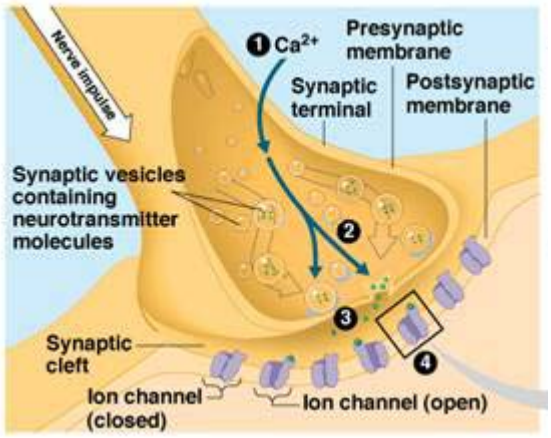

Figure 1. Anatomy of a typical chemical synapse. The inner structure of the presynaptic button is also shown (taken from FSU, 1999).

The exocytosis of neurotransmitters from synaptic vesicles involves vesicle-targeting and fusion events similar to those that occur at many points in the secretory pathway. The same types of proteins- including T-SNARE and V-SNAREs, α, β, and γ SNAP proteins, and NSF- participate in both systems. However, exocytosis of neurotransmitters at chemical synapses differs from other secretory pathways in two

critical ways: (a) Secretion is tightly coupled to arrival of the action potential at the axon terminus, and (b) synaptic vesicles are recycled locally after fusion with the plasma membrane, a process that takes less than one minute. (Lodish *et al*., 2000).

Depolarization of the plasma membrane cannot, by itself, cause synaptic vesicles to fuse with the plasma membrane. In order to trigger vesicle fusion, an action potential must be transduced into a chemical signal – namely, a localized rise in the cytosolic Ca^{2+} concentration. The transducers of the electric signals are voltage-gated Ca^{2+} channels localized to the region of the plasma membrane adjacent to the synaptic vesicles. The membrane depolarization due to arrival of an action potential opens these channels, permitting an influx of Ca^{2+} ions into the cytosol from the extracellular medium. The amount of Ca^{2+} that enters an axon terminal through voltage-gated Ca^{2+} channels is sufficient to raise the level of Ca^{2+} in the region of the cytosol near the synaptic vesicles from < 0.1 μM, characteristic of the resting state, to 1-100 μM. Ca^{2+} ions binds to proteins that connect the synaptic vesicle with the plasma membrane, inducing membrane fusion and thus exocytosis of the neurotransmitter. The extra Ca^{2+} ions are rapidly pumped out of the cell by Ca^{2+}-ATPases, lowering the cytosolic Ca^{2+} level and preparing the terminal to respond again to an action potential. (Lodish *et al*., 2000).

Patch-clamping experiments show that voltage-gated Ca^{2+} channels, like voltage-gated Na^{+} channels, open transiently upon depolarization of the membrane. Two pools of neurotransmitter-filled synaptic vesicles are present in axon terminals: those "docked and primed" at the plasma membrane, which can be readily exocytosed, and those in reserve in the active zone near the plasma membrane. Each rise in Ca^{2+} triggers exocytosis of about 10 percent of the docked vesicles. (Lodish *et al*., 2000).

3. Synaptic vesicles

Synaptic vesicles are small abundant organelles and homogeneous in size (~20-nm radius). Their only known function is to take up and release neurotransmitters. Purified vesicles have a protein:phospholipid ratio of 1:3. Many proteins that have been associated with synaptic vesicles are probably present only on a subset of vesicles or bind transiently to the vesicles, and the number of proteins that are constitutive parts of all synaptic vesicles may be comparatively small. (Südhof, 2004).They can be readily purified from the brain and their proteins isolated. The synaptic-vesicle membrane contains V-type ATPases, which generate a low intravesicular pH, and a proton-coupled neurotransmitter antiporter, which imports neurotransmitters from the cytosol. (Lodish *et al*., 2000). They also contain transport proteins including intrinsic membrane proteins; proteins associated via posttranslational lipid modifications, and peripherally bound proteins. (Südhof, 2004).

The vesicles are linked together by synapsin, a fibrous phosphoprotein structurally related to other cytoskeletal proteins that bind the fibrous proteins actin and spectrin. Synapsin is localized to the cytosolic surface of all synaptic-vesicle membranes and constitutes 6 percent of vesicle proteins. Thicker filaments radiate from the plasma membrane and bind to vesicle-associated synapsin; probably these interactions keep the synaptic vesicles close to the part of the plasma membrane facing the synapse. Synapsin knockout mice, although viable, are prone to seizures; during repetitive stimulation of many neurons in such mice, the number of synaptic vesicles that fuse with the plasma

membrane is greatly reduced. Thus synapsins are thought to recruit synaptic vesicles to the active zone. Synapsins are substrates of cAMP-dependent and Ca^{2+}-calmodulin (CaM)– dependent protein kinases, a rise in cytosolic Ca^{2+} triggers their phosphorylation, causing their release from the cytoskeleton increasing the number of vesicles available for fusion with the plasma membrane. (Lodish *et al*., 2000).

Rab3A is a neuron-specific GTP-binding protein similar in sequence and function to other Rab proteins that control vesicle traffic in the secretory pathway. Rab3A is located in the membrane of synaptic vesicles and appears to be essential for localization of vesicles to the active zone. Rab3A knockout mice are viable, but repetitive stimulation of certain neurons in such mice causes a reduction in the number of synaptic vesicles able to fuse with the plasma membrane. (Lodish *et al*., 2000).

The principal V-SNARE in synaptic vesicles is VAMP (vesicle-associated membrane protein), also called synaptobrevin. This V-SNARE binds syntaxin and SNAP25, the principal T-SNAREs in the plasma membrane of axon terminals. SNAP proteins and NSF assist in the disassociation of VAMP from T-SNAREs after vesicle fusion. (Lodish *et al*., 2000).

Another protein in the synaptic vesicle membrane called synaptotagmin contains four Ca^{2+} binding sites in its cytosolic domain. Several types of evidence support the hypothesis that synaptotagmin is the key Ca^{2+}-sensing protein that triggers fast vesicle exocytosis. (Lodish *et al*., 2000).

At low Ca^{2+} levels found in resting cells, synaptotagmin apparently binds to a complex of the plasma membrane proteins neurexin and syntaxin. The presence of synaptotagmin blocks the binding of other essential fusion proteins to the neurexin-syntaxin complex, thereby preventing vesicle fusion. When synaptotagmin binds Ca^{2+} it is displaced from the complex, allowing other proteins to bind and thus initiating membrane docking and fusion. (Lodish *et al*., 2000)

Neurotransmitter-filled synaptic vesicles are docked at a specialized region of the presynaptic plasma membrane known as the active zone. The docked vesicles then go through a maturation process called priming to become fusion competent. Voltage-gated Ca^{2+} channels open during an action potential. The resulting pulse of intracellular Ca^{2+} triggers fusion-pore opening of ready-releasable vesicles. In most synapses, release is stimulated by Ca^{2+} influx through P/Q-($Ca_V2.1$) or N-type Ca^{2+}-channels ($Ca_V2.2$). Even at rest, synapses have a finite but low probability of release; causing spontaneous events of exocytosis that are reflected in electrophysiological recordings as miniature postsynaptic currents. Ca^{2+} influx triggers at least two components of release that are probably mechanistically distinct: A fast, synchronous phasic component is induced rapidly, in as little as 50μs after a Ca^{2+} transient develops, and a slower asynchronous component continues for > 1s as an increase in the rate of spontaneous release after the action potential. Both components of release are strictly Ca^{2+} dependent but change differentially upon repetitive stimulation. (Südhof, 2004).

4. Brain modulator protein: calmodulin

Initial biochemical studies on calmodulin (CaM) already pointed towards a high expression level in the brain; this protein was identified as a modulator of 3':5'-cyclic nucleotide phosphodiesterase. The modulator protein represents approximately 1% of the

soluble protein present in the initial bovine brain homogenate supernatant. The overall yield of bovine brain modulator protein obtained was 40mg/kg of brain (13% from the original homogenate). The bovine brain modulator has two sets of Ca^{2+}- binding sites. High affinity binding (k_d = 1 x 10^{-6} M) of 2 mol of Ca^{2+} bound/18,000 g of protein was observed. Two additional mol of Ca^{2+}/18,000 g of protein bound with a dissociation constant of 8.6 x 10^{-4} M. A number of other Ca^{2+}- binding proteins have been isolated from brain, the S-100 protein fraction from brain, and other small acidic Ca^{2+} binding proteins Wolff *et al*., 1972 have reported the isolation and characterization of a Ca^{2+} binding phosphoprotein from porcine brain, later it was known that CaM can be phosphorylated. The physicochemical properties of bovine brain modulator protein are very similar to those of rabbit skeletal muscle Troponin C, which regulates myosin action in muscle contraction. This modulator protein arose early in eukaryotic evolution as a mediator of calcium second messenger function, and the interaction sites on both modulator protein and the enzymes it regulates have been highly conserved (Watterson *et al.*, 1980).

CaM is expressed in high concentrations in the brain (from 10 to 100 μM in different areas of the brain). The average dissociation constant (k_d) for the four Ca^{2+} binding sites of ~ 15 μM, the physiological calcium concentrations lies between 0.1 and 10 μM, this apparent discrepancy was resolved when it was shown that CaM-protein complexes show heterotropic positive cooperativity for Ca^{2+} binding. This allows CaM-regulated proteins to be activated in the presence of normal physiological concentrations of free Ca^{2+}. (Xia and Storm, 2005).

In resting neurons, much of the CaM is associated with three proteins: neuromodulin, neurogranin and regulator of CaM signaling (RCS), which are thought to regulate the levels of free CaM or control the activity of CaM. Neuromodulin contributes to synaptic plasticity by controlling the levels of free CaM available presynaptically. (Xia and Storm, 2005)

5. The EF-hand superfamily of proteins: calmodulin plasticity

Each CaM molecule binds four Ca^{2+} ions (see Figure 2). Binding of Ca^{2+} causes CaM to undergo a conformational change that enables the Ca^{2+}-CaM complex to bind to and activate many enzymes, such as myosin light-chain kinase (MLCK), which regulates myosin activity. Because Ca^{2+} binds to CaM in a cooperative fashion, a small change in the level of cytosolic Ca^{2+} leads to a large change in the level of active CaM. The Ca^{2+}-CaM complex also activates several protein kinases that, in turn, phosphorylate transcription factors, thereby modifying their activity and regulating gene expression. (Lodish *et al*., 2000).

The CaM superfamily is a major class of Ca^{2+} sensor proteins, which collectively play a crucial role in various cellular signaling cascades through regulation of numerous target proteins in a Ca^{2+} dependent manner. (Ikura and Ames, 2006).

CaM contains four EF-hand motifs; with highly conserved amino acid sequences in all eukaryotes (see Figure 3). Typically, a pair of EF-hand motifs in tandem array constitutes a stable structural unit, together generating cooperativity in the binding of Ca^{2+} ions. Many EF-hand proteins, such as CaM and members of the neuronal calcium

sensor family, consist of four EF-hand motifs. This results in two globular structural units in a single protein. (Ikura and Ames, 2006).

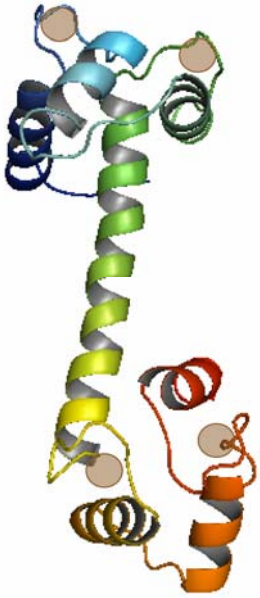

Figure 2. Molecular model of CaM X-ray crystallographic structure (Babu *et al*., 1988). The calcium ions are depicted as brown spheres.

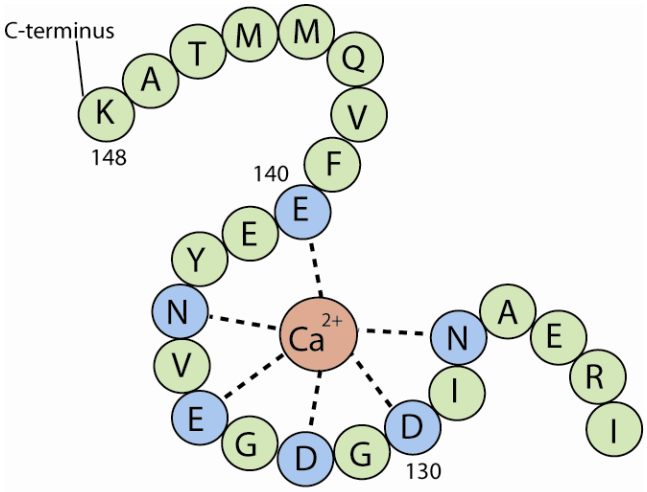

Figure 3. Model of the EF-hand motif. The coordination of a calcium ion is mediated by six amino acid residues from the loop, shown in blue (adapted from Lodish *et al*., 2000).

The direct interaction with Ca^{2+} enables these Ca^{2+} sensor proteins to change their conformation from the inactive state (P) to the intermediate state (Ca^{2+} -P*), which is a prerequisite to the formation of an active conformation in complex with a target (Ca^{2+}-P**-E*) required to transform the target protein from its inactive state (E) to the active state (E*)

$$P \rightleftharpoons Ca^{2+}\text{-}P^* \rightleftharpoons Ca^{2+}\text{-}P^{**}\text{-}E^*$$

The first conformational transition is essential to the Ca^{2+} sensory function and is universal to all Ca^{2+} sensor proteins. The second conformation change plays a critical role in the activation and recognition of specific targets. (Ikura and Ames, 2006).

CaM regulates numerous target proteins that are functionally and structurally diverse. The first structure determined for CaM in complex with a target protein showed a remarkable conformational change in CaM's two EF-hand domains upon binding to a peptide derived from myosin light chain kinase (MLCK). This structure revealed that the central domain linker is highly flexible and can be bent dramatically upon binding to the target protein. The flexibility of the domain linker permits the orientation of the two domains of CaM to change independently to accommodate the structural nature of the target protein. In addition, two hydrophobic anchoring residues from the smooth muscle MLCK peptide (Trp-800 and Leu-813) bind simultaneously to the hydrophobic pocket in N- and C-terminal domains, which is extremely rich in methionine residues. (Ikura and Ames, 2006).

CaM can adopt largely different, global conformations depending on the structural entity that CaM binds. In addition to plasticity of the protein fold, the amino acid side chains that interact with target proteins, in particular the methionine residues are remarkably flexible. The protein conformational plasticity of CaM emerged as a means of achieving functional diversity rather than employing the more traditional approach of genetic polymorphism. (Ikura and Ames, 2006).

Among the numerous CaM target proteins, CaM-dependent serine/theronine kinases are the substrate family best characterized with respect to their structural and functional CaM interaction mechanisms. Previous studies on CaM kinase II, CaM kinase kinase, and myosin light chain kinases showed that CaM could assume at least three different conformations by virtue of a flexible linker connecting two globular domains responsible for binding both Ca^{2+} ions and its target proteins. These interactions all involve short helices (approximately 20 residues) formed by the CaM binding domain of the kinases. From these complexes, defined CaM recruitment motifs currently fall into three groups (1-10, 1-14, and 1-16^{-}), which are distinguished by their spacing of bulky hydrophobic and basic amino acid residues (see Figure 4). The binding mode of these different synthetic peptides was resolved when the atomic resolution structures of three CaM-peptide complexes from smooth muscle myosin light chain kinase (smMLCK) (Meador *et al*., 1992), skeletal muscle myosin light chain kinase (skMLCK) (Ikura *et al*., 1992) and CaM-dependent kinase IIα (Meador *et al*., 1993).
Another CaM binding motif is the so-called "IQ motif", corresponding to an IQxxxRGxxxR consensus sequence, which appears in tandem repeats and bind multiple CaM molecules in a predominantly Ca^{2+} independent manner. (Hoeflich and Ikura, 2002).

CaM-dependent serine/theronine protein kinases and the phophatase calcineurin are all known to use a similar mechanism underlying CaM-dependent activation, namely autoinhibitory domain (AID) displacement. In these cases, the CaM binding site is often adjacent or within an autoinhibitory domain of the enzyme which contains a pseudosubstrate region. CaM binding to the target induces a conformational rearrangement that displaces the pseudosubstrate inhibitory domain and allows for full enzyme activity (see Figure 5). (Hoeflich and Ikura, 2002).

Figure 4. CaM peptide recognition motifs. The hydrophobic anchors of the amphiphilic α-helix are highlighted in red

The crystal structure of *Bacillus anthracis* adenylyl cyclase (Drum *et al.*, 2002), the edema factor (EF) of this pathogenic bacterium revealed a new CaM interaction mode. The EF activation involves active site remodeling. This process involves rearrangement of key switches to create the active site from an area that is totally solvent exposed in the CaM-free state. CaM trapping by EF may be a key factor in regulating its selective activity in the host cells. EF might also be more stable in the CaM-bound state as compared to the CaM-free state, thereby increasing resistance to proteolytic turnover and lengthening its half-life time in cells. (Hoeflich and Ikura, 2002).

In addition to the release of autoinhibitory domains and active site remodeling, a third mechanism is now known for CaM action: CaM-induced dimerization of membrane proteins as a system underlying ion channel activation. (Hoeflich and Ikura, 2002).

Small conductance Ca^{2+}-activated potassium (SK) channels play a fundamental role in regulating neuronal excitability. SK channels use K^+ as their charge carrier, but are gated solely by intracellular Ca^{2+} ions at the sub-micromolar level, such as occur during an action potential in many neurons. (Hoeflich and Ikura, 2002).

A unique feature of SK channel α-subunits is constitutive association with CaM. This interaction is maintained both in the presence or absence of Ca^{2+}. However, channel gating also requires a Ca^{2+}-dependent interaction. Schumacher and colleagues (2001) have shown from the crystal of the Ca^{2+}-loaded CaM/SK2 complex that the complex presents as two CaM molecules tightly sandwiching two K^+ channel domains. This is the first observation of a 2:2 CaM-target complex and the active tetrameric form of the channel would likely require two sets of 2:2 dimers. CaM uses a modular strategy in which the carboxy-terminal EF hands mediate tethering to the channel and the amino-terminal EF hands are responsible for Ca^{2+}-induced dimerization leading to channel gating and direct coupling between changes in intracellular Ca^{2+} concentrations and altered membrane potential. In this 2:2 arrangement, CaM adopts a very elongated structure thereby facilitating interaction of single CaM molecule with 3 α helices. (Hoeflich and Ikura, 2002).

CaM has been also shown to play a prominent role in modulating the hallmark feedback inhibition or CDI (Ca^{2+}-dependent inactivation) of P/Q- and L-type voltage-

dependent Ca^{2+} channels, and cyclic nucleotide-gated channels of the visual and olfactory systems. Fallon and collaborators (2005) solved the crystal structure of CaM bound to the hydrophobic IQ domain of the cardiac $Ca_V1.2$ calcium channel. The structure shows that parallel binding of CaM to the IQ domain is governed by hydrophobic interactions and it represents the conformation that CaM assumes in calcium dependent facilitation. In the case of L-type channels, Ca^{2+}-sensitive CaM association occurs via a standard IQ motif in the pore-forming α_1 subunit of the channel. As in the case with SK channels, binding of Ca^{2+} to only a single CaM lobe is sufficient to trigger gating, in this channel system, it is the C-terminal CaM domain which binds the Ca^{2+} ions. The picture that emerges is one in which CaM interacts in a bipartite manner with ion channels: one CaM module mediating constitutive binding and the other transmitting Ca^{2+} dependence. (Hoeflich and Ikura, 2002).

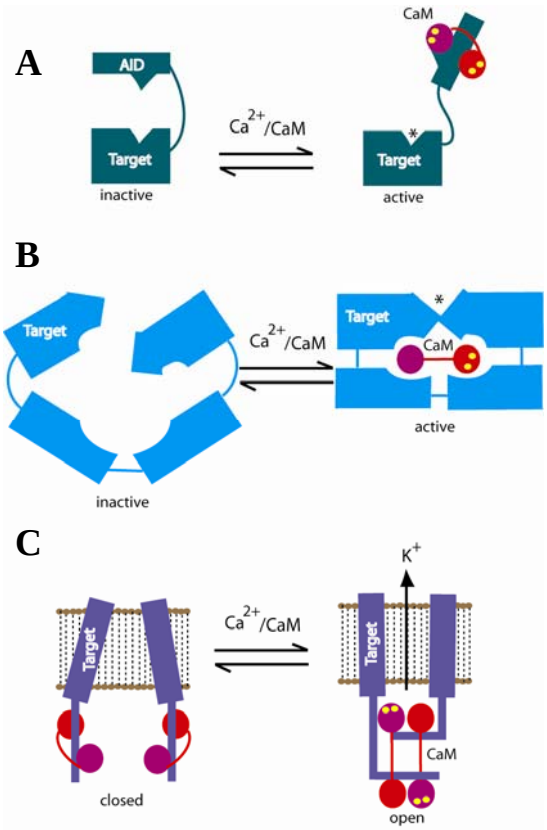

Figure 5. Different activation models for CaM binding partners. **A.** Relieving autoinhibition. **B.** Active site remodeling. **C.** Dimerization. Calcium ions are depicted in yellow and active sites by asterisks (adapted from Hoeflich and Ikura, 2002).

Most physiological relevant CaM targets are proteins, but CaM also binds to a number of synthetic peptides corresponding to CaM binding domains, to peptide hormones and toxins, as well as to small drug like molecules. (Vetter and Leclerc, 2003).

The CaM/CaMKIIα complex is of ellipsoidal shape and much more compact (50 x 30 x 30 Å) than Ca^{2+}/CaM without the peptide (maximal length of 65 Å). The central linker region is unwound and allows the C- and N-terminal lobes to bend by 100^o and to rotate by 120^o relative to their orientation seen in the Ca^{2+}/CaM crystal structure. The

peptide is bound in an α-helical conformation and is engulfed by Ca^{2+}/CaM into a hydrophobic channel formed by bringing the C- and N-terminal lobes close together. (Vetter and Leclerc, 2003).

Matsubara and collaborators (2004) solved the crystal structure of Ca^{2+}-CaM bound to a myristoylated peptide derived from the N-terminal domain of CAP-23/NAP-22. The binding of CAP-23/NAP-22 to CaM is dependent on myristoylation; only the myristoylated recombinant protein binds to CaM.

Yap and collaborators (2003) solved the solution structure of CaM in complex with a peptide from the plant glutamate decarboxylase (GAD). The interaction is atypical, since the C-terminal domain of CaM of GAD interacts simultaneously with two GAD peptides.

The domain orientation of CaM in the CaM-GADp complex is affected by the large dimeric peptide volume. This volume is significantly larger (5600 $Å^3$) than the peptide volumes in the CaM crystal complexes with smMLCKp (1765 $Å^3$), CaM-dependent protein kinase I peptide (2413 $Å^3$), Ca^{2+}/CaM-dependent protein kinase II peptide (1611 $Å^3$) and Ca^{2+}/CaM-dependent protein kinase kinase peptide (2275 $Å^3$). In accommodating the larger GADp volume, CaM does not wrap around the peptides completely. Backbone $\{^1H\}$-^{15}N NOE relaxation measurements indicate that in complex with GADp, the interdomain linker exhibits some flexibility but is more rigid compared to Ca^{2+}-loaded CaM. (Yap *et al*., 2003).

6. Regulated exocytosis

Fusion of a transport vesicle with its target membranes is a fundamental process essential to cellular organization and function of all eukaryotic cells. Several protein families involved in fusion are conserved from yeast to human, and are shared not only by constitutive and regulated exocytosis but also by various intracellular membrane fusion events. The conserved protein families include soluble N-ethyl-maleimide-sensitive factor attachment protein receptors (SNAREs), ATPase N-ethylmaleimide-sensitive factor (NSF), Munc18/Sec1, RabGTPases, and protein components of the exocyst complex. (Li and Chin, 2003).

Compared with other forms of membrane fusion, synaptic vesicle exocytosis is much more tightly regulated both in time and space. Temporally, Ca^{2+}-triggered secretion of neurotransmitters occurs in less than a millisecond after the arrival of an action potential. Spatially, synaptic vesicle exocytosis takes place only at the active zone, and nowhere else along the axonal membrane. Synaptic vesicle exocytosis utilizes several regulatory components, including synaptotagmin, complexin, Munc13, and RIM, which do not have homologues in yeast. (Li and Chin, 2003).

The best-characterized candidate Ca^{2+} sensor in triggering fast neurotransmitter release is synaptotagmin, an integral membrane protein of synaptic vesicles with two Ca^{2+}-binding C_2 domains. The C_2A domain of synaptotagmin has been shown to bind three Ca^{2+} ions, whereas the C_2B domain binds two Ca^{2+} ions. Synaptotagmin binds via both C_2 domains to phospholipids in a Ca^{2+}-dependent manner with half-maximal binding Ca^{2+} concentrations in the range of 5-20μM, which correspond very well with physiological Ca^{2+} levels for triggering neurotransmitter release at some synapses. (Li and Chin, 2003).

Complexin I and II are two closely related ~15-kDa cytosolic proteins originally identified based on their brain-specific expression and ability to bind neuronal SNARE complexes. Double-knockout mice lacking both complexins are perinatally lethal with a marked deficit in fast Ca^{2+}-triggered neurotransmitter release, suggesting that complexins positively regulate a late step of synaptic vesicle exocytosis. Complexin and synaptotagmin are able to bind simultaneously to the assembled SNARE complex. (Li and Chin, 2003).

A crucial step in synaptic vesicle exocytosis is priming, which confers fusion competence to docked vesicles, enabling them to undergo rapid exocytosis upon Ca^{2+} influx. (Li and Chin, 2003).

Synaptic vesicle priming requires the Munc13/UNC-13 family of proteins. UNC-13 was originally identified in *C.elegans* genetic screens for uncoordinated mutants. Munc13s are mammalian UNC-13 homologues; they are 200-kDa multidomain proteins (see Figure 6) which are encoded by three distinct genes: Munc13-1, Munc13-2, and Munc13-3. These Munc13 isoforms are differentially expressed in brain, where they are specifically localized to the active zone (Silinsky and Searl, 2003).

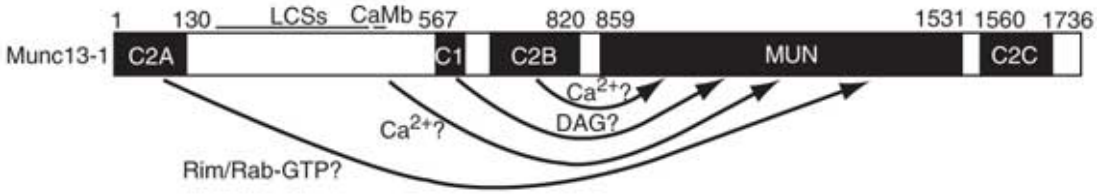

Figure 6. Domain structure of Munc13-1. Arrows illustrate the regulation of MUN domain activity by the diverse agents that mediate presynaptic plasticity processes at the N-terminal region of Munc13-1. Low-complexity sequences (LCSs) and the CaM binding domain (CaMb) are represented by thin lines above. (Taken from Basu *et al*., 2005).

Neurotransmitter release was completely eliminated in the deletion mutants of *C. elegans* and *Drosophila*, and this effect is independent on the nature of the neutortransmitter. When the munc13-1 isoform was deleted in mice, the glutamate release was decreased by 90%. This decrease in secretion was associated with a decrease in the RRP (and thus primed vesicles) as assessed by applying sucrose and quantifying the avalanche of asynchronous release that ensues upon sucrose addition. The regions of Munc13 that bind RIM and syntaxin are both essential for neuronal function. (Silinsky and Searl, 2003).

When Munc13-1 is overexpressed in chromaffin cells, there is a threefold increase in secretion. This increase is due to a threefold larger size of both RRP and SRP and a threefold increase in the sustained component. (Rettig and Neher, 2002).

Munc13/UNC-13 proteins contain a C_1 domain that binds to the endogenous second-messenger diacylglycerol (DAG) and its analogue phorbol ester, and serve as high-affinity diacylglycerol/phorbol ester receptor in brain. (Li and Chin, 2003).

DAG is one of the most important second messengers in mammalian cells. (Brose and Rosenmund, 2002). Munc13s are functional presynaptic DAG/phorbol ester receptors, which, similar to PKCs, translocate to the plasma membrane upon phorbol

ester binding. Studies with genetically modified mice that express mutant Munc13-1 lacking the phorbol ester-binding site instead of the wild-type Munc13-1 from the endogenous locus demonstrated that neurons expressing the mutant Munc13-1 fail to exhibit the robust increase in release in response to phorbol ester treatment. (Leenders and Sheng, 2005).

Electrophysiological analysis of Munc13-1 and Munc13-2 single- and double-knock-out mice suggests that activity-dependent diacylglycerol-mediated Munc13 activation underlies a pre-synaptic form of short-term plasticity termed augmentation. (Brose and Rosenmund, 2002).

Munc13-1 interacts with the N-terminal coiled-coil domain of syntaxin 1 and this interaction appears to be compatible with SNARE complex assembly, suggesting that Munc13-1 bind to the open conformation of syntaxin 1. In *C.elegans*, UNC-13 is able to transiently interact with UNC-18 bound to the closed conformation of syntaxin and displace UNC-18 from syntaxin. Munc13 interacts with at least five other proteins, namely RIM, CaM, Doc2 (an ARF6 exchange factor msec7-1), and a brain-specific spectrin isoform β-spIIIΣ1. (Li and Chin, 2003).

RIM was originally identified in a yeast two-hybrid screen as a 180-kDa, active zone-specific protein that binds specifically to the GTP-bound form of Rab3. The RIM mutant phenotypes are much weaker than Munc13-1 and UNC-13 mutants, suggesting that RIM has a regulatory instead of an essential, executing role in synaptic vesicle exocytosis (see Figure 7). (Li and Chin, 2003).
RIM1 knockout mice exhibited a selective, 60% decrease in expression levels of Munc13-1, but not Munc13-2 or other presynaptic proteins, suggesting that RIM1 normally associates with Munc13-1. (Li and Chin, 2003). In addition to Rab3 and Munc13-1, RIM1 also interacts with SNAP-25, synaptotagmin, Ca^{2+} channels, RIM-BPs, cAMP-GEFII, and liprins. (Li and Chin, 2003).

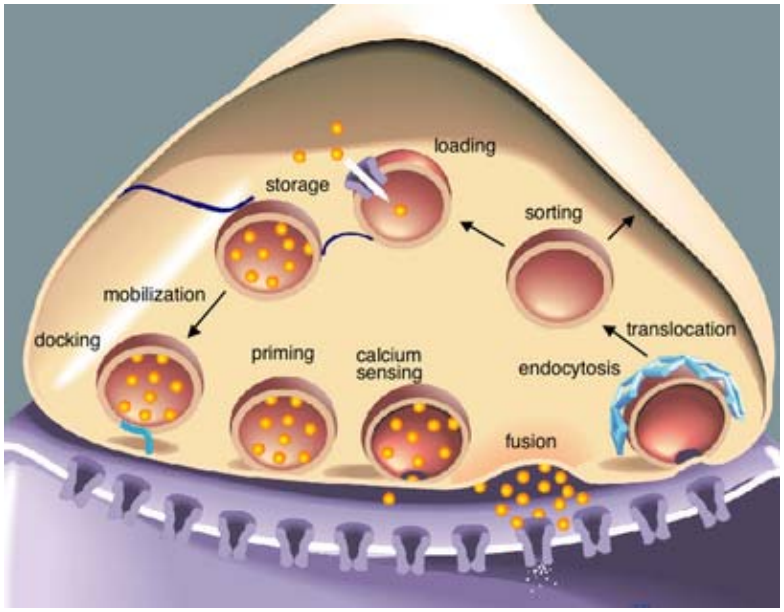

Figure 7. Neurotransmitter vesicle endo- and exocytotic cycle in a presynaptic button (taken from Richmond, 2005).

Junge and collaborators (2004) reported that CaM binds to Munc13-1 and ubMunc13-2 in a Ca^{2+} -dependent manner via an evolutionary conserved CaM recognition motif. CaM binding to Munc13 proteins caused increased priming activity and ready-releasable pool (RRP) sizes. Thus, the activation of the CaM/Munc13 complex by residual calcium represents a molecular correlate for the phenomenon of Ca - dependent vesicle pool refilling. This mechanism controls short-term plasticity characteristics and is likely to be evolutionary conserved.

7. Presynaptic plasticity

Two principal points of regulating presynaptic plasticity exist: (a) the peak Ca^{2+} concentration produced by an action potential, *i.e.*, the conversion of an action potential to a Ca^{2+} current; and (b) the release probability per given Ca^{2+} concentration, *i.e.*, the conversion of a Ca^{2+} signal to exocytosis. Both types of regulation are important. The peak Ca^{2+} concentration depends in principle on the shape of the action potential, the open probability of the Ca^{2+} channels, and the Ca^{2+} concentration present at the time when the Ca^{2+} channels open. All of these three parameters can be regulated. The release probability per peak Ca^{2+} concentration is highly variable and depends on two principal parameters: the number of release-ready vesicles, and the Ca^{2+} responsiveness of the vesicles. The release probability per Ca^{2+} concentration varies characteristically between different types of synapses and changes during cAMP-dependent presynaptic long-term potentiation (LTP). The number of release-ready vesicles decreases during repetitive stimulation, causing a short-term depression with a magnitude that depends on the pool size and kinetics. (Südhof, 2004).

Release of neurotransmitters and hormones is known to proceed in fractions of seconds or even milliseconds after the free Ca^{2+} concentration, $[Ca^{2+}]$, rises. However, it is clear that vesicles have to undergo a number of steps (translocation, docking, priming) before they are ready to fuse in such a rapid manner. These steps are likely to be slower. First, a rapid burst of exocytosis, by vesicles that had been in a release-competent state at the time of the Ca^{2+} increase. This would be followed by a much slower, sustained response (at sustained high $[Ca^{2+}]$) by vesicles that have to undergo preceding, rate-limiting reactions before they can fuse under those conditions. This expectation forms the basis for a possible kinetic distinction between manipulations that affect late-acting molecules and those that are important during earlier steps. (Rettig and Neher, 2002).

Manipulations of the Ca^{2+} sensor should alter the timing of the exocytotic burst. In contrast priming factors would primarily influence the sustained component and/or the amplitude of the exocytotic burst, that is, the number of release-competent vesicles immediately before the stimulus. Detailed kinetic analysis of data from adrenal chromaffin cells revealed that exocytotic burst, after flash-induced liberation of $[Ca^{2+}]$ from "caged" Ca, is not homogeneous. Rather, one has to assume that there are two populations of vesicles that release at largely different rates. (Rettig and Neher, 2002).

Upon photolysis of caged Ca^{2+}, Ca^{2+} triggers release at the calyx of held with a high degree of cooperativity, similar to other synapses. Release was undetectable at Ca^{2+} concentrations of < 1 μM, became measurable at 1-2 μM Ca^{2+}, resembled the release observed during a normal action potential at > 5 μM Ca^{2+}, and saturated at > 20 μM Ca^{2+}.

Thus fast release, at this synapse, is triggered by Ca^{2+} binding to a highly cooperative Ca^{2+} sensor with relatively high apparent Ca^{2+} affinity (k_d 5-25 μM).

The precise Ca^{2+} dependence of release was fitted by different models that led to qualitatively similar but numerically distinct conclusions. In both models, the Ca^{2+} sensor contains 5 Ca^{2+} -binding sites. (Südhof, 2004).

As a result of the high cooperativity of the Ca^{2+} sensor, the relationship of the Ca^{2+} concentration to release is supralinear. This supralinearity restricts release to the brief time period during which the Ca^{2+} transient is above threshold and terminates release rapidly even though residual Ca^{2+} remains. These studies quantitatively described the Ca^{2+} -binding properties of a Ca^{2+} sensor only for fast release but provided little information about the Ca^{2+} sensor for asynchronous release or the adaptations of the release machinery during repetitive stimulation. (Südhof, 2004).

The speed with which Ca^{2+} triggers release (<400 μsec) suggests that Ca^{2+} binding to the Ca^{2+} sensor only induces fusion-pore opening and does not initiate a complex reaction cascade. Fusion pores form an aqueous connection across fusing bilayers and are likely to be at least partly lipidic. (Südhof, 2004).

Following exocytosis, synaptic vesicle membranes and protein constituents are retrieved from the plasma membrane by endocytosis, and locally recycled for future rounds of exocytosis. (Li and Chin, 2003).

In Figure 8 a flash of ultraviolet light rapidly elevated [Ca^{2+}] from a basal level of about 300 nM to about 20 μM. As a consequence, membrane capacitance increased rapidly by about 600 fF. This increase signals the release of about 240 vesicles, because each vesicle fusing with the plasma membrane enlarges its area, contributing about 2.5 fF. (Rettig and Neher, 2002).

The capacitance increases at a rate of about 50 fF/s, which corresponds to an on going rate of exocytosis of about 20 vesicles per second. These would be vesicles that undergo a priming reaction and release immediately (at high [Ca^{2+}]) when they reach the release-competent state. This priming reaction is intimately linked to the initiation of SNARE complex formation. (Rettig and Neher, 2002).

A direct kinetic separation of Ca^{2+}-dependent triggering and priming reactions, as in the case of the flash experiment, is not possible in most nerve terminals. However, in hippocampal cells, vesicle pool sizes at any given moment can be determined as the cumulative release induced by a short sucrose application. This measurement allows studying the recovery of vesicle pools after strong stimuli and estimation of the release probability by relating a given response to the pool size. In this way, vesicle recruitment or priming can be distinguished from Ca^{2+} triggering. (Rettig and Neher, 2002).

To describe calcium kinetics in spines correctly, a detailed knowledge of influx and efflux pathways is necessary. Several influx pathways for calcium into dendritic spines have been identified. They include voltage-gated calcium channels, NMDA-receptor and AMPA-receptor channels and calcium release from two types of intracellular stores. Less is known about calcium clearance mechanisms in spines and their functional importance. The efflux pathways influence maximum peak amplitudes of calcium increases and how long intracellular calcium stays elevated. Both are important parameters that impact on synaptic plasticity. Two main efflux pathways are described; firstly, calcium extrusion mechanisms exist in spines and dendrites, which pump calcium into the endoplasmic reticulum. It is not clear to what extent other extrusion mechanisms,

such as plasmalemmal sodium-calcium exchange or mitochondrial calcium uptake, contribute to this process. Secondly, assuming a concentration gradient between spine head and dendrite, buffered calcium diffusion through the spine neck is an additional calcium clearance mechanism. Distal spines are more susceptible to long-term depression than proximal spines; differences in calcium kinetics found between distal and proximal spines can cause a different susceptibility to synaptic plasticity. Thus compartmentalization of small ions such as calcium might be one of the major functions of dendritic spines. (Holthoff and Tsay, 2002).

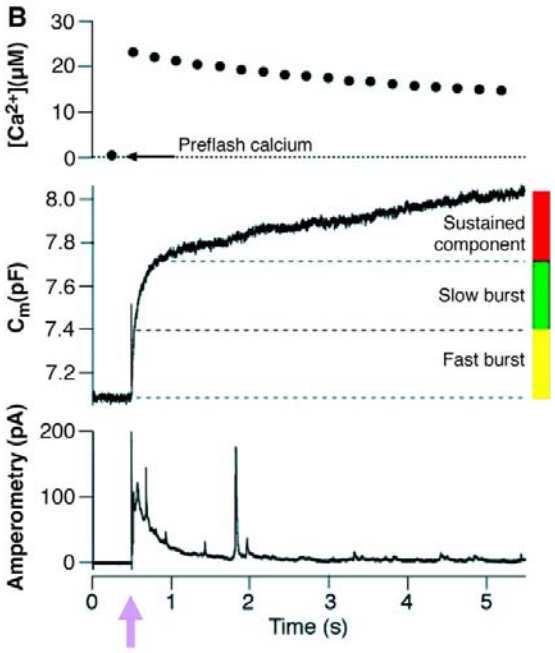

Figure 8. Flash photolysis response. When a flash causes a step increase of cytosolic $[Ca^{2+}]$ from a basal level of about 300 nM to 20 μM (upper trace). Membrane capacitance (middle trace) and the amperometric signal, as measured by a carbon fiber microelectrode (lower trace), are shown. Membrane capacitance increases in proportion to the number of chromaffin granules that fuse with the plasma membrane. The color code assigns parts of the trace to the fusion of vesicles from the ready-releasable pool RRP (yellow) or slowly-releasable pool SRP (green) or to slow priming (with release immediately following) of previously unprimed vesicles (red) (Taken from Rettig and Neher, 2002).

8. Active Zones and the presynaptic plasma membrane

The active zone is composed of an electron-dense, biochemically insoluble material located at the presynaptic plasma membrane precisely opposite the synaptic cleft. There are six large non-membrane proteins that are each encoded by multiple genes, bind to each other, and probably form a humongous single complex at the active zone: Munc13s and RIMs are multidomain proteins that interact with each other and many other synaptic components. Piccolo and Bassoon, homologous and very large proteins, are part of the cytomatrix. ERCs(ELKS/Rab3-interacting molecule/CAST) are coiled-coil proteins whose C-terminus binds to RIMs, and RIM-BPs are SH3-domain

proteins that also bind to RIMs. α-liprins bind to RIMs, ERCs, and receptor protein tyrosine phosphatases. (Südhof, 2004).

9. Allosteric modulation of the presynaptic Ca^{2+} sensor for vesicle fusion

Modulation of the release probability of releasable vesicles in response to Ca^{2+} influx ($Prob_{Ca}$) is involved in mediating several forms of synaptic plasticity, including short-term depression, short-term augmentation, and potentiation induced by protein kinases. Activation of protein kinase C (PKC) enhances synaptic transmission at a variety of synapses and may underlie certain forms of synaptic plasticity. The enhancement is mediated by an increase of transmitter release. After the Ca^{2+} influx, transmitter release depends on two factors, the size of a pool of vesicles immediately available for release and the averaged release probability of vesicles in this pool in response to the Ca^{2+} influx ($Prob_{Ca}$). (Wu and Wu, 2001).

Modulation of the $Prob_{Ca}$ is often a pathway by which synaptic strength is regulated. For example, modulation of the $Prob_{Ca}$ is involved in mediating short-time depression, short-term synaptic augmentation, and enhancement of transmitter release that is induced by the activation of protein kinase A. Although modulation of the $Prob_{Ca}$ plays an important role in regulating synaptic strength, its underlying mechanisms are unclear. Three potential mechanisms may modulate the $Prob_{Ca}$: (1) modulation of the affinity of the Ca^{2+} sensor to Ca^{2+}, (2) modulation of the number of Ca^{2+} ions required to bind the Ca^{2+} sensor and trigger release, and (3) modulation of any step at the release machinery to Ca^{2+}. (Wu and Wu, 2001).

Wu and Wu (2001) showed that phorbol myristate acetate (PMA) increased the $Prob_{Ca}$ without affecting the releasable pool or the rate of vesicle mobilization. PMA shifted the sigmoidal relationship between the capacitance jump and the Ca^{2+} current integral to the left. After fitting the sigmoidal curves with the Hill equation, the EC_{50} was reduced by approximately one-half by PMA. These results suggested that PMA increases the $Prob_{Ca}$ by increasing the apparent affinity of the release machinery to Ca^{2+}. This was the first example showing that modulation of the release machinery downstream of the Ca^{2+} sensor is involved in mediating modulation of the $Prob_{Ca}$ and thus the synaptic strength. The protein kinase C inhibitor BIS did not block PMA-induced enhancement of the capacitance jump completely in calyx-type synapses; the 83% enhancement got reduced to a 25% enhancement. It is likely that the remaining effect of PMA on the capacitance jump in the presence of BIS involves the diacylglycerol/phorbol ester binding protein Munc13-1. (Wu and Wu, 2002).

Lou and collaborators (2005) found that phorbol dibutyrate (PDBu) increases the intracellular Ca^{2+} sensitivity of vesicle fusion in response to sub-maximal Ca^{2+} stimuli. In pituitary cells, phorbol esters increase Ca^{2+} sensitivity by increasing the vesicle pool depletion time constants; however such an increase is not apparent in the Calyx of Held.

Synaptic vesicle fusion at resting $[Ca^{2+}]_i$ does not appear to be constitutive. Rather it is regulated by phorbol esters as well as by Ca^{2+}, although the Ca^{2+} cooperativity is low close to baseline $[Ca^{2+}]_i$. Evidence for a low Ca^{2+} cooperativity close to resting $[Ca^{2+}]_i$ has also been obtained at neuromuscular synapses. This low Ca^{2+} cooperativity is functionally relevant, because it prevents a large increase in asynchronous release activity

during moderate elevations of residual $[Ca^{2+}]_i$, which would be expected if a steeply Ca^{2+} -dependent mechanism operated close to baseline $[Ca^{2+}]_i$. (Lou *et al*., 2005).

10. Kinetics of the neurotransmitter release

The Ca^{2+} -dependent priming of vesicles occurs on the time scale of tens of seconds, and it can enlarge the size of the releasable pool by up to a factor of 5. (Rettig and Neher, 2002).

Two isoforms of Munc13 produce two distinct forms of short-term plasticity, one (Munc13-1) characterized by short-term depression at moderate stimulation frequencies and another one (Munc13-2) by a Ca^{2+}- and stimulation-dependent augmentation. (Rettig and Neher, 2002).

11. C_1 domain as membrane localization module in Munc13-1

Shen and collaborators (2005) solved the solution structure of Munc13-1 C_1 domain; the overall conformation of the Munc13-1 C_1 domain is analogous to that of the PKCδ C_1B domain, but the ligand-binding region showed striking structural differences. A conserved tryptophan residue occludes the DAG/PE-binding site in the munc13-1 C_1 domain. Thus, the munc13-1 C_1 domain needs to experience a considerable conformational change for ligand binding. The fact that W588 packs against the ligand-binding site in the Munc13-1 C_1 domain but not in the PKCδ C_1B domain appears to arise from differential conformational preferences of the backbone of loops 1 and 2, and perhaps from slight overall structural differences between the two C_1 domains, rather than from contacts between the W588 aromatic ring and specific side chains of the munc13-1 C_1 domain. (Shen *et al*., 2005).

The occlusion of the DAG-binding site observed in the structure of the Munc13-1 C_1 domain is expected to impose a kinetic barrier for ligand binding and hence decrease the binding on rate constant (k_{on}). (Shen *et al*., 2005).

Phorbol esters produce various physiological effects on cells in a variety of tissues, with one of the most commonly observed effects being the promotion of tumor growth. Phorbol esters activate protein kinase C (PKC) and after extended incubation periods, cause down regulation of the enzyme. Phorbol esters act as stable substitutes of the natural activator of PKC, diacylglycerol. (Silinsky and Searl, 2003).

Phorbol ester binding does not produce a significant conformational change within the activator binding domain. Rather, it acts to cover the polar interior of the groove and completes a contiguous hydrophobic surface over a large portion of the domain. Phorbol esters activate PKC by altering the nature of the protein surface and by stabilizing the membrane-inserted state, rather than by inducing a conformational change at the activator-binding site. (Zhang *et al.*, 1995).

The regulatory domain of PKC contains the binding sites for phorbol esters, the C_1 domains. These domains are the natural receptors for the endogenous ligand DAG, which is formed from membrane phospholipids (predominantly phosphatidylinositol bisphosphate) after the activation of phospholipase C (PLC) by a wide variety of biological modulators and neurotransmitters. The C_1 region is a zinc-finger receptor, a common term for these regions because of their richness in cysteine residues, even

though the domain is not structurally related to the zinc-finger proteins that bind nucleic acids. The purpose of the C_1 domain is to help recruit proteins to membranes. The binding of phorbols in the C_1 domain provides a hydrophobic cover allowing the complex to be inserted and anchored into membranes with little conformational change. After insertion into the membrane, the catalytic domain of PKC is activated and, with the appropriate substrates, phosphorylation ensues. (Silinsky and Searl, 2003).

There are other important receptors for phorbol esters, like Unc13, the chimaerins, DAG kinase γ, RasGRP (which activates Ras and similar small G-proteins) and protein kinase D1, an enzyme essential for targeting proteins to the cell surface. (Silinsky and Searl, 2003).

High affinity binding (k_d ~1 nM) of phorbol esters to PKC requires phospholipids, and acidic phospholipids are the most efficient cofactors for ligand binding. However, phorbol esters have been shown to bind in the absence of phospholipids with a reduced affinity (k_d ~ 0.165 μM) (Kazanietz *et al*., 1995). DAG or phorbol esters are required for the reversible recruiting of PKC to membranes, a process referred to as "PKC translocation". The conserved C_1 and C_2 domains in PKC isozymes play a key role in membrane association. (Kazanietz, 2002).

The C_1 domain, a motif of 50 or 51 amino acids located in the N-terminal regulatory region of PKC, is the minimum domain required for phorbol ester/DAG binding. This domain is duplicated in tandem (C_1A and C_1B) in cPKCs, nPKCs, and in PKCμ/PKD. The C_1 domains are rich in cysteine and possess the motif $HX_{12}CX_2CX_{13/14}CX_2CX_4HX_2CX_7C$, where H is histidine, C is cysteine, and X is any other amino acid. The two histidines and five of the cysteines coordinate two Zn^{2+} ions in each C_1 domain. The mutation of any of the essential histidines or cysteines affects the structural integrity of the domain and consequently disrupts ligand binding. Ligand binding to the C_1 domain leads to a large-scale conformational change in PKC that result in the allosteric activation of the enzyme and stimulation of its phosphotransferase activity. (Kazanietz, 2002).

In the C_1 domain crystal structure of PKCδ, the phorbol ester binding does not produce a significant conformational change within the activator binding domain. Rather, it acts to cover the polar interior of the groove and completes a contiguous hydrophobic surface over a large portion of the domain. The long-chain lipid tails of PKC activators are probably not directly involved in binding to PKC, but instead retain the activator within the membrane. The retention of the long-chain phorbol esters in the membrane means that the favorable free energy of protein-phorbol binding can be used to drive the insertion of the protein into the membrane. (Zhang *et al*., 1995).

There is experimental evidence which shows that chimaerins, Munc13s and RasGRPs redistribute in response to phorbol esters. Studies using GFP-β2-chimaerin revealed a cytoplasmic staining in the absence of phorbol ester stimulation and a significant translocation both to the plasma membrane and to the perinucleus after phorbol ester treatment. (Kazanietz, 2002).

Evidence for phorbol ester-induced translocation of Munc13 isozymes has been reported in human embryonic kidney 293 cells transiently transfected with GFP-fused Munc13 constructs. All three Munc13 isoforms translocate to the plasma membrane in response to PMA. Phorbol esters promote a transient interaction of Munc13-1 with the calcium-binding protein DOC2. (Kazanietz, 2002).

Both DOC2A and DOC2B translocate to the plasma membrane in the presence of $[Ca^{2+}]_i$ below 0.5 μM. In depolarized neurons, both DOC2 isoforms associated reversibly with the neuronal plasma membrane but with a different sensitivity. Thus both DOC2 isoforms may contribute to short-term plasticity of the nervous system. The elevation of $[Ca^{2+}]_i$, which causes the translocation of DOC2 to the membrane, may accelerate the priming activity of Munc13. In contrast to synaptotagmin, the DOC2 proteins are optimally adapted to sense residual $[Ca^{2+}]_i$ in a timescale of seconds (Groffen *et al*., 2006).

The enzymatic activity of the different isoforms of the phopholipase C family of proteins results in the hydrolysis of phosphatidylinositol 4,5-bisphosphate, which contains mainly polyunsaturated fatty acids, to inositol 1,4,5-trisphosphate and polyunsaturated DAGs. Polyunsaturated DAG second messenger molecules are inactivated by the activity of diacylglycerol kinases (Brose and Rosenmund, 2002).

DAG- and phorbol-ester-mediated subcellular translocation of PKD1 is essential for protein transport from the trans-Golgi network to the cell surface (Brose and Rosenmund, 2002).

Studies of PKC function that rely on the use of phorbol esters as an investigative tool have to be interpreted with caution. As in the case for C_1-domain-directed PKC activators, C_1-domain-directed PKC inhibitors are non-specific pharmacological tools that bind with comparable affinity to other C_1 domain proteins. Such non-specific inhibitors include one of the PKC inhibitors used most widely in the past, calphostin C. For the functional separation of PKC-specific effects from those mediated by alternative DAG/phorbol ester receptors, some of the most useful pharmacological tools are ATP-binding site inhibitors. However, some of the most specific bisindolylmaleimide-derived PKC inhibitors are partially toxic in certain situations (Brose and Rosenmund, 2002).

12. Priming activity of Munc13 proteins

The control of the priming activity of the MUN domain (residues 859-1531) may be the focal point of a variety of presynaptic plasticity processes that are regulated by diverse agents such as Ca^{2+}, DAG and Rab3 and that are believed to mediate information processing in the brain (Basu *et al*., 2005).

The overexpression of the Munc13-1 MUN domain rescues release in cultured excitatory and inhibitory hippocampal autaptic neurons from Munc13-1 and Munc13-2 double-knockout mice. In contrast, the rescue with the MHD1-2 fragment (residues 1045-1531) was unsuccessful (Basu *et al*., 2005).

There is still conflicting data on this point, Stevens and collaborators (2005) identified a different minimal Munc13-1 domain that is responsible for its priming activity, this region mapped to the C-terminus of Munc13-1 residues 1100-1735.

The Ready Releasable Pool size is reduced in Munc13-1^{H567K} mutant neurons, but evoked response amplitudes are unaltered, resulting in a relatively higher vesicular release probability (P_{vr}) compared with wild-type (*wt*) neurons. The activation of the Munc13-1 C_1 domain increases the number of vesicles released only when the hypertonic stimulus is submaximal and does not cause any additional potentiation of responses during saturating osmotic challenges. Thus C_1 domain activation does not affect the RRP *per se* but lowers the energy threshold for fusion of vesicles within the pool. The

activation of the Munc13-1 C_1 domain accelerates vesicular release in general, consistent with the model of a lowered energy barrier for fusion. The Munc13-1^{H567K} C_1 mutant mimics PDBu-mediated C_1 domain activation (Basu *et al*., 2007).

The activation of Munc13 C_1 domain causes a left shift of the sensitivity to sucrose indicating that the activation of the C_1 domain lowers the energy threshold for fusion of vesicles. Thus Munc13 C_1 domain activation impacts vesicular release after vesicles have been primed to form the RRP, and hence Munc13s are not only priming proteins but also play a role as post-priming modulators of neurotransmitter release. In the case of augmentation, it includes among other likely processes the Ca^{2+} and activity-dependent stimulation of N-terminal Munc13 domains by Ca^{2+}/CaM and by DAG (Basu *et al*., 2007).

The dual mode of Munc13 function equips synapses with the ability to effectively regulate vesicular release probability. In their activated state, Munc13s lower the energy barrier for vesicle fusion such that vesicles can be released at twofold to fourfold higher rates. Primed synaptic vesicles may possibly be equipped with SNARE complexes with variable fusogenic potentials depending on the associated Munc13 conformation (Basu *et al*., 2007).

Kalla and collaborators (2006) showed by Fluorescence Recovery After Photobleaching of Munc13-1-EYFP knock-in neurons the presence of two Munc13-1-EYFP pools: one with an exchange time constant of ~ 3 min that represents ~ 40% of total synaptic Munc13-1-EYFP, and a second pool, which exchanged more slowly (time constant of ~80 min), that represents ~60% of the total Munc13-1-EYFP. The quickly exchanging Munc13-1-EYFP pool most likely represents proteins whose diffusion is hindered by transient and weak proteinaceous interactions, because its exchange rate is still much slower than expected for free diffusion. In contrast, the slowly exchanging Munc13-1-EYFP pool may represent Munc13-1-EYFP anchored to the synaptic plasma membrane, the submembranous cytoskeleton, and the active zone protein network via high-affinity proteinaceous interactions (Kalla *et al*., 2006).

Another imaging study done by Nofal and collaborators (2007) with the use of total internal reflection fluorescence microscopy (TIRFM), which enables the real-time visualization of vesicles, near the plasma membrane in their different molecular states, revealed that the nearly immobile vesicles with a caging diameter (CD) of 101 nm represent primed vesicles because the pool of vesicles displaying this type of mobility was significantly increased after PMA treatment and Munc13-1 overexpression and decreased during tetanus toxin expression. In contrast, the movement of docked but unprimed vesicles is restricted to a confined region CD ~220 nm.

Lu and collaborators (2006) studied the homodimerization of the C_2A domain of Munc13-1 and its heterodimerization to the zinc-finger domain of RIM1α. Munc13-1 may exist in solution as a homodimer that needs to be disrupted in order to bind to α-RIMs at the active zone. The physiological role of Munc13-1 homodimerization is unclear, but it is plausible that it may play an inhibitory role by hindering α-RIM binding or it may help to stabilize Munc13-1 in the cytoplasm, before engaging in interactions at the active zone.

The C_2 domains present in UNC13 homologues could serve as a Ca^{2+} sensor which responds to the Ca^{2+} influx required for exocytosis. Therefore, the question arises as to the function of a potential second type of Ca^{2+} sensor provided by the binding of

CaM to dUNC13. One possibility is that each UNC13 protein really has only one Ca^{2+} sensor and that is supplied in some isoforms by the C_2 domain and in others through Ca^{2+}/CaM. An alternative proposal is that some UNC13 proteins may be regulated by Ca^{2+} via both C_2 domains and CaM. Such dual regulation may provide a mechanism for extremely rapid as well a sustained responses to highly transient increases in Ca^{2+}. Dual binding of Ca^{2+} to CaM and C_2 domain may enable UNC13 proteins to sense the Ca^{2+} rise within few microseconds and sustain the response for several hundred microseconds to several milliseconds. (Xu *et al*., 1998).

13. Study of macromolecular structure with nuclear magnetic resonance

All multidimensional heteronuclear NMR experiments correlate a heteronuclear resonance with a proton resonance by transfer of coherence (or polarization) between the heteronuclear (S) and proton (I) spins. Regardless of the specific protocol utilized to effect coherence transfer, the NMR experiment can start with excitation of either I or S spin polarization and must end with detection of either I or S spin magnetization. The overall sensitivity S/N of heteronuclear correlation NMR experiments is proportional to $\gamma_{ex}\gamma_{det}^{3/2}[1-\exp(-R_{1,ex}T_c)]$, where γ_{ex} and γ_{det} are the gyro magnetic ratios of each nucleus excited at the beginning of the sequence and detected at the end of the sequence, respectively; T_c is the recycle time of the experiment; and $R_{1,ex}$ is the spin-lattice relaxation rate constant of the excited nucleus. Therefore, indirect proton detection is used whenever possible in order to maximize sensitivity. (Cavanagh *et al*, 1996).

Stable isotope labeling provides coherence pathways for multi-dimensional experiments that can either be selected for or filtered out. Whenever possible it is advantageous to observe less sensitive nuclei (such as ^{13}C and ^{15}N) indirectly through coherences with ^{1}H (Markley and Kainosho, 1993).

The complete assignment of the NMR spectrum of a protein involves three tasks:

1) sorting of NMR peaks by amino acid type
2) linking of the peaks (sorted by amino acid type) by sequential NMR connectivities
3) alignment of these linked groups of peaks with the protein sequence

The three tasks can be carried out separately, but they usually are combined in iterative searches as the assignment proceeds. Secondary structural elements (α-helix, β-sheet, and turns) give rise to characteristic patterns of sequence dependent NOEs; such additional information can be used to verify or extend assignments (Wühtrich, 1986).

Amino acid selective stable isotope labeling provides a powerful means of accomplishing the first task. With proteins labeled uniformly with ^{13}C and/or ^{15}N, sorting is accomplished by classifying resonances from each residue according to its spin system type. With uniform dual $^{13}C/^{15}N$-labelling signals can be sorted cleanly for all 20 amino acids (Wühtrich, 1986).

The multinuclear spin systems of proteins labeled with ^{13}C and ^{15}N extend from one residue to the next by virtue of $^{1}J_{CC}$ and $^{1}J_{CN}$ coupling along the peptide backbone (Figure 9). Heteronuclear 2D, 3D, and 4D experiments have been developed that exploit coupling along the peptide backbone to provide sequence-specific assignments in proteins labeled completely with ^{13}C and ^{15}N. In principle the 4D triple-resonance approach should provide backbone assignments with as few as two data sets. The 3D

approach requires more data sets but may be applicable to larger proteins. There are two categories for sequential assignment in uniformly labeled proteins; the first one relies on sequential through-space (NOE) connectivities. Common types of sequential, stable isotope-assisted NOEs are: $(^{15}N\text{-}^{1}H)_i\ldots(^{1}H\text{-}^{15}N)_{i+1}$, $(^{13}C_{\alpha,\beta,\gamma}\text{-}^{1}H)_i\ldots(^{1}H\text{-}^{15}N)_{i+1}$. The second one relies on sequential through-bond connectivities. These are provided by a range of 1D-4D experiments, where redundancy of connectivities or higher dimensionality is used to resolve overlap problems (Sattler *et al*., 1999).

Additional isotope-assisted 3D and 4D methods support side chain and NOE assignments. An approach commonly used with larger proteins is to simplify the assignment problem by collecting high dimensional (3D and 4D) NMR data. Such data have fewer redundancies in assignment pathways than 2D data so that the solution can be found without testing all possible assignment pathways against all the data (Sattler *et al*., 1999).

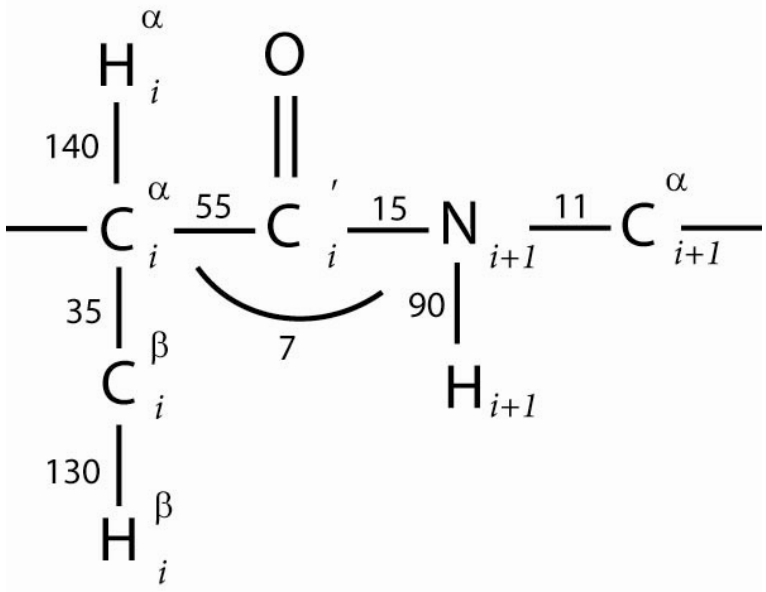

Figure 9. Schematic representation of the coupling pathways that can be exploited in making sequential assignments along the peptide backbone form through-bond coupling connectivities with proteins labeled with ^{13}C and ^{15}N, ^{1}J coupling constant values are in Hz (adapted from Sattler *et al*., 1999).

The introduction of heteronuclear triple resonance experiments relying exclusively on $^{1}J/^{2}J$ couplings (Ikura *et al.*, 1990), which allow to order independent of conformation the resonance peaks of ^{1}H, ^{15}N and ^{13}C in uniformly labeled proteins has yielded a large number of experiments and new assignment strategies. (Sattler *et al*., 1999). With the use of deuterium labeling, it has been possible to extend the study of proteins with molecular weights above 30kDa (LeMaster, 1990; Grzesiek *et al*., 1993).

Transverse Relaxation –Optimized Spectroscopy (TROSY) allows to study large biological macromolecules, these pulse sequences attenuate T_2-relaxation at high magnetic fields by mutual cancellation of dipole/dipole and CSA relaxation mechanisms (Sattler *et al*., 1999).

The original assignment strategy employs the 3D experiments HNCO, HNCA, HN(CO)CA, HCACO and HCA(CO)N to exclusively correlate the resonances of the

peptide backbone ($H^N(i)$, N(i), $C_\alpha(i)$, $H_\alpha(i)$, $C_\alpha(i\text{-}1)$, $H_\alpha(i\text{-}1)$, C'(i) and C'(i-1). With the inclusion of the 3D experiments CBCA(CO)NH and HNCACB, the sequential assignment can be improved, since the information about the chemical shifts of the C_α and C_β carbons is especially valuable, because they are characteristic of the different types of amino acids and can therefore help to position a sequentially connected stretch of amino acids within the known primary sequence (Sattler *et al*., 1999).

The NMR pulse sequences for the assignment of uniformly ^{13}C-, ^{15}N-labelled proteins are composed of a large number of pulses that have to be applied at three or four different frequencies in order to excite ^{1}H, ^{15}N, aliphatic ^{13}C and ^{13}C' resonances. Signal gets lost as a result of miscalibration or pulse imperfection accumulate, accurate calibration of pulses and good RF homogeneity of the probe on all frequency channels is essential. Especial techniques and the use of pulse field gradients in the design of pulse sequences have led to improved signal to noise and better artifact suppression in NMR experiments (Sattler *et al*., 1999).

The pulse sequence for the 3D-HNCO and 3D-HNCA experiments are identical, except for the interchange of C^α and C' pulses. Two types of cross peaks are observed in the HNCA experiment, the correlations $H^N(i)$, N(i), $C_\alpha(i)$ and $H^N(i)$, N(i), $C_\alpha(i\text{-}1)$ because both the couplings $^1J_{C\alpha(i),N(i)}$ = 11Hz and $^2J_{C\alpha(i-1),N(i)}$= 7Hz are of similar size. In contrast, only the correlations $H^N(i)$, N(i), C'(i-1) are observed in the HNCO, since $^1J_{C'(i-1),N(i)}$ = 15Hz, while $^2J_{C'(i),\,N(i)} \approx 0$ Hz. The transfer pathway starts on a nucleus (the H^N in these experiments) and the magnetization is detected on the same nucleus, after chemical shifts of other nuclei have been followed, this type of experiment is called "out and back". The magnetization can also be transferred from a starting nucleus to another nucleus to be detected. This type of experiment is called "transfer experiment" (Sattler *et al*., 1999).

The HN(CA)CO experiment correlates the chemical shifts of $H^N(i)$, N(i) and C'(i). In analogy to the HNCO experiment, cross peaks involving the resonances of C'(i-1) and $C_\alpha(i\text{-}1)$ can also be observed, depending on the relaxation properties of the protein. The HN(CA)CO experiment is derived from the HNCA experiment. Starting on the amide protons, magnetization is transferred via the amide nitrogens to the C_α spins. For the following magnetization transfer between the C_α and the C' spins either an HMQC- or an HSQC-type based experiment can be used. Analogously to the HNCA experiment two cross peaks are expected. The intraresidual peak correlating to $C_\alpha(i)$ originates from $N \rightarrow C_\alpha$ transfer via the $^1J_{C\alpha,N}$ coupling and the sequential cross peak to $C_\alpha(i\text{-}1)$ originates from $N \rightarrow C_\alpha$ transfer via the $^2J_{C\alpha,N}$ coupling (Sattler *et al*., 1999).

The 3D CBCA(CO)NH experiment is a transfer experiment, which uses a relay-COSY step $C_\beta/C_\alpha \rightarrow C_\alpha$ to correlate the chemical shifts H^N(i), N(i), C_α(i-1) and C_β(i-1). The magnetization is transferred from $H_{\alpha,\beta}$ to the directly bound $C_{\alpha,\beta}$ followed by constant time chemical shift evolution of $C_{\alpha,\beta}$. After the relay-COSY step, the C_β, C_α coupling is refocused and the magnetization is transferred from C_β/C_α to the amide nitrogen in two INEPT steps, followed by constant time chemical shift evolution of the amide nitrogens (t_2). The magnetization is detected (t_3) after transfer to the amide protons using a INEPT sequence. The transfer amplitudes for C_β and C_α cross peaks in the CBCA(CO)NH experiment depend on the carbon multiplicity of the carbon spins (Sattler *et al*., 1999).

The 3D HNCACB experiment uses an "out and back" magnetization transfer

$$H^N \rightarrow N \rightarrow C_\alpha \rightarrow C_{\alpha,\beta}(t_1) \rightarrow C_\alpha \rightarrow N(t_2) \rightarrow H^N(t_3)$$

The relay-COSY transfer C_β, $C_\alpha \rightarrow C_\alpha$, which is used in the CBCA(CO)NH and CBCANH experiments, is efficient for proteins up to 20kD molecular weight. For smaller proteins with more favorable relaxation properties, it is also possible to transfer magnetization from all side-chain resonances to the C_α nucleus by homonuclear C,C-TOCSY transfer and via C' and N to the amide protons. Such experiments are less sensitive than the relay-COSY experiments, because the magnetization originating from all nuclei is distributed into the whole spin system, with only a small part being transferred to the C_α. In addition, it is difficult to find a mixing time, τ_m that yields a good transfer for all aliphatic side-chain carbons of all amino acids to their C_α carbon (Sattler *et al*., 1999).

The 3D HCCH-TOCSY experiment is used to assign aliphatic ^1H,^{13}C spin systems and to link them to the sequentially assigned backbone resonances. In an $H_nC(i)$ - … - $H_mC(j)$- spin system a 3D H(C)CH-TOCSY experiment connects chemical shifts H(i), H(j) and C(j). This connectivity information yields the complete assignment of the ^1H and ^{13}C resonances, because the aliphatic proton chemical shifts of a given spin system are found at the ^{13}C chemical shift of all the carbon frequencies involved in that spin system (Sattler *et al*., 1999).

The assignment of aromatic resonances is usually complicated because of strong coupling between ^1H and the ^{13}C spins within the aromatic ring system and short relaxation times. In the INEPT transfer based experiments, magnetization is transferred from H_β to C_β spins to the quaternary $^{13}C_\gamma$ nuclei using selective pulses for the aromatic C_γ spins, and adjusting the power level of the C_β pulses such that the C_γ spins are not affected. After carbon relay transfers to the protonated aromatic carbons, the magnetization is finally detected on the H_δ or H_ε protons (Sattler *et al*., 1999).

Methionine C_ε methyl groups play an essential role in CaM binding to its numerous target sequences. For structure determination by NMR is important to obtain unambiguous assignments of these methyl groups. A pulse sequence based on ^{13}C-^{13}C correlation has been introduced by Bax *et al*., 1994. The magnetization transfer in this 3D-HMBC experiment is as follows: $H_\varepsilon \rightarrow H_\varepsilon C_\gamma(MQ,t_1) \rightarrow H_\varepsilon \rightarrow C_\varepsilon(t_2) \rightarrow H_\varepsilon(t_3)$ where MQ referes to heteronuclear H_ε-C_γ multiple quantum coherence. The first part of the sequence corresponds to the original HMBC pulse scheme, but for uniformly ^{13}C-enriched proteins, the de- and rephrasing delays, Δ, must be adjusted to an integer multiple of $1/^1J_{C\varepsilon H}$ to minimize generation of Hε-Cε multiple –quantum coherence. This stage is followed by a constant-time HSQC experiment, where the duration of the constant time, 2T, is adjusted to $1/(2^1J_{CC})$. This choice for 2T acts as a methionine methyl filter, because the signal of all other carbons is greatly reduced by $^1J_{CC}$ dephasing (Bax *et al*., 1994).

In flexible and unfolded proteins, ^1H and ^{13}C chemical shift dispersions are very poor and this poses a serious problem in obtaining sequence specific assignments by the standard procedures. ^{15}N chemical shift dispersions are very good even in unfolded proteins. The possibility of direct identification of H^N and ^{15}N chemical shifts of neighboring residues in the HNN spectrum suggests an easy strategy for rapid assignment of resonances along the polypeptide chain. The F1-F3 planes help to identify the ^{15}N chemical shifts, while the F2-F3 planes enable to identify the corresponding H^N chemical

shifts. These features provide many starting points for a backbone walk. (Panchal *et al*., 2001).

The Nuclear Overhauser Effect (NOE) is a consequence of modulation of the dipole-dipole coupling between different nuclear spins by the Brownian motion of the molecules in solution, and the NOE intensity can be related to the distance *r* between preirradiated and observed spin by an equation of the general form

$$\text{NOE} \propto \langle 1/r^6 \rangle \cdot f(\tau_c)$$

the second term in the equation is a function of the *correlation time* τ_c, which accounts for the influence of the motional averaging process on the observed NOE. Because of the low sensitivity for observation of NOEs, the accuracy of integration of line intensities is also limited by low S/N. Fundamental difficulties can arise when trying to correlate experimental NOE intensities with distances, for example, because of spin diffusion or the prevalence of intramolecular mobility in macromolecules (Wühtrich, 1986).

In polypeptides a ^{1}H-^{1}H bidimensional NOESY spectrum can be divided into six areas containing the following connectivities:

a. NH; aromatics-NH; aromatics.

b. NH; aromatics-αH; δH of Pro; βH of Ser and Thr

c. NH; aromatics-aliphatic side chains

d. αH; δH of Pro; βH of Ser and Thr; δH of Pro; βH of Ser and Thr

e. αH; δH of Pro; βH of Ser and Thr-aliphatic side chains

f. Aliphatic side chains-aliphatic side chains

to minimize interference with the solvent resonance, the regions d, e, and f are preferably studied in D_2O solution. (Wühtrich, 1986)

Three interresidue ^{1}H-^{1}H distances in the primary polypeptide structure are defined: Sequential distances are those between backbone protons or between a backbone proton and a β proton in residues that are nearest neighbors in the amino acid sequence, for example $d_{\alpha N}(i,i+1)$ and $d_{NN}(i,i+1)$. Medium-range distances are all nonsequential interresidue distances between backbone protons or between a backbone proton and a β proton within a segment of five consecutive residues. Long-range backbone distances are between backbone protons in residues that are at least six positions apart in the sequence. (Wühtrich, 1986)

The NMR structure determination of a protein commonly involves the preparation of uniformly ^{13}C/^{15}N-labeled, soluble protein, the acquisition of a set of 2D and 3D NMR experiments, NMR data processing, peak picking, chemical shift assignment, NOE assignment and collection of conformational restraints, structure calculation, refinement, and validation. (Wühtrich, 1986).

In order to extract informative distance constraints from a NOESY spectrum, its cross-peaks have to be assigned, *i.e.* the pairs of hydrogen atoms that give rise to the observed cross-peaks need to be identified. These NOESY assignments are based on ^{1}H chemical shifts values that result from previous sequence-specific resonance assignments. (Herrmann *et al*., 2002).

Dipolar couplings contain unique “long-range” information not available from NOEs or J couplings, as they orient all vectors relative to a single axis system. For directly bonded pairs of atoms, the internuclear distance is accurately known, and the measured dipolar couplings provide information on the orientation of the internuclear bond vector. For a protein of unknown structure, a reasonable estimate for A_a can be

obtained from the range of dipolar couplings observed. The value of A_r can be determined in a stepwise iterative manner. In contrast, the orientation of the alignment tensor floats freely during structure calculations. (Tjandra and Bax, 1997).

14. Study of macromolecular dynamics with nuclear magnetic resonance

Dynamics reflect the molecule's successive passing through different conformational states and represents its "fourth dimension" in space and time. (Brüschweiler, 1994).

The dynamics of spin density operator σ is governed by the Liouville-von Neumann equation

$$(\mathrm{d}/\mathrm{d}t)\sigma(t) = -i\hat{\mathrm{H}}\sigma(t) - \Gamma\{\sigma(t) - \sigma_0\}$$

where $\hat{\mathrm{H}}$ and Γ describe the Hamiltonian and relaxation superoperators, respectively. Coherent coherence transfer experiments, such as COSY, TOCSY, and INEPT, on one hand exploit the properties of $\hat{\mathrm{H}}$ giving rise to *deterministic* spin dynamics in scalar coupled spin-systems. On the other hand, relaxation experiments, such as NOESY, ROESY, heteronuclear NOE, T_1, T_2, and $T_{1\rho}$ experiments, depend critically on Γ and monitor spin dynamics induced by *stochastic* time modulated interactions. Deterministic spin dynamics are indispensable for the characterization of connectivities in scalar J-coupling networks and are therefore most valuable for spin resonance assignments in complex spectra. Relaxation experiments such as NOESY and ROESY are mainly used as a source of information about averaged internuclear distances of protons for the generation of an (averaged) structure. Experiments measuring heteronuclear NOE values and T_1-, T_2-, and $T_{1\rho}$- relaxation times allow assessing local molecular mobility as well as medium to fast time scale conformational exchange. (Brüschweiler, 1994).

Although the interplay of the deterministic part $\hat{\mathrm{H}}$ with the stochastic part Γ can be too complex for analytical calculations, a practical approach in the case of NOESY and ROESY experiments, give good results for the relaxation periods or mixing times, at least in an initial rate regime. (Brüschweiler, 1994).

The total spin Hamiltonian can be split into a deterministic and a stochastic part

$$\mathrm{H}_{\mathrm{tot}}(t) = \mathrm{H}_{\mathrm{det}} + \mathrm{H}_{\mathrm{stoch}}(t),$$

the deterministic part of the Hamiltonian operator $\mathrm{H}_{\mathrm{det}}$ in liquids consists of three terms

$$\mathrm{H}_{\mathrm{det}} = \mathrm{H}_Z + \mathrm{H}_J^{\mathrm{iso}} + \mathrm{H}_{RF},$$

H_Z is the time-averaged Zeeman term representing the coupling of the spin-induced nuclear magnetic moments with the external magnetic field $\mathbf{B}_0$, which defines the *z* axis of the laboratory coordinate system

$$\mathrm{H}_Z = \sum_{k=1}^{\mathrm{N}} \omega_{0k}\mathrm{I}_{kz}$$

where ω_{0k} is the Larmor frequency of spin *k* defined as $\omega_{0k} = -\gamma_k B_0(1-\sigma_k^{\mathrm{iso}})$· γ_k is the gyromagnetic ratio of spin *k* and σ_k^{iso} its time-averaged isotropic chemical shift. I_{kz} is the spin operator I_z acting exclusively on the Liouville-subspace belonging to spin *k*. The Hamiltonian is given in multiples of $h/2\pi$ and has the unit $\mathrm{rad}\cdot\mathrm{s}^{-1}$. (Brüschweiler, 1994).

The coupling of the spins to a linearly polarized radio frequency (rf) field of strength $2\mathrm{B}_1$ oscillating along an axis in the *xy*-plane of the laboratory frame with

frequency ω and phase φ with respect to the *x*-axis is best described in the rotating frame with frequency ω around the *z*-axis. (Brüschweiler, 1994).

$$H_{RF} \cong -\gamma B_1 \{F_x \cos(\varphi) + F_y \sin(\varphi)\},$$

where

$$F_x = \sum_{k=1}^{N} I_{kx} \text{ and } F_y = \sum_{k=1}^{N} I_{ky}$$

H_J^{iso} represents the time-averaged, indirect, electron-mediated, scalar spin-spin coupling

$$H_J^{iso} = 2\pi \sum_{k<l} J_{kl} \mathbf{I}_k \cdot \mathbf{I}_l = 2\pi \sum_{k<l} J_{kl} \{I_{kx} I_{lx} + I_{ky} I_{ly} + I_{kz} I_{lz}\}$$

$$= 2\pi \sum_{k<l} J_{kl} \{\tfrac{1}{2}(I_{k+} I_{l-} + I_{k-} I_{l+}) + I_{kz} I_{lz}\},$$

where the shift operators I_{k+} are defined by $I_{k\pm} = I_{kx} \pm i I_{ky}$ J_{kl} denotes the scalar coupling constant between spin *k* and *l* is expressed in units of Hz.

Of practical relevance are couplings between spins separated by less than four chemical bonds. Many multidimensional heteronuclear NMR applications exploit the sensitivity gain achieved by the transfer of magnetization via J-couplings from a spin species with higher γ, normally ^{1}H, to a spin with lower γ, such as ^{13}C or ^{15}N using the INEPT or DEPT techniques. (Brüschweiler, 1994).

The structural information carried by vicinal ^{3}J-coupling constants concerning torsion angles is obtained using Karplus relationships. They have the general form

$$^3J_{kl} = A\cos^2\chi + B\cos\chi + C,$$

where *A*, *B*, *C* are empirical constants and χ is the torsion angle defined by the locations of the two coupled spins together with the two intervening atoms. In the weak coupling limit, *i.e.*, in the case where the chemical-shift difference of the spins *k* and *l* is much larger than their scalar coupling J_{kl} (which is always true in the heteronuclear case), first order perturbation theory yields a good approximation for the description of coupling effects and H_J^{iso} simplifies to

$$H_J^{iso} = 2\pi \sum_{k<l} J_{kl} I_{kz} I_{lz},$$

in this limit the effect of H_J^{iso} on the spin density matrix σ can be calculated analytically on the basis of a few simple transformation rules summarized in the product operator formalism. Examples are:

$$I_x \xrightarrow{H_J^{iso}} I_x \cos(\pi J_{IS} t) + 2 I_y S_z \sin(\pi J_{IS} t)$$

and cyclic permutations in *x*, *y*, and *z*. (Brüschweiler, 1994).

The *stochastic* part $H_{stoch}(t)$ of the total Hamiltonian can be chosen to have a time average of zero. It manifests itself in the spectrum in the form of relaxation and exchange effects. Neglecting chemical shift anisotropy, the main contributions to $H_{stoch}(t)$ for spin systems consisting of spin ½ nuclei are the dipolar interaction $H_{DD}(t)$ and time-dependent parts of H_Z and H_J^{iso} caused by internal molecular dynamic processes.

$$H_{stoch}(t) = H_{DD}(t) + H_Z(t) + H_J^{iso}(t)$$ (Brüschweiler, 1994).

The time-modulation of $H_J^{iso}(t)$ can have two different origins. Intramolecular motion can cause a time-dependence in the scalar coupling constant J_{kl}^{iso}; the relaxation mechanism based on this effect is called scalar relaxation of the first kind. Alternatively,

fluctuation in $H_J^{iso}(t)$ can be caused by a relaxation time of spin *S*, which takes part in the interaction $H_J^{iso}(t)$, that is much shorter than $1/J_{kl}$. In this case, the *S* spin contribution to $H_J^{iso}(t)$ can be treated like a lattice vector which decorrelates longitudinally with the time constant T_1 and transversally with T_2. The resulting relaxation mechanism is called scalar relaxation of the second kind. (Brüschweiler, 1994).

A chemical shift fluctuation $H_Z(t)$ on a time scale much faster than the inverse of the shift fluctuation leads to line-broadening and dependence of $T_{1\rho}$ on the rf-field strength B_1.

As a consequence of the isotropy of space (composed of spin space and real space), any spin Hamiltonian *H* transforms under a rotation, which is applied identically to spin space and real space, like a scalar. H can be expressed as a tensor contraction of irreducible tensor operators $\{T_k^q\}$ of rank *k* in spin space and irreducibly transforming spherical harmonics $\{F_k^q\}$ of rank *k* in normal space

$$H = \sum_k c_k \sum_{q=-k}^{k} (-1)^q F_k^{-q} T_k^q,$$

where c_k is the interaction strength of the component of rank *k*. An irreducible tensor operator $\{T_k^q\}$ of order k is defined as a set of 2k + 1 operators $\{T_k^q\}$, $q = -k, -k+1, \ldots, k-1, k$ that fulfill

$$[J_z, T_k^q] = qT_k^q \text{ and } [J_\pm, T_k^q] = T_k^{q\pm1}\sqrt{k(k+1)-q(q\pm1)}$$

$k = 2$ for $H_{DD}(t)$, $k = 1$ for $H_Z(t)$, and $k = 0$ for $H_J^{iso}(t)$. The tensor operators have simple transformation properties under three-dimensional rotations $R(\alpha,\beta,\gamma)$

$$R(\alpha,\beta,\gamma)T_k^m R^{-1}(\alpha,\beta,\gamma) = \sum_{m'=-k}^{k} T_k^{m'} D^k_{m',m}(\alpha,\beta,\gamma),$$

where α, β, γ are the three Euler angles and $D^k_{m',m}$ the Wigner rotation matrix elements of order *k*. The $\{T_k^q\}$ can be transformed easily into the interaction frame induced by the interaction dominant in H_{det}. (Brüschweiler, 1994).

$H_{DD}(t)$ refers to the magnetic dipole-dipole interaction of two nuclei *I* and *S* connected by the vector $\mathbf{r}_{IS}$ which has an orientation described by the polar angles $\Omega_{DD}^{lab} = (\theta^{lab},\phi^{lab})$ with respect to the laboratory frame

$$H_{DD}(t) = \xi(1/r^3_{IS}) \sum_{q=-2}^{2} (-1)^q F_2^{-q}(\Omega_{DD}^{lab}(t)) T_2^q(\mathbf{I},\mathbf{S})$$

(Brüschweiler, 1994).

The prefactor $\xi = -\sqrt{24\pi/5}(\mu_0/4\pi)(h/2\pi)\gamma I \gamma S$ is chosen such that the lattice functions F_2^q are identical to the normalized second order spherical harmonics $Y_2^q(\theta,\phi)$ given by

$$Y_2^0(\theta,\phi) = \sqrt{5/16\pi}(3\cos^2\theta - 1)$$
$$Y_2^{\pm1}(\theta,\phi) = \pm\sqrt{15/8\pi}\sin\theta\cos\theta e^{\pm i\phi}$$
$$Y_2^{\pm2}(\theta,\phi) = \sqrt{15/32\pi}\sin^2\theta e^{\pm i2\phi}$$

(Brüschweiler, 1994).

The irreducible spin tensor operators $T_2^q(\mathbf{I},\mathbf{S})$ are in the case of the dipole-dipole interaction H_{DD} given by

$$T_2^0(\mathbf{I},\mathbf{S}) = 1/\sqrt{6}(2I_zS_z - \tfrac{1}{2}(I_+S_- + I_-S_+))$$
$$T_2^{\pm2}(\mathbf{I},\mathbf{S}) = \tfrac{1}{2}(I_\pm S_\pm)$$

H_{DD} depends on the orientation of the molecule with respect to the external magnetic field $\mathbf{B}_0$ and on the distance between the interacting spins. Therefore, molecular dynamics taking place in real space is reflected in the form of time-modulated interactions in spin-space. This is the basis of any NMR relaxation experiment in solution. At a given time the values of the stochastically fluctuating Hamiltonians differ from the different spin systems, *i.e.*, molecules, in the ensemble. This is in contrast to the deterministic Hamiltonian. Although the interaction strength of H_{DD} can be in the order of 10 KHz, considerably larger than the magnitude of H_J^{iso}, H_{DD} has within first order perturbation theory no effect on the resulting 1D spectrum, *i.e.*, H_{DD} does not cause peak shifts and peak splittings. This is a consequence of the rapid rotational tumbling of peptides and proteins with correlation times between 10^{-10} and 10^{-7} s and the fact that H_{DD} is a traceless operator. However, H_{DD} plays a significant and for spin ½ systems often dominant role for spin relaxation. (Brüschweiler, 1994).

The model free approach introduced by Lipari and Szabo (1981) aims at a description relying on a minimum number of parameters to circumvent over interpretation of the experimental relaxation data and relates a generalized meaning to the parameters. The parameter set consists of two correlation times reflecting the overall tumbling motion and internal time scale of intramolecular motion and an order parameter S^2 representative of the orientational restriction of the involved internuclear vector. A restriction lies in an ambiguity due to the fact, that the dipolar Hamiltonian is invariant under exchange of the two involved spins. For instance, absence of angular motion implies $S^2 = 1$, but $S^2 = 1$ does not imply absence of angular motion. The advantage of the approach is that it gives spatially resolved, direct information about the extent and time scale of motion being present. Furthermore, it provides both intuitive and quantitative insight into the interplay of measurable relaxation rates and internal motion and serves as a convenient interface between experiments and more detailed motional models. (Brüschweiler, 1994).

A type of motion which is always present for molecules in solution is the overall rotational tumbling. It is the rotational analogue to the Brownian translational diffusion and also a consequence of intermolecular collisions. For biomolecules dissolved in simple solvents the overall tumbling corresponds to a small step diffusion process. Tensor interactions which depend on the orientation of the molecule in the laboratory frame, such as $H_{DD}(t)$, couple directly to the tumbling, whereas $H_Z(t)$ and $H_J^{iso}(t)$ remain unaffected by the tumbling since they depend on internal coordinates only. The overall rotational tumbling therefore decouples these two classes of interactions and as a result, relaxative interference between them cannot occur. Hence, for the first class both rotational tumbling and internal dynamics influence the resulting relaxation rates, whereas for the second class relaxation is induced by intramolecular motion only. (Brüschweiler, 1994).

For $H_{DD}(t)$ in the isotropic case, using the transformation properties of spherical harmonics of order two, the following correlation function is obtained

$$C_{\mu\nu}^{q}(\tau) = \langle c_\mu(0)c_\nu(\tau)Y_2^{q}(\Phi_\mu^{lab}(0))Y_2^{q}{}^*(\Phi_\nu^{lab}(\tau))\rangle$$
$$= \sum_{rr'} \langle D_{rq}^{(2)}(\Omega(0))D_{r'q}^{(2)}{}^*(\Omega(\tau))\rangle \cdot \langle c_\mu(0)c_\nu(\tau)Y_2^{r}(\Phi_\mu^{mol}(0))Y_2^{r'}{}^*(\Phi_\nu^{mol}(\tau))\rangle,$$

where Φ_μ^{lab}, Φ_ν^{mol} denote polar angles (θ,φ) of the internuclear vector of interaction μ in the laboratory frame and the molecule fixed frame, respectively. Ω, which is the

argument of the Wigner matrix $D_{rq}^{(2)}$, represents the three Euler angles (α,β,γ) relating the laboratory frame to the molecular frame for different times. Rotational tumbling affects only the first factor of the previous equation and the averaging can be carried out by solving the rotational diffusion equation

$$(df/d\tau) = D\nabla^2_{rot} f \text{ with } f(0) = \delta(\Omega(0)),$$

where ∇^2_{rot} is the angular part of the Laplacian operator in spherical coordinates leading to

$$\langle D_{rq}^{(2)}(\Omega(0)) D_{r'q}^{(2)*}(\Omega(\tau))\rangle = (1/5)e^{-6D\tau\delta r,r'},$$

where D is the rotational diffusion constant. After substitution into the correlation function equation it yields

$$C_{\mu\nu}^{q}(\tau) = (1/5)e^{-6D\tau} \sum_{r=-2}^{2} \langle c_\mu(0) c_\nu(\tau) Y_2^r(\Phi_\mu^{mol}(0)) Y_2^{r*}(\Phi_\nu^{mol}(\tau))\rangle \quad (1)$$

(Brüschweiler, 1994).

The correlation function $C_{\mu\nu}^{q}(\tau)$ does not depend on the index q. This is a direct consequence of the isotropy of the solvent and applies also in the case of anisotropic tumbling. In the case of a rigid molecule the quantities c_μ, c_ν, Φ_μ^{mol}, and Φ_ν^{mol} are time independent and the sum can be simplified by the use of the addition theorem of spherical harmonics

$$((2l + 1) / 4\pi) P_k(\cos\theta_{\mu\nu}) = \sum_{q=-k}^{k} Y_k^q(\Phi_\mu) Y_k^{q*}(\Phi_\nu)$$

(Brüschweiler, 1994).

The equation (1) can be rewritten

$$C_{\mu\nu}(\tau) = (1 / 4\pi) e^{-\tau/\tau c} c_\mu c_\nu P_2(\cos\theta_{\mu\nu}),$$

where the rotational tumbling correlation time is defined by $\tau_c = 1/6D$. (Brüschweiler, 1994).

The Fourier transform of the previous equation leads to the spectral density $J_{\mu\nu}(\omega)$

$$J_{\mu\nu}(\omega) = (1 / 4\pi) c_\mu c_\nu P_2(\cos\theta_{\mu\nu})(2\tau_c/(1+\omega^2\tau_c^2)) \quad \text{(Brüschweiler, 1994).}$$

For auto-correlation relaxation experiments (*e.g.*, NOESY) where μ = ν and thus $\theta_{\mu\mu} = 0$, the structurally important information is contained in the distance dependent term c_μ^2 only. For cross-correlation experiments, on the other hand, additional geometric information can be obtained from the term $P_2(\cos\theta_{\mu\nu})$.(Brüschweiler, 1994).

The diffusion coefficient D can be related to the hydrodynamic molecular radius R_h according to the Einstein-Stokes relationship

$$R_h = kT/8\pi\eta D,$$

where η is the solvent viscosity. (Brüschweiler, 1994).

The decorrelation of a tensor of rank 1, *e.g.* a vector attached to a molecule, is obtained similarly

$$\langle\cos(\Omega\text{-}\Omega')\rangle = e^{-2D\tau},$$

where Ω-Ω′ is the angle between the two directions Ω and Ω′, which are adopted at times 0 and τ, respectively. (Brüschweiler, 1994).

A protein in solution undergoes constant random thermal motions within a stable equilibrium structure. These motions involve displacements of individual atoms, bonds, functional groups, side-chains, local regions of the backbone, secondary structure elements, and entire folded domains. Many proteins also undergo thermally driven transitions, called conformational changes, between two or more equilibrium structures. (Falke, 2002).

Both types of motions can play important functional roles. Random thermal motions and the average conformation can both change substantially when a protein is modified by substrate or ligand binding, docking to another macromolecule, or covalent modification (such as phosphorylation). Such changes often have important functional consequences for the tuning of binding affinities and the switching of regulatory proteins. (Falke, 2002).

Dynamics play a role in certain aspects of enzyme function, but the links between dynamics and catalysis remain unclear. In the first step of an enzyme-catalyzed reaction, substrate binding typically induces a conformational change within the enzyme, thereby enclosing the substrate in a cavity protected from solvent or places the catalytic residues near the substrate. An even more fascinating structural rearrangement may occur during the catalytic step of the reaction, when the complex moves from the ground state to the transition state. Such transient rearrangement could simply serve to accommodate the structural changes in the substrate as the transition state is reached or could actively contribute to catalysis by preferentially stabilizing the transition state. Yet, because the transition state exists only fleetingly, enzyme dynamics during transition state formation and decay have never been directly detected during an enzyme-catalyzed reaction in solution. (Falke, 2002).

Early experiments provided evidence for rotation of bulky aromatic side chains as a function of temperature within the hydrophobic core of small globular proteins. This showed that proteins were dynamic over a spectrum of time scales and complemented the static pictures of protein structure that were already emerging from X-ray diffraction. We now know that there is an intimate relation between dynamics and molecular function. Nuclear magnetic resonance (NMR) spectroscopy is uniquely suited to study many of these dynamic processes, because site-specific information can be obtained for motions that span many time scales, from rapid bond librations (picoseconds) to events that take seconds. (Mittermaier and Kay, 2006).

Many biochemical events occur on the microsecond to millisecond time scale, and it is of considerable interest to characterize the conformational transitions that are involved in such processes. However, intermediates are often formed only transiently and are populated at levels that are not amenable to traditional structural approaches. (Mittermaier and Kay, 2006).

When internal motions and molecular tumbling cause reorientation of the ^{1}H-^{15}N bond vector with respect to the external magnetic field, the local magnetic field at the site of the ^{15}N spin that derives from the directly attached ^{1}H magnetic dipole fluctuates (see Figure 10).

Although the local dipolar interaction between ^{1}H and ^{15}N spins averages to zero because of the molecular tumbling, the time-dependent variations in the field lead a spin system that has been perturbed by radio-frequency pulses to return, or relax, to thermal equilibrium. Because the fluctuations of the local magnetic fields are sensitive to internal motions, measurement of NMR relaxation rates provides a direct avenue to extracting dynamic parameters. (Mittermaier and Kay, 2006).

A pair of basic nitrogen-spin relaxation experiments are used to probe backbone dynamics in proteins. The ^{15}N relaxation experiments monitor either the recovery of ^{15}N z-magnetization to its equilibrium position (T_1) or the decay of magnetization orthogonal to the Z axis to its zero equilibrium value (T_2). The ^{1}H spin has a magnetogyric ratio (γ)

that is 10 times larger than that of ^{15}N, and the inherent sensitivity of the NMR experiment scales as $\gamma^{5/2}$; therefore experimental sensitivity is optimized by shuffling magnetization from an amide ^{1}H to its directly coupled ^{15}N and then back again to ^{1}H for detection as a 2D data set. One peak is obtained for each (^{1}H-^{15}N) pair in the protein, with an intensity proportional to $\exp(\tau/T_i)$ where T_i is the T_1 or T_2 value of the particular ^{15}N nucleus and τ is a variable relaxation delay; relaxation times are measured by recording a series of spectra and fitting the peak intensities as a function of τ. The values of T_i so obtained are usually interpreted in terms of generalized order parameters that describe the amplitude of bond vector motions and time constants that indicate the time scale of the internal motions, but specific models can be used as well. (Mittermaier and Kay, 2006).

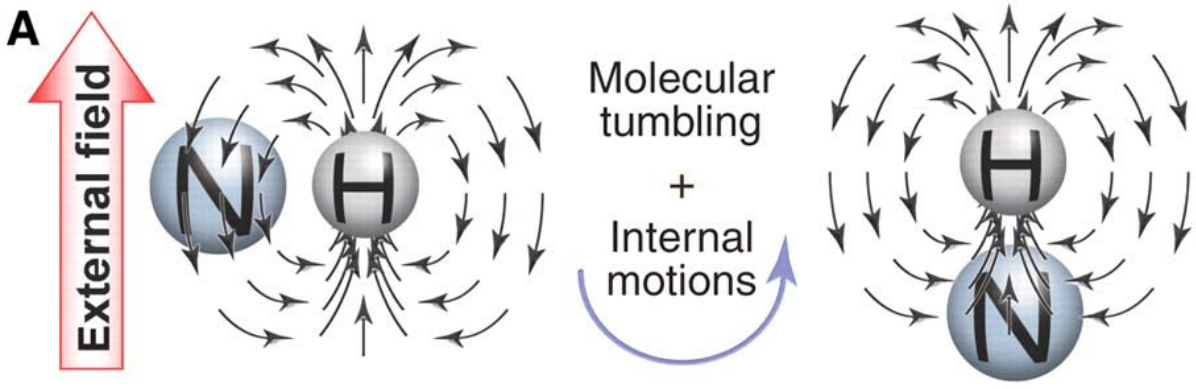

Figure 10. Orientation-dependent magnetic field experienced by an amide ^{15}N nucleus due to the directly bonded proton (taken from Mittermaier and Kay, 2006).

When a protein is not dissolved in isotropic solution but rather in a media that leads to fractional alignment (typically about 0.1 %), the dipolar interaction does not average to zero. Instead, for a fixed orientation of the ^{1}H-^{15}N spin vector, the effective magnetic field at the ^{15}N spin is either increased or decreased depending on the ^{1}H spin state, leading to dipolar splittings in spectra. These splittings are a rich source of structural information, because they report on the orientation of bond vectors with respect to an external coordinate frame (the magnetic field). However, there is also potential for studies of biomolecular dynamics because motions that modulate local fields over a broad time regime (picosecond to millisecond) can affect dipolar splittings. (Mittermaier and Kay, 2006).

Recently, new NMR experiments have been developed to provide site-specific information about protein motions spanning a range of time scales. Some of the new applications involve large molecular complexes, where motion is likely to be critical for function. NMR methods exploiting the TROSY (transverse relaxation optimized spectroscopy) principle have emerged for both backbone positions and side chain methyl groups. (Mittermaier and Kay, 2006).

Upon placement of a molecule in a magnetic field, a magnetic dipole moment is induced which is proportional to the susceptibility, χ. For diamagnetic molecules ($\chi<0$), induced moments will oppose the field while for paramagnetic molecules ($\chi>0$), induced moments will be along the field. These induced moments will in turn interact with the magnetic field. Molecules of non-spherical symmetry will exhibit an orientational

dependence of this interaction due to their anisotropic distribution of electron density. Thus, the susceptibility is a tensorial quantity and the orientation dependent energy of interaction, *W*, can be written,

$$W = 1/\mu_0(-\tfrac{1}{2}\mathbf{B}\cdot\chi\cdot\mathbf{B}),$$

the size of the interaction energy (*W*) depends on the square of the magnetic field strength (B_0^2) and the magnetic susceptibility tensor, χ. Variations in *W* with orientation arise from the anisotropic part of the χ tensor, and if these variations are large enough compared to the thermal energy, kT, a measurable degree of orientational order will be induced (Tjandra and Bax, 1997).

Cooperatively aligned media are generally applicable to the widest range of systems. Moreover, the degree of solute alignment is usually higher and often tuneable. Direct magnetic field alignment, often allows independent determination of the degree of alignment, and thus, may become the method of choice for binding or dynamic studies (Tjandra and Bax, 1997).

The dipolar couplings provide direct information on the orientations of the corresponding bond vectors relative to the protein's magnetic susceptibility tensor. These constraints are therefore fundamentally different from the strictly local NOE and J coupling constraints (Tjandra and Bax, 1997).

Unfortunately, the magnetic interaction energy for an individual macromolecule is generally so weak that only in favourable systems, and with considerable effort, can these dipolar couplings be measured with sufficient accuracy. With the use of a an aqueous, dilute, liquid crystalline (LC) phase, an adjustable degree of molecular alignment can be obtained, it allows the direct measurement of ^{1}H-^{15}N and many other types of dipolar interactions with high accuracy (Tjandra and Bax, 1997).

In full analogy to the case of magnetic susceptibility anisotropy, where dipolar couplings define the orientation of the interaction relative to the magnetic susceptibility tensor, a molecular alignment tensor **A** is defined, which can be decomposed into an axially symmetric component A_a and a rhombic component A_r. The magnitude and orientation of **A** is not known a priori but is determined from the measured dipolar couplings. The observed residual dipolar coupling between two nuclei, P and Q, is given by

$$D_{PQ}(\theta,\phi) = S(\mu_0/4\pi)\gamma_P\gamma_Q h[A_a(3\cos^2\theta-1) + 3/2A_r\sin^2\theta\cos2\phi]/4\pi^2 r^3_{PQ},$$

where *S* is the generalized order parameter for internal motion of the vector PQ, μ_0 is the magnetic permeability of vacuum, γ_P and γ_Q are the magnetogyric ratios of P and Q, *h* is Planck's constant, r_{PQ} is the distance between P and Q, and θ and ϕ are cylindrical coordinates describing the orientation of the PQ vector in the principal axis system of **A**. Values of S^2 obtained from ^{15}N or ^{13}C relaxation experiments typically range from 0.7 to 0.9, that is, *S* falls between 0.85 and 0.95. Values for A_a and A_r depend on the shape of the protein and vary with the bicelle concentration, which is adjusted to yield and A_a of $\sim10^{-3}$. (Tjandra and Bax, 1997).

For such small alignment values, only dipolar couplings between nearby nuclei give rise to observable splittings, which keeps the NMR spectrum simple. If there is also a scalar coupling J between the two nuclei, the observed splitting corresponds to $J_{PQ} + D_{PQ}$. For one-bond ^{1}H-^{13}C, ^{1}H-^{15}N, or ^{13}C-^{13}C interactions, J_{PQ} is relatively large and its sign is known. The change from the isotropic to the aligned phase then yields the magnitude and sign of D_{PQ}. For pairs of protons that are not J coupled, only the

magnitude of D_{PQ} is obtained, and additional experiments need to be developed to obtained information about the sign of this coupling. (Tjandra and Bax, 1997).

For a protein of unknown structure, a reasonable estimate for A_a can be obtained from the range of dipolar couplings observed. The value of A_r can be determined in a stepwise iterative manner. In contrast, the orientation of the alignment tensor floats freely during structure calculations. For directly bonded pairs of atoms, the internuclear distance is accurately known, and the measured dipolar coupling provides information on the orientation of the internuclear bond vector. (Tjandra and Bax, 1997).

Small changes in chemical shift between the LC and isotropic states [$\leq$0.1 ppm for ^{15}N and ^{13}C; $\leq$0.01 ppm for ^{1}H] result from incomplete averaging of chemical shift anisotropy (CSA) in the aligned state. In principle, it is possible to separate this CSA effect from the temperature dependence of the chemical shift, thereby providing access to the potentially important structural information contained in the CSA tensor. (Tjandra and Bax, 1997).

An arbitrary reference frame can be chosen, that is fixed within the molecule, allowing the description of the orientation of the *ij*th internuclear vector in terms of its time independent polar angles θ and ϕ. Likewise, at any instant in time, the orientation of the magnetic field can be described in terms of its polar angles $\zeta(t)$ and $\xi(t)$, which are time dependent due to overall reorientation of the molecule (see Figure 11). The $P_2(\cos\theta(t))$ term is expanded making use of the spherical harmonic addition theorem,

$$P_2(\cos\theta(t)) = (4\pi/5) \sum_{q=-2}^{2} Y_2^q{}^*(\theta\phi) Y_2^q(\zeta(t)\ \xi(t)),$$

where the Ys refer to the normalized spherical harmonics. The formula for the dipolar couplings becomes

$$D_{ij}^{res} = -(\mu_0/4\pi)(\gamma_i\gamma_j h/2\pi^2 r^3_{ij})(4\pi/5) \sum_{q=-2}^{2} Y_2^q{}^*(\Phi)\langle Y_2^q(\Omega(t))\rangle, \qquad (2)$$

where $\Phi = (\theta,\phi)$ and $\Omega(t) = (\zeta(t)\ \xi(t))$ have been used to represent the polar angles of the internuclear vector and the magnetic field relative to the molecule fixed frame, respectively.

When combined with knowledge of the structure of the molecule or molecular fragment, measurement of dipolar couplings corresponding to at least five independent dipolar interaction vectors will allow all five averages to be determined. This procedure corresponds to a determination of Saupe's order tensor, originally formulated in a Cartesian representation:

$$D_{ij}^{res} = -(\mu_0/4\pi)(\gamma_i\gamma_j h/2\pi^2 r^3_{ij})(4\pi/5) \sum_{kl} S_{kl}\cos(\alpha_k)\cos(\alpha_l) \qquad \text{(Prestegard } \textit{et al.}\text{, 2000).}$$

The internal geometry is represented by direction cosines describing the orientation of the internuclear vector within the molecular frame. Overall motion and orientation of the alignment frame is absorbed into the elements S_{kl}, which form the order tensor, a traceless, symmetric 3 X 3 matrix having just five independent elements. The Cartesian and spherical representations are related by the following linear transformations:

$$S_{xz} = \sqrt{3}/8\sqrt{(4\pi/5)}\ (\langle Y_2^1(\Omega(t))\rangle - \langle Y_2^{-1}(\Omega(t))\rangle)$$

$$S_{yz} = i\sqrt{3}/8\sqrt{(4\pi/5)}\ (\langle Y_2^{-1}(\Omega(t))\rangle - \langle Y_2^1(\Omega(t))\rangle)$$

$$S_{xy} = i\sqrt{3}/8\sqrt{(4\pi/5)}\ (\langle Y_2^2(\Omega(t))\rangle - \langle Y_2^{-2}(\Omega(t))\rangle)$$

S_{xx}- S_{yy} = $\sqrt{3}/2\sqrt{(4\pi/5)}$ ($\langle Y_2^2(\Omega(t))\rangle$ - $\langle Y_2^{-2}(\Omega(t))\rangle$)

S_{zz} = $\sqrt{(4\pi/5)}$ ($\langle Y_2^0(\Omega(t))\rangle$ (Prestegard *et al*., 2000).

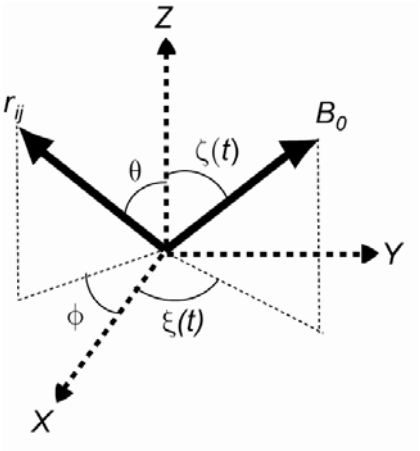

Figure 11. Orientation of the internuclear vector and the magnetic field relative to a molecule fixed frame. The time dependence of the magnetic field vector arises due to molecular reorientation (taken from Prestegard *et al*., 2000).

The extraction of molecular orientation information from order information contained in the above expressions is achieved by diagonalization of the order tensor. The principle values can be recast into an order parameter for the most ordered axis, S_{zz}, and an asymmetry parameter, $\eta = (S_{xx}- S_{yy})/ S_{zz}$, which describes the deviation from axially symmetric ordering. The transformation leading to diagonalization also relates the orientation of the principal alignment axes to the initial molecular frame, and hence, describes the mean orientation of the molecule, or a fragment of a molecule, relative to the magnetic field. This transformation is frequently represented in terms of three Euler angles. (Prestegard *et al*., 2000).

Working in the principal axis frame described by the three Euler angles, only two of the averages in equation (2) remain nonzero. These two averages can also be related to the anisotropies of a generalized alignment tensor, as well as to elements of the Saupe order tensor,

$\langle Y_2^0(\Omega(t))\rangle = \sqrt{(5/4\pi)}\, S_{zz} = \sqrt{(5/4\pi)}\, A_a$

$\langle Y_2^{\pm 2}(\Omega(t))\rangle = \sqrt{(5/24\pi)}\, (S_{zz}- S_{yy}) = \sqrt{(5/32\pi)} A_r$,

for cases in which alignment is achieved due to interaction between the magnetic field and the anisotropic magnetic susceptibility of the molecule, an analytical description of the magnitudes of overall alignment can be formulated, provided that solute molecules do not interact with one another. (Prestegard *et al*., 2000).

$A_a = \Delta\chi[B^2/15\mu_0 kT]$, $A_r = \delta\chi[B^2/15\mu_0 kT]$

Both structural and motional variation affect measured residual dipolar couplings, and, in general, the effects must be separated before conclusions about either structure or internal motion can be drawn. (Prestegard *et al*., 2000).

Lanthanides can impart a large paramagnetic anisotropy and, hence, greatly enhance levels of alignment. Dysprosium and Terbium are the lanthanide ions with the highest magnetic susceptibility anisotropy. (Prestegard *et al*., 2000).

The electronic properties of lanthanides are peculiar in that spin-orbit interactions are very large, larger in fact than ligand field effects. Spin-orbit interactions couple the orbital, L, and spin, S, angular momenta. The resulting free ion terms are characterized by J values which are vector combinations of L and S. (Bertini and Luchinat, 1996).

Ligand field effects split the J manifold in a way that is not easily predicted without specific calculations. However, the overall splitting is such that many of the levels are appreciably populated at room temperature. Ligand field effects remove the spherical symmetry around the metal ion and cause magnetic susceptibility anisotropy. (Bertini and Luchinat, 1996).

Magnetic susceptibility anisotropies are tensorially additive; and depending on the relative orientation of the resulting magnetic susceptibility tensors, constructive or destructive addition may result. (Prestegard *et al*., 2000).

A broad class of applications involves replacement of native metals in metalloproteins with paramagnetic ions of similar ionic radii. One class of proteins for which this approach has been successfully applied is the calcium binding proteins. (Prestegard *et al*., 2000).

For paramagnetic systems, the paramagnetic susceptibility tensor will often dominate the susceptibility, and paramagnetic contribution to the tensor can be calculated independently from the measurement of a sufficiently large number of pseudocontact shifts. Moreover, the measurement of pseudocontact shifts can provide an independent measure of order that is less sensitive to internal motions. (Prestegard *et al*., 2000).

One of the inherent limitations that arise in the analysis of dipolar data stems from the fact that dipolar coupling measurements do not have a one-to-one correspondence to a pair of polar angles describing the orientation of the interaction vector. A given residual dipolar coupling measurement can only restrict the orientation of the corresponding internuclear vector to two cones. Addition of data corresponding to other vectors rigidly related to the first can reduce the number of possible solutions. (Prestegard *et al*., 2000).

In an unpaired electron-nucleus system, the $\mathbf{I}\cdot A_{dip}\cdot\mathbf{S}$ term of the Hamiltonian describes the dipolar part of the electron-nucleus coupling. For a single unpaired electron with spin angular momentum, ŝ, this term can be written as

$$H_{dip} = (\mu_0/4\pi)h\gamma_N\mu_B\{(2l_N\cdot\mathbf{I}/\mathbf{r}^3{}_N) + g_e[(3(\mathbf{r}_N\cdot\hat{s})(\mathbf{r}_N\cdot\mathbf{I})/\mathbf{r}^5{}_N) - (\hat{s}\cdot\mathbf{I}/\mathbf{r}^3{}_N]\},$$

where l_N is the electron orbital angular momentum and $\mathbf{r}_N$ is the electron-nucleus distance. The part of the Hamiltonian containing l_N accounts for the magnetic anisotropy contribution to the coupling. By substituting the metal-nucleus distance r for $\mathbf{r}_N$, the metal-centered dipolar shift (or pseudocontact shift) can be expressed in terms of the magnetic susceptibility anisotropy for any spin system S:

$$(\Delta\nu/\nu_0)^{dip} = (1/4\pi 2r^3)[(3\cos^2\theta-1)(2/3\chi_{zz} - 1/3\chi_{xx}-1/3\chi_{yy}) + \sin^2\theta\cos2\Omega(\chi_{xx}-\chi_{yy})] \quad (3)$$

by assuming negligible zero field splitting and with some approximations, χ and g can be related by

$$\chi = \chi_M/N_A = \mu_0\,(g^{-2}\mu_B{}^2S(S+1)/3kT,$$

the previous equation becomes

$$(\Delta\nu/\nu_0)^{dip} = (\mu_0/4\pi)(\mu_B{}^2S(S+1)/18kTr^3)\{[2g^2{}_{zz} - (g^2{}_{xx}+g^2{}_{yy})](3\cos^2\theta-1) + 3(g^2{}_{xx}-g^2{}_{yy})\sin^2\theta\cos2\Omega\}, \quad (4)$$

where θ and Ω are the angles formed by *r* with the molecular *z* axis and by the projection of *r* on the *xy*-plane with the molecular *x* axis. The magnitude of the dipolar shift does not depend on any magnetic property of the particular nucleus. (Bertini and Luchinat, 1996).

In the case where the symmetry of the magnetic susceptibility tensor is axial, equations 3 and 4 take the more familiar form

$(\Delta\nu/\nu_0)^{dip} = (1/4\pi 3r^3)(3\cos^2\theta-1)(\chi_\parallel - \chi_\perp)$

$(\Delta\nu/\nu_0)^{dip} = (\mu_0/4\pi)(\mu_B^2 S(S+1)/9kTr^3)\ (3\cos^2\theta-1)(g^2_\parallel - g^2_\perp)$ (Bertini and Luchinat, 1996).

The pseudocontact shifts provide information for the determination of the position of the protein atoms in the metal frame. Conversely, they also permit the determination of the position of the metal ion in the protein frame. (Bertini *et al*., 2002).

The pseudocontact shifts relative to one metal ion can provide only the absolute values of the coordinates of all atoms in any rigid domain, as the angular dependence is provided by quadratic trigonometric functions. Therefore, there is an intrinsic degeneracy in the problem, since eight positions for any domain are possible. Four of these solutions can be excluded as they lead to amino acid structures with the wrong chirality. The residual four-fold degeneracy can be removed, for instance, by measuring the pseudocontact shifts relative to two different metal ions, having magnetic susceptibility tensors with no principal axis in common. (Bertini *et al*., 2002).

Residual dipolar couplings in paramagnetic compounds, like pseudocontact shifts, can be used as structural constraints. However, they can provide information on the relative orientation of internuclear pairs only, and not on the distance of the pairs from the metal ion.

Pseudocontact shifts and residual dipolar couplings have been proved experimentally to be consistent with one another and with the NOEs. (Bertini *et al*., 2002).

15. Paramagnetic tagging of diamagnetic proteins

The use of external alignment media is widely use for structure determination and dynamic studies of proteins, however the introduction of a paramagnetic centre in a diamagnetic biomolecule induces an alignment with different biophysical properties giving access to complementary and novel dynamic information on the system. One such application is the incomplete labelling of a homodimer with a paramagnetic tag leading to two sets of signal that contain information about the relative orientation and contact surfaces of the homodimer. Another application is the study of domain motions in multidomain proteins. In the presence of interdomain motion, there is a reduction in the magnitude of the axial component of the alignment tensor of the domain which is not tagged for the two-domain model protein CaM. (Rodríguez-Castañeda *et al*., 2006). [$4Ca^{2+}$]CaM has ample conformational freedom in solution. Bertini and collaborators (2004) aligned paramagnetically the N-terminal domain of a CaM mutant with a lanthanide ion; they found that the distribution of the conformational space was non-uniform. Within all possible conformations, there must be some with less favourable orientations of the C-terminal domain.

Various small paramagnetic tags that are attached to proteins via cysteine side-chains have been introduced. The Ethylene-diamine-tetraacetate (EDTA) derived tags have been used by Gaponenko and collaborators (2004) for the study of homodimers.

Ikegami and collaborators (2004) made use of EDTA derived tags which do not form new stereocenters when ligated to lanthanides. They have dissociation constants in the 10^{-18} M range (Leonov *et al*., 2005) therefore can be used for the investigation of metal binding proteins. These tags have been used to study the peptidyl prolyl cis/trans isomerase from *E.coli*, trigger factor (Haberz *et.al*, 2006) and different activated states of CaM in this thesis.

16. Calmodulin dynamics

The first static picture of CaM came from its x-ray crystallographic structure (Babu *et al*., 1988). The structure revealed a dumbbell like shape, where the two domains are linked by a long helix. Fallon and Quiocho (2003) crystallized a closed compact structure of Ca^{2+} CaM with a sharp bent in the helix linker and a more compact N-terminal domain.

Chou and collaborators (2001) determined the solution structure of Ca^{2+} ligated CaM from residual dipolar couplings measured in a liquid crystalline medium. The C-terminal domain solution structure is similar to the X-ray crystal structure; however the EF hands of the N-terminal domain are considerably less open.

Various studies undertaken in solution have widened the picture of the numerous interdomain orientations of Ca^{2+}-CaM; moreover the relative orientation of the different domains is important for their physiological function. Early small angle X-ray scattering studies in solution carried out on Troponin C and CaM (Heidorn and Trewhella, 1988) already suggested a closer distance between the domains as seen in the crystal structure by Babu *et al*. 1988. Kataoka and collaborators (1991) studied two CaM/peptide complexes derived from the Ca^{2+} pump with SAXS. The C20W peptide complex revealed an interatomic length distribution function, P(*r*), similar to that of CaM alone, indicating that the CaM/C20W complex retained an extended, dumbbell-shaped structure. By contrast, the binding of C24W resulted in the formation of a globular structure similar to those observed with many other CaM-binding peptides, like the smooth muscle myosine light chain kinase peptide (smMLCK) for instance.

Elshorst and collaborators (1999) solved the solution structure of the CaM complex with the C20W peptide of the calcium pump. The structure revealed that this peptide binds solely to the C-terminal domain of CaM.

As heteronuclear NMR experiments became available in isotopically enriched proteins, Barbato and collaborators (1992) showed through ^{15}N relaxation that the residues of the central linker 78-81 of CaM had a very high degree of mobility. They argued that this mobility was responsible for the fact that, from a ^{15}N relaxation view point, the N- and C-terminal halves reorient nearly isotropically. The motional correlation times for the two halves were slightly different and compatible with the difference in size of their structured regions. These findings support the "flexible tether" hypothesis, where the central helix only serves to keep the two domains in close proximity for binding to their target. In addition, each domain within CaM undergoes independent diffusion at a faster rate than the overall tumbling of the protein. The interdomain motion of each domain was characterized by an order parameter and a time constant on the nanosecond time scale. (Chang *et al*., 2003).

In the absence of calcium, CaM adopts a well-folded structure with numerous slowly exchanging backbone amide protons. Its dynamics could not be described adequately by a model of an isotropically tumbling protein with fast, small, amplitude internal motions. The ^{15}N T_1 data measured at 51 and 61 MHz ^{15}N frequency were incompatible with a model of a rigid protein tumbling anisotropically. Significantly better agreement with the measured relaxation data was obtained in a model where the individual domains have restricted mobility on a time scale of about 3 ns, superimposed on the overall tumbling of the molecule which occurs on a time scale which is about 4 times slower. (Tjandra *et al*., 1995).

Substantial line broadening of many of the ^{15}N resonances in the C-terminal domain is caused by conformational exchange, on a time scale of a few hundred microseconds. (Tjandra *et al*., 1995).

For apoCaM, NMR relaxation data provided strong evidence that the C-terminal domain exists in a dynamic equilibrium between its regular, closed apo- state and an open conformation that is similar to that of the Ca^{2+} -ligated state. (Tjandra *et al*., 1995).

The relative orientations of the N- and C-terminal domains are nearly random in solution, in addition the interhelical angles in the N-terminal domain also differ by as much as 25^{o} from what is seen in the crystalline state. Not only the hydrophobic clefts, which are lined with flexible Met residues, provide a pliable interaction surface, the relative helix orientations are also easily changed in order to optimize target binding. (Tjandra *et al*., 1995).

Chang and collaborators (2003) reported a significant drop in the slow order parameter from 35 to 43 ^{o}C, indicating and unexpected increase in the amplitude of interdomain motions. The simplest explanation is that the flexibility of the central helix increases. They suggest that the disordered region of the central helix (residues 78-81) doubles in size on going from 35 to $43^{o}C$ because residues 74-77 partially "melt".

The available conformational space is quite ample and spans beyond the cone suggested by the ^{15}N relaxation data from Chang and Tjandra (2001), which senses the motions in the nano- to picosecond scale, whereas pseudocontact shifts and residual dipolar couplings are averaged by motions spanning a time scale that extends down to milliseconds. Thus, slower motions than those affecting relaxation measurements may contribute to the sampling of conformational space in CaM. (Bertini *et al*., 2004).

The C-terminal rDCs arise from averaging among very diverse orientations. Therefore, pendulum-like motions, no matter how ample, that do not imply also a rotation of the C-terminal domain about the axis of its first helix, are not sufficient in averaging the rDCs down to the small values observed. However not all C-terminal orientations are equally probable, since the rDCs don't average to zero. Electrostatic repulsion between the negatively charged domains may contribute to the different probabilities of sterically accessible conformations. (Bertini *et al*., 2004).

Single molecule fluorescence experiments (Johnson, 2006) have also shown that CaM exists in conformational sub-states. These sub-states were observed in FRET distributions with bin times up to 800 μs. If conformational interchange occurred on a faster time scale, conformational averaging would result in narrowing of the FRET distribution. The absence of such narrowing shows that the conformational interchange must occur on a longer time scale.

In order to explore further the time scale of conformational interchange, single-molecule fluorescence burst FRET trajectories were selected with durations of several milliseconds. Occasional jumps from one conformational sub-state to another occur on the millisecond time scale. Interchange on this time scale has implications for the function of CaM. The millisecond interchange of conformational sub-states of CaM may permit rapid exploration of conformational space for molecular recognition of target binding domains. (Johnson *et al.*, 2005).

Recent advances in the field of molecular dynamics which allow longer simulations, have contributed to the understanding of CaM function in its different activated states. During the 4-ns apoCaM trajectory, the interdomain distance fluctuated in the 29-39 Å range, with an average of 33 Å. For the [$4Ca^{2+}$]-CaM trajectory, the interdomain distance remained between 34 and 41 Å. The average distance was 38 Å. During the CaM:smMLCK peptide complex simulation the interdomain distance falls in the 22-25 Å range, with an average value of 24 Å. Thus the simulation results indicate that large-scale domain motions occur in calcium-free and calcium-loaded CaM, while such motions are absent in the collapsed CaM-peptide complex. (Yang *et al*., 2003).

Wang and collaborators (2005) studied the dynamics of CaM and CaM/smMLCK peptide complex based on the transverse cross-correlated relaxation rates between ^{13}CO chemical shift anisotropy and the ^{13}CO-$^{13}C\alpha$ dipolar interactions which are sensitive to the motion of the ^{13}CO-$^{13}C\alpha$ bond vector.

In the presence of ligand, the two domains of CaM form a clam-shell around the bound peptide. Only small structural changes occur within the N- and C-terminal domains. The ligand-induced conformations are accompanied by the diminishment in the amplitude of sub-nanosecond time scale dynamics of the methyl-bearing side chains, as detected by deuterium relaxation in methyl groups (Wand, 2001). In contrast, the amplitude of sub-nanosecond time scale dynamics of the protein backbone as monitored by ^{15}N relaxation in amide NH groups is not affected, except for the region bridging the two globular domains. These findings implied that peptide binding causes a major loss of conformational entropy of the side chains, but seemed to indicate that the entropy of the backbone was not affected by the binding process. However, the ^{13}CO-$^{13}C\alpha$ vectors report a significant loss in dynamics upon ligand binding, suggesting that the entropy of the backbone does contribute to the binding free energy. (Wang *et al*., 2005).

In contrast to the view afforded by the ^{15}N relaxation data, the ^{13}CO-$^{13}C\alpha$ cross-correlated relaxation data reveal that the backbone of un-ligated CaM contains residual motion, which is affected and partially quenched upon binding of the target domain. The change in backbone dynamics as sensed by the ^{13}CO environment is not sensed at all by the NH vector, despite the fact that both are part of the same peptide plane. The apparent lack of full correlation of the NH and ^{13}CO-$^{13}C\alpha$ detectors of protein backbone motion may be explained by anisotropic local motion of the peptide planes and/or dynamic pyrimidalization of the nitrogen atom which partially decouples the motion of the NH vector from that of the peptide plane. (Wang *et al*., 2005).

CaM shows two different types of allosteric behaviour: (i) cooperativity between calcium-binding sites and (ii) cooperativity between its target- and calcium-binding sites. The allosteric coupling between calcium- and peptide-binding sites is reciprocal, with the Ca^{2+} binding affinity of CaM increasing 30-100-fold in the presence of smMLCKp.

Igumenova and collaborators (2005) studied the dynamics of different CaM mutants in complex with the smMLCK peptide; they found that the backbone dynamics of these mutants in complex with Ca^{2+} and smMLCKp was indistinguishable from that of the wild-type complex. In contrast, for three of the mutants the dynamic properties of methyl-bearing side chains were found to be very different compared to those of the wild-type complex. Both local and long-range perturbation of the methyl dynamics exist. This behaviour does not correlate with chemical shift perturbations imposed by the mutations. Thus, the three mutants D58N, D95N, and E84K, have an altered allosteric behaviour comparable to that of the wild-type protein.

Larsson and collaborators (2001) studied the interaction of CaM with the dimeric basic helix-loop-helix transcription factor SEF2-1 using NMR. The stoichiometry of this interaction is one dimeric peptide binding two CaM molecules. The binding does not occur via the classical wrap-around binding mode; CaM interacts with SEF2-1mp in a more open conformation. In addition, the peptide does not form an α-helix. In a backbone dynamics study by ^{15}N-spin relaxation, the same group reported in 2005 that all CaM residues experience internal motion with an effective correlation time of ~2.5 ns with squared order parameter (S^2) of ~0.75. This could be attributed to motions of the N- and C-terminal domains of the CaM dimer in the complex. The data were consistent with a motional model in which the two N-terminal and two C-terminal CaM domains in the dimeric CaM:SEF2-1mp complex undergo a small-scale wobbling motion with half-angle of ~20^o as estimated from S_s^2=0.75. However, the internal motion involving reorientation of the CaM monomers cannot be excluded. Residues with significant exchange broadening were found, they clustered in the CaM:SEF2-1mp binding interface, the CaM:CaM interface, and in the flexible helix connecting the CaM N- and C-terminal domains, and have similar exchange times (~50μs), suggesting a cooperative mechanism.

II. MATERIALS AND METHODS

1. Polymerase chain reaction (PCR) based-cloning of the different Munc13-1 protein expression constructs

To clone the different Munc13-1 constructs the oligonucleotide primers for the PCR were designed for directed cloning into the different expression vectors with two different restriction sites in the 5' regions. The amplification generates a target fragment whose termini carry new restriction sites that can be used for directional cloning into plasmid vectors. The purified fragment and the vector are digested with the appropriate restriction enzymes, ligated together, and transformed into *E.coli* (see Figure 12). (Sambrook and Russell, 2001).

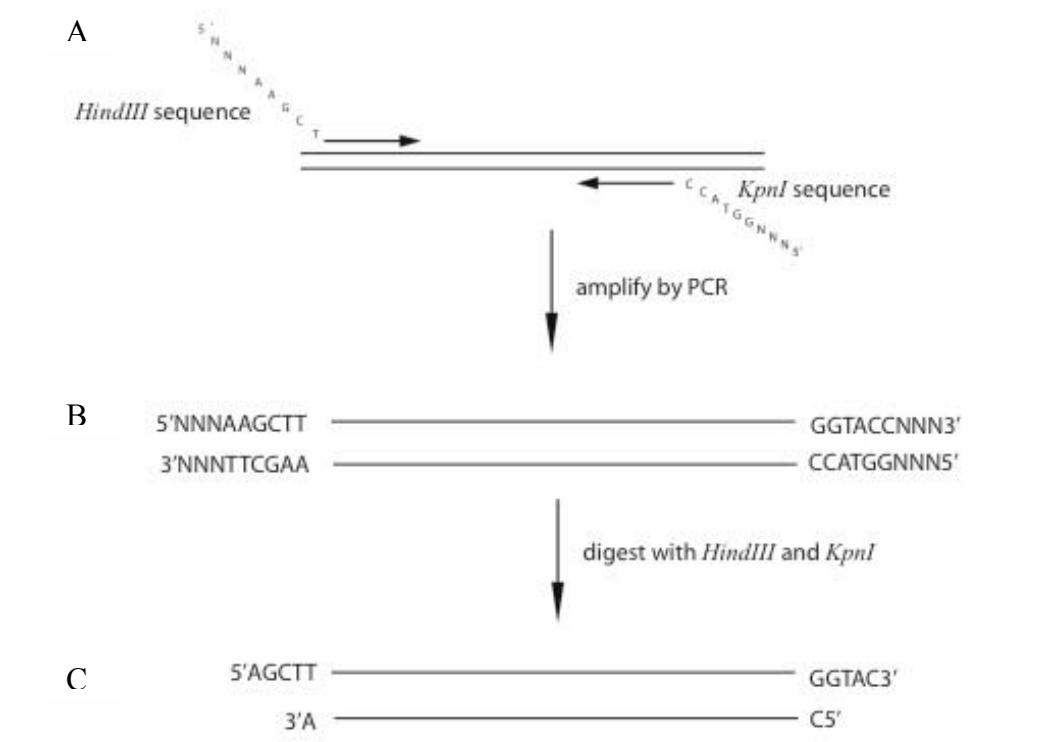

Figure12. PCR-based cloning strategy. The sense strand primer contains the sense strand of a restriction site, and the antisense primer contains the complementary sequence of a second restriction site. (A) To achieve high efficiency digestion, additional nucleotides must be included on both sides of the restriction endonuclease sequence. (B) Amplification by PCR produces a specific product with an *HindIII* site at the 5' end and a *KpnI* site at the 3' end. (C) Digestion with *HindIII* and *KpnI* produces a PCR product that can be cloned directionally. (Adapted from Sambrook and Russell, 2001).

a. Polymerase chain reaction (PCR)

Oligonucleotide primers

Munc13-1 (447-631) including the CaM binding site and the C_1 domain **Munc185**

M13c1-1 5' GAGCATATGGGATCCGCTGAGGAGGGCCAGGAAG 3'
M13c1-2 5' GCGGGATCCCATGGCTGAGGAGGGCCAGGAAG 3'
M13c1-3 5' CGACTCGAGGAATTCTTAGTCTTCAGCGCCATGCTTAGAAC 3'
M13c1-5 5' GAGGGTACCAGATCTATGGGTCATCACCATCACCATCA 3'

Munc13-1 (567-631) C_1 domain **Munc65**

M13c1-4 5' GAGCATATGGGATCCCACAACTTCGAGGTGTGGACG 3'
M13c1-3 5' CGACTCGAGGAATTCTTAGTCTTCAGCGCCATGCTTAGAAC 3'

Munc13-1 (458-492) CaM binding site **Munc36**

M1334aa-1 5' GAGGGATCCAGGGCCAAAGCCAACTGGTTG 3'
M1334aa-2 5' CGAGAATTCTTAGCCTTTGAACCACAGAGACTTGGA 3'
M1334aa-3 5' CGAAAGCTTTTAGCCTTTGAACCACAGAGACTTGGA 3'

The oligonucleotide primers were obtained in a lyophilized form from *Invitrogen*. 400 µl of TE buffer (10 mM TRIS, 1 mM EDTA, pH 8.0) were added to reconstitute them. The UV spectrum was measured to verify their purity and estimate their concentration.

Plasmid DNA vectors for protein expression :

pET 16b (*Novagen*) with a Tobacco Etch Virus protease cleavage site introduced
pGEX 2T (*Pharmacia*)
pET Duet-1 (*Novagen*)
pMAL

The cDNA of the *munc13-1* gene was kindly provided by Prof. Nils Brose Max-Planck for Experimental Medicine. For the PCR, 1µl of the *munc13-1* cDNA (10 ng/µl) was taken as template for the amplification. The reaction was done in a total volume of 50 µl. In a 250 µl *eppendorf* PCR tube, 5 µl of the 10X PCR reaction buffer, 1 µl of 20 mM dNTP, 1ul of the 200 µM oligonucleotide, sterile (*Millipore)*-water to reach the 50µl volume and 0.5 µl of the *Pfu* DNA polymerase. The polymerase chain reaction was done in a PCR sprint thermal cycler (*Hybaid*) using the following cycle:
10 minutes initial denaturation step at 95^{o}C
25 cycles consisting of a 30 sec denaturing step at 95^{o}C;
30 sec annealing step at 55^{o}C;
And a 30 sec extension step at 68^{o}C.
A 10 minutes final extension step at 68^{o}C.

The PCR product was checked with a 1 % (m/v) agarose gel electrophoresis. Briefly, 0.3 g of agarose were dissolved in 30 ml of Tris-borate-EDTA buffer (TBE) and boiled in the microwave for 1 minute; when the solution cooled to approximately 40^{o}C, 1 µl of a 1 % (m/v) ethidium bromide solution was added and then poured into the casting cassette. After the gel solidified it was put into the electrophoresis chamber containing the TBE buffer. The molecular weight marker and the samples, containing 4ul of 6x loading buffer, were loaded. The electrophoresis was carried out for one hour at a constant voltage of 80 V.

After the polymerase chain reaction; the product was purified with a PCR cleaning kit previous to the reaction with the restriction enzymes.

b. Restriction digestion of the PCR products

The restriction digestion of PCR fragments may work very well with non-purified PCR fragments, however when the purpose of the generated fragments is their cloning into a vector, it is advisable to purify the PCR products, since the *Taq*-polymerase its active at 37^{o}C and can therefore fill the cohesive ends leading to an unsuccessful cloning. An additional problem for the restriction of the PCR products is the fact that some restriction enzymes have

very little activity when the recognition sequence is located at the end of the sequence, for this purpose it is advisable to design the primers with at least three additional bases upstream of the recognition site. In general it is possible to carry a double digest, which means to do the restriction reaction with two enzymes at the same time. For this purpose, a buffer should be used in which both enzymes possess enough activity (above 75%) (Mülhardt, 2003).

The purified PCR products were obtained in a final volume of 28 µl. For cloning into the pET16b (TEV) expression vector the PCR product was digested with the *NcoI* and *XhoI* restriction enzymes (*MBI Fermentas*) in the 2X yellow TANGO buffer with Bovine Serum Albumin (BSA) (*MBI Fermentas*). The restriction digestion reaction was done in a total volume of 50 µl. 10 µl of the 10X yellow TANGO buffer with BSA, the total amount of the PCR product, 10ul of sterile (*Millipore*)-water, 1ul of *NcoI* (10U[1]/µl) and 1ul of *XhoI* (10U/µl) were mixed in a 1.5 ml *eppendorf* tube. For cloning into the pGEX-2T expression vector, the PCR product was digested with the *BamHI* and *EcoRI* restriction enzymes (*MBI Fermentas*) in the 2X yellow TANGO buffer with BSA in the same manner as above. For cloning into the multiple cloning site-2 (MCS2) of the pET Duet-1 expression vector, the PCR product was digested with *NdeI* and *XhoI* restriction enzymes (*MBI Fermentas*) in the 1X red TANGO buffer with BSA. The restriction digestion reaction was done in a total volume of 50 µl. 5 µl of the 10X red TANGO buffer, the total amount of the PCR product, 15 µl of sterile (*Millipore*)-water, 1µl of *NdeI* (10U/µl) and 1ul of *XhoI* were mixed in a 1.5 ml *eppendorf* tube. All the reactions were performed overnight at 37°C to ensure complete digestion of the PCR products. To remove the restriction enzymes, the restricted PCR products were purified with the PCR cleaning kit mentioned above.

c. Preparation of the plasmid DNA expression vectors for cloning

Plasmids are circular double stranded DNA molecules, which can replicate in an independent fashion from the bacterial genome. The minimum composition of a plasmid consists of an origin of replication *ori*, a gene for the selection (usually an antibiotic resistance gene) and a cloning site, where the desired DNA is inserted into the plasmid. In addition, it is possible to introduce various sequences, for example a second selection marker or a promoter for directing the expression of the inserted gene (Mülhardt, 2003).

The cloning site contains various recognition sites for restriction enzymes, which usually are only present once in the vector. This allows to cut the vector for cloning, avoiding the fragmentation of the vector in many pieces. In theory it suffices a single recognition site to insert a DNA fragment, however most of the plasmid vectors contain ten to twenty of such recognition sites to allow flexibility in the cloning strategies, and these series of recognition sites are called multiple cloning sites (MCS).

1µg of vector DNA was digested with the different restriction enzymes in the same manner as done for the PCR products. The only difference was that the reaction digestion was done just for 1 hour to prevent any star activity of the restriction enzymes. After the restriction digestion was complete the vector DNA was dephosphorylated by the addition of 1ul of Calf Intestine Phosphatase (1U/µl) (*MBI Fermentas*) and further incubation at 37°C for 1 hour. The vector plasmid DNA was loaded into a 1 % (m/v) agarose gel, gel-extracted and purified with a gel extraction purification kit (*Qiagen*).

d. Ligation reaction

To ensure a favorable stoichiometric ratio between the restricted PCR product and the plasmid DNA vector for the ligation reaction to take place, it is desirable to have around 3

[1] The unit of the restriction enzyme is defined as the amount of enzyme needed for digesting completely 1µg of the DNA substrate in 60 minutes at the correct temperature and buffer in a total volume of 50µl.

molar excess of the insert to the vector. The ligation reaction was done in a total volume of 20 µl: 2 µl of the 10X ligation buffer, 100 ng of vector DNA, typically around 1ul, the necessary amount of insert to achieve the favorable ligation reaction conditions, sterile (*Millipore*)-water and 1 µl of T4 DNA ligase (*MBI Fermentas*). The ligation reaction was done overnight at 16^{o}C.

e. Transformation of the ligated plasmid DNA

The classical method to make bacteria competent for transformation is carried out with calcium chloride. The chemical competent bacteria give 10^6 to 10^8 colonies per µg of Test-DNA (Mülhardt, 2003).

The ligated plasmid DNA needs to be amplified, for that purpose, 4 µl of the ligation reaction were added to 50 µl of chemical competent *Escherichia coli* (XL2-Blue) cells and incubated on ice for 30 minutes. The cells were exposed to a heat-shock at 42^{o}C for 45 seconds and then incubated on ice for 2 minutes. 600 µl of pre-warmed LB medium at 37^{o}C were added and the cells were grown for 1 hr at 37^{o}C prior to plating them on LB-agar plates containing ampicillin (50µg/ml). The LB-agar plates were incubated overnight at 37^{o}C.

f. Plasmid DNA amplification and purification

At least two colonies for each ligation reaction were picked and used for inoculating 5ml of LB medium with 50µg/ml ampicillin; the cultures were grown overnight at 37^{o}C. A glycerol stock to preserve the clones at -80^{o}C was prepared by adding 500 µl of 50% (v/v) glycerol to 500 µl of culture.

To purify the plasmid DNA from the *E.coli* culture the alkaline lysis protocol was used with the aid of a mini-prep Plasmid DNA purification kit (*Qiagen*). This protocol purifies the plasmid DNA from the bacterial chromosomal DNA based on the different renaturation properties of the circular plasmid DNA and the genomic DNA; the high alkaline solution denatures the DNA and upon neutralization the plasmid DNA renatures fast, while the much larger chromosomal DNA remains in a single stranded conformation and precipitates (Mülhardt, 2003). Briefly, the cultures were centrifuged at 5,000 rpm for 10 minutes. The supernatant was discarded and the cells were resuspended with 250 µl of RNAse containing buffer; the cells were lysed adding 250 µl of lysis buffer (0.2 M sodium hydroxide/1 %(w/v) sodium dodecyl sulphate). The lysates were neutralized with 300 µl of neutralization buffer (3 M potassium acetate pH 5.5) in order to precipitate potassium-acetate together with the protein-genomic DNA complexes. The precipitate was removed by centrifugation in a table-top centrifuge for 10 minutes at 16,000 g. The supernatant was added to a silica column and purified washing with an ethanol containing buffer. The plasmid DNA was eluted from the silica matrix with 50 µl of the elution buffer and the concentration was determined measuring the UV spectrum.

g. Screening, DNA sequencing and transformation of positive clones

To verify that the purified plasmid DNA is the desired clone; the clones were screened, for this purpose, the plasmid DNA was digested with the same restriction enzymes used for the cloning. A 1% (m/v) agarose gel electrophoresis was performed to visualize which clones were positive.

For the PCR-based cloning of DNA it is essential to sequence the insert DNA to confirm the 100 % identity of the coding region with the original DNA source. The sequencing was done by a commercial service company. 600 ng of the purified plasmid DNA

and 20 pmol of the sequencing oligonucleotide primer were sent in a total volume of 7 µl in a 250 µl *eppendorf* cup.

1 µl of the purified plasmid DNA were added to 50 µl of heat shock transformation competent *E.coli* BL21(DE3) cells and incubated for 30 minutes on ice. The cells were exposed to 42°C for 45 seconds and then incubated on ice for 2 minutes. 600 µl of pre-warmed LB medium at 37°C were added and the cells were grown for 1 hr at 37°C prior to plating them on LB-agar plates containing ampicillin (50µg/ml). The LB-agar plates were incubated overnight at 37°C.

h. Protein overexpression test in LB medium and protein solubility

For the heterologous expression of proteins in bacteria, a common organism is *E.coli*, since it is an intensively studied bacterium, which yields large amounts of protein. It is common to introduce at the beginning or at the end of the cDNA an additional coding sequence, to obtain a fusion protein with special characteristics. For example the common histidine-tag (a polyhistidine sequence of 6-8 amino acids) allows an efficient purification by means of immobilized metal affinity chromatography (IMAC) columns. It is also possible to introduce a protease recognition site, *e.g.* Thrombin to cut the fusion tag after the purification (Mülhardt, 2003).

After the cloning succeeded, it was decisive to test the overexpression of the desired Munc13-1 construct. For this purpose, a 2 ml LB with 50µg/ml ampicillin culture was grown overnight at 37°C and used to inoculate 100 ml of LB medium with 50µg/ml ampicillin. The culture was grown at 37°C for several hours; the growth was monitored measuring the absorbance at 600 nm. The overexpression of the protein was induced by the addition of 0.5 mM isopropyl thio-β-galactoside (IPTG) when the cells have reached an absorbance of 0.6. The overexpression was carried out for 4 hours at 37°C and then the cells are harvested by centrifugation at 5,000 g for 15 minutes. A small aliquot of the cells were directly lysed with the SDS-PAGE laemmli buffer by heating for 3 minutes at 95°C and the lysates were run in a protein mini-gel to compare the protein content of the cells before and after induction. Another critical issue concerns the protein solubility after the lysis, since this is essential for the purification of the protein under native conditions. After harvesting the cells; the lysis was done according to the purification protocol for the different tagged versions of the constructs. The lysis of the hexahistidine tagged proteins was done in the following buffer: 20 mM NaH_2PO_4, 150 mM NaCl, 1mM dithiotreitol (DTT), 10 mM Imidazole, pH 8.0 supplemented with 200 µM $ZnCl_2$, 1mg/ml of lysozyme, 0.5 mM Phenylmethylsulfonate fluoride (PMSF), 1 tablet of EDTA-free complete protease inhibitor. The lysis buffer of the GST-tagged proteins was done in 1X PBS buffer (50 mM NaH_2PO_4, 150 mM NaCl, pH 7.4) supplemented with 1 tablet of complete protease inhibitor, 1mg/ml of lysozyme, 200 µM of $ZnCl_2$, 0.5 mM PMSF and 1 mM DTT. The cells were disrupted by ultrasound sonication six times for 20 seconds with a power of 60%. The cell debris was separated by centrifugation at 45,000 g for 45 minutes at 4°C. The protein content of the supernatant and pellet fractions was evaluated with SDS-PAGE.

The composition of the SDS-polyacrylamide gel is the following:

17.5% separating gel

Acrylamide solution (30% acrylamide, 0.8% bisacrylamide) 3ml
1M TrisHCl, pH 8.8 1.88 ml
10% SDS 50µl
10% APS 50 µl
TEMED 2.5 µl

3% stacking gel

Acrylamide solution (30% acrylamide, 0.8% bisacrylamide) 250 µl

1M TrisHCl, pH 6.8 313 µl
10% SDS 25 µl
10% APS 25 µl
TEMED 2 µl
dd H_2O 1.88 ml

The electrophoresis was carried out at a constant current of 25mA per mini-gel in a 1X Running Buffer. The composition of the 10x Running Buffer (pH 8.3) was the following: 30 g Tris Base, 144 g glycine, 10 g SDS and ddH_2O to 1 liter.

The protein samples needed to be denatured and reduced in order to analyze their electrophoretic properties under non-native conditions. The composition of this denaturing loading buffer was the following: 4x Sample Buffer or Laemmli buffer (8 ml): 4.0 ml ddH_2O, 1.0 ml of 0.5 M Tris-HCl, 0.8 ml of glycerol, 1.6 ml of 10% (w/v) SDS, 0.4 ml of β-mercaptoethanol and 0.2 ml of 0.05% (w/v) bromophenol blue.

Dynamic Light Scattering (DLS) measurements after the size exclusion chromatography were also done on the CaM/Munc185 complex. For this purpose, the protein was concentrated to 100 µM. To remove suspended particles the protein solution was filtered through a 22 µm pore size membrane and ultracentrifugation was performed at 60,000 g for 1 hour. The DLS measurement relies on the Brownian motion of a macromolecule. When a light beam is directed onto a solution with spherical particles the Brownian motion causes a Doppler shift when the light hits the moving particle, changing the wavelength of the incoming light. This change is related to the size of the particle. It is possible to compute the sphere size distribution and give a description of the particle's motion in the medium, measuring the diffusion coefficient of the particle and using the autocorrelation function. (Sartor, 2003)

2. PCR-mediated Site-directed mutagenesis

Oligonucleotide-directed mutagenesis is used to test the role of particular residues in the structure, catalytic activity, and ligand-binding capacity of a protein. In the absence of a three-dimensional structure, one relies on informed guesses concerning the structure of the protein and the contribution of individual residues to protein stability and function. A major problem is distinguishing mutations that affect local structures from those that have profound effects on the folding or stability of the entire protein (Sambrook and Russell, 2001).

A synthetic oligonucleotide encoding the desired mutation is annealed to the target region of the wild-type template DNA where it serves as a primer for intitiation of DNA synthesis in vitro. The extension of the oligonucleotide by a DNA polymerase generates a double-stranded DNA that carries the desired mutation. The mutated DNA is then inserted at the appropriate location of the target gene, and the mutant protein is expressed (Sambrook and Russell, 2001).

In vitro mutagenesis using double-stranded DNA templates and selection of mutants with *DpnI*: In this method, two oligonucleotides are used to prime DNA synthesis by a high-fidelity polymerase on a denatured plasmid template. The two oligonucleotides both contain the desired mutation and have the same starting and ending positions on opposite strands of the plasmid DNA. In this protocol, the entire lengths of both strands of the plasmid DNA are amplified in a linear fashion during several rounds of thermal cycling, generating mutated plasmid containing staggered nicks on opposite strands. The products of the linear amplification reaction are treated with the restriction enzyme *DpnI*, which specifically cleaves fully methylated $G^{Me6}ATC$ sequences. *DpnI* will digest the bacterially generated DNA used as template for amplification, but it will not digest DNA synthesized during the course of the reaction in vitro. *DpnI*-resistant molecules, which are enriched in the desired mutants, are recovered by transforming *E.coli* to antibiotic resistance. Depending on the complexity of the

mutation, and the length of the template DNA, between 15% and 80% of the transformed colonies will contain plasmids with the desired mutation (Sambrook and Russell, 2001).
Site-directed mutagenesis in the C-terminal domain of *X. laevis* CaM and on rat Munc13-1 was performed using the Stratagene QuikChange® site-directed mutagenesis kit. The oligonucleotide primers were ordered from *Invitrogen* (see Table1).

Table 1. Oligonucleotide primers for site-directed mutagenesis

Mutation	Primers	
CaM S101C	CaM17 (+) strand	5' GGAACGGCTACATC**TGC**GCTGCTGAATTACG 3'
	CaM18 (-) strand	5' CGTAATTCAGCAGC**GCA**GATGTAGCCGTTCCC 3'
CaM T110C	CaM19 (+) strand	5' CGTCACGTCATG**TGC**AACCTCGGGGAGAAGTTAACAGACG 3'
	CaM20 (-) strand	5' CGTCTGTTAACTTCTCCCCGAGGTT**GCA**CATGACGTGACG 3'
CaM T146C	CaM21 (+) strand	5' GAGTTTGTACAAATGATG**TGC**GCAAAGTGAAGAGTCTAGAATCG 3'
	CaM22 (-) strand	5' CGATTCTAGACTCTTCACTTTGC**GCA**CATCATTTGTACAAACTC 3'
Munc13-1 W489A	M13c1-8 (+) strand	5' GAGATGTCCAAGTCTCTG**GCG**TTCAAAGGCGGCCCT 3'
	M13c1-11 (-) strand	5' AGGGCCGCCTTTGAA**CGC**CAGAGACTTGGACATCTC 3'
Munc13-1 W572Y	M13c1-14 (+) strand	5' CACAACTTCGAGGTG**TAC**ACGGCCACCACTCCCACC 3'
	M13c1-15 (-) strand	5' GGTGGGAGTGGTGGCCGT**GTA**CACCTCGAAGTTGTG 3'
Munc13-1 W588A	M13c1-10 (+) strand	5' TGCGAGGGGCTGCTG**GCG**GGCATCGCGCGG 3'
	M13c1-13 (-) strand	5' CCGCGCGATGCC**CGC**CAGCAGCCCCTCGCA 3'

The oligonucleotide primers were reconstituted in ddH_2O to obtain an approximate concentration of 1µg/ml; the A_{260} was measured to determine the exact concentration of each primer. The reaction mix was prepared as following (all mixing steps done on ice): 2.5 µl of 10x reaction buffer, 1 µl (39 ng) of the pET28a CaM wild type clone, 0.5 µl of oligonucleotide primer, 0.5 µl of dNTP (20mM each) mix, 14 µl of ddH_2O and 0.5 µl of *Pfu* Turbo DNA polymerase (2.5 U/µl)
Thermal cycling was done according to following scheme:
1) 95°C 30 sec
2) 95°C 30 sec
   55°C 1 min
   68°C 12 min
   16 cycles
3) 68°C 10 min final extension
4) 4°C

The products obtained after the thermal cycling were stored at -20°C. The samples were thawed on ice prior digestion, then 0.5 µl of *DpnI* restrictase (10 U/µl) were added and the samples were incubated at 37°C for 1h. The mixture after incubation was used to transform competent *E.coli* (XL2-Blue) bacteria. For each CaM and Munc13-1 mutant a 50 µl aliquot of competent cells was thawed on ice, 1 µl of plasmid-containing solution was added followed by 30 min incubation on ice. A heat pulse was applied (45 sec, 42°C) and the cells

were incubated on ice for additional 2 min. After this 0.5 ml of LB-medium preheated at 42°C were added and cells were incubated at 37°C, 220 rpm for 1 h.

Incubation mix was shortly centrifuged, the pellet resuspended in 100 µl of LB medium and plated onto LB plates (70 µg/ml kanamycin for CaM and 50 µg/ml ampicillin for Munc13-1). After overnight incubation at 37°C two colonies from each plate were picked and grown into 3 ml LB-medium containing with kanamycin or ampicillin overnight at 37°C.

3. Overexpression of the different proteins in Minimal Medium for uniform isotope labeling

The expression vector was transformed into *E.coli* strain BL21 (DE3) and kept as glycerol stock at –80°C. A small amount of the glycerol stock was taken with a sterile loop and streaked into a LB agar plate containing the appropriate antibiotic (50 µg/ml of ampicillin and/or 70 µg/ml kanamycin). The plate was incubated overnight at 37°C to obtain single colonies. A colony was picked and was inoculated into 3 ml of LB medium (with 50 µg/ml ampicillin and/or 70 µg/ml kanamycin); the culture was incubated at 37°C for at least 6 hours. 50 ml of M9 minimal medium with trace elements (containing 50 µg/ml of ampicillin and/or 70µg/ml of kanamycin) were prepared and inoculated with 500 µl of the previous LB culture and grown overnight at 37°C.

1L of minimal medium were prepared; the composition for 1L of (^{15}N and/or ^{13}C labeled) M9 minimal medium was the following: 6.78 g of Na_2HPO_4, 3 g of KH_2PO_4, 0.5 g of NaCl, 2 mM $MgSO_4$, 0.1 mM $CaCl_2$, 30 mg of thiamine hydrochloride, 4 g of (^{13}C-labeled or natural abundance) glucose and 1 g of (^{15}N-labeled or natural abundance) ammonium chloride, pH 7.4. In addition, 10 ml of the following stock solution of trace elements were added: 0.06 g/l of $FeSO_4 \bullet 7H_2O$, 0.0115 g/l of $MnCl_2 \bullet 2H_2O$, 0.008 g/l of $CoCl_2 \bullet 6H_2O$, 0.007 g/l of $ZnSO_4 \bullet 7H_2O$, 0.003 g/l of $CuCl_2 \bullet 2H_2O$, 0.0002 g/l of H_3BO_3, 0.0025 g/l of $(NH_4)_6Mo7O_2 \bullet 4H_2O$.

The (^{15}N and/or ^{13}C labeled) M9 medium was inoculated with the 50 ml overnight culture in M9 medium and the bacteria were grown at 37°C to an $O.D._{.600nm}$ of 0.6. The expression of the protein was induced with 0.5 mM IPTG for different amount of time and at different temperatures, depending on the protein to be expressed. To harvest, the cells were centrifuged at 5,000 g for 15 minutes. The pellet was stored at –80°C until the purification was done.

4. Purification of the hexahistidine-tagged Munc13-1 proteins

The 6XHis-tagged recombinant proteins can be easily purified by binding with strong affinity and high selectivity to Ni-NTA agarose. The Ni-NTA agarose is comprised of Sepharose CL-6B coupled to Ni-NTA. The agarose matrix combines nitrilotriacetic acid (NTA), a tetradentate chelating ligand, in a cross-linked 6% agarose structure. NTA binds Ni^{2+} ions by four coordination sites. This design allows for a high binding affinity of the fusion protein with minimal nonspecific binding. The Ni-NTA matrix allows for binding of approximately 5 to 10 mg of 6 his-tagged proteins per milliliter of resin. Proteins bound to the Ni-NTA agarose are eluted either by competition binding imidazole, or with a low pH buffer.
The soluble hexahistidine-tagged Munc13-1 proteins were bound for 1 hour at room temperature to 4ml of Ni-NTA agarose (*Qiagen*) previously equilibrated with the His-purification wash buffer (20 mM NaH_2PO_4, 150 mM NaCl, 20 mM imidazole, pH 8.0). The Ni-NTA-agarose was retained in a disposable 10 ml pierce column and it was washed 5 times with 10 ml of wash buffer. The hexahistidine tagged Munc13-1 protein was eluted 4 times with 2 ml of elution buffer (20 mM NaH_2PO_4, 150 mM NaCl, 300 mM imidazole, pH 8.0).

The Munc185-$(his)_6$ protein was insoluble, however when it was co expressed with CaM it was soluble and CaM co-purified with Munc185-$(his)_6$. The Munc65-$(his)_6$ protein was soluble, but the yield after elution from the Ni-NTA agarose was rather low.

The CaM/Munc185-$(his)_6$ complex was dialyzed overnight against 2L of TEV cleavage buffer (50 mM Tris, 100 mM NaCl, 1mM DTT, pH 8.0) at 4^{o}C. To cleave the hexahistidine tag, 20 units of TEV protease were added per 1mg of fusion protein and incubated at room temperature for 3 hours. To remove the hexahistidine tag and the TEV protease, the cleaved protein solution was incubated for 1 hour at room temperature with 2 ml of Ni-NTA agarose, previously equilibrated with his-wash buffer. The resin was retained with a 5 ml Pierce column and the flow through containing the cleaved CaM/Munc185 complex was obtained. The resin was washed 3 times with 1 ml of his-wash buffer. The different fractions were analyzed by SDS-PAGE. The CaM/Munc185 complex was further purified by size exclusion chromatography on a *Superdex* 75 (HI-LOAD) gel filtration column (*Pharmacia*). The complex containing fractions after the Ni-NTA agarose purification were dialyzed against the gel filtration buffer (20 mM HEPES, 300 mM NaCl, 1mM DTT, pH 8.0) and concentrated by ultrafiltration with a 10 kDa *Vivaspin* membrane device prior to injection to the gel filtration column.

5. Purification of the GST-tagged Munc13-1 proteins

The glutathione-S-transferase (GST)-fusion protein is a common affinity purification tag, which has affinity for immobilized glutathione. Glutathione-resin based purifications require that the GST domain is soluble and properly folded. The gentle elution condition (10mM reduced glutathione) avoids target protein denaturation.

The soluble GST-tagged Munc13-1 proteins were bound for 1 hour at room temperature to 2 ml of GST-Sepharose previously equilibrated with 1X PBS. The GST-Sepharose was retained in a disposable *Pierce* 10 ml column and it was washed 4 times with 1X PBS. The GST-tag was cleaved overnight at room temperature on the column by the addition of 10 Units of thrombin per mg of fusion protein. The flow-through containing the Munc13-1 protein was recovered and the GST-Sepharose was washed 3 times with 1 ml of 1X PBS. The GST-Munc185 fusion protein was insoluble; it was only soluble when co-expressed with CaM. However the hexahistidine-tagged version of the complex was preferred, since the yield was better. The GST-Munc65 fusion protein was soluble, it was purification by GST-Sepharose affinity chromatography and the N-terminal GST tagged was cleaved with thrombin. The Munc13-1 C1 domain was further purified by reverse-phase High Performance Liquid Chromatography (RP-HPLC) using a C18 (*vydac*) preparative column with a linear acetonitrile-water 0.1% (v/v) trifluoroacetic acid elution gradient. The fractions containing the Munc65 protein were lyophilized and reconstituted with 0.05 % (v/v) TFA. The refolding of the Munc65 protein was achieved with the addition of a 3 molar excess of $ZnCl_2$ and increasing the pH to 6.5 with a diluted sodium hydroxide solution (0.05 M).

The GST-Munc36 fusion protein was insoluble; however the overnight co-expression with CaM at 20^{o}C gave a soluble complex that co-purified with CaM. The purification of the Munc13-1(457-492) peptide after the thrombin cleavage was also done by RP-HPLC under the same conditions as for the Munc65 protein. The fractions containing the Munc13-1(457-492) peptide were lyophilized and dissolved in water; the pH was adjusted with NaOH to 6.5 before addition of CaM to avoid precipitation.

6. Purification of CaM

The purification procedure for CaM used in this work is based on early biochemical work done on CaM; it exploits the hydrophobic properties of CaM in its calcium bound state.

It has the advantage, that it is not necessary to introduce an affinity tag, which decreases the total yield. In addition, depending on the protease used in the removal of the tag, a non-native glycine may remain in the primary sequence.

The bacterial pellet was thawed on ice and resuspended in 40 ml of lysis buffer (50mM Tris, pH 7.4, 4mM $MgCl_2$, 8 mg Lysozyme, 1 tablet of Complete ™ inhibitor mix (*Roche*)). The mixture was stirred for 30 min, then 2 mg of DNAse I were added and stirred for additional 30 min. EDTA was added up to a final concentration of 1 mM (from a 500 mM stock solution, pH 8.0). The mixture was treated by ultrasound sonication (8 pulses of 20 sec, TT13 tip, 60-100% intensity) to disrupt the cells. The lysed cells were centrifuged at 45,000 g for 45 min.

After centrifugation, the supernatant was collected and EDTA added up to a final concentration of 2.5 mM. Trichloroacetic acid (TCA) was added up to final concentration of 2.84%, from a 50% (w/v) stock solution. The pH was adjusted to 6.0 (with 5 M NaOH). The solution was stirred for 1 h and the precipitate was removed by centrifugation at 45.000 g for 20 min. TCA was added to the supernatant up to a final concentration of 3.4%. The solution was stirred for 1 h followed by centrifugation at 45,000 g for 20 min. The pellet was collected and dissolved in 10 ml of 1 M Tris, pH 7.4, 0.5 mM PMSF. The sample was dialyzed overnight against 2 L of dialysis buffer (50 mM Tris, pH 7.4, 0.5 mM PMSF).

EDTA was added to the dialyzed sample up to a final concentration 5mM and 10 ml of Phenyl-Sepharose were equilibrated with buffer A (50 mM Tris, pH 7.4, 0.5 mM PMSF, 5mM EDTA).

The dialyzed sample was incubated with the Phenyl-Sepharose for 3 h with stirring. The incubation mixture was passed through a glass filter; the resin was washed with 10 ml of fresh buffer A and $CaCl_2$ was added to the flow-trough up to a final concentration of 15 mM.
The 15-ml Phenyl-Sepharose column was equilibrated with buffer B (50 mM Tris, pH 7.4, 0.5 mM PMSF, 1 mM $CaCl_2$, 1.4 mM β-mercaptoethanol) and the flow-through after the batch purification step was loaded. The column was washed with 3 column volumes of buffer B and then with buffer C (50 mM TrisHCl, pH 7.4, 0.5 mM PMSF, 1 mM $CaCl_2$, 1.4 mM β-mercaptoethanol, 0.5 M NaCl) until a stable baseline was reached. The CaM elution was carried out using buffer D (50 mM TrisHCl, pH 7.4, 1.4 mM β-mercaptoethanol, 5mM EDTA), 1 ml fractions were collected and analyzed by SDS-PAGE. In each case 5,0 µl of sample solution were mixed with 5.0 µl of sample buffer and boiled at 95^{o}C for 2 min. Fractions containing CaM were combined and dialyzed against NMR-buffer (20 mM Bis-Tris, 150 mM KCl, 10 mM $CaCl_2$, pH 6.8)

The protein concentration after dialysis was estimated by UV-spectrophotometry (A_{280}=0.246, 0.5 mg/ml of CaM). 50 µl of this solution was taken for Electrospray Ionization Mass spectrometry (ESI-MS) analysis, for this purpose the sample was dialyzed against 20 mM NH_4Ac buffer, pH 6.5. After dialysis, the sample was concentrated using Centricon ™ membranes, MWCO 10.000 until a final volume of 0.6 ml (1 mM CaM) was reached. Then it was washed two times with NMR-buffer (2 ml of buffer each time) to remove β-mercaptoethanol and to increase the Ca^{2+} concentration.

For the samples used in paramagnetic alignment studies, the CaM cysteine mutant was derivatized with the paramagnetic tag (S-Methanesulfonyl-L-cysteaminyl-1-carbonic-acid-ethylenediamine-N,N,N',N'-tetraacetic acid, MS-EDTA). The total volume of the concentrated protein solution (in NMR buffer) was mixed with a 3-fold molar excess of tag (1 mg/ml solution in H_2O). The sample was left for 20 min at room temperature; the excess of tag was removed by washing with NMR-buffer 2 times in a *centricon* membrane (10 kDa cutoff) with 2 ml each time and the sample was stored at 4°C.

7. Purification of the Munc13-1-185aa protein

The Munc185-$(his)_6$ protein could not be expressed alone in a soluble form; for this reason the approach of the co-expression with CaM chosen. However, it was of interest to study the free protein as well, for this reason a method to dissociate the complex was developed. From the primary sequence of the two proteins it was expected that they differ significantly in their isolectric point (pI); for this reason ion exchange chromatography was the method of choice for the biochemical separation. Since the CaM/Munc13-1 interaction is calcium dependant, the complex was dialyzed against a high concentration of EDTA (50 mM) and pH 8.8 to remove calcium from CaM. Afterwards it was dialyzed against the cation exchange buffer (25 mM sodium acetate, 25 mM EDTA, pH 5.5). At this pH, Munc185 was positively charged and could be bound to the SP column. CaM has a pI of 4.4 and does not bind to the column at this pH. The elution of the Munc185 protein from the column was achieved with a linear gradient with 1M sodium chloride as target concentration. Alternatively, the same cation exchange chromatographic method can be used under denaturing conditions to avoid precipitation of Munc185; since it aggregates in the absence of CaM. Due to its aggregaton at the concentrations needed for NMR, it was not possible to record any NMR spectra.

8. Electrospray ionization mass spectrometry (ESI-MS)

For the paramagnetic tagging of the different cysteine CaM mutants it was essential to verify the completeness of the reaction with the tag. For this purpose the ESI-MS spectrum of the free protein was measured as reference spectrum. After the reaction proceeded, the ESI-MS spectrum of the tagged protein was recorded. The mass spectra were recorded in a *WATERS* ESI-Mass spectrometer in the positive mode, with a cone voltage of 30 eV. The samples had a protein concentration of 5 μM and were in 20 mM ammonium acetate buffer with 50% (v/v) acetonitrile and 0.1% (v/v) trifluoroacetic acid.

9. NMR measurements

The recordings were done in Bruker *AVANCE* spectrometers at ^{1}H NMR frequency of 900, 800, 700 and 600 MHz. The experiments were performed at 298K, 303K or 308K. The spectra were processed and analyzed using the following software: XWIN-NMR, NMR-pipe (Delaglio *et al*., 1995), NMR Draw, Felix (*Accelerys Inc*.), Sparky (Goddard and Kneller, 1999) and PALES (Zweckstetter and Bax, 2000). The acquisition parameters are found in table 2.

The most basic experiment used in biomolecular NMR is the heteronuclear single quantum coherence spectrum (HSQC), a pictorial representation of the pulse sequence is shown in Figure 13. Other pulse sequences used in this work are found in the Apendix.

A total of five NMR samples were used for the solution structure determination of the CaM/Munc13-1(457-492) peptide complex. Three samples consisted of uniformly (^{15}N and $^{15}N/^{13}C$) labelled CaM complexed with unlabelled Munc13-1 synthetic peptide (residues 459-492: The first sample ($^{13}C,^{15}N$) was dissolved in 90 % (v/v) H_2O, 10% (v/v) D_2O and used for sequential assignment spectra involving the exchangeable NH group; the second one (^{15}N) aligned by adding filamentous bacteriophage (Pf1) solution to a final concentration of 15 mg/ml. (*Asla Labs*). The third sample ($^{13}C,^{15}N$) was dissolved in 99 % (v/v) D_2O for certain NMR experiments were optimal water suppression was needed. The last two samples consisted of uniformly ($^{13}C,^{15}N$) labelled Munc13-1 (457-492) peptide complexed to natural abundance CaM, dissolved in 90 % (v/v) H_2O, 10 % D_2O for all sequential assignment and NOESY spectra and another one with 16mg/ml Pf1 cosolvent for rDC measurements.

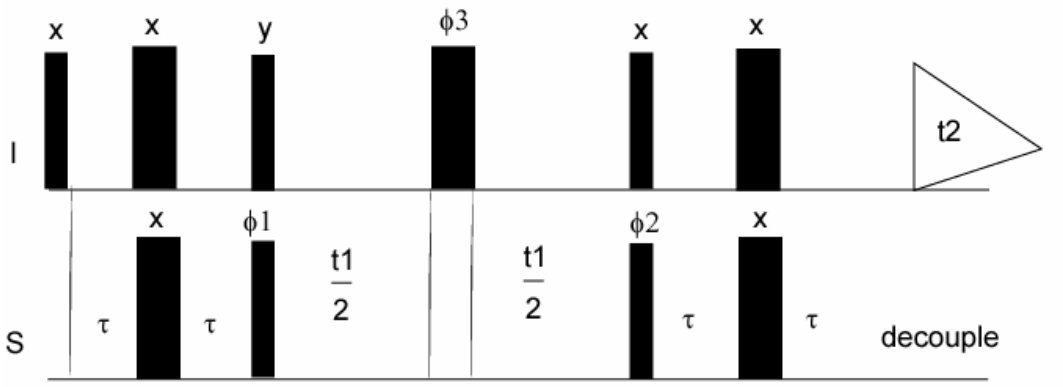

Figure 13. Pulse sequence for the ^{1}H detected heteronuclear single quantum coherence (HSQC) experiment. Thin bars represent 90° pulses and thick bars represent 180° pulses. The phase of each pulse is indicated above the bar. The phase cycling is ϕ1= x, -x; ϕ2 = 2(x), 2(-x); ϕ3 = 4(y), 4(-y); and receiver = 2(x, -x, -x, x) (Adapted from Cavanagh *et al*., 1996).

Table 2. NMR spectra acquired for the solution structure determination of the CaM/Munc13-1 (457-492) peptide complex

Sample conditions	Experiment	Spectral frequency	Complex points		
		MHz	D_1	D_2	D_3
^{15}NCaM/Munc13-1 (459-492) in 90% H_2O, 10% D_2O	2D-^{1}H-^{15}N HSQC	900	2048	128	-
^{15}NCaM/Munc13-1 (459-492) in 90% H_2O, 10% D_2O with 16mg/ml Pf1	2D-^{1}H-^{15}N IPAP-HSQC	900	2048	800	-
^{15}N,^{13}C CaM/Munc 13-1 (459-492) in 90% H_2O, 10% D_2O	3D-^{1}H-^{15}N NOESY-HSQC, t_{mix} 100 ms	900	2048	48	128
	3D-HNCO	700	2048	46	46
	3D-HN(CA)CO	600	1024	60	60
	3D-HNCACB	700	1024	40	25
	3D-CBCA(CO)NH	600	1024	58	24
	3D-H(CC)(CO)NH-TOCSY	700	2048	30	64
	3D-(H)CC(CO)NH-TOCSY	700	2048	70	30
	2D-^{1}H-^{13}C HSQC	600	2048	128	-
Lyophilized, then dissolved in D_2O	Series of 2D-^{1}H-^{15}N HSQC	600	2048	128	-
^{15}N,^{13}C CaM/Munc 13-1 (459-492) in 99.9 % D_2O	3D-^{1}H-^{13}C NOESY-HSQC t_{mix} 120 ms	700	2048	48	58
	3D-HCCH-TOCSY	600	2048	128	64
	2D-^{1}H-^{13}C HSQC	700	2048	128	-
	3D-^{1}H-^{13}C NOESY-HSQC (aromatic region) t_{mix} 130 ms	700	2048	48	40
	2D-HBCB(Caro)HE	600	2048	46	-
	2D-HBCB(Caro)HG	600	2048	46	-
	3D-^{1}H-^{13}C HMBC	700	2048	48	120

	(Methionines)				
$^{15}N,^{13}C$ Munc13-1 (457-492)/CaM in 90% H_2O, 10% D_2O	2D-^{1}H-^{15}N HSQC	600	1024	128	-
	3D-^{1}H-^{15}N NOESY-HSQC and 3D-^{1}H-^{13}C NOESY-HSQC shared version, t_{mix} 120 ms	600	2048	180	114
	3D-HNCO	900	1024	64	32
	3D-HN(CA)CO	600	1024	48	46
	3D-HNCACB	600	1024	50	100
	2D-CBCA(CO)NH	600	1024	29	60
	3D-H(CC)(CO)NH-TOCSY	600	1024	26	50
	3D-(H)CC(CO)NH-TOCSY	600	1024	30	52
	3D-HCCH-TOCSY	600	2048	32	128
Lyophilized, then dissolved in D_2O	Series of 2D-^{1}H-^{15}N HSQC	800	2048	128	-
$^{15}N,^{13}C$ Munc13-1 (457-492)/CaM) in 90% H_2O, 10% D_2O with 16mg/ml Pf1	2D-^{1}H-^{15}N IPAP-HSQC	600	1024	512	-

The one-bond ^{1}H-^{15}N residual dipolar couplings were obtained from a Heteronuclear ^{15}N-^{1}H Single Quantum Coherence 2D NMR spectrum (Refer to Figure 13). For an accurate measurement of the scalar and dipolar couplings it was essential to record at least 512 real points in the indirect dimension. A good digitization of the FID was achieved by zero filling to 8192 real plus imaginary points. The FID was Fourier transformed, the phase was corrected in the direct dimension and the FID was apodized with a sine-bell function. The frequency value from the center of the peak in the 2D spectrum was read out with the Sparky program after centering the peak. For couplings measurements In-Phase Anti-Phase (IPAP)-HSQC spectra were recorded (Ottiger *et al*., 1998). With this pulse sequence, two sub-spectra are generated, the first one contains only the up field component and the second the downfield component of a doublet. This type of spectrum has the advantage of reducing the overlap in comparison to the coupled HSQC spectrum.

10. Docking and structure calculation approaches for the CaM/Munc13-1(457-492) peptide complex

For the automatic assignment of NOESY spectra and structure calculation the combined automated NOE assignment and structure determination (CANDID) procedure introduced by Herrmann and collaborators (2002) was used. It combines features from NOAH and ARIA, such as the use of three-dimensional structure-based filters and ambiguous distance constraints, with the new concepts of network-anchoring and constraint-combination that further enable an efficient and reliable search for the correct fold in the initial cycle of *de novo* NMR structure determinations.

Among the guidelines for the successful performance of CANDID the input chemical shift list must contain more than 90% of the non-labile and backbone amide ^{1}H chemical shifts, the average backbone root mean square deviation (RMSD) o the mean coordinates for the structured parts of the polypeptide chain should be below 3.0 Å for the bundle of conformers used to represent the structure from CANDID cycle 1 and the RMSD drift between the mean atom coordinates after the first and the last CANDID cycles calculated for

the backbone heavy atoms of the structured part of the polypeptide chain should be smaller than 3.0 Å, and it should not exceed the average RMSD to the mean coordinates after cycle 1 by more than 25% (Herrmann *et al*., 2002).

An initial model of CaM complexed with the Munc13-1(457-492) peptide for the CANDID approach was not available. The initial trial to run CANDID using an extended structure of CaM linked with the Munc13-1(457-492) peptide failed to give a bundle of structures with a RMSD of less than 3 Å in the structured regions after the first cycle; for this reason a docking approach was used to generate an initial model. Based on the information of the chemical shifts, the residual dipolar couplings and the intermolecular NOE data for the bound Munc36 the initial model of the complex was generated.

Clore (2000) showed that accurate docking can be achieved by rigid body minimization using a target function that comprises only three terms, consisting of intermolecular NOE and $^1D_{NH}$ dipolar coupling restraints, supplemented by an intermolecular van der Waals repulsive potential.

The Rosetta *de novo* structure prediction method was used for obtaining the initial backbone conformation of the Munc13-1(457-492) peptide. Rosetta is based on a picture of protein folding in which local sequence segments rapidly alternate between different possible local structures, and folding occurs when the conformations of these local segments combine to form low energy global structures. The distribution of conformations sampled by an isolated chain segment is approximated by the distribution of conformations adopted by that sequence segment and related sequence segments in the protein structure database. Non-local interactions are optimized by a Monte Carlo search through the set of conformations that can be built from the ensemble of local structure fragments for each sequence segment. The procedure results in structures that have low free energy local and non-local interactions. (Bonneau *et al*., 2002).

The backbone torsion angle prediction package TALOS (Torsion Angle Likelihood Obtained from Shifts and sequence similarity. TALOS reads the experimental protein chemical shift tables and converts them to secondary chemical shifts before entering them in the database. TALOS evaluates the similarity in amino acid sequence and secondary shifts for a string of three sequential amino acids relative to all triplets of sequential residues contained in the database. The dihedral constraints for the backbone torsion angles obtained from TALOS are available immediately after completion of the resonance assignment and therefore can be used at the very early stages of structure calculation. (Cornilescu *et al*., 1999)

The side chains of Munc36 where added with the *What if* program (Vriend, 1990). The rigid body minimization protocol was done as described by Clore (2000), 500 steps of rigid body minimization with the force constants for the dipolar coupling (k_{dip}), NOE-derived interproton distance (k_{NOE}) and quartic repulsive van der Waals repulsion (k_{vdw}) terms set to 0.1 kcal* mol^{-1}*Hz^{-2}, 0.01 kcal*mol^{-1}*$Å^{-2}$, and 4 kcal*mol^{-1}*$Å^{-4}$, respectively. This was followed by 100 cycles of rigid body minimization (500 steps per cycle) in which k_{dip}, k_{NOE}, and k_{vdw}, where slowly increased from 0.1 to 0.5 kcal*mol^{-1}*Hz^{-2}, 0.01 to 30 kcal*mol^{-1}* $Å^{-2}$, and 0.004 to 1.0 kcal*mol^{-1}*$Å^{-4}$, respectively. This was finally followed by 500 steps of rigid body minimization with the values of k_{dip}, k_{NOE} and k_{vdw} set to 0.5 kcal*mol^{-1}*Hz^{-2}, 60 kcal*mol^{-1}*$Å^{-2}$, 3 kcal*mol^{-1}*$Å^{-4}$.

For torsion angle dynamics (TAD) calculations with DYANA the molecule is represented as a tree structure consisting of a base rigid body that is fixed in space and *n* rigid bodies, which are connected by *n* rotatable bonds. The degrees of freedom are exclusively torsion angles, i.e. rotation about single bonds. Each rigid body is made of one or several mass points (atoms) for which the relative positions are invariable. The tree structure starts from a "base", typically at the N-terminus of the polypeptide chain, and terminates with "leaves" at the ends of the side-chains and at the C-terminus. The rigid bodies are numbered from 0 to *n*. The base has the number 0. Each other rigid body, with a number $k \geq 1$, has a

single nearest neighbor in the direction towards the base, which has a number p(k) < k. The torsion angle between the rigid bodies p(k) and k is denoted by θ_k. The conformation of the molecule is uniquely specified by the values of all torsion angles, $\theta = (\theta_1, \ldots, \theta_n)$. All three-dimensional vectors are in an inertial frame of reference that is fixed in space. For each rotatable bond, $\vec{e}_k$ denotes a unit vector in the direction of the bond, and $\vec{r}_k$ is the position vector of its end point, which is subsequently used as the "reference point" of the rigid body k in the inertial reference frame. (Güntert *et al*., 1997).
The DYANA standard simulated annealing protocol consists of the following steps:
(1) Perform 100 conjugate gradient minimization steps at level 3, i.e. including only distance constraints between atoms up to three residues apart along the sequence, followed by further 100 minimization steps including all constraints.
(2) Perform N/5 TAD steps at a constant high reference temperature, Thigh, where N is the user-defined total number of TAD steps. The initial time-step, Δt = 2 fs, is adapted such as to achieve a relative accuracy of energy conservation of $\varepsilon^{ref} = 0.005$.
(3) Perform 4N/5 TAD steps with reference values for temperature and the relative accuracy of energy conservation of:

$$T^{ref}(s) = (1-s)^4 T_{high}$$
$$\varepsilon^{ref}(s) = 0.005*0.002^s$$

The parameter s varies linearly from 0 in the first time-step to 1 in the last time-step.
(4) Perform 200 TAD steps at zero reference temperature and ε^{ref} =0.0001. Initial velocities are those from the last time-step of step 3 above, and the length of the initial time-step is set to one fourth of the last time-step.
(5) Perform 1000 conjugate gradient minimization steps, including all constraints. The default values for the initial temperature, T_{high} = 9600 K. The default value for N is 4000.

Refinement of the CaM/Munc13-1 (457-492) peptide complex in explicit solvent was done in a full molecular dynamics force field including electrostatic and Lennard-Jones non-bonded potentials, since the interaction with the solvent is one way to improve the quality of the structures (Linge *et al*., 2003).

11. Data analysis of residual dipolar couplings and pseudocontact shifts

The measured NH residual dipolar couplings from the sterically aligned (with Pf1) or paramagnetically aligned samples of CaM in its different activated states need to be analyzed for each domain separately. The reason for this is precisely the flexible linker joining the two domains. The flexibility impaired by the linker allows each domain to sample numerous orientations in the time-scale sampled by dipolar couplings and a global analysis of the rDC data done without taking care of these considerations would fail.

Thus the rDC data was divided into N-terminal domain (residues 2-76) and C-terminal (residues 84-146). The N-terminal amide (residue 1) is not observable in the HSQC spectrum due to fast exchange with the solvent and the last two residues in CaM are too flexible and therefore disordered in different high-resolution structures.

There are high resolution NMR structures available for the N-terminal domain of apoCaM (1F70.pdb) and holoCaM (1J7O.pdb) and for the C-terminal domain of apoCaM (1F71.pdb) and holoCaM (1J7P.pdb). These structures have been refined with numerous rDC data (Chou *et al*., 2001 and Chou *et al*., 2000) and were taken as molecular models for fitting the experimental rDCs measured in this work.

The program PALES (Zweckstetter and Bax, 2000) was used for all the rDC data analysis. The primary NH rDC data was analyzed by two different routines: First, a histogram of the rDC data was generated and the principal components of the alignment tensor values (d_{zz}, d_{yy} and d_{xx}) were obtained in this form. Alternatively, the rDC data was fitted to the simulated rDC data derived from the high resolution molecular models with a Singular Value

Decomposition (SVD) algorithm. In addition, to the values of the principal components of the alignment tensor, this second routine provides more information on the alignment tensor: A linear correlation between the experimental rDCs and the back-calculated rDCs is obtained. If the SVD algorithm is run repeatedly, statistics about the alignment tensor values are also obtained, this permits to gain access to the precision of the obtained results.

The Pseudocontact shift data was measured in the ^{1}H dimension as the difference in the resonance values of the shifted NH cross peak and the reference (isotropic) NH cross peak. The PCS values were fitted to the back-calculated PCS derived from the coordinates of the same high-resolution molecular models of CaM used in the rDC data analysis. For this purpose, the metal position was located by a grid search minimizing the root-mean square deviation of the experimental PCS and calculated ones.

Once the position of the metal was precisely located, the distance between the metal ion and each amide was measured in the molecular model. The distances were plotted against the PCS values and a power fit was applied to the data, since there is a r^3 dependency for the PCS values on the metal-amide distance. An upper bound r^3 function was applied maximizing the angular values of the PCS expression $(3\cos^2\theta-1)$ and $(\sin^2\theta\cos 2\Omega)$.

III. RESULTS

1. Cloning, overexpression and purification of CaM and Munc13-1 proteins

a.Cloning of Munc13-1 (457-492) (Munc13-1-36aa)

The results for the PCR amplification are shown in Figure 14. The Munc13-1(457-492) insert for the pGEX2T vector runs in the agarose gel as a double stranded DNA of around 100 base-pairs (bp); this corresponded very well to the expected length of the PCR product. The Munc13-1(457-492) insert for the pMAL vector also had an apparent molecular weight corresponding well to the expected one.

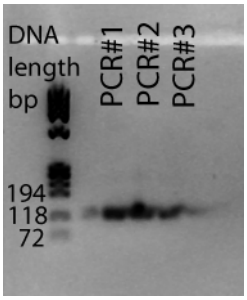

Figure 14. 2% (w/v) agarose gel electrophoresis for the PCR product of the Munc13-1(457-492) DNA insert for the pGEX2T cloning.

The agarose gel for the restriction digest of the positive clones is shown in Figure15; this confirmed that the desired insert was cloned successfully. Since the PCR based cloning, relies on the fidelity of the polymerase enzyme used it is essential to sequence the insert region of the plasmid DNA to ensure the whole sequence of the insert is correct. This is not so critical for the *Pfu* DNA polymerase enzyme due to its proof-reading activity, but is good practice especially for structural studies.

Figure 15. 1% (w/v) agarose gel electrophoresis for three positive clones for the pGEX2T-Munc13-1(457-492) construct cleaved with *BaMHI* and *EcoRI*.

b. Cloning of Munc13-1 (567-631) C_1 domain (Munc13-1-65aa)

The agarose gel electrophoresis for the PCR products of the amplification reaction is shown in Figure 16. The Munc65 insert had an apparent molecular weight corresponding to a double stranded DNA of around 260 bp; this agreed well with the expected length of the PCR product. After cloning, the positive clones were digested with the restriction enzymes *NdeI* and *XhoI* for the pET16b construct and *BaMHI* and *EcoRI* for the pGEX constructs. The agarose gel for the restriction digest of the positive clones is shown in Figure 16; this confirmed that the desired insert was cloned successfully. All the clones were positive and the first two clones were sequenced.

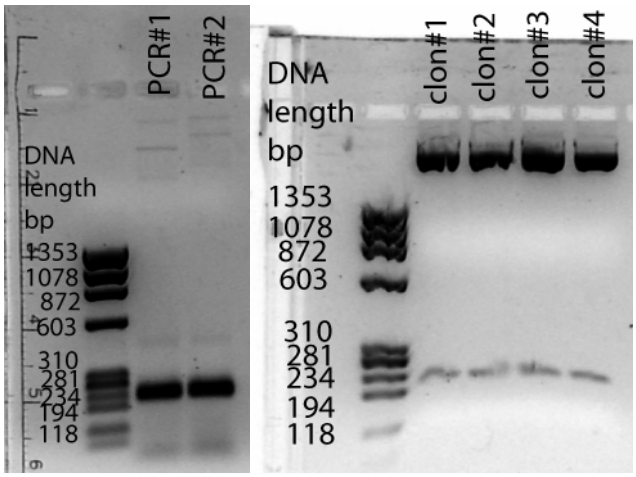

Figure 16. 1% (w/v) agarose gel electrophoresis for the PCR products of the Munc65 insert for the cloning into pET16b, pGEX2T and pGEX2T-TEV expression vectors (left) and restriction analysis of the positive pGEX2T-TEV-Munc65 constructs (right).

c. Cloning of Munc13-1 (447-631) (Munc13-1-185aa)

The agarose gel electrophoresis for the PCR products of the amplification reaction is shown in Figure 17. The Munc185 insert had an apparent molecular weight corresponding to a double stranded DNA of around 600 bp; this agreed well with the expected length of the PCR product. The agarose gel for the restriction digest of the positive clones of the pET16b-Munc185 construct is shown in Figure 17; this confirmed that the desired insert was cloned successfully. All the clones analyzed were positive. The first two clones were sequenced.

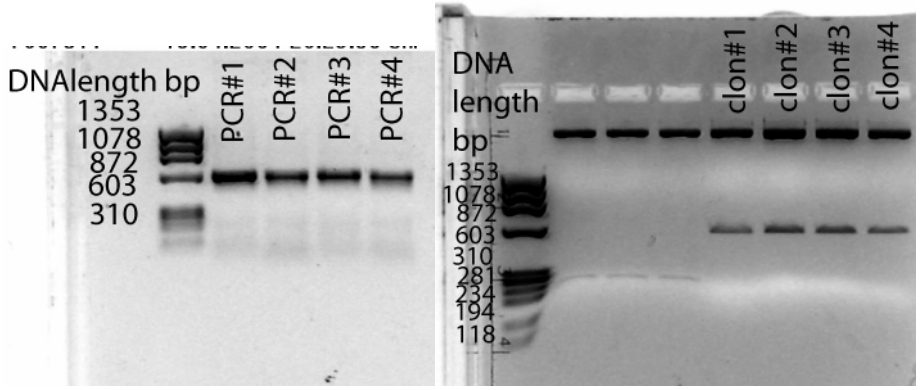

Figure 17. 1% (w/v) agarose gel electrophoresis for the PCR products of the Munc185 insert for the cloning into pET16b, pGEX2T and pETDuet-1 expression vectors (left) and restriction analysis of the positive pET16b-Munc185 constructs (right).

d. Site directed mutagenesis

All the desired mutations for CaM and Munc13-1 were obtained with the Quick-Change kit from *Stratagene*. Each mutation was verified by DNA sequencing of the plasmid DNA of the expression construct.

e. Overexpression and purification of the Munc13-1(457-492)

The N-terminal GST fusion protein of Munc13-1(457-492) could be expressed in the desired amounts after the induction with 0.5 mM IPTG as shown in the SDS-PAGE in Figure 18. Since there was a low solubility and there were several proteolytic products of the GST-Munc13-1(457-492) fusion protein, a co-expression approach with CaM was chosen to

protect the Munc13-1(457-492) from proteolytic cleavage and to increase its solubility. In the SDS-PAGE in Figure 18 two soluble bands corresponding to CaM and GST- Munc13-1(457-492) in the soluble fraction of the cell lysate were found.

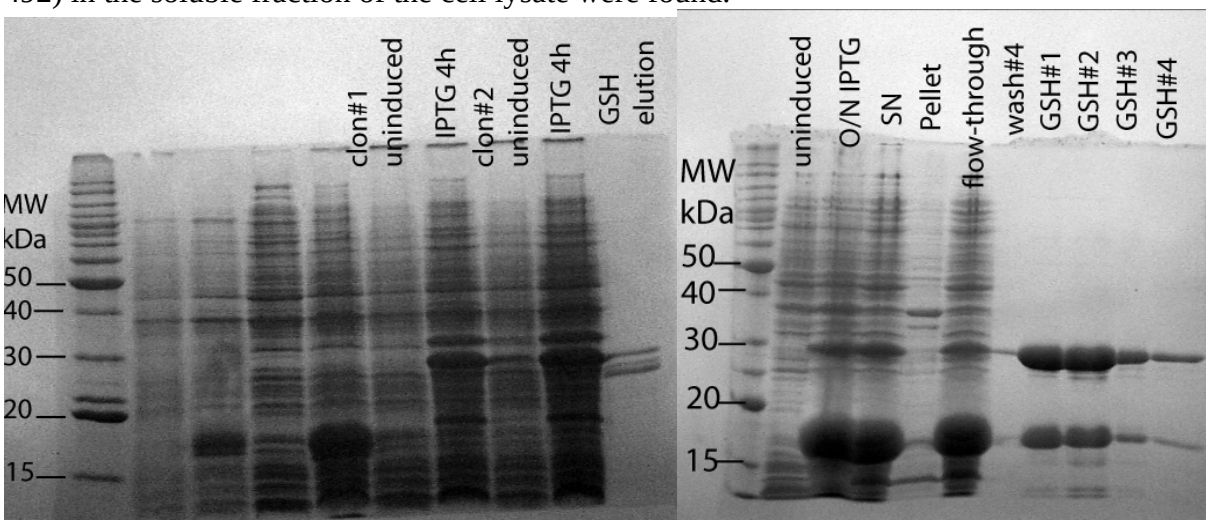

Figure 18. 12% (v/v) polyacrylamide SDS-PAGE for the overexpression and purification analysis of the pGEX2T- Munc13-1(457-492) construct (left) and for its co-expression with CaM (right).

The GST- Munc13-1(457-492)/CaM complex was co-purified by means of its affinity tag with GST-Sepharose beads, the TEV cleavage was unsuccessful. For this reason it was necessary to sub-clone the Munc13-1(457-492) insert into the pGEX2T vector which contains a thrombin recognition site between the N-terminal fusion GST and the Munc13-1(457-492) peptide. The cleavage with thrombin was successful as can be seen in the gel in Figure 19. To separate the Munc13-1(457-492) peptide from CaM, a preparative RP-HPLC method with a C18 column (*Vydac*) was used. The chromatogram is shown in Figure 19. The Munc13-1(457-492) peptide eluted at a retention time of 22.8 minutes and CaM at a retention time of 29.8 minutes. The identity of each peak was confirmed with ESI-Mass spectrometry. The mass for $^{13}C,^{15}N$ CaM was 17588 Da and for the $^{13}C,^{15}N$ Munc13-1 (457-492) peptide was 4407.6 Da.

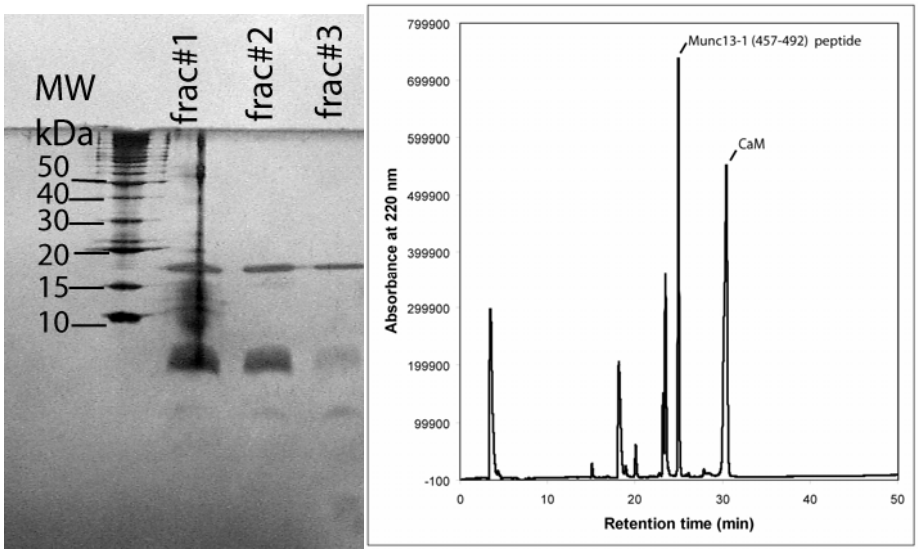

Figure 19. 17.5% Munc13-1 (457-492) peptide purification. Polyacrylamide SDS-PAGE of the fractions from the GST-Sepharose column after cleavage with thrombin (left). On the right the chromatogram of the RP-HPLC separation of the Munc13-1(457-492) peptide from CaM is shown.

The N-terminal Maltose-binding protein (MBP) fusion protein of Munc13-1(457-492) could be expressed in high amounts after its overnight induction with 0.5 mM IPTG at 22^{o}C as shown in the SDS-PAGE in Figure 20. The fusion protein was soluble and could be purified by means of its affinity tag with amylose-Sepharose resin. The fractions after the elution with maltose were verified with SDS-PAGE (Figure 20). The TEV cleavage was successful, however the amounts of Munc13-1(457-492) peptide were not large enough and therefore the co-expression approach with CaM was chosen for the overexpression of the uniformly isotopically enriched material for the NMR experiments.

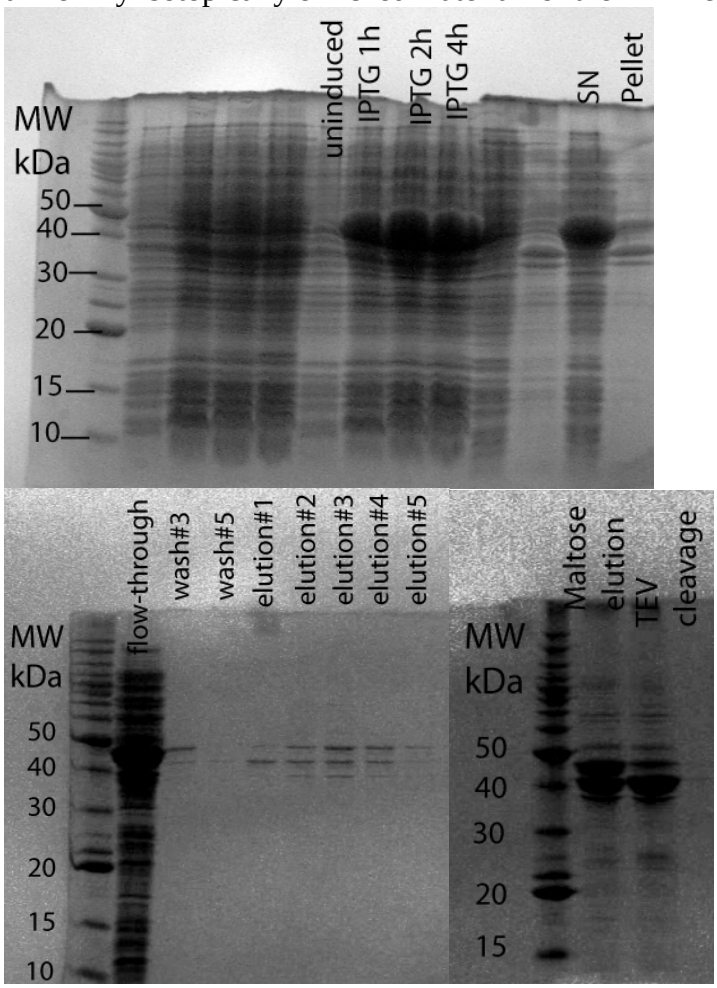

Figure 20. 12% (v/v) polyacrylamide SDS-PAGE for the overexpression of the MBP-Munc13-1(457-492) fusion protein (left), the elution from the amylose-Sepharose column with maltose (right) and its cleavage with TEV protease (down-left).

f. Overexpression and purification of the Munc65 protein

The N-terminal hexahistidine fusion protein of Munc65 could not be expressed in the desired amounts; in general it is difficult to over express low molecular weight proteins in bacteria. Since these small polypeptides are more prone to proteolytic degradation. The results of the purification are shown in the SDS-PAGE in Figure 21.

The N-terminal GST fusion protein of Munc65 could be expressed in the desired amounts after the overnight induction with 0.5 mM IPTG at 22^{o}C as can be seen in the SDS-PAGE shown in Figure 22. The fusion protein was highly soluble as can be seen from the soluble part of the lysate fraction in the gel. The purification was achieved by affinity chromatography with the GST-Sepharose beads; the fractions from the elution with 50 mM reduced glutathione were analyzed by SDS-PAGE (see Figure 22). The cleavage with TEV protease was unsuccessful. For this reason, a similar approach as for the Munc36 protein was

followed. The fusion protein was successfully cleaved with thrombin. The fractions after the cleavage are shown in Figure 22. A preparative RP-HPLC run in a C18 column (*Vydac*) was performed to separate the Munc65 protein from the GST tag. The chromatogram is shown in Figure 22. The Munc65 protein eluted at a retention time of 19.5 minutes and the GST tag eluted at a retention time of 29 minutes in the acetonitrile-water gradient. The identity of the proteins was confirmed with ESI-Mass spectrometry.

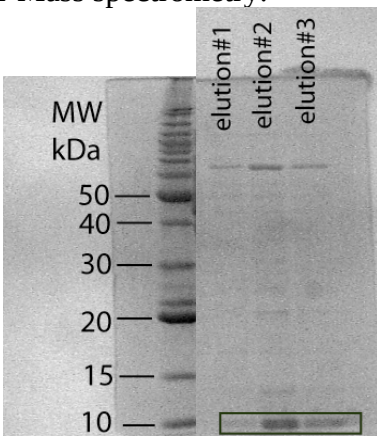

Figure 21. 12 % (v/v) polyacrylamide SDS-PAGE for the NI-NTA purification of the Munc65aa-$(his)_6$ protein.

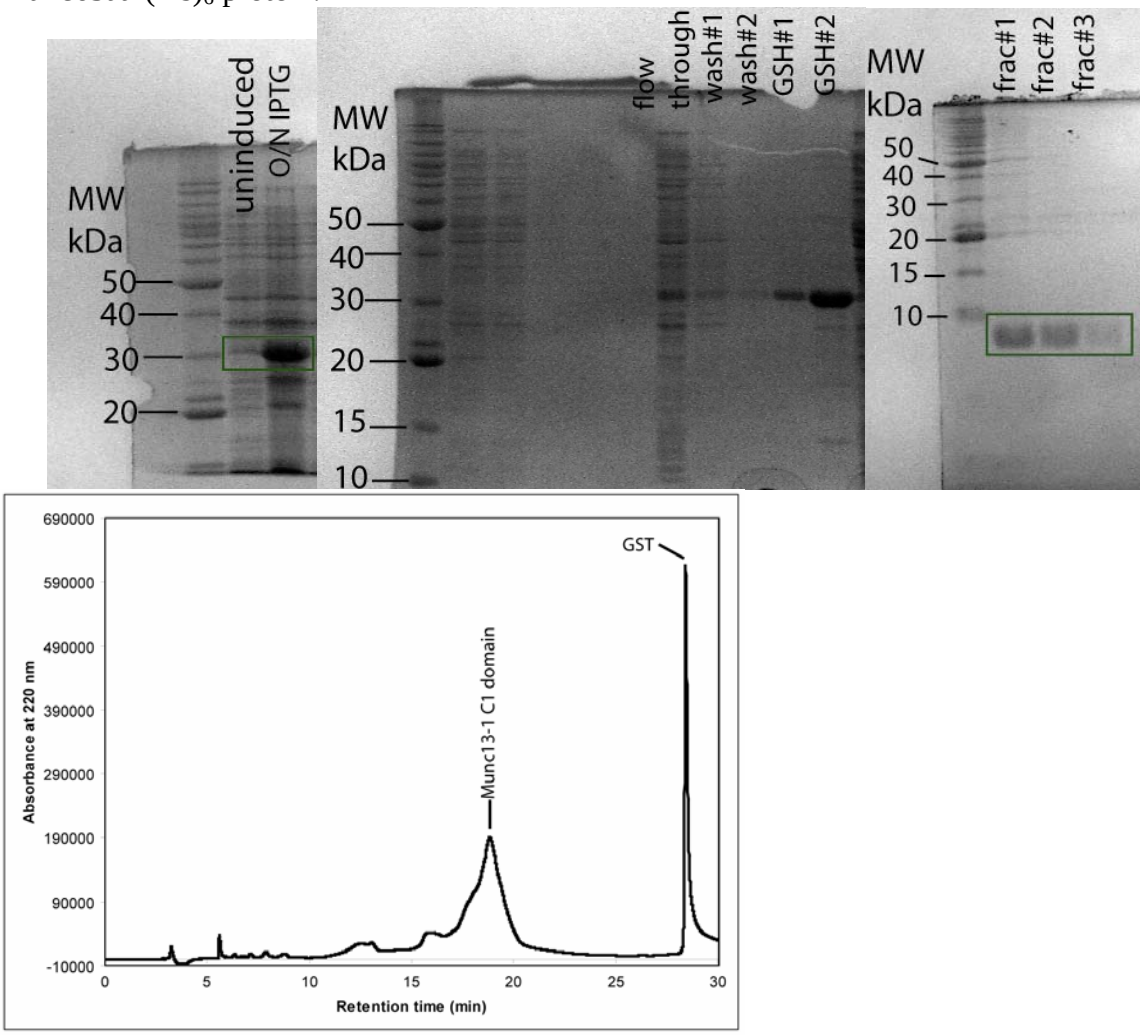

Figure 22. 12 % (v/v) Polyacrylamide SDS-PAGE for the overexpression of the GST-Munc65aa fusion protein (left); its purification with the GST-Sepharose column (middle) and after cleavage with thrombin (right). At the bottom, the chromatogram of the RP-HPLC separation of the Munc65 protein from the GST tag is shown.

g. Overexpression and purification of the Munc185 protein

The N-terminal hexahistidine fusion protein of Munc185 could be expressed in the desired amounts. However the protein was found in the pellet fraction after the lysis, see Figure 23. For this reason a co-expression approach was chosen to increase the stability and solubility of the Munc185 protein in the presence of its interaction partner CaM (Figure 24).

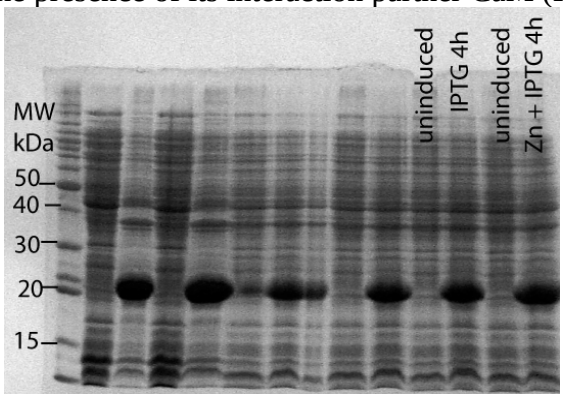

Figure 23. 12 % (v/v) polyacrylamide SDS-PAGE for the over expression of the pET16b-Munc185aa construct.

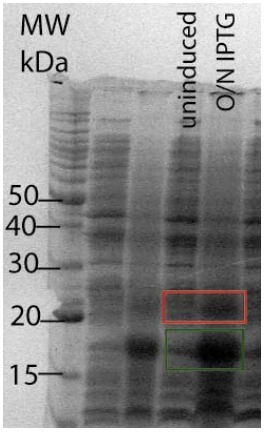

Figure 24. 12 % (v/v) polyacrylamide SDS-PAGE for the co-expression of the pET16b-Munc185aa and pET28a CaM constructs in *E.coli* BL21 (DE3) with both ampicillin and kanamycin to achieve the co-expression.

The co-expression was done initially by co-transformation of *E.coli* BL21(DE3) bacteria with the pET16b-TEV Munc185 construct and the pET28a CaM construct which are resistant to two different antibiotics. Afterwards the cloning into the pETDuet-1 vector succeeded and the co-expression could be done from a single plasmid DNA with ampicillin resistance (Figure 25).

The CaM/Munc185aa complex was highly soluble and was found mainly in the supernatant fraction after the lysis. The complex was co-purified by means of the hexahistidine affinity tag in the Munc185 protein with a Ni-NTA agarose column. The elution was done upon increasing the amount of imidazole to 300 mM. The elution fractions are shown in Figure 25. The CaM/Munc185 interaction appeared to be of high affinity since it remained as a bound complex after the Ni-NTA purification step. The $(his)_6$ tag was removed by cleavage with TEV protease (see Figure 26).

A further purification step with size-exclusion chromatography was done to obtain a homogenous sample. The chromatogram and SDS-PAGE analysis of the eluted fractions is shown in Figure 26. The CaM/Munc185 complex was in equilibrium between a monomeric (1:1) and a dimeric (2:2) species. To obtain an idea of the hydrodynamic radius of these two different species of the complex, a dynamic light scattering (DLS) analysis was done (see

Figure 26). 89 % of the the monomeric (1:1) species had a hydrodynamic radius of 5.7 nm, which agreed well with the expected molecular weight of 38 kDa; whereas 11 % consisted of a large oligomeric species with a hydrodynamic radius of ~ 100 nm. The dimeric (2:2) species had a hydrodynamic radius of 17.2 nm; this value did not agree well with the expected molecular weight of 76 kDa, suggesting that this complex deviates from a globular shape.

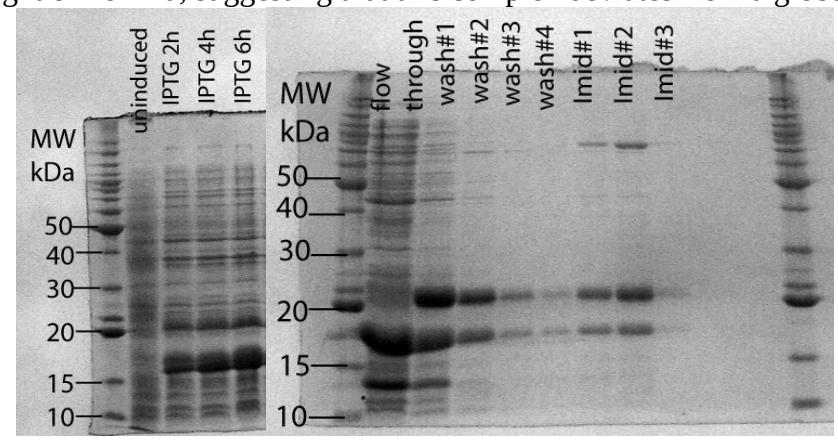

Figure 25. Overexpression of the CaM/Munc185aa complex from the pETDuet-1(CaM-Munc185aa) construct (left) and purification by metal affinity chromatography with Ni-NTA agarose (right).

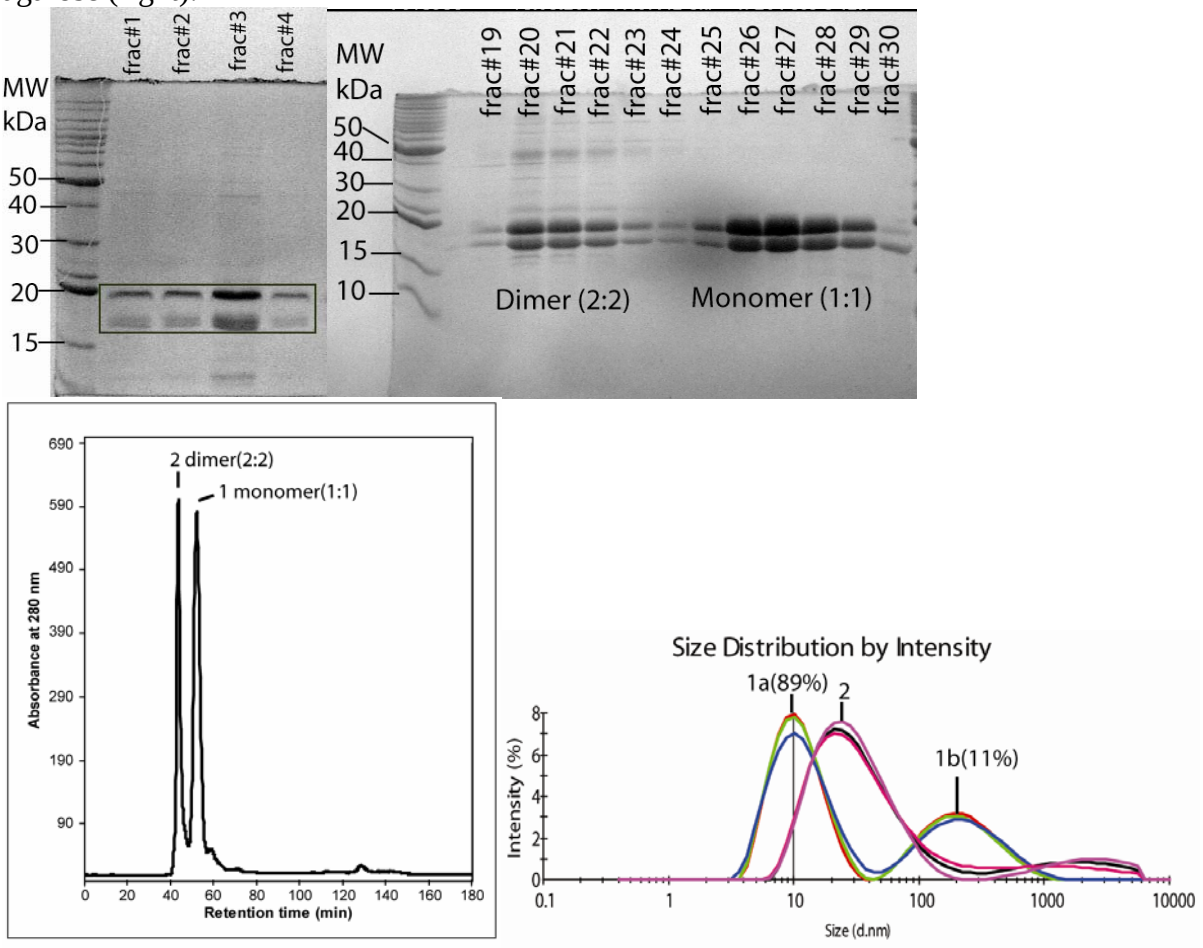

Figure 26. Purification of CaM/Munc185aa. 12%(v/v) Polyacrylamide SDS-PAGE of the collected fractions after the TEV-cleavage of the CaM/Munc185aa complex (upper-left). Chormatogram of the size-exclusion run for the CaM/Munc185aa complex (lower-left) and 12% (v/v) polyacrylamide SDS-PAGE of the elution fractions containing the monomeric and dimeric species of the CaM/Munc185aa complex (upper-right). On the lower-right panel, the DLS profiles for the two different CaM/Munc185aa complex species is shown.

The N-terminal GST fusion protein of Munc185 could be expressed in high amounts. However the protein was found in the pellet fraction after the lysis. The co-expression approach with CaM was also tried in this case to increase its solubility. Indeed, the CaM/GST-Munc185 complex was highly soluble and could be co-purified with GST-Sepharose beads (Figure 27).

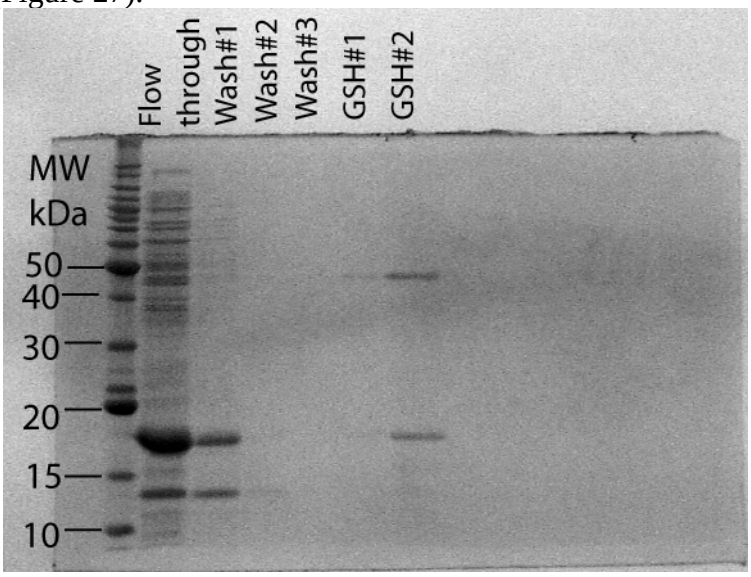

Figure 27. 12%(v/v) polyacrylamide SDS-PAGE for the purification of the CaM/GST-Munc185aa complex.

h. Overexpression and purification of calmodulin

CaM was over expressed in high amounts and was found mainly in the supernatant fraction after the lysis (Figure 28). After a bulk purification step with Trichloroacetic acid (TCA) precipitation; CaM was purified by hydrophobic interaction chromatography on a phenyl-Sepharose column; the chromatogram and the SDS-PAGE analysis of the fractions containing CaM are shown in Figure 28. The elution was achieved with a buffer containing EDTA; CaM could be purified in high amounts and with high purity.

i. Biochemical separation of Munc185 from calmodulin

The Munc185 appeared to be unstable in the absence of its interaction partner CaM. However at low concentrations (< 10µM) it remains soluble. It is possible to disrupt the strong interaction of the CaM/Munc185 complex with large amounts of EDTA (50mM) and a pH of 8.8. Afterwards, the proteins were separated by cation exchange chromatography at a pH of 5.5. The chromatogram is shown in Figure 29. The eluted fractions were analyzed by SDS-PAGE (Figure 29). The free protein could be added to uniformly ^{15}N-labeled CaM for NMR studies.

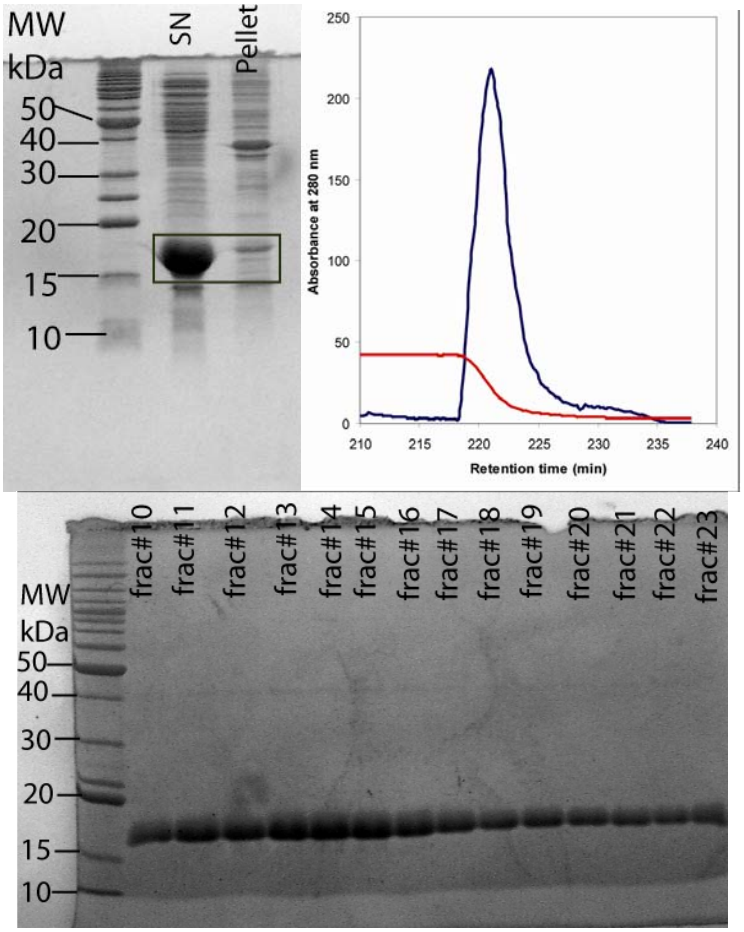

Figure 28. CaM purification. 12 % (v/v) Polyacrylamide SDS-PAGE showing the supernatant and pellet fractions of the CaM cell-lysate (left). The chromatogram of the Phenyl-Sepharose column is shown on middle. On the right a 12% (v/v) polyacrylamide SDS-PAGE shows the CaM containing fractions eluted from the Phenyl-Sepharose column.

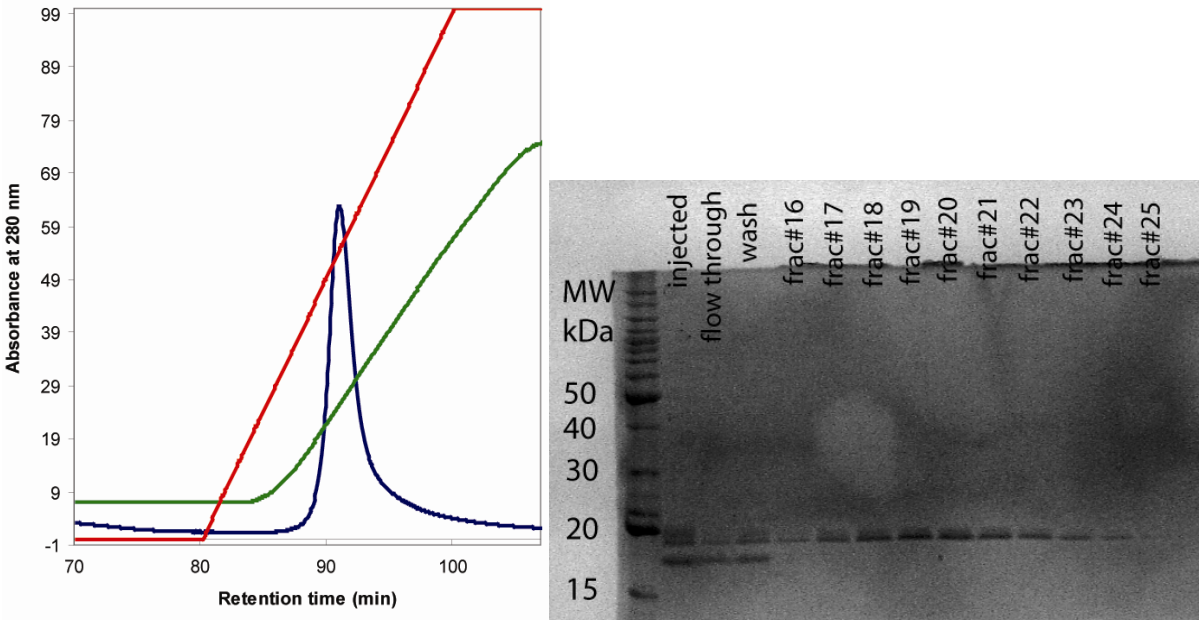

Figure 29. Biochemical separation of Munc185aa. The chromatogram of the SP-Sepharose column is shown on the left side, the blue trace represents the absorbance at 280 nm, the red trace represents the linear NaCl gradient and the green trace represents the conductivity. On the right, a 12 % (v/v) polyacrylamide SDS-PAGE shows the content of the collected fractions after elution with high NaCl concentrations.

2. Biophysical characterization of CaM and Munc13-1 proteins

a. NMR studies on the $^{15}N,^{13}C$ CaM/Munc13-1(459-479) peptide complex

The HSQC-based titration of the Munc13-1(459-479) synthetic peptide corresponding to the CaM binding site identified by Junge *et al.* 2004 to ^{15}N CaM showed that the peptide binds with sub-micromolar affinity and had a slow-exchange on the NMR time scale (Figure 30).

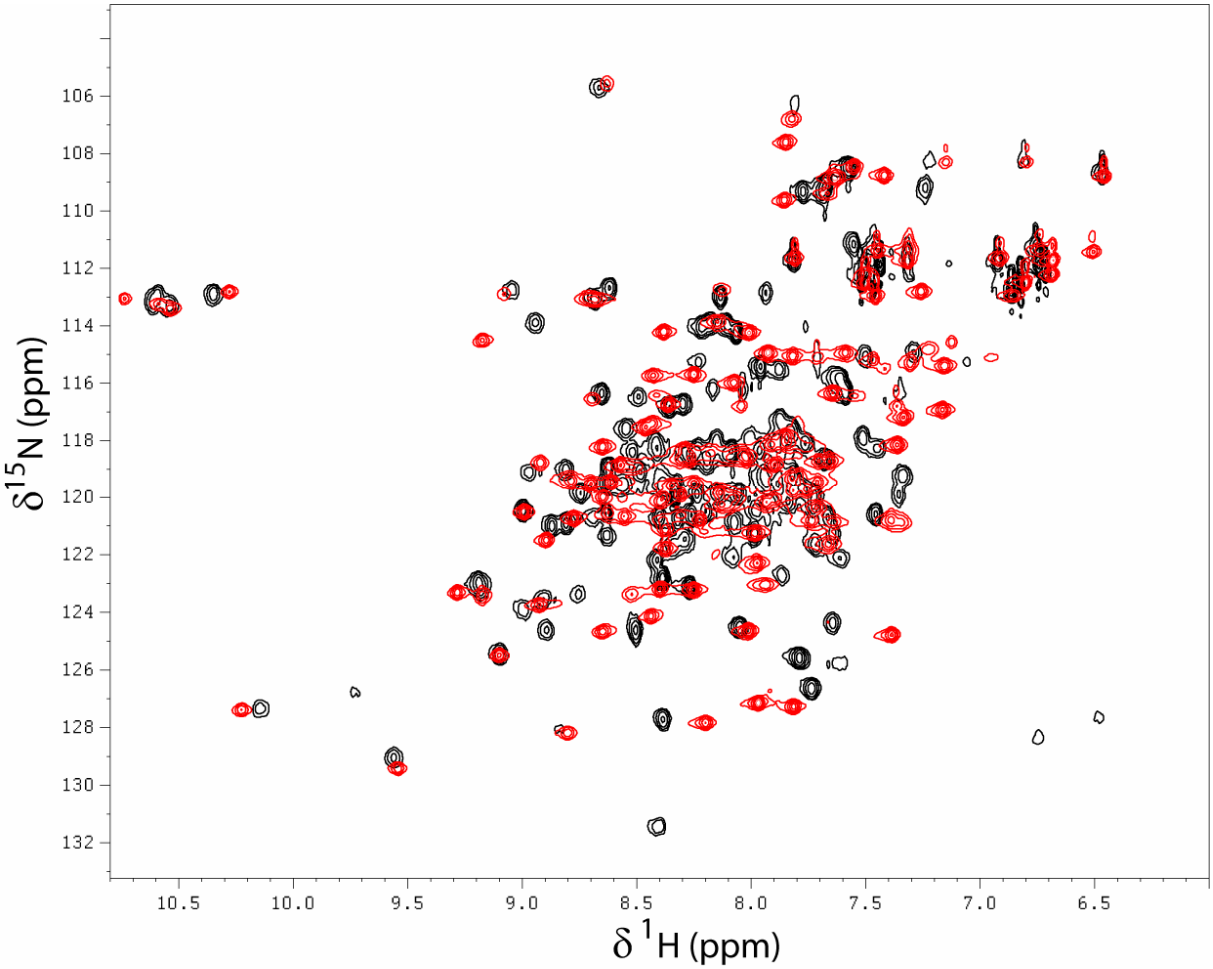

Figure 30. ^{1}H-^{15}N HSQC spectrum of the uniformly labelled ^{15}NCaM/Munc13-1(459-479) peptide complex in 20mM Bis-Tris, 150 mM KCl, 10 mM $CaCl_2$, pH 6.8 (in red) and of free CaM measured at 30^{o}C (in black).

The amide resonances are a very sensitive probe for studying macromolecular interactions; the chemical shift is sensitive to both direct interaction with a binding partner and to induced conformational change in the macromolecule. To quantify the change in the HSQC spectra a chemical shift perturbation plot (see Figure 31) gave an overview of the effects upon binding of the Munc13-1(459-479) peptide to CaM. The chemical shift perturbation is a weighted average of the change in the ^{1}H resonance and the ^{15}N resonance corrected for the difference in magnetogyric ratio.

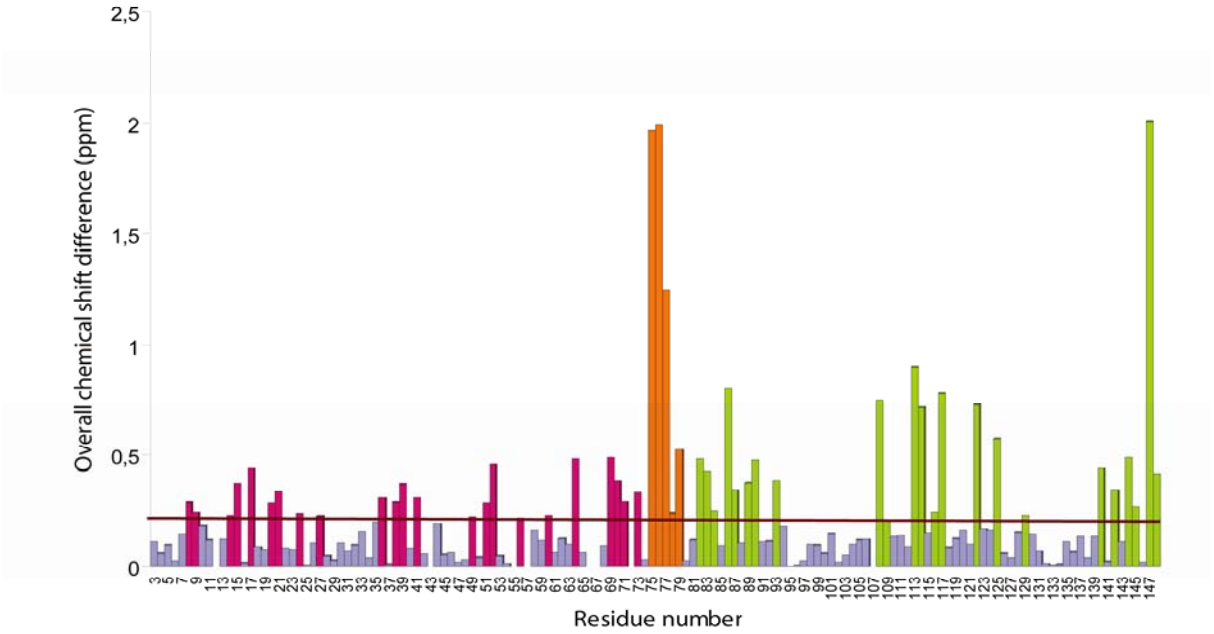

Figure 31. Chemical shift perturbation plot for CaM upon binding to the Munc13-1 (459-479) peptide. The largest perturbations are shown in green for the C-terminal domain of CaM, in orange for the linker region and in magenta for the N-terminal domain of CaM.

The chemical shift perturbation upon binding of the Munc13-1 (459-479) peptide indicated that the interaction was stronger to the C-terminal region of CaM; since the chemical shift changes in the N-terminal domain were rather small. It has been shown, that the binding of many of the CaM targets is antiparallel; for this reason, it was rationalized that if the peptide was extended C-terminally it could be possible to observe additional chemical shift changes in the N-terminal region of CaM. Thus, a 34 amino acids -long peptide was chemically synthesized: Munc13-1 (459-492).

b. NMR studies on the ^{13}C ,^{15}N CaM/Munc13-1(459-492) peptide complex

Upon extending the peptide sequence towards its C-terminus an additional hydrophobic motif appeared to bind to the N-terminal domain of CaM. This was observable in the overlaid HSQC spectra (Figure 32); the changes were quantified with the aid of a chemical shift perturbation plot (Figure 33).

The hypothesis that the C-terminal extension of the Munc13-1 (459-479) peptide could interact with the N-terminal domain appeared to be correct; since more chemical shift changes and larger in magnitude were observed in the N-terminal region of CaM for this longer peptide.

Junge *et al.*, 2004 also reported that the Munc13-1 (459-479) peptide interacted with CaM in the absence of calcium. To map the region of apoCaM, which could be affected upon binding with this Munc13-1 peptide, a titration experiment was done in the presence of 5mM EDTA (see Figure 34).

The CaM/Munc13-1 interaction in the absence of calcium appeared to be in the intermediate- exchange regime on the NMR time scale, since many of the NH cross peaks broadened beyond detection. However, few peaks showed fast-exchange behaviour. This result indicated that the Munc13-1 peptide binds apoCaM with lower affinity (by several orders of magnitude) than in the presence of calcium. Since the assignment of apoCaM was available; the changes observed in the HSQC spectra upon peptide addition were mapped in

the apoCaM structure (Figure 37). In addition, the same titration experiment was done for a synthetic peptide of the Munc13-1 homologue ubMunc13-2 (382-402), similar results were obtained; however the binding surface appeared to be smaller, *i.e.* less NH cross peaks were perturbed.

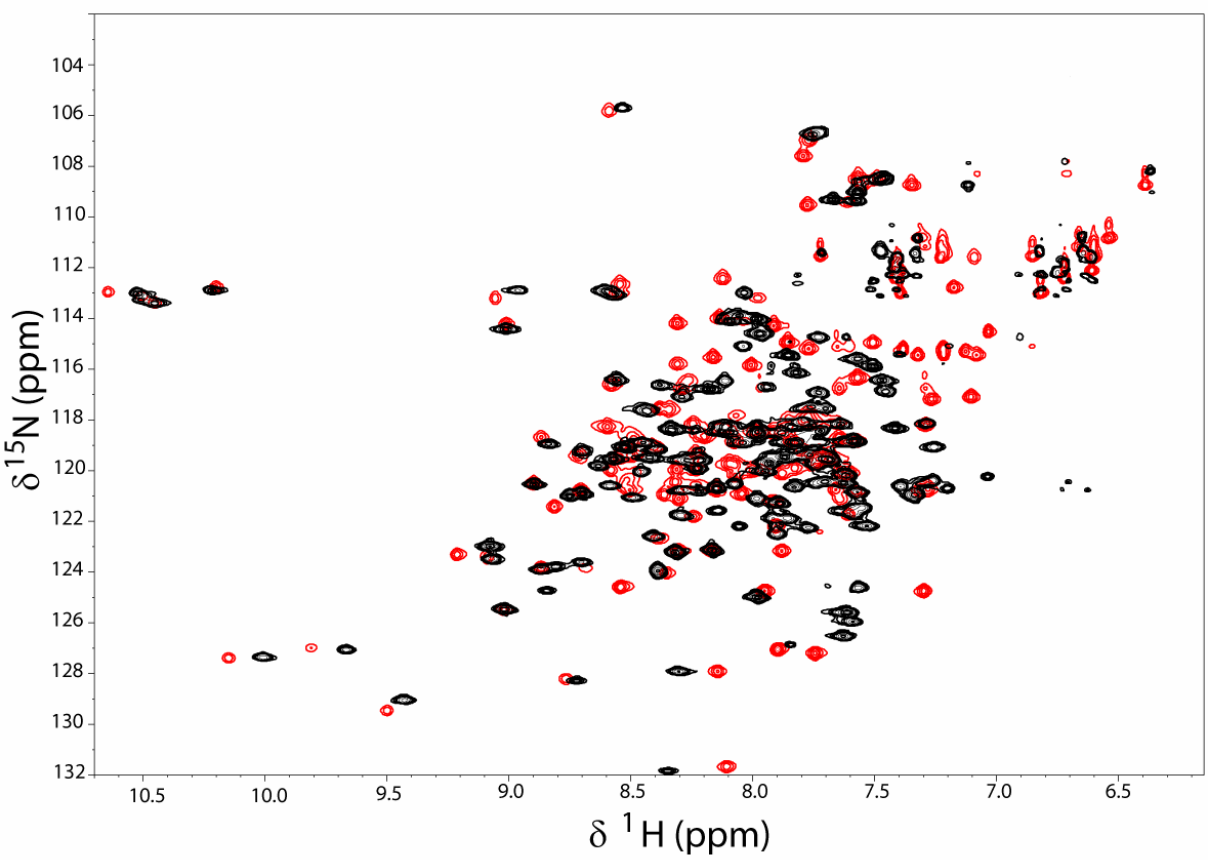

Figure 32. Overlaid ^{15}N-^{1}H HSQC spectra of ^{15}N CaM (black) and ^{15}NCaM/Munc13-1(459-492) peptide complex (red).

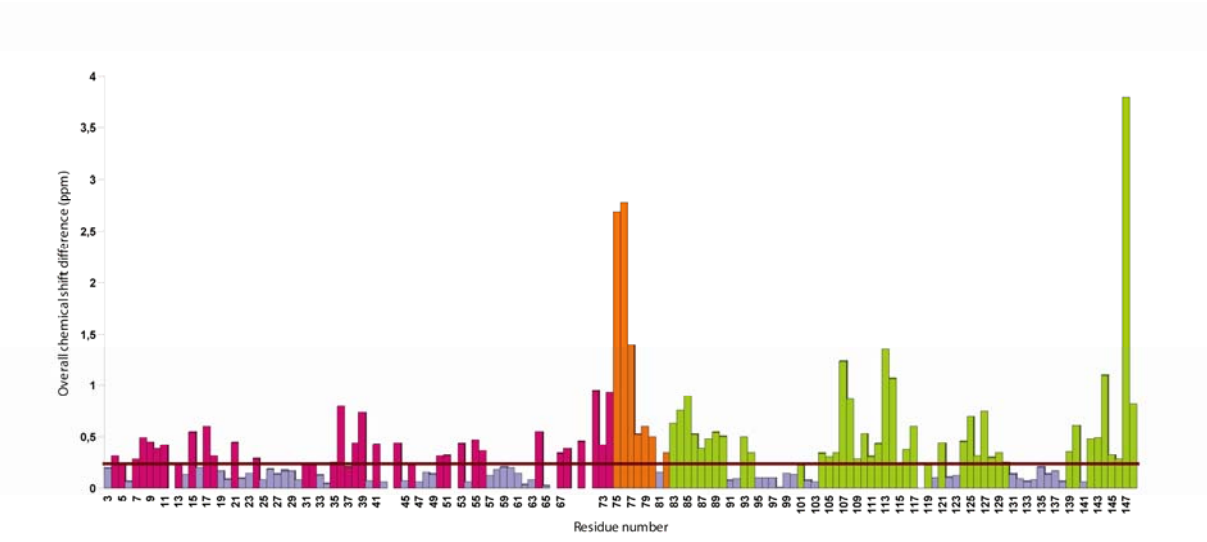

Figure 33. Chemical shift perturbation plot for the amide region in CaM upon binding to the Munc13-1 (459-492) peptide. The residues affected in the C-terminal domain, linker region and N-terminal domain are shown in green, orange and magenta, respectively.

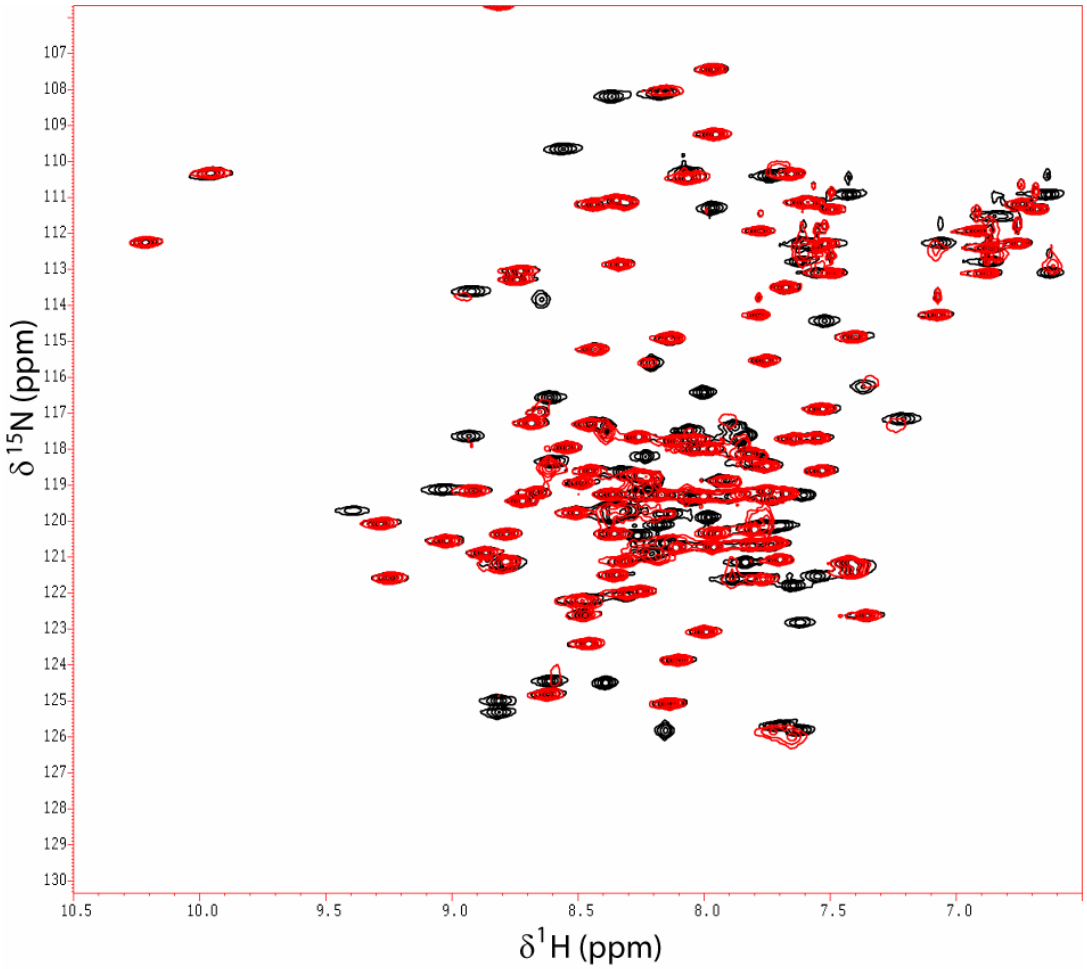

Figure 34. Overlaid ^{15}N-^{1}H HSQC spectra for apoCaM in black and apoCaM/Munc13-1 (459-479) peptide complex in a 1:0.5 stoichiometric ratio in red.

To get an idea of the binding affinity of this interaction; one of the few peaks that showed a fast-exchange behaviour was analyzed (see Figure 35). The peptide:apoCaM molar ratio was plotted against the chemical shift change (Figure 36). This saturation curve or isoterm was fitted with a hyperbolic function to obtain the dissociation constant (k_d) of the binding. The dissociation constant extracted from the binding isotherm was ~1 mM.

To gain insight into the CaM/Munc13-1 interaction along the activation coordinate of CaM, the CaM/Munc13-1 (459-492) complex was titrated with EDTA to remove the bound calcium. Three distinct states could be defined based on the HSQC spectra: (a) The inactive state apoCaM/Munc13-1; (2) a half-activated state [2Ca^{2+}]CaM/munc13-1; (3) and the fully activated state holoCaM/Munc13-1. These three states could be easily recognized in the HSQC spectra focusing on the low field shifted glycines, which coordinate the calcium ion, belonging to the four different EF-hand motifs of CaM (Figure 38).

Remarkably, the chemical shift of the Glycine 134 which belongs to the EF-hand 4, did not show a chemical shift change upon calcium removal in the presence of the Munc13-1 peptide; it had a ^{1}H and ^{15}N chemical shift of 10.32 and 112.34 ppm, respectively. This argues for a similar chemical environment and possibly similar conformation for this EF-hand in the three different activated states discussed above. The ^{1}H and ^{15}N chemical shift for G134 in free apoCaM are 8.5 and 109.6 ppm, respectively.

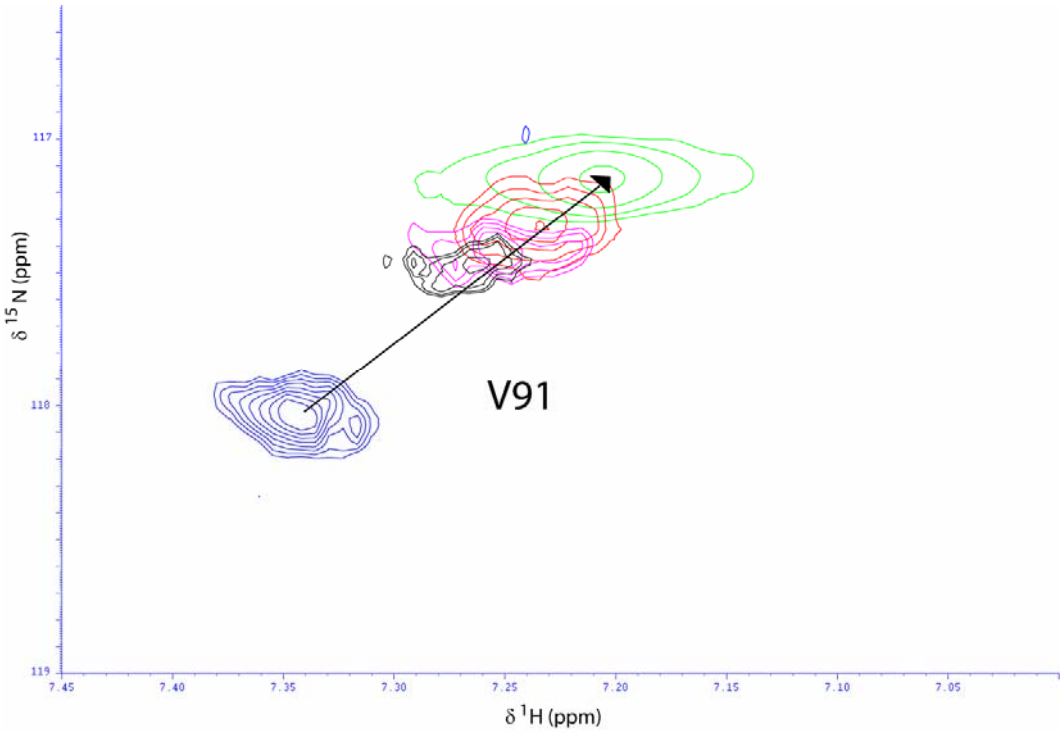

Figure 35. Overlaid ^{15}N-^{1}H spectra of apoCaM with increasing amounts of Munc13-1 (459-479) peptide. It shows just the progressive migration of the Valine 91 NH cross peak; characteristic of the fast-exchange regime behaviour on the NMR time scale.

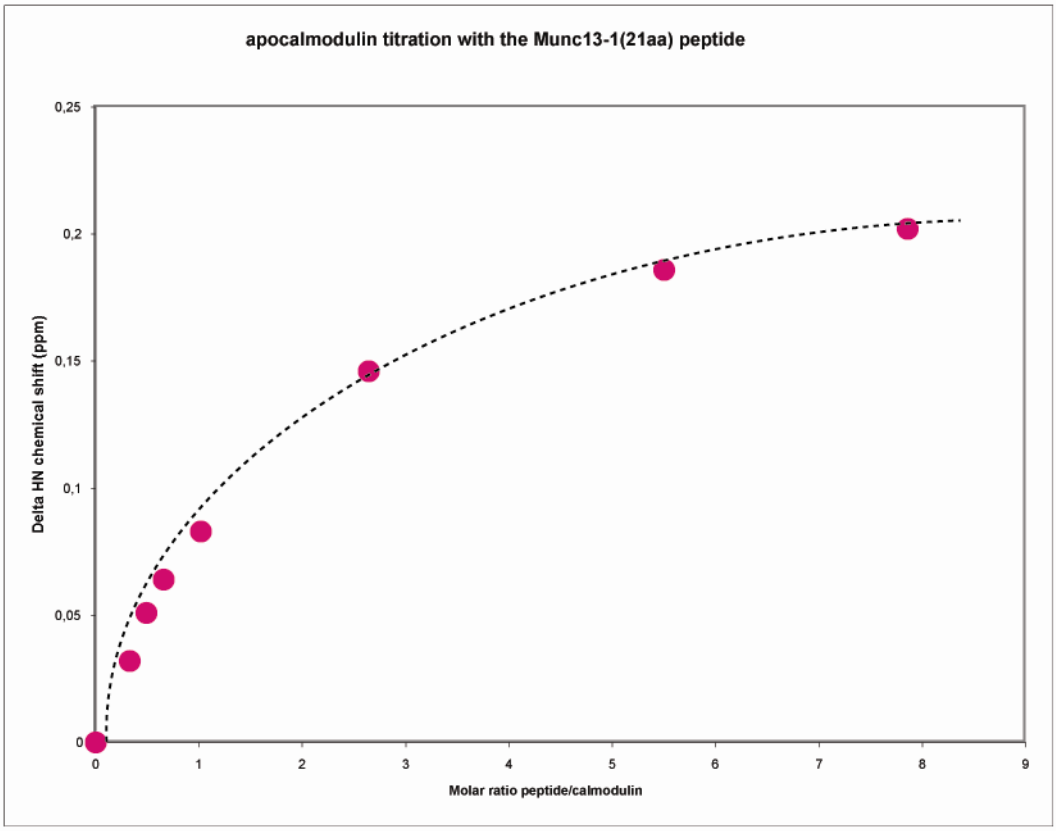

Figure 36. Saturation binding curve for the Valine 91 NH cross peak of ^{15}N labelled apoCaM upon increasing amounts of Munc13-1 (459-479) peptide.

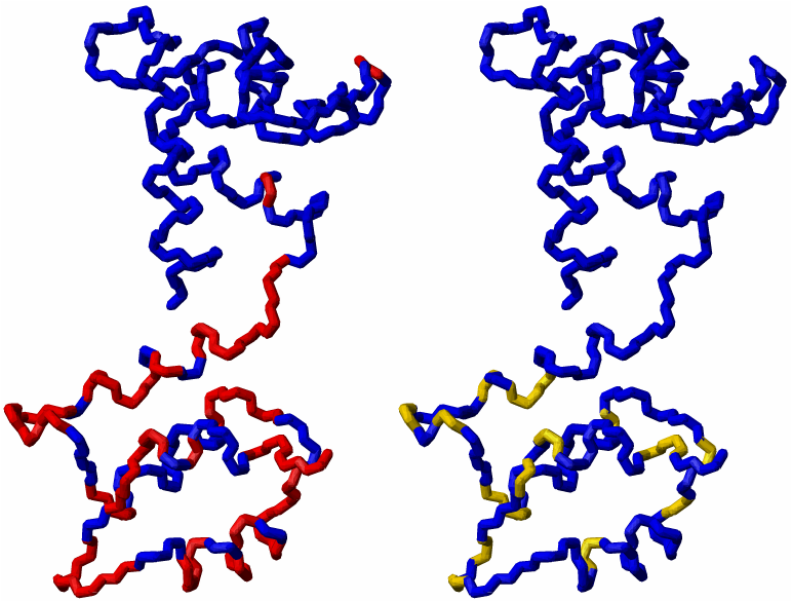

Figure 37. Mapping of the residues in apoCaM affected by the binding of the Munc13-1 (459-479) peptide in red, mainly the C-terminal domain (bottom) was affected. On the right side, the residues affected by the binding of ubMunc13-2 (382-402) to apoCaM are shown in yellow; just residues in the C-terminal region were affected.

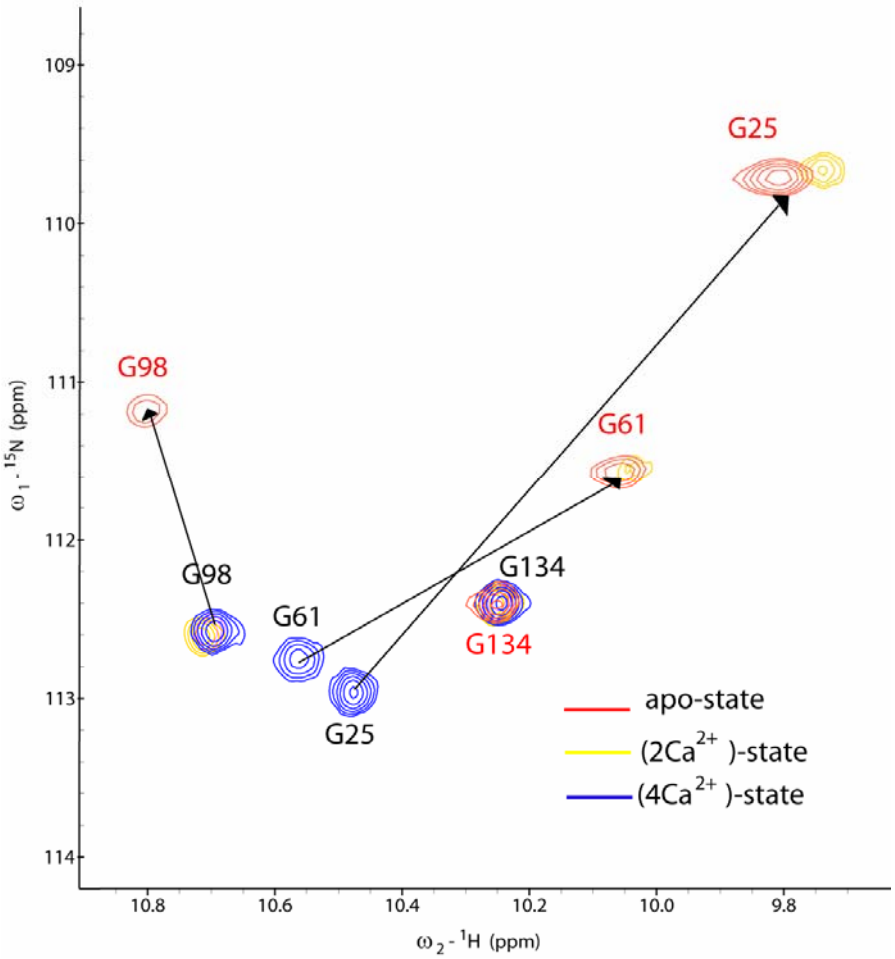

Figure 38. Overlaid ^{1}H-^{15}N HSQC of the CaM/Munc13-1(459-492) complex at three different activated states. The red one is in the absence of calcium; the yellow with two calcium ions bound to the C-terminal domain of CaM; and the blue one in the holo- state or [$4Ca^{2+}$]-bound state.

c. NMR studies of the $^{13}C,^{15}N$ Munc13-1(457-492) peptide binding to CaM

To unravel the Munc13-1 conformational changes upon CaM binding, a recombinant uniformly ($^{13}C,^{15}N$)-labelled peptide was studied by NMR. The first goal was to determine which conformation the free peptide had in solution. Since the peptide aggregated in solution at the concentrations needed for NMR, the sequential resonance assignment was done in the presence of urea. However, a ^{1}H-^{15}N-HSQC measured on a diluted sample also showed a random-coil pattern. The ^{15}N- ^{1}H HSQC spectrum measured in 8 M urea is shown in Figure 39.

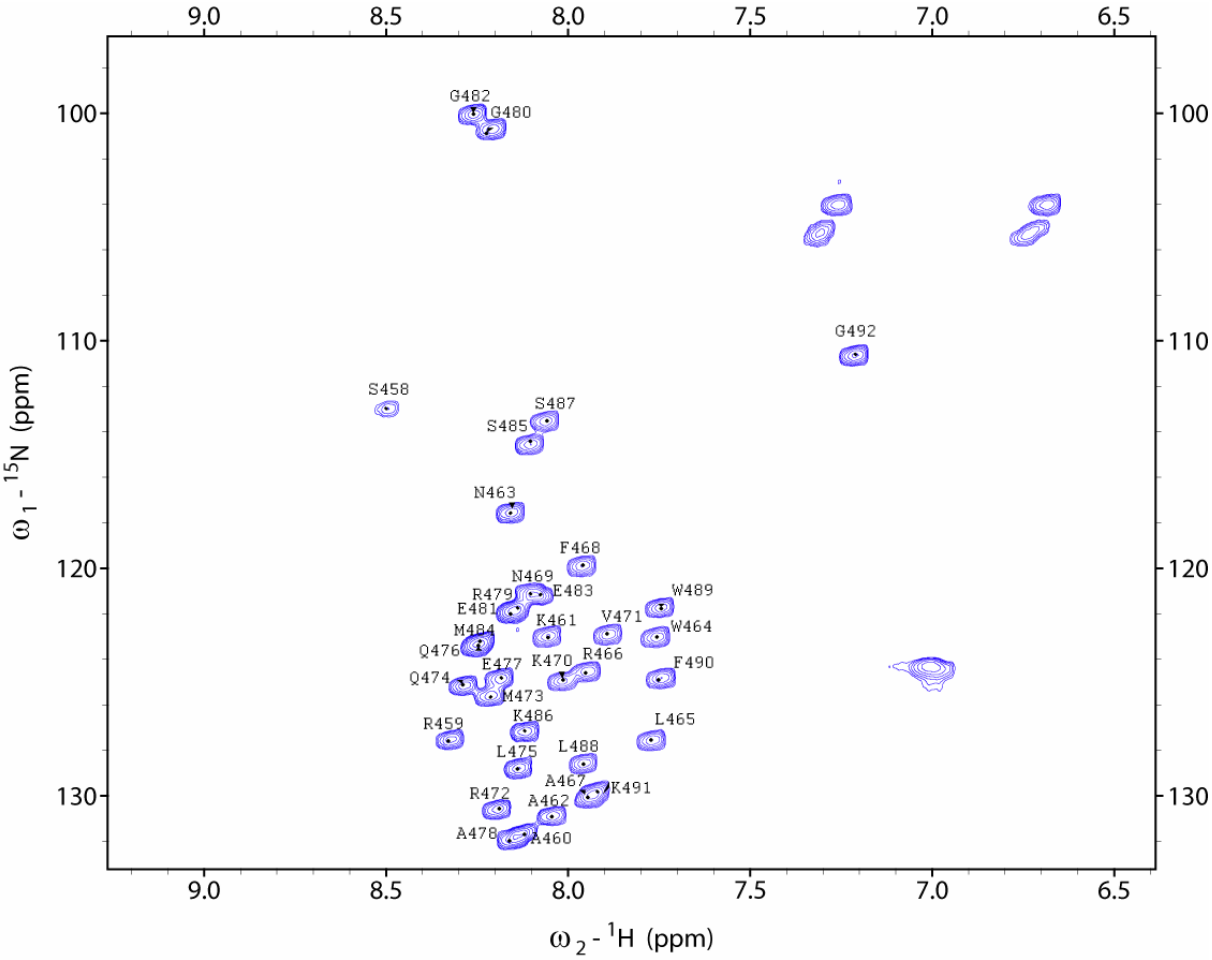

Figure 39. ^{15}N -^{1}H HSQC spectrum of the $^{13}C,^{15}N$ Munc13-1(457-492) peptide in 8 M urea at pH 6.8. All of the amide cross peaks were assigned with the aid of triple resonance experiments.

The sequential backbone resonance assignment of the $^{13}C,^{15}N$ Munc13-1(457-492) free peptide in 8 M urea was done with the aid of triple resonance experiments like 3D-HNCO and 3D-HN(CA)CO (see Table 3). In unfolded polypeptides there is a low dispersion in the proton and carbon chemical shifts; therefore, a full sequential assignment was only possible with the aid of the 3D-HNN experiment (see Figure 40). This experiment is popular for unfolded proteins, because it has two nitrogen evolution periods and the nitrogen chemical shift is the one with largest dispersion in unfolded polypeptides.

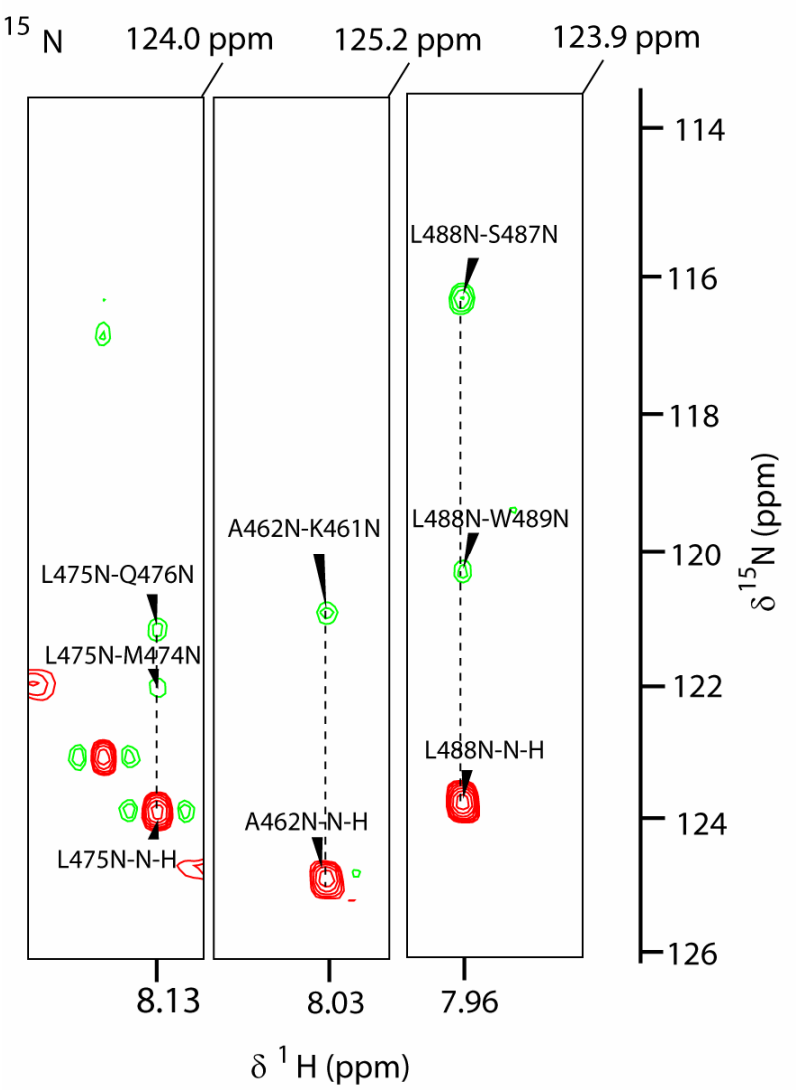

Figure 40. Strip plots of the 3D-HNN spectrum for three diagonal peaks of the ^{13}C,^{15}N Munc13-1(457-492) peptide in 8 M urea. The diagonal peak had a positive phase (red) and the cross-peaks to (*i*+1) and (*i*-1) evolved with negative phase (green).

Afterwards, the resonances of the ^{13}C,^{15}N-Munc13-1 (457-492) peptide were assigned in its bound state in the presence of unlabelled CaM. For this purpose, several triple resonance experiments were done to assign all the chemical shifts of the backbone and side chain resonances (see Table 3).

The ^{15}N-^{1}H HSQC of the labelled Munc13-1 (457-492) peptide bound to CaM is shown in Figure 41. The ^{1}H chemical shift dispersion upon CaM binding increased significantly; it is well known that a larger dispersion for the NH resonances involves protein folding (to α-helical conformation in this case).

The changes in the HSQC spectra between free Munc13-1 (457-492) peptide and the CaM-bound peptide were quantified with the aid of a chemical shift perturbation plot (Figure 42). The largest changes were observed in the N-terminal region of the peptide. Significant chemical shift perturbations were also observed in the C-terminal hydrophobic tail of the peptide.

Table 3. NMR experiments for the sequential backbone and side chain resonance assignment of the $^{13}C,^{15}N$ Munc13-1 (457-492) peptide

Sample	Experiment	Resonance assignment
Free $^{13}C,^{15}N$ Munc13-1 (457-492)	3D-HNCO	C'(*i*-1) to NH
	3D-HN(CA)CO	C'(*i*-1) and C'(*i*) to NH
	3D-HNN	N (*i*-1) and N(*i*+1) to NH
CaM bound $^{13}C,^{15}N$ Munc13-1 (457-492)	3D-HNCO	C'(*i*-1) to NH
	3D-HN(CA)CO	C'(*i*-1) and C'(*i*) to NH
	3D-CBCA(CO)NH	CB,CA (*i*-1) to NH
	3D-HNCACB	CB,CA (*i*-1) and CB,CA (*i*) to NH
	3D-H(CC)(CO)NH-TOCSY	Aliph.H (*i*-1) to NH
	3D- (H)CC(CO)NH-TOCSY	Aliph. C(*i*-1) to NH
	3D-HCCH-TOCSY	Aliph.C and Aliph.H intra side-chain
	2D-HBCB(Caro)Hγ and 2D-HBCB(Caro)Hδ	Aromatic side-chains to CB-HB

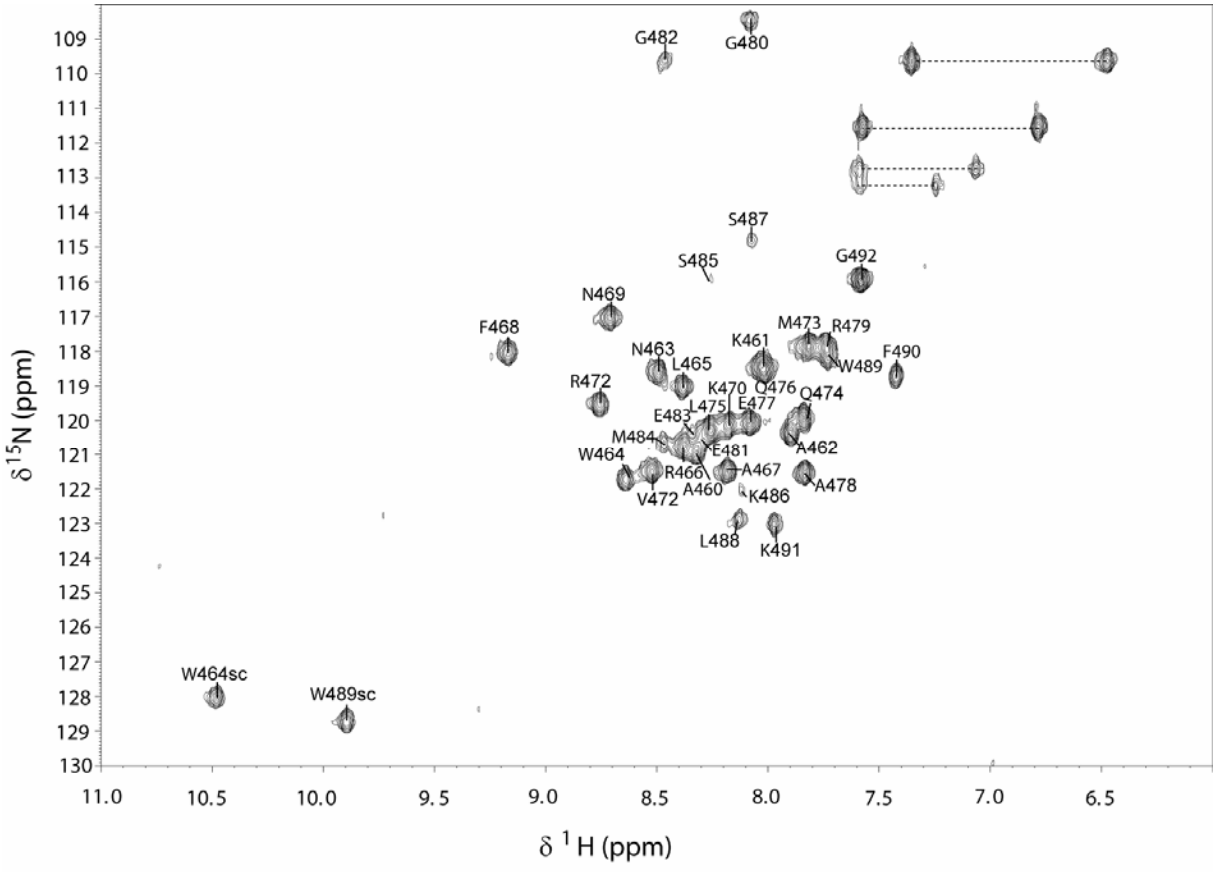

Figure 41. ^{1}H-^{15}N HSQC of the bound $^{13}C,^{15}N$ Munc13-1(457-492) peptide to CaM. The amide cross-peaks were assigned with the aid of various triple-resonance experiments.

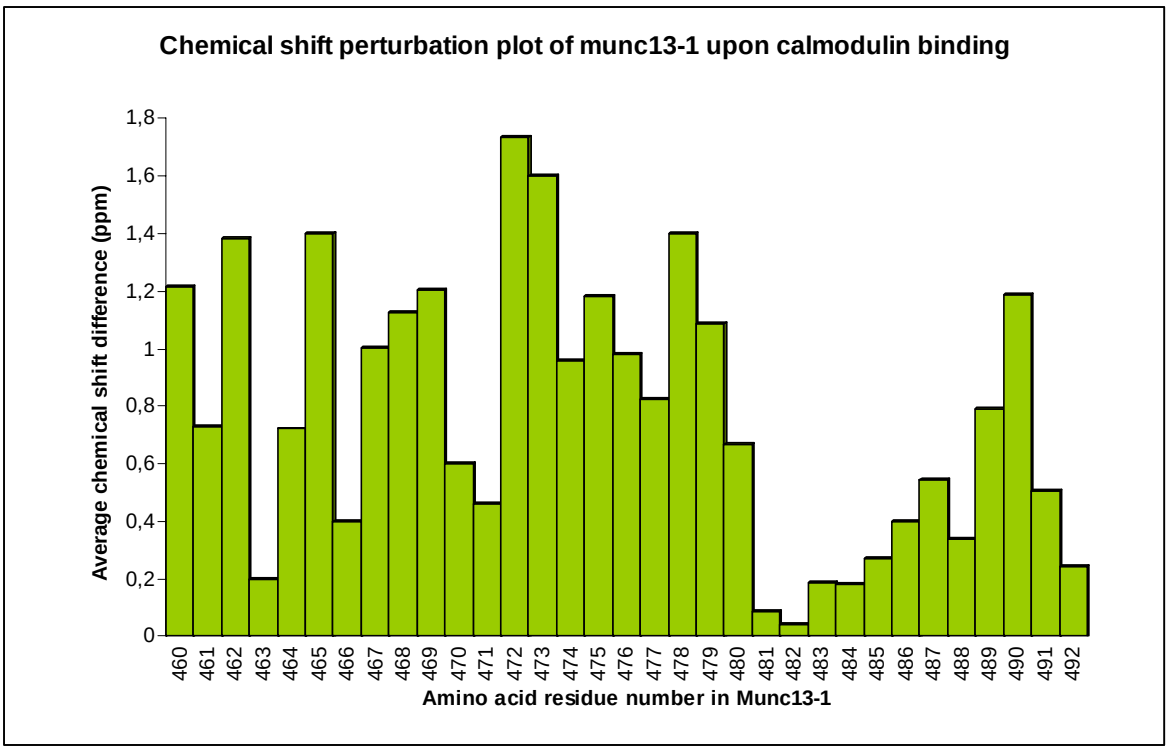

Figure 42. Chemical shift perturbation plot of the Munc13-1 (457-492) peptide upon binding to CaM. Large chemical shift changes were observed in the N-terminal part of the peptide and a second significant perturbation was observed in the C-terminal hydrophobic tail.

The Munc13-1 (457-492) peptide was also titrated with apoCaM. The ^{15}N-^{1}H HSQC spectrum was almost identical to the one in the presence of holoCaM (Figure 43). Thus, it appears that the low affinity interaction between apoCaM and Munc13-1 described above in section *b*, already induces the α-helical conformation of the Munc13-1(457-492) peptide.

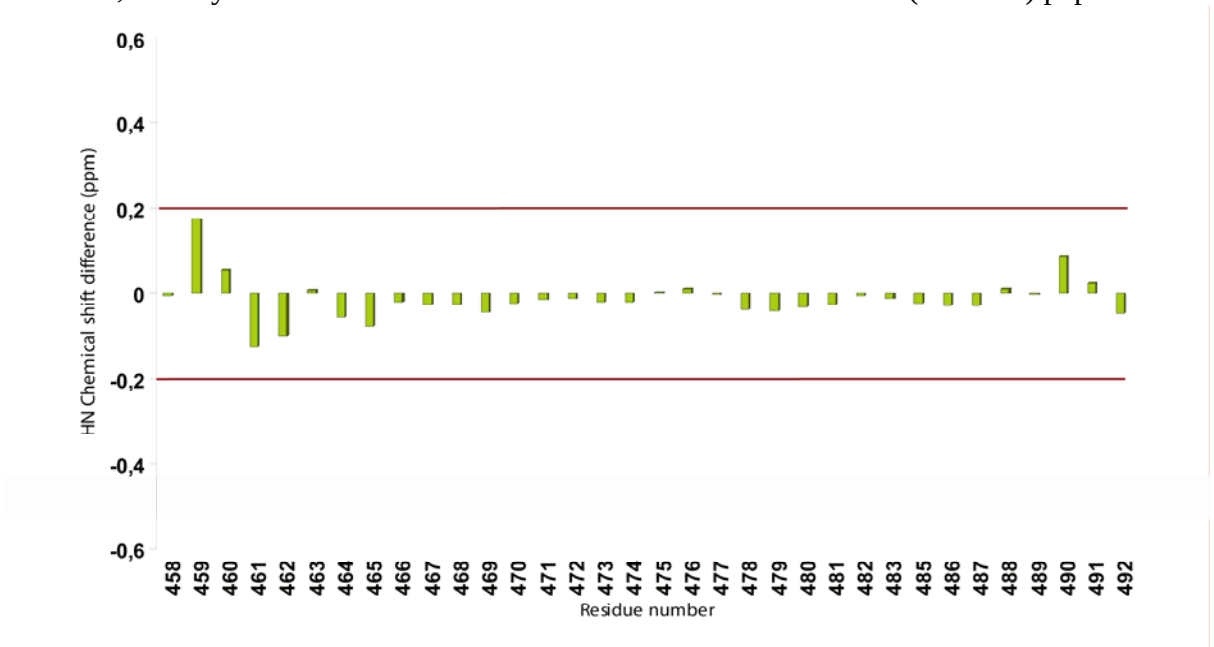

Figure 43. Chemical shift difference for the amide ^{1}H resonances between the Munc13-1 (457-492)/CaM and Munc13-1 (457-492)/apoCaM peptide complexes. The HSQC spectra were almost identical, no significant perturbations were observed.

To derive hydrogen bond restraints and to determine the buried part of the CaM-bound Munc13-1 (457-492) peptide, a deuterium exchange experiment was done. The amide resonances that are hydrogen bonded and that are buried in the hydrophobic pocket of CaM showed a slower rate of exchange (see Figure 44).

d. NMR studies of the CaM binding region and the C_1 domain of Munc13-1 (Munc185)

There are remarkable physiological similarities between the Munc13-1 phorbol ester insensitive (H567K) mutant and the CaM insensitive (W464R) mutant. For this reason it was of interest to study the protein-protein interaction of CaM with a larger construct of Munc13-1 which included its C_1 domain, which binds the phorbol ester.

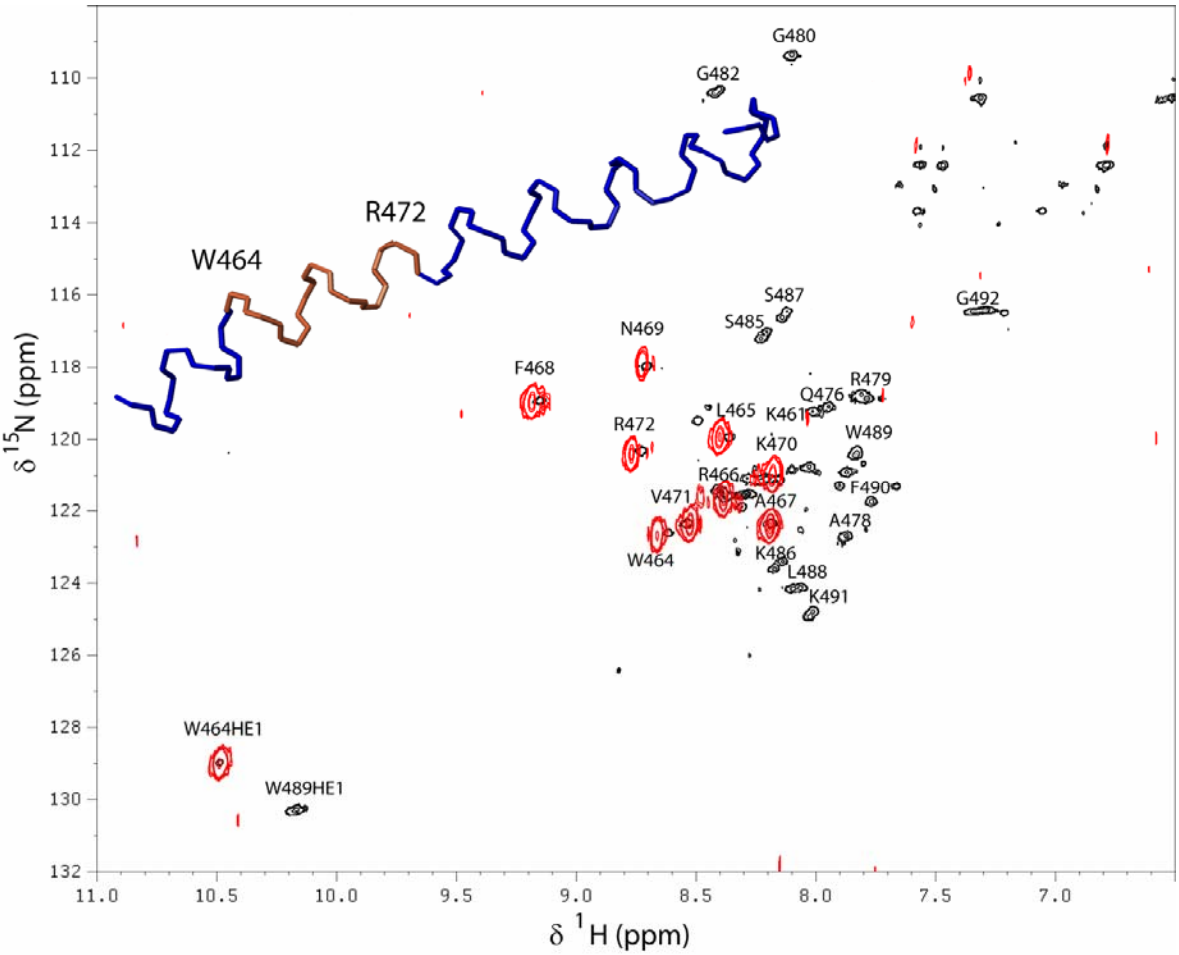

Figure 44. Overlaid ^{15}N-^{1}H HSQC spectra of the bound ^{15}N, ^{13}C Munc13-1(457-492) peptide to CaM in 90% H_2O and 10% D_2O (black) and in 99% D_2O (red) after 4 hours at 35^{o}C. In the top left corner the helical region of the peptide which was protected from exchange is shown in light brown colour.

The co-expression of the ^{15}N CaM/^{15}N Munc13-1(185aa) *wt* complex was successful in the pET Duet-1 construct, obtaining enough protein for NMR measurements. During the purification procedure using size-exclusion chromatography, monomer-dimer equilibrium was observed. The dimeric (2:2) complex was very stable and could be separated from the monomeric complex. The ^{15}N-^{1}H HSQC spectrum of the monomeric sample is shown in Figure 45. The overlaid HSQC spectra of the dimeric (2:2) and monomeric (1:1) CaM/Munc13-1(185aa) *wt* samples is shown in Figure 46.

Although the backbone sequential resonance assignment of this complex was not undertaken; the general appearance of the spectrum was very similar to that one of the CaM/Munc13-1 (459-492) peptide complex and numerous amide cross-peaks where at the same position and easily identified.

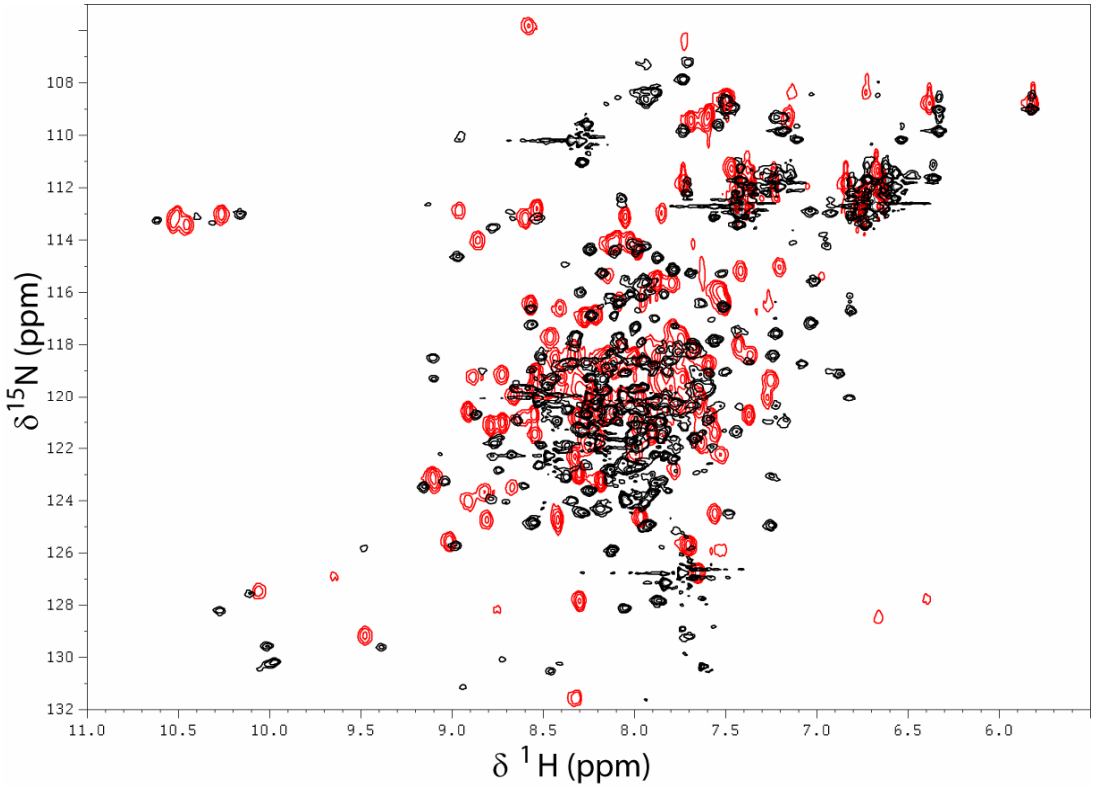

Figure 45. ^{15}N-^{1}H HSQC of the ^{15}N CaM (red) and ^{15}N CaM/^{15}N Munc13-1(185aa) *wt* monomeric (1:1) complex (black).

From the appearance of the HSQC spectrum of the dimeric (2:2) complex, it was evident that many of the amide cross-peaks broadened (*i.e.* the line-width increased) and some of them broadened beyond detection. To quantify these effects, the intensities for each of the peaks that overlaid well to the CaM/Munc13-1(459-492) peptide complex cross-peaks were compared between the two species and are shown in Figure 47.

The regions mostly affected in the dimer-monomer equilibrium mapped to the N-terminal domain of CaM (see Figure 48) and the C_1 domain of Munc13-1. This suggested that there is a conformational exchange equilibrium process between these two domains in the µs to ms time scale in this dimeric (2:2) species.

e. Tryptophan Nε-Hε1 side chain *heterogeneity as evidence of a switch mechanism in the calcium coupling mechanism of CaM and Munc13-1*

From the studies on the CaM/Munc13-1(457-492) peptide complex it was determined that CaM had a bipartite interaction with Munc13-1, *i.e.* the C-terminal domain interacted with the amphiphilic α-helix (1-5-8) motif and the N-terminal domain interacted with a hydrophobic LW motif at the C-terminal tail of the peptide. The question that arose was whether the small hydrophobic LW motif in the C-terminal tail of the peptide was also binding to the N-terminal domain of CaM in the context of the larger Munc13-1 (185aa) construct.

The analysis of the tryptophan Nε-Hε1 side-chain region for the CaM/Munc13-1 (457-492) peptide and CaM/Munc13-1 (185aa) complexes revealed the presence of heterogeneity in both the W489 and W588 Nε-Hε1 side-chain resonances (Figures 49).The identity of each

tryptophan Nε-Hε1 side-chain was unambiguously identified with the aid of two CaM/Munc13-1(185aa) mutant samples (W489A and W588A).

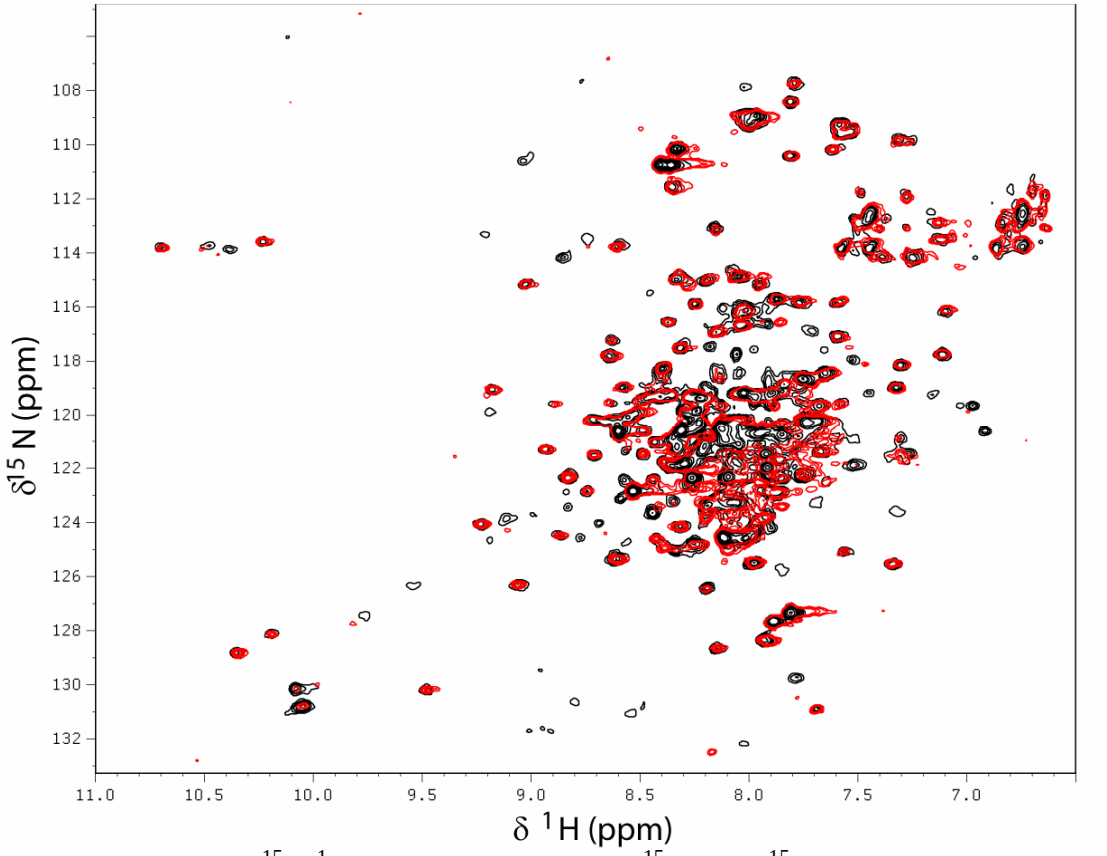

Figure 46. Overlaid ^{15}N-^{1}H HSQC spectra for the ^{15}N CaM/^{15}N Munc13-1(185aa) *wt* monomeric (1:1) complex (black) and dimeric (2:2) complex (red).

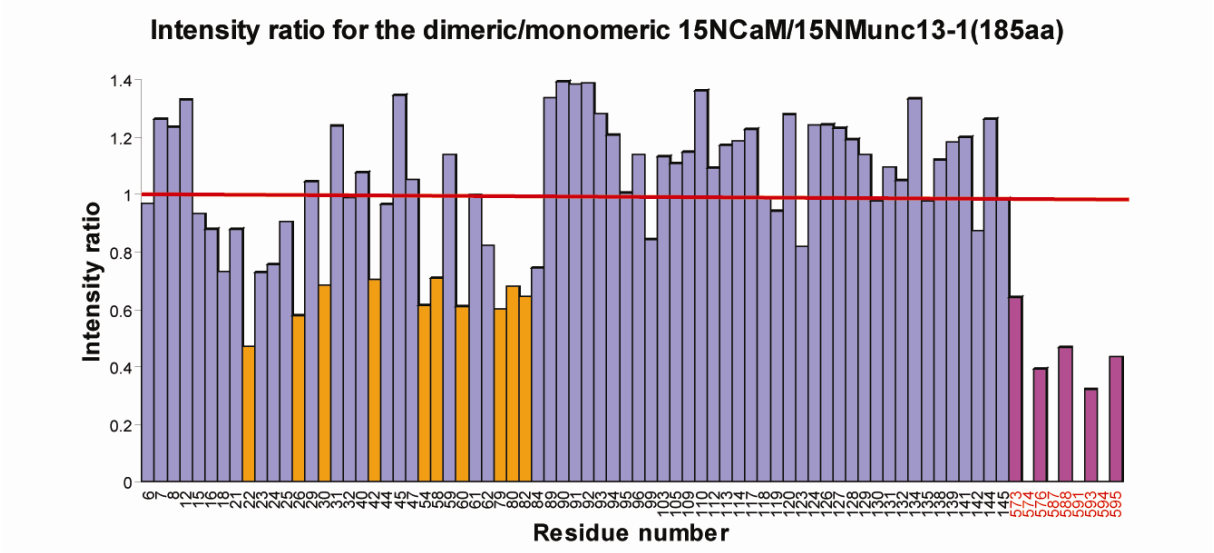

Figure 47. Intensity ratio of the amide cross-peaks between the monomeric (1:1) and dimeric (2:2) ^{15}N CaM/^{15}N Munc13-1(185aa) *wt* complexes. The regions affected were the C_1 domain of Munc13-1 (residues labelled in red) shown in magenta and some amides in the N-terminal domain of CaM shown in orange.

Figure 48. Residues in the N-terminal domain of CaM that showed line-broadening upon dimerization with Munc13-1 (185aa).

The heterogeneity could have arisen either from different χ rotamer populations of the tryptophan side chain with slow exchange on the NMR time scale or from two different complex states a tryptophan-bound or –free state. However, evidence coming from the assigned W588 tryptophan Nε-Hε1 side-chain resonance in the absence of CaM discussed below in section *f*, argues for two distinct complex states and therefore are labelled as free side chain (sc) and bound side chain (bsc) in all the spectra. For W489, the bsc resonance represents 19.2 % of the total volume and for W588, the bsc resonance represents 60.5 % of the total volume.

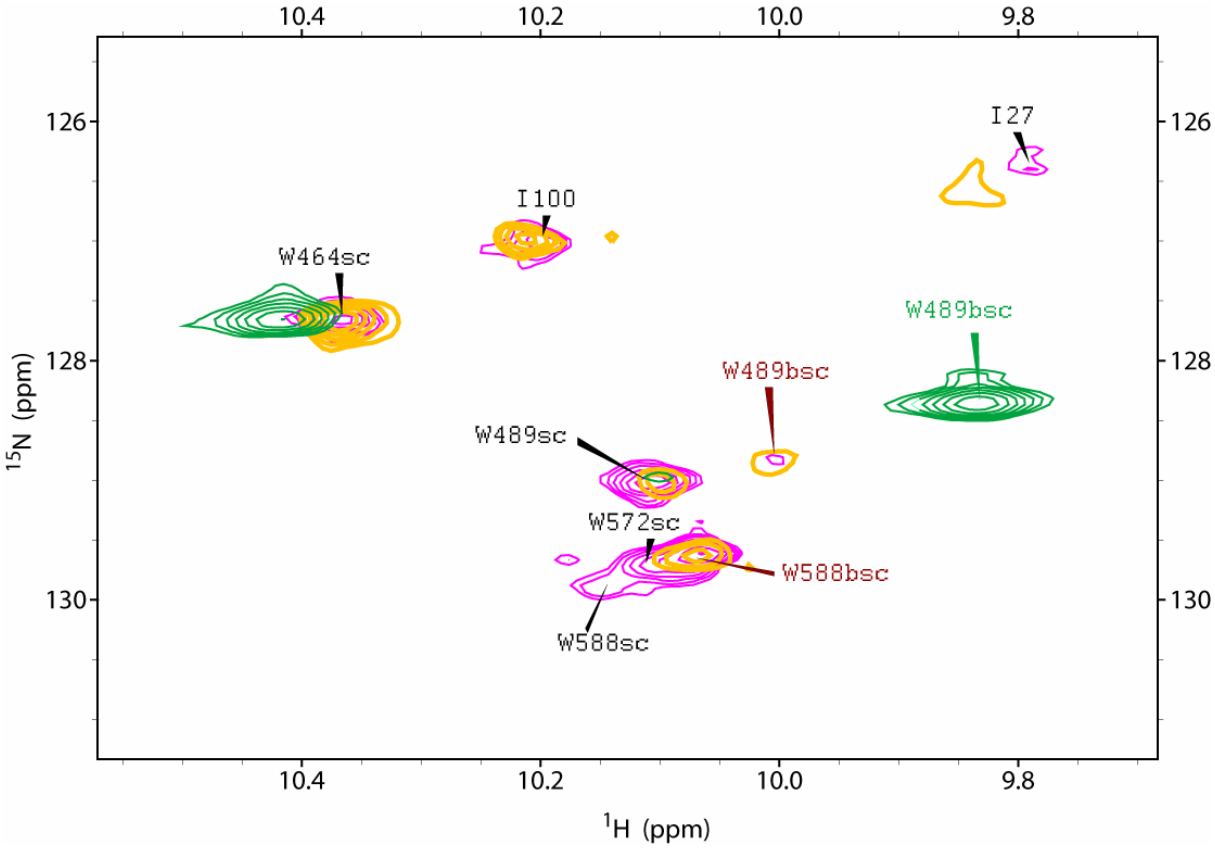

Figure 49. Overlaid ^{15}N-^{1}H HSQC spectra showing the tryptophan Nε-Hε1 side-chain region for the ^{13}C,^{15}N Munc13-1(457-492) bound peptide (green); the ^{15}N CaM/^{15}N Munc13-1(185aa) *wt* monomeric (1:1) complex (magenta); and dimeric (2:2) complex (orange).

None of the mutations (W489A and W588A) appeared to resolve the heterogeneity observed in the tryptophan Nε-Hε1 side-chain. Assuming that the heterogeneity arises from two different complex states, a switch calcium-gating mechanism model was proposed: the N-terminal domain of CaM could switch between the hydrophobic motif in the W489 region and the hydrophobic motif in the W588 region within the C_1 domain of Munc13-1. Nonetheless, the description of a direct contact by intermolecular NOEs or pseudocontact shifts, for example, between the W588 residue and CaM would provide a definite proof. If this proof is provided, it would represent a structural correlate to the physiological observations in the functional mutant studies of the phorbol insensitive (H567K) Munc13-1 and the CaM insensitive (W464R) Munc13-1 mutants mentioned before.

f. NMR studies of the C_1 domain of Munc13-1 (Munc65)

Based on the studies done on the CaM/Munc13-1(185aa) construct it was also of interest to study the C_1 domain of Munc13-1 in the absence of CaM. Although the NMR structure of this domain has been reported before by Shen *et al*., 2005; there is no resonance assignment available in the Biological Magnetic Resonance Data Bank (BMRB); the only assignments come from the few labels in the HSQC spectrum reported in that publication.

In order to identify the free tryptophan Nε-Hε1 side chains of the C_1 domain of Munc13-1 a 1D-^{1}H spectrum with presaturation of the water resonance was measured (Figure 50) and compared to the published spectrum.

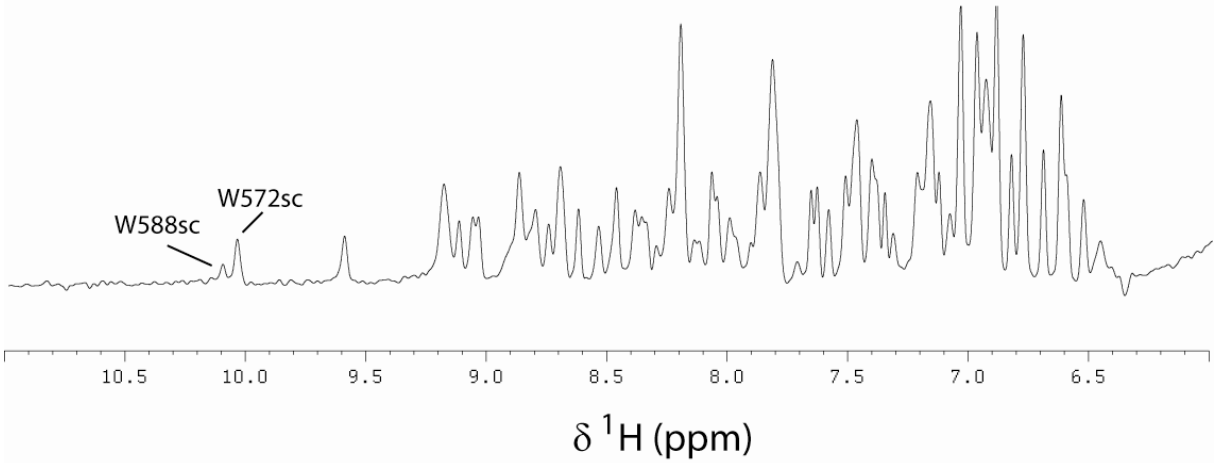

Figure 50. 1D-^{1}H spectrum for the amide region of unlabelled Munc13-1 C_1 domain (65aa) at 900MHz.

Afterwards, with the availability of a ^{15}N labelled sample, a ^{15}N-^{1}H-HSQC of the C_1 domain of Munc13-1 was also recorded (Figure 51) for comparison purposes to the published spectrum mentioned above.

The tryptophan Nε-Hε1 side-chain region of the Munc13-1 C_1 domain HSQC spectrum was overlaid to that one of the ^{15}N CaM/^{15}N Munc13-1 (185aa) *wt* complex (Figure 52). The lack of heterogeneity for the W588 Nε-Hε1 side-chain in the C_1 domain alone, suggested that in the complex with CaM, the heterogeneity should have arisen either from the direct interaction with CaM or from an intramolecular interaction with an element upstream from the C_1 domain of Munc13-1.

g. NMR studies of ^{15}N CaM/^{15}N Munc13-1(185aa) complex with its agonist: phorbol dibutyrate (PDBu)

The ^{15}N CaM/^{15}N Munc13-1(185aa) *wt* dimeric (2:2) complex was treated with a slight excess of the C_1 domain agonist phorbol dibutyrate (PDBu) to observe its effect on the ^{15}N-^{1}H HSQC spectrum; two resolved areas of the spectrum are shown in Figure 53.

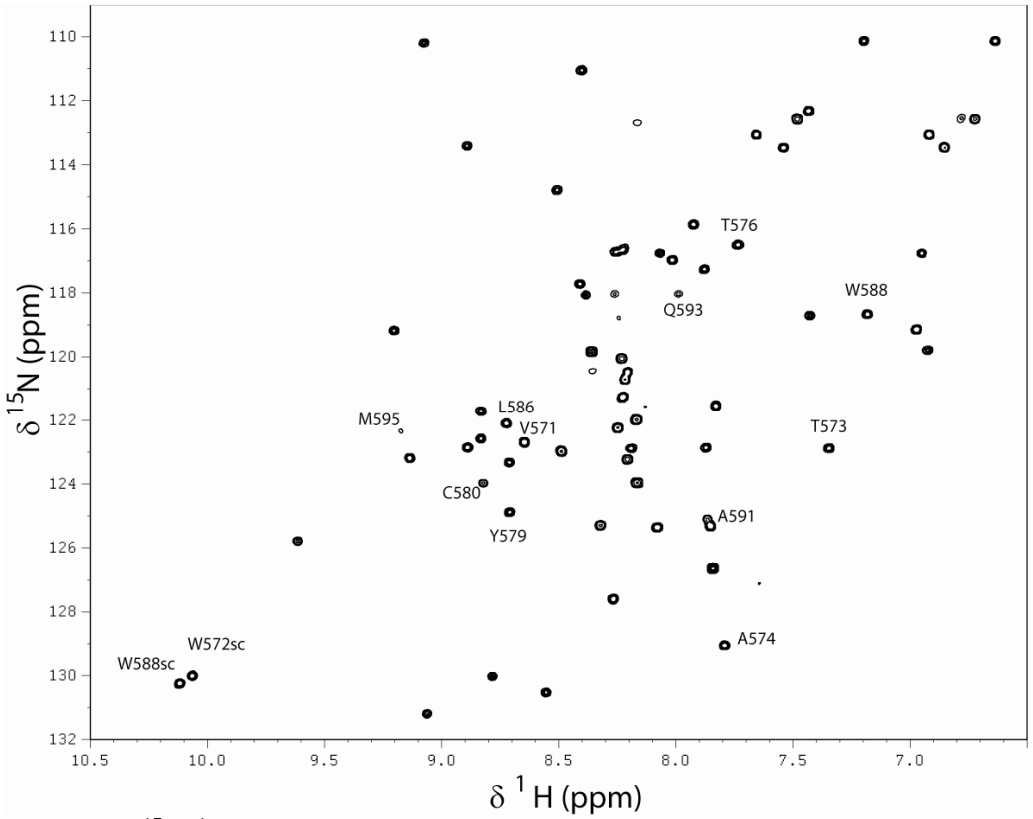

Figure 51. ^{15}N-^{1}H HSQC of the C_1 domain of Munc13-1 (100µM) in 20 mM Bis-Tris, 150 mM KCl, 5 mM $CaCl_2$ recorded at 25°C with 1024 and 256 real points in the t_2 and t_1 dimensions, respectively.

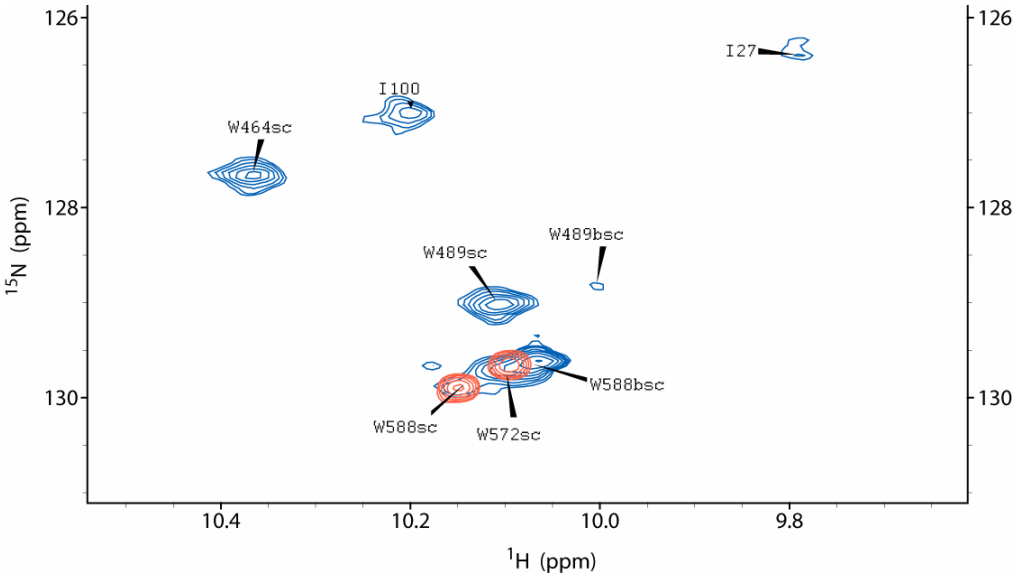

Figure 52. Overlaid ^{15}N-^{1}H HSQC spectra for the ^{15}N CaM/^{15}N Munc13-1(185aa) *wt* monomeric (1:1) complex in blue and the ^{15}N Munc13-1 C_1 domain in red.

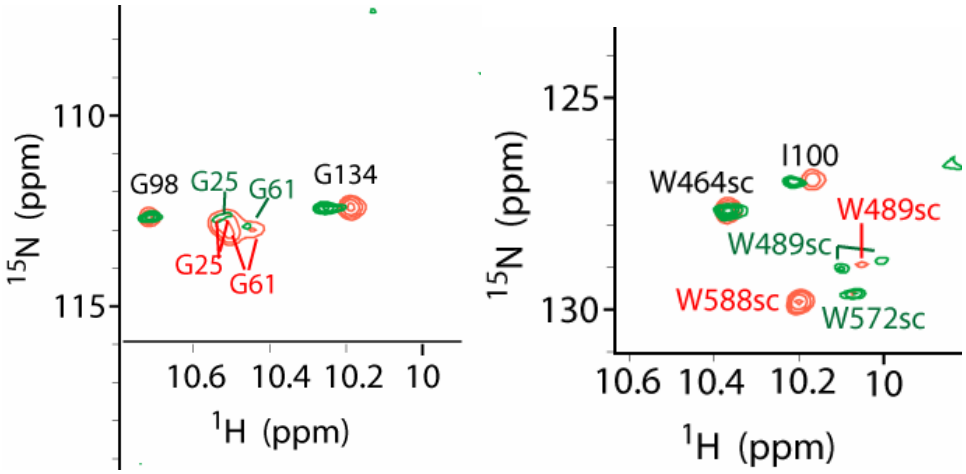

Figure 53. Overlaid ^{15}N-^{1}H HSQC spectra of the ^{15}N CaM/^{15}N Munc13-1(185aa) *wt* dimeric (2:2) complex in the inactive state (green) and in its active state (red) in the presence of a slight excess of the C_1 domain agonist PDBu.

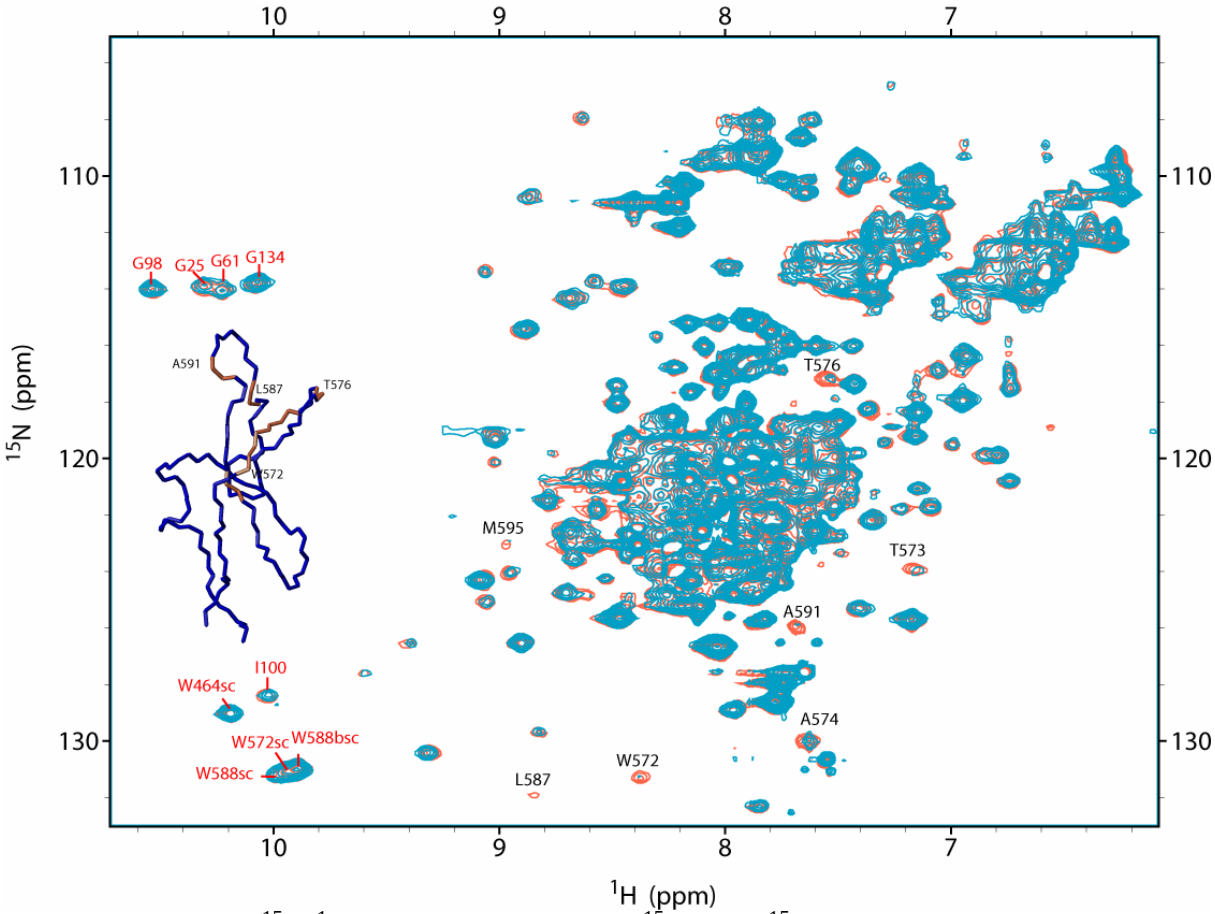

Figure 54. Overlaid ^{15}N-^{1}H HSQC spectra for the ^{15}N CaM/^{15}N Munc13-1(185aa) W489A mutant monomeric (1:1) complex in its inactive state (red) and in its activated state with a slight excess of the agonist PDBu (in light blue). In the left side of the spectrum the backbone structure of the C_1 domain of Munc13-1 shows the regions affected by PDBu in light brown. The residues with red labels are the ones analyzed in the (2:2) complex; they were not affected by the PDBu addition in this sample.

The effects of the agonist on the ^{15}N CaM/^{15}N Munc13-1(185aa) *wt* dimeric (2:2) complex were clearly visible. There were chemical shift perturbations as well as a shift in the

conformational exchange equilibrium previously described in the *d* section, since the line shape and S/N ratio of several amide cross-peaks improved significantly. The broad resonances for the G25 and G61 cross-peaks sharpened and doubled in the activated state. In the tryptophan Nε-Hε1 side-chain region, the broad W588 resonance in the inactive spectrum had a low field ^{1}H chemical shift change of ~ 0.2 ppm in the presence of PDBu. The heterogeneity of the W489 resonance observed in the inactive state was lost in the presence of PDBu and a single cross peak was observed with a chemical shift between the free and bound complex states. The changes in the C-terminal domain of CaM appeared to be less pronounced consistent with the bipartite interaction model of this complex.

The same agonist activation experiment was done for the ^{15}N CaM/^{15}N Munc13-1(185aa) W489A monomeric (1:1) complex. The overlaid spectra are shown in Figure 54.

The effects of the agonist PDBu on the monomeric (1:1) state of the ^{15}N CaM/^{15}N Munc13-1(185aa)W489A mutant complex were more moderate than those for the dimeric (2:2) complex. Nonetheless, there was clear binding of the ligand to the described binding pocket of the C_1 domain. The binding was in the intermediate exchange regime on the NMR time-scale. The effects are shown in Figure 55.

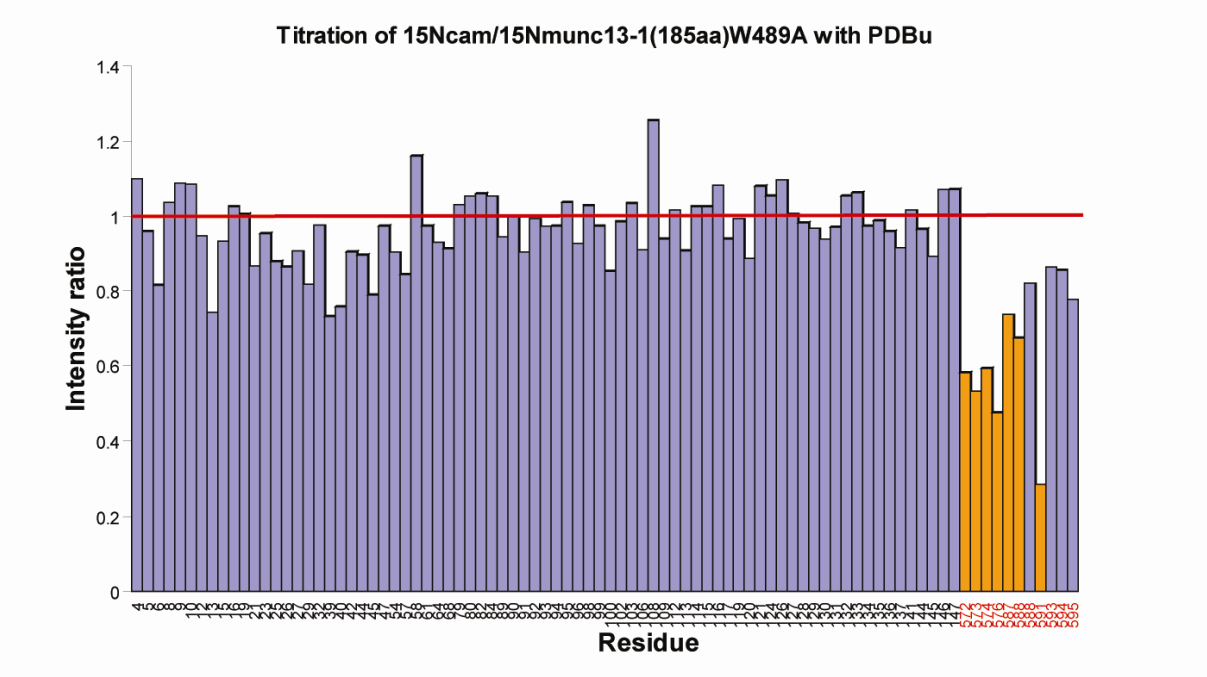

Figure 55. Intensity ratio of the amide cross-peaks for the ^{15}N CaM/^{15}N Munc13-1(185aa) W489A mutant in the absence and presence of its agonist PDBu.. The CaM residues are labelled in black font and the Munc13-1 residues in red font. The amide cross-peaks greatly affected are shown in orange.

The residue most affected by the PDBu binding to the ^{15}N CaM/^{15}N Munc13-1(185aa)W489A monomeric complex was A591 in the binding pocket of the C_1 domain of Munc13-1. The intensity change upon agonist addition was followed, to observe its saturation curve (Figure 56).

The isotherm binding followed a sigmoidal curve suggesting cooperativity; the stoichiometry appeared to be (1:1) as expected. Cooperative binding of active site ligands follows the Monod-Wyman-Changeux (MWC) model of allostery, in this model, equilibrium between two conformational states, T and R are assumed. The equilibria between liganded and unliganded forms are described in terms of two microscopic binding constants, k_T and k_R, where $k_R > k_T$. An equilibrium constant *L* connects the unliganded forms (Kensal *et al*. 2006). Since the CaM/Munc13-1(185aa) complex has a monomer (1:1)-dimer (2:2) equilibrium such an allosteric activation model could be possible. NMR studies done on a model enzyme

showing allosterism (aspartate transcarbamoylase), have demonstrated that although the spectrum reveals just the T form of the enzyme, titrations with MgATP clearly perturbed the R-T equilibrium (Velyvis *et al*., 2007). In the system studied here, the observed cooperativity for the agonist binding is interesting from the physiological point of view, since it has been reported previously that there is an allosteric positive cooperativity between calcium and phorbol esters in electrophysiological measurements done on the Calyx of Held synapse (Lou *et al*., 2005). Additional experiments in the presence of phosphatidyl-serine to mimic the phospholipid bilayer of the plasma membrane would need to be done in order to confirm this model rigorously.

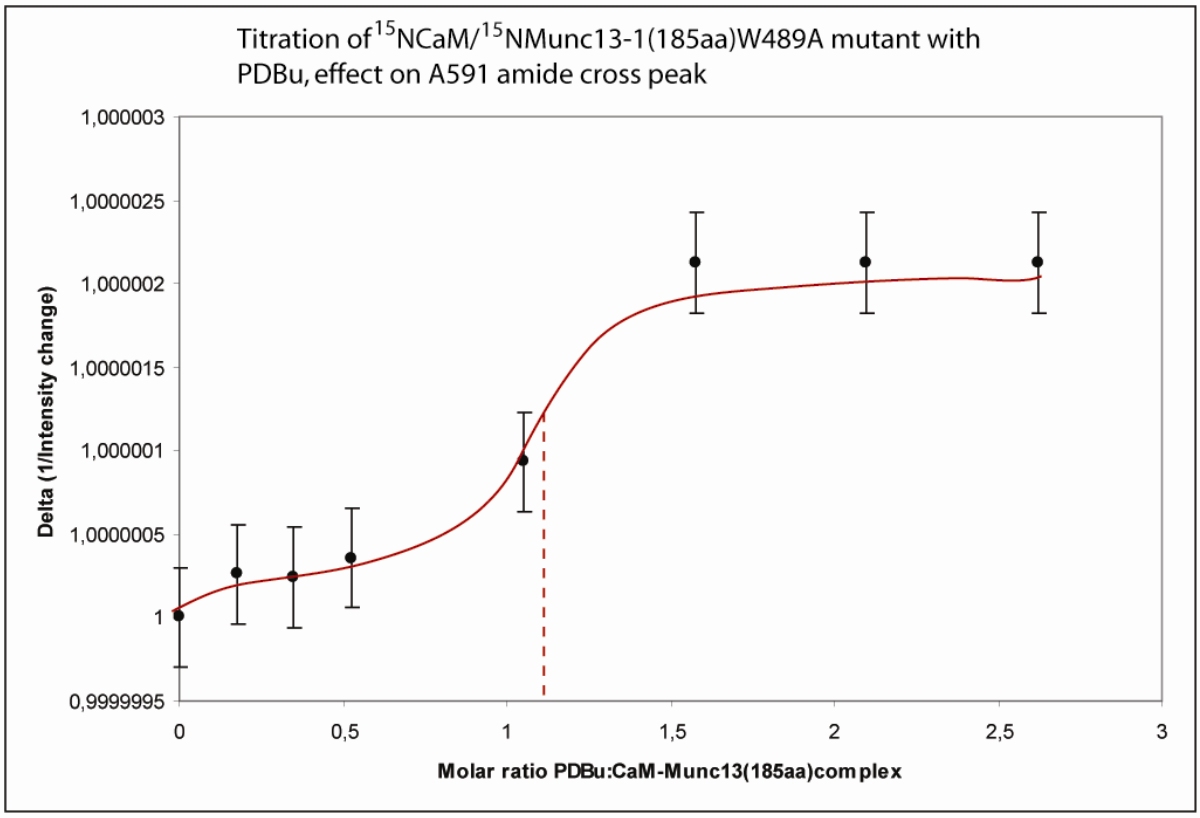

Figure 56. Binding curve of the C_1 domain agonist PDBu to the ^{15}N CaM/^{15}N Munc13-1(185aa) W489A monomeric (1:1) complex based on the decrease in the A591 NH cross peak intensity.

h. Sequential backbone and side-chain resonance assignment for the ^{13}C,^{15}N CaM/Munc13-1(459-492) peptide complex

For the sequential backbone and side chain resonance assignment, a series of triple resonance experiments were performed (see Table 4).

In biomolecular NMR, the ^{1}H-^{15}N HSQC spectrum of the amide resonances in a polypeptide represent its fingerprint and the identification of each cross-peak is essential for various studies like protein-ligand interactions; the assigned HSQC spectrum for the ^{13}C,^{15}N CaM/Munc13-1(459-492) peptide complex is shown in Figure 57.

In this section, some strip plots of the various 3D experiments were extracted to illustrate the sequential assignment strategy. The 3D-HNCACB and the 3D-CBCA(CO)NH correlate the Cβ and Cα of amino acid pairs to the NH cross-peak (Figure 58).

Table 4. NMR experiments for the sequential resonance assignment of the backbone and side chain atoms in the $^{13}C,^{15}N$ CaM/Munc13-1(459-492) peptide complex

Sample	Experiment	Resonances assigned
$^{13}C,^{15}N$CaM/Munc13-1 H_2O	HNCO	C'(i-1) to NH
	HN(CA)CO	C'(i-1) and C'(i) to NH
	CBCA(CO)NH	CB,CA (i-1) to NH
	HNCACB	CB,CA (i-1) and (i) to NH
	H(CC)(CO)NH-TOCSY	Aliph. H (i-1) to NH
	(H)CC(CO)NH-TOCSY	Aliph. C (i-1) to NH
$^{13}C,^{15}N$CaM/Munc13-1 D_2O	HCCH-TOCSY	Aliph. C and Aliph. H
	HBCBCaroHγ and HBCBCaroHδ	Aromatic H side-chains
	HMBC-CH_3ε Methionine	Methionine CH_3ε side-chains

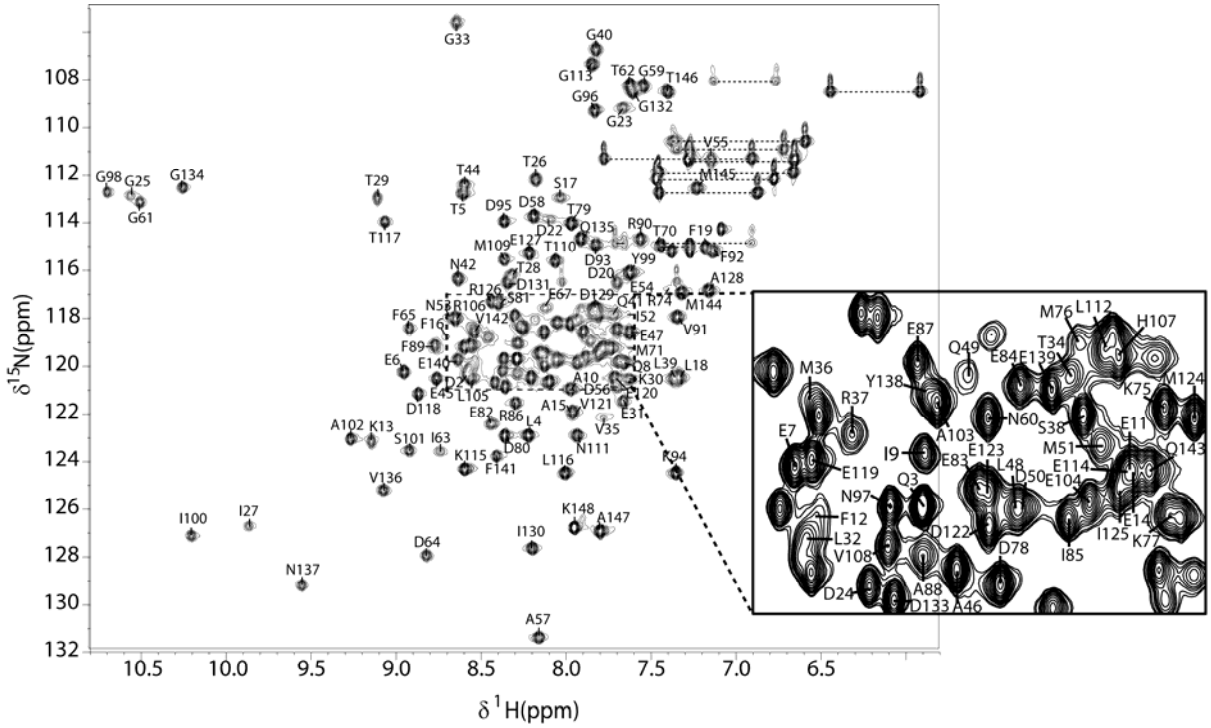

Figure 57. Assigned ^{1}H-^{15}N-HSQC spectrum of the $^{13}C,^{15}N$CaM/Munc13-1(459-492) peptide complex measured at 308K. The highly overlapped central region is enlarged on the right side.

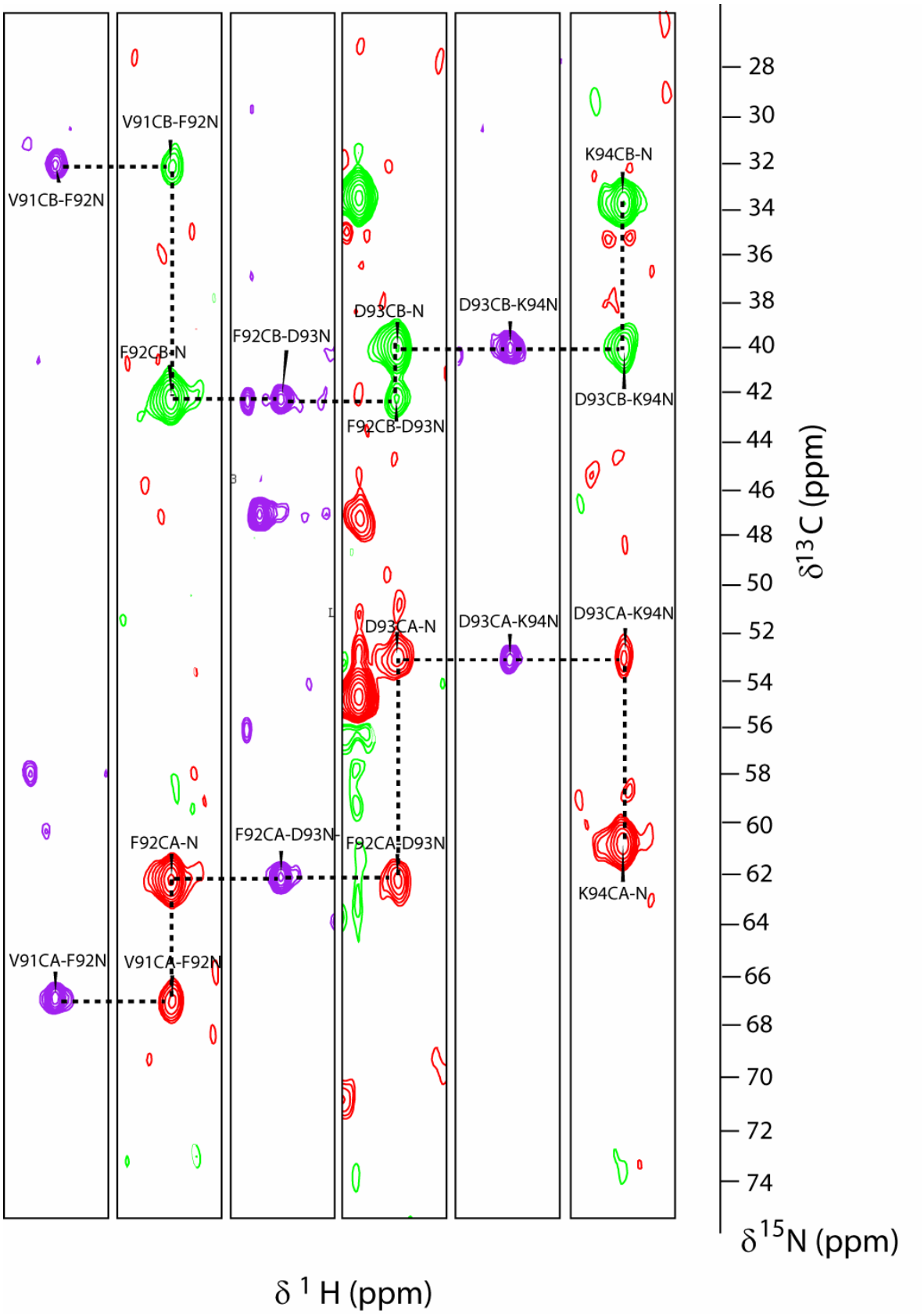

Figure 58. Strips extracted from the 3D-CBCA(CO)NH spectrum in purple and from the 3D-HNCACB spectrum in red/green to illustrate the connectivity information to obtain the sequential resonance assignment of the backbone nuclei.

The backbone assignment was also corroborated with the inter-residue carbonyl connectivity. For this purpose the 3D-HNCO and 3D-HN(CA)CO experiments were also recorded, processed and analyzed (Figure 59).

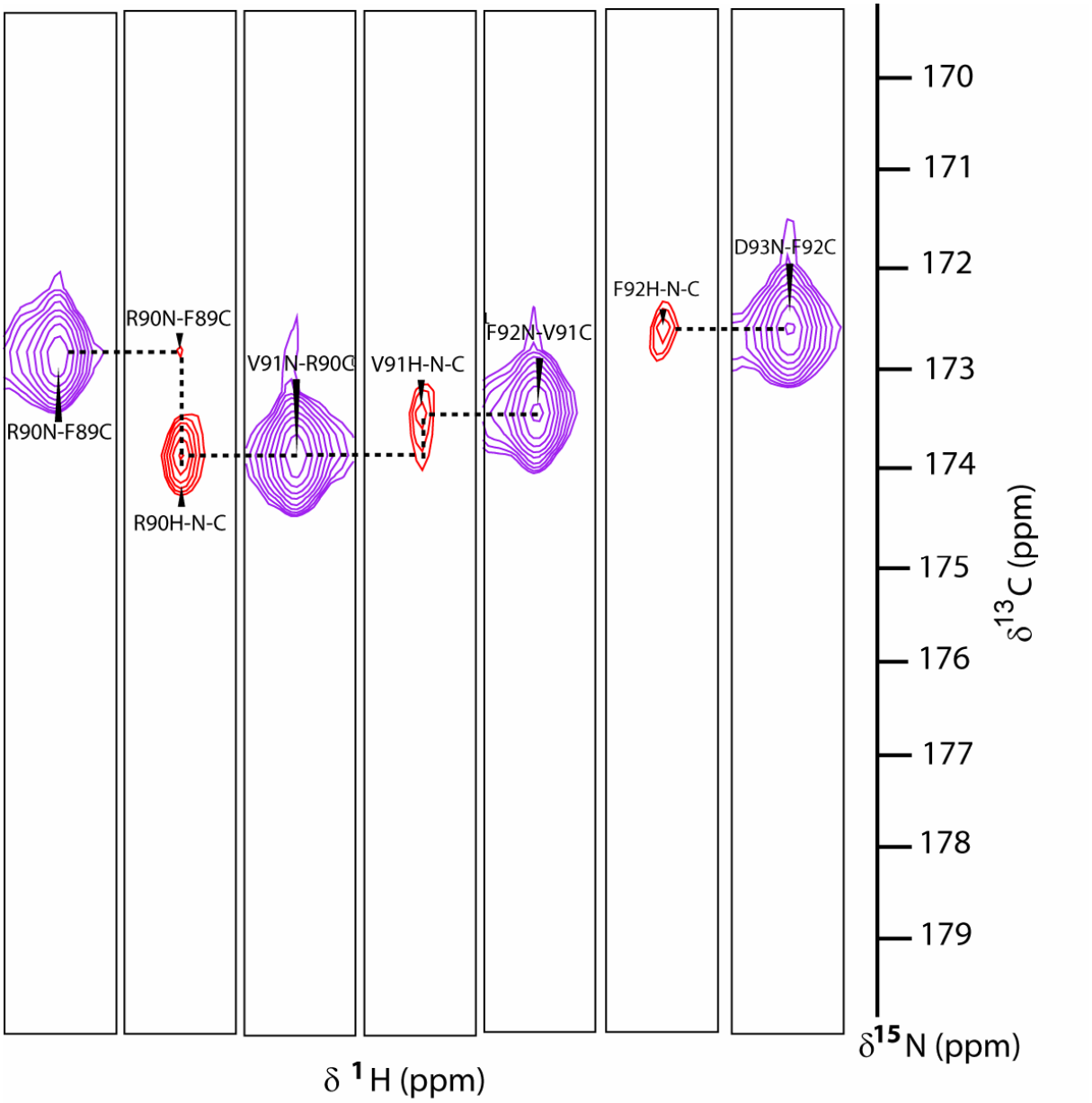

Figure 59. Strips from the 3D-HNCO spectrum (purple) and from the 3D-HN(CA)CO spectrum (red) for residues F89 to D93 were extracted to illustrate the sequential connectivity information that aids in the backbone sequential resonance assignment.

As can be seen in Figure 60, the overlap of the aliphatic side-chain resonances is very large; for this reason a series of 3D experiments were done to assign the side-chain of each amino acid residue in CaM to the backbone resonances. The aliphatic Carbon resonances were initially assigned using the 3D-(H)CC(CO)NH-TOCSY experiment (Figure 61).

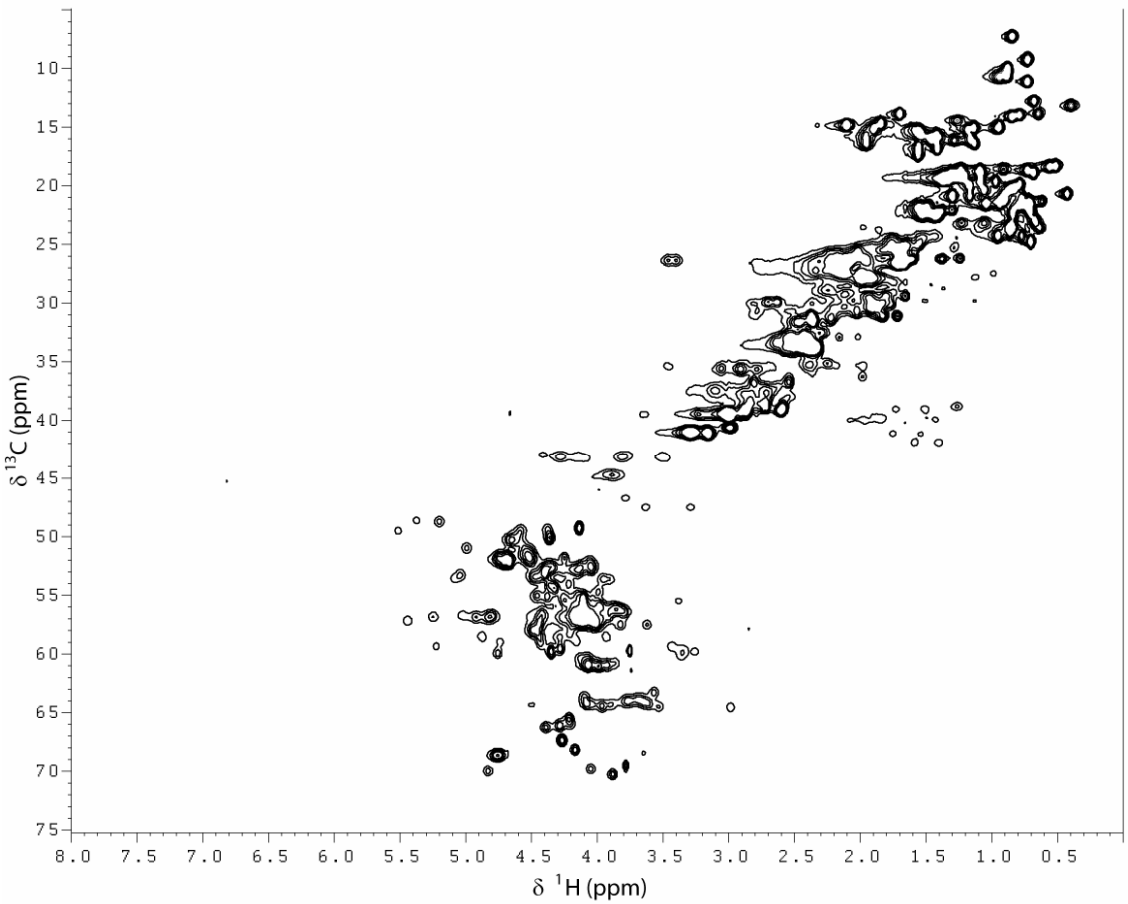

Figure 60. ^{13}C-^{1}H HSQC spectrum of ^{13}C,^{15}N CaM/Munc13-1(459-492) complex in 99% D_2O

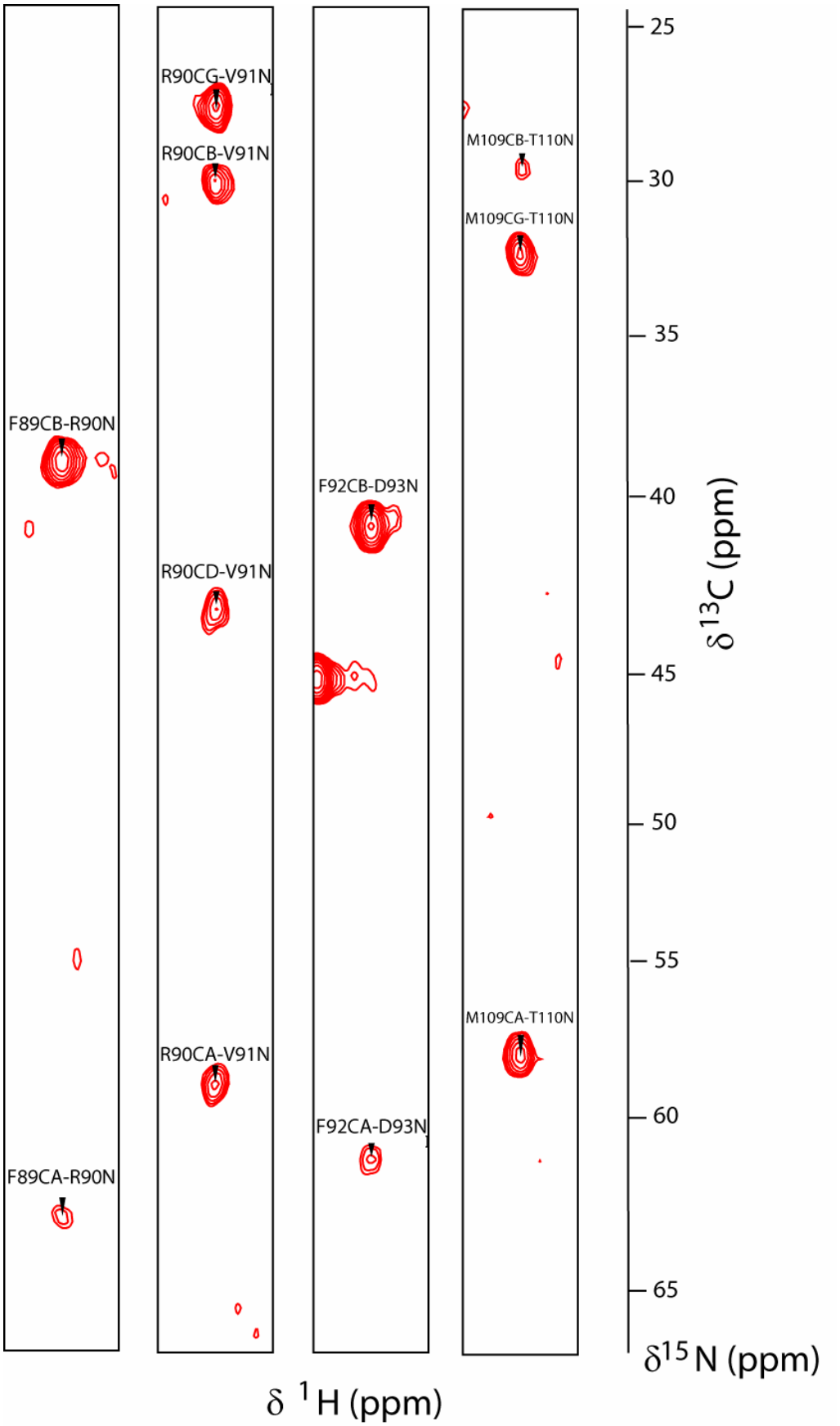

Figure 61. Strips extracted from the 3D-(H)CC(CO)NH-TOCSY spectrum to illustrate the assignment of the aliphatic carbons from different side-chains to the amide cross-peak in the backbone.

The aliphatic proton resonance were assigned with the 3D-H(CC)(CO)NH-TOCSY experiment (Figure 62).

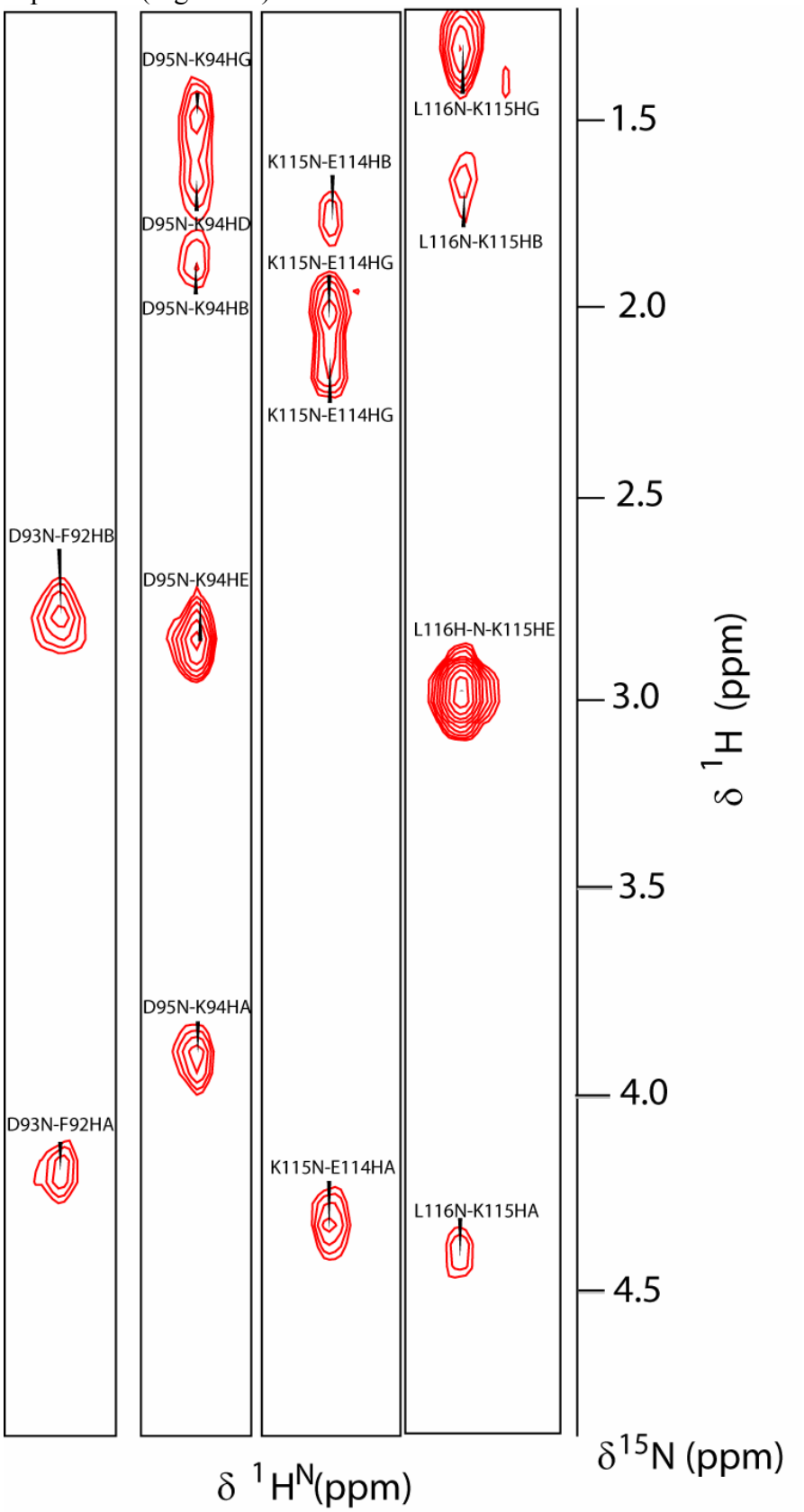

Figure 62. Strips extracted from the 3D-H(CC)(CO)NH-TOCSY spectrum to illustrate the assignment of the side-chain protons to the amide resonance in the backbone.

To confirm and complete the side-chain resonance assignment a 3D-HCCH-TOCSY experiment was also recorded, processed and analyzed (Figure 63).

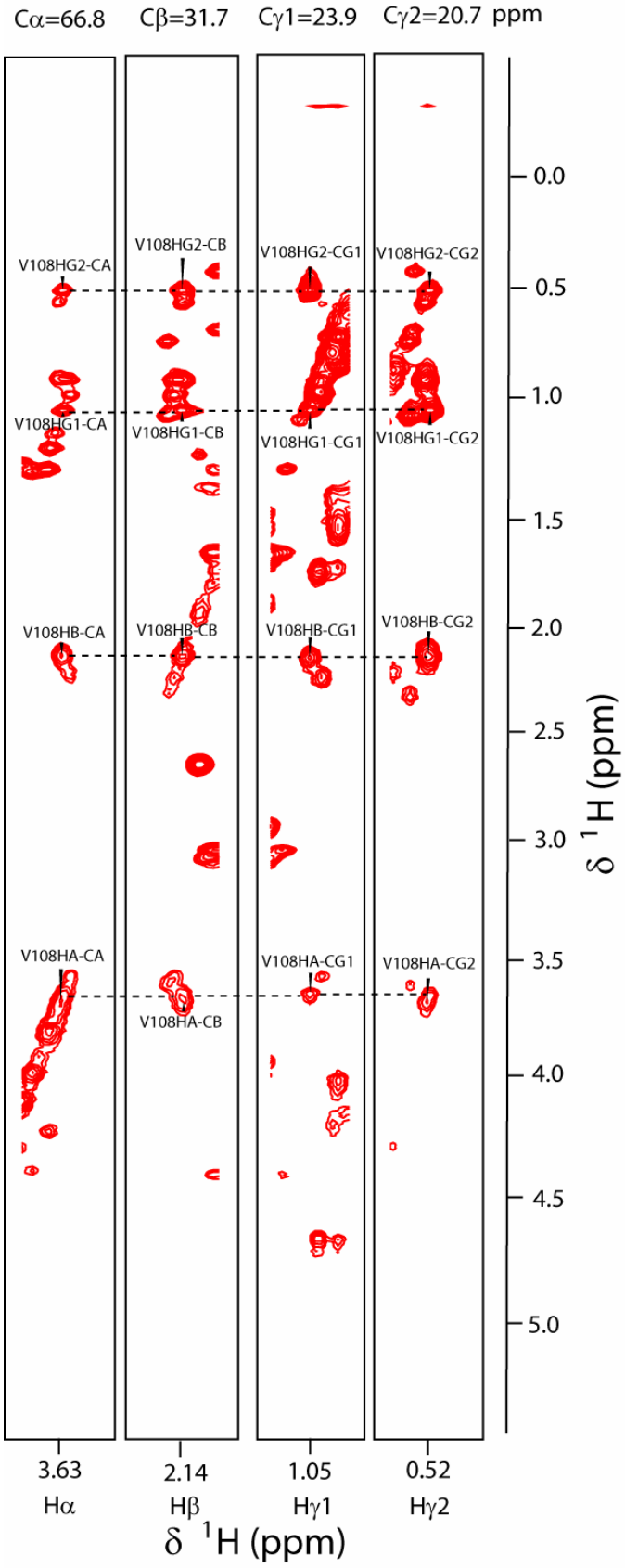

Figure 63. Strips selected from the 3D-HCCH-TOCSY spectrum to illustrate the side-chain assignment of Valine108. Unambiguous assignment can be obtained with this spectrum, since there is redundant information.

The aromatic side-chains were assigned by the aid of two spectra named 2D-HBCB(Caro)HE and 2D-HBCB(Caro)HD (Figure 64); the first one evolves the chemical shift of the Hε and the second one those of the Hδ of the aromatic side-chains; they are correlated to the Cβ-Hβ resonance of the aromatic side-chain.

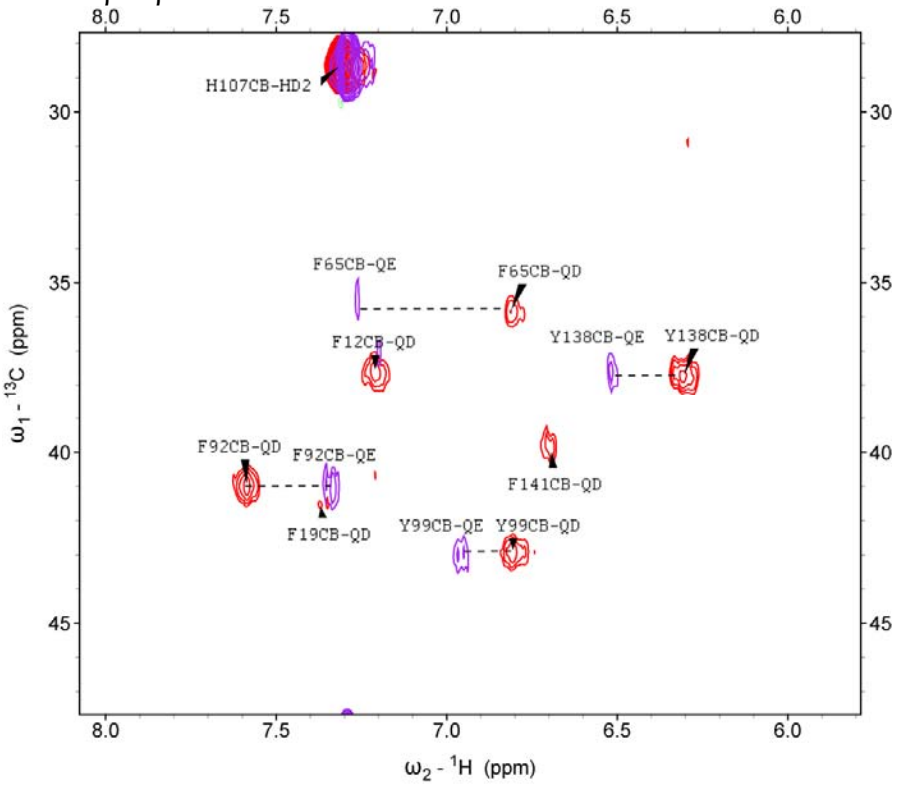

Figure 64. Overlaid 2D-HBCB(Caro) spectra for the aromatic side chain proton assignments (Hε and Hδ). The spectrum that correlates the Hε proton to the Cβ-Hβ resonance of the aromatic side-chain is shown in purple; the one that correlates the Hδ proton to the Cβ-Hβ resonance is shown in red.

CaM has nine methionine residues in its primary sequence, well above the average for a 148 aa protein; this is because the methionine methyl side-chains are important for building plastic hydrophobic contacts with its targets. Thus, the unambiguous assignment of the ε-methyl resonances of the methionines is essential for the study of protein-protein interactions involving CaM. The ε-methyl resonances were assigned with the aid of a HMBC type of experiment (See Figure 65) developed by Bax *et al*., 1994.

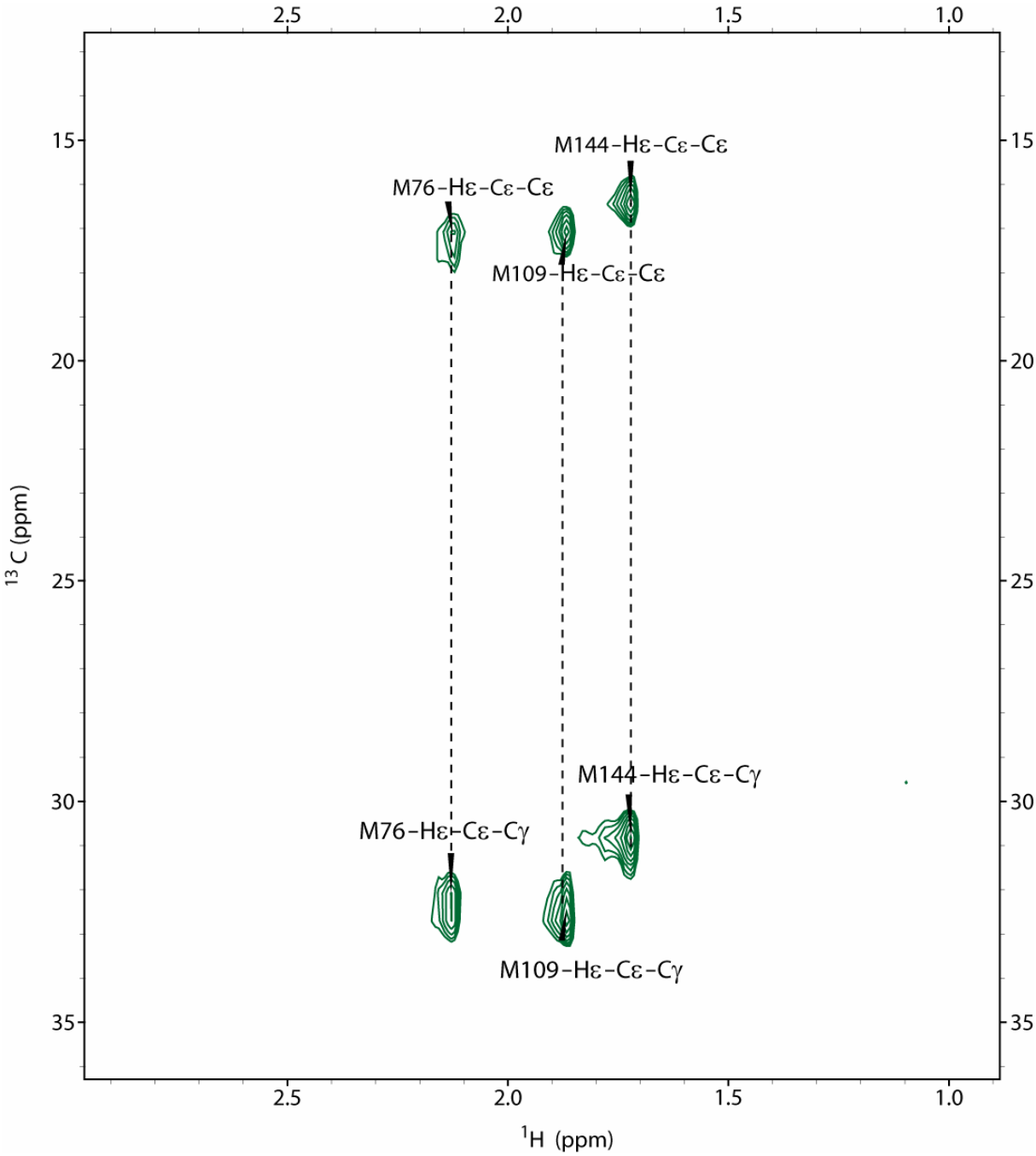

Figure 65. 3D-HMBC spectrum for methionine ε-CH_3 assignment. The ε-CH_3 resonance is correlated to the Cγ resonance of the methionine side-chain.

i. Long-range NMR restraints for the structure determination of the CaM/Munc13-1 (457-492) peptide complex

The distance restraints for the solution structure determination of a biomolecule with NMR come primarily from NOE signals between the different protons in the biomolecule, at a distance less to 5 Å. Different 3D-NOESY-HSQC spectra were recorded to obtain all the restraints needed for the structure determination.

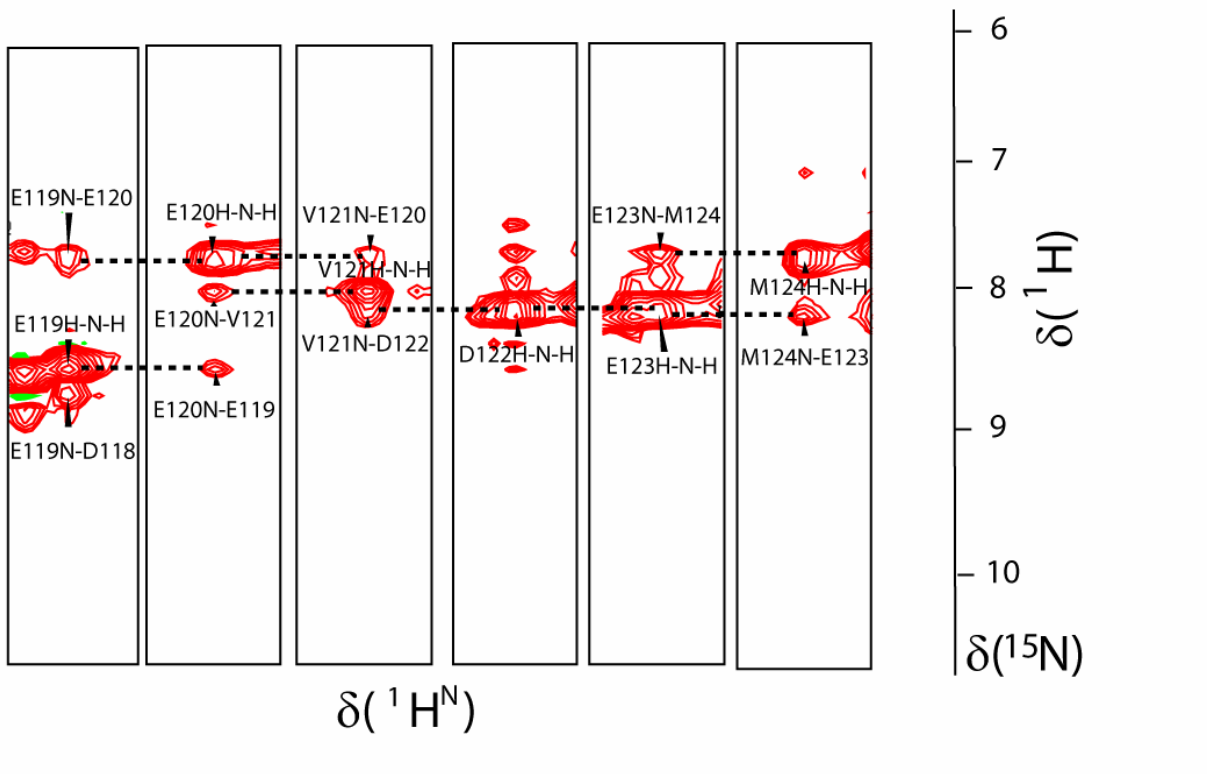

Figure 66. Selected amide cross peaks of the 3D-^{15}N (edited) NOESY-HSQC for ^{13}C,^{15}N CaM/Munc13-1(459-492) peptide complex showing the amide sequential connectivity.

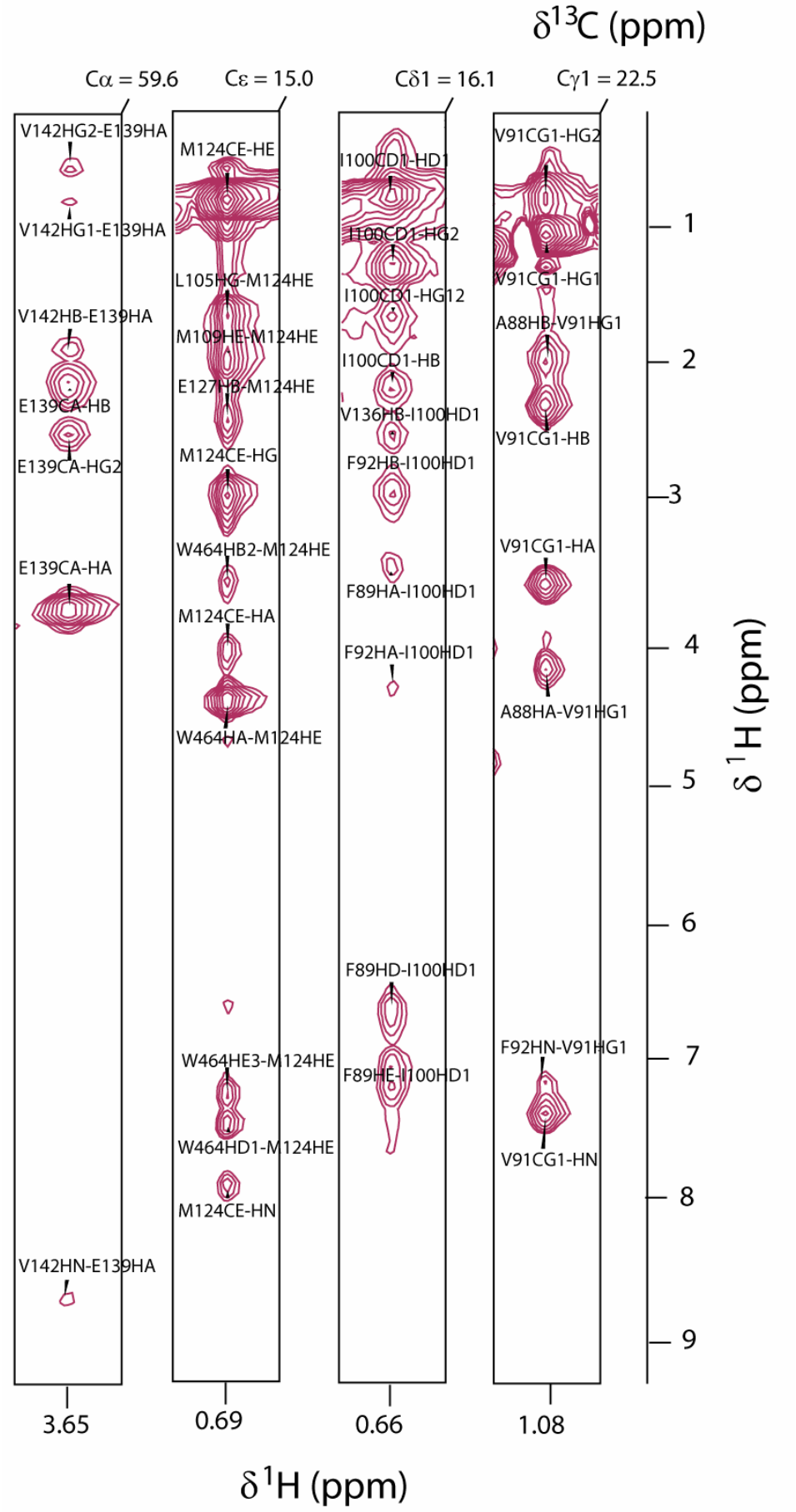

Figure 67. Selected aliphatic cross peaks of the 3D-^{13}C(edited) NOESY-HSQC for ^{13}C,^{15}N CaM/Munc13-1(459-492) peptide complex.

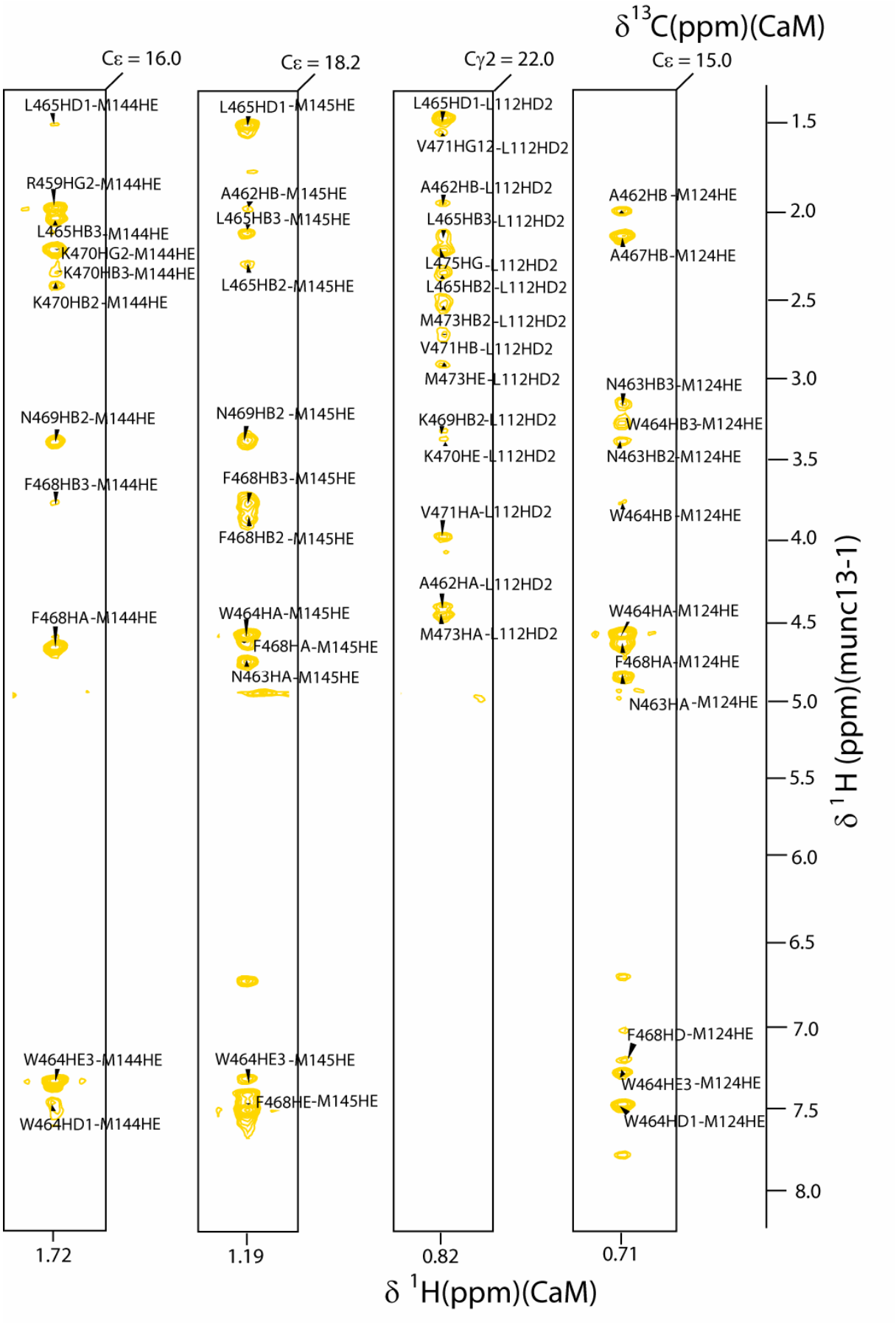

Figure 68. Selected aliphatic cross-peaks of CaM that show intermolecular NOEs to the Munc13-1(459-492) peptide in the 3D-(^{13}C-filtered)-NOESY-HSQC

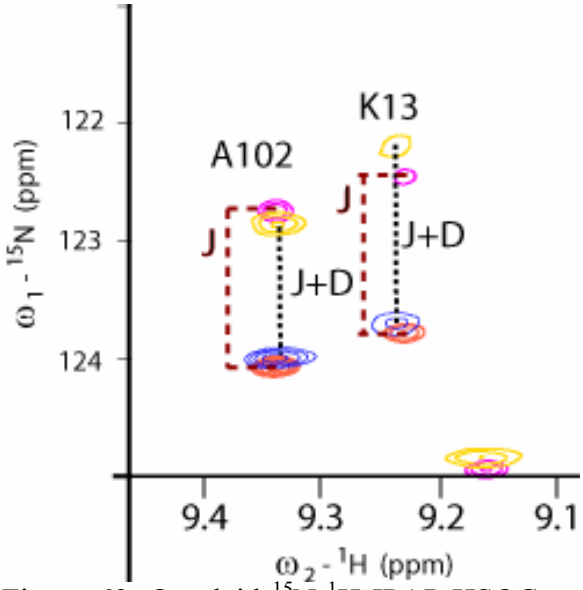

Figure 69. Overlaid ^{15}N-^{1}H IPAP-HSQC spectra for ^{15}N CaM/Munc13-1(459-492) complex (enlarged at two amide cross-peaks for illustration purposes) with bacteriophage Pf1 as cosolvent (blue and yellow) and in isotropic conditions (pink and red).

Additional long-range restraints in biomolecular NMR come from residual dipolar couplings (rDCs). To extract these restraints, a reference spectrum was measured to obtain the ^{1}JNH coupling constants and an aligned sample was used to measure the ^{1}JNH + ^{1}DNH couplings, where the rDC information was obtained upon subtraction to the reference spectrum (see Figure 69).

Since the rDCs report on the internuclear bond orientation with respect to the static magnetic field, B_0, they are very sensible to changes in the backbone conformation upon complex formation. The measured NH rDCs for the CaM/Munc13-1(459-492) peptide complex were compared to the simulated ones based on the refined NMR structure of free CaM from Chou *et al*., 2001. The correlation plots (Figure 70) showed that the backbone conformation of CaM was not perturbed much upon the binding of the peptide. This is not unexpected, since it is well known that most of the CaM-target interactions are mainly mediated by side chains.

In order to gain insight into the interdomain dynamics of the CaM/Munc13-1 (459-492) peptide complex, a lanthanide-binding paramagnetic tag was attached to the C-terminal domain of CaM through a cysteine mutant (T146C) (Ikegami *et al*., 2003). The paramagnentic alignment mechanism differs from the steric one and therefore it provides non-redundant information. In the paramagnetically aligned sample, the center of alignment is localized to the unpaired electron in the lanthanide ion. For this reason, in a two-domain protein like CaM, the alignment obtained in the domain which does not contain the lanthanide ion is reporting on the motion of this domain with respect to the statically aligned domain.

Bertini *et al*., 2005, reported a reduced alignment tensor by a factor of 10 (axial component) for the C-terminal domain of CaM when the N-terminal domain of CaM was paramagnetically aligned using the metal binding site of CaM with a bound Tb^{3+} ion. In this study, for the CaM/Munc13-1 (459-492) peptide complex, a reduced alignment tensor by a factor of ~5 was observed (The correlation plots are shown in Figure 71).

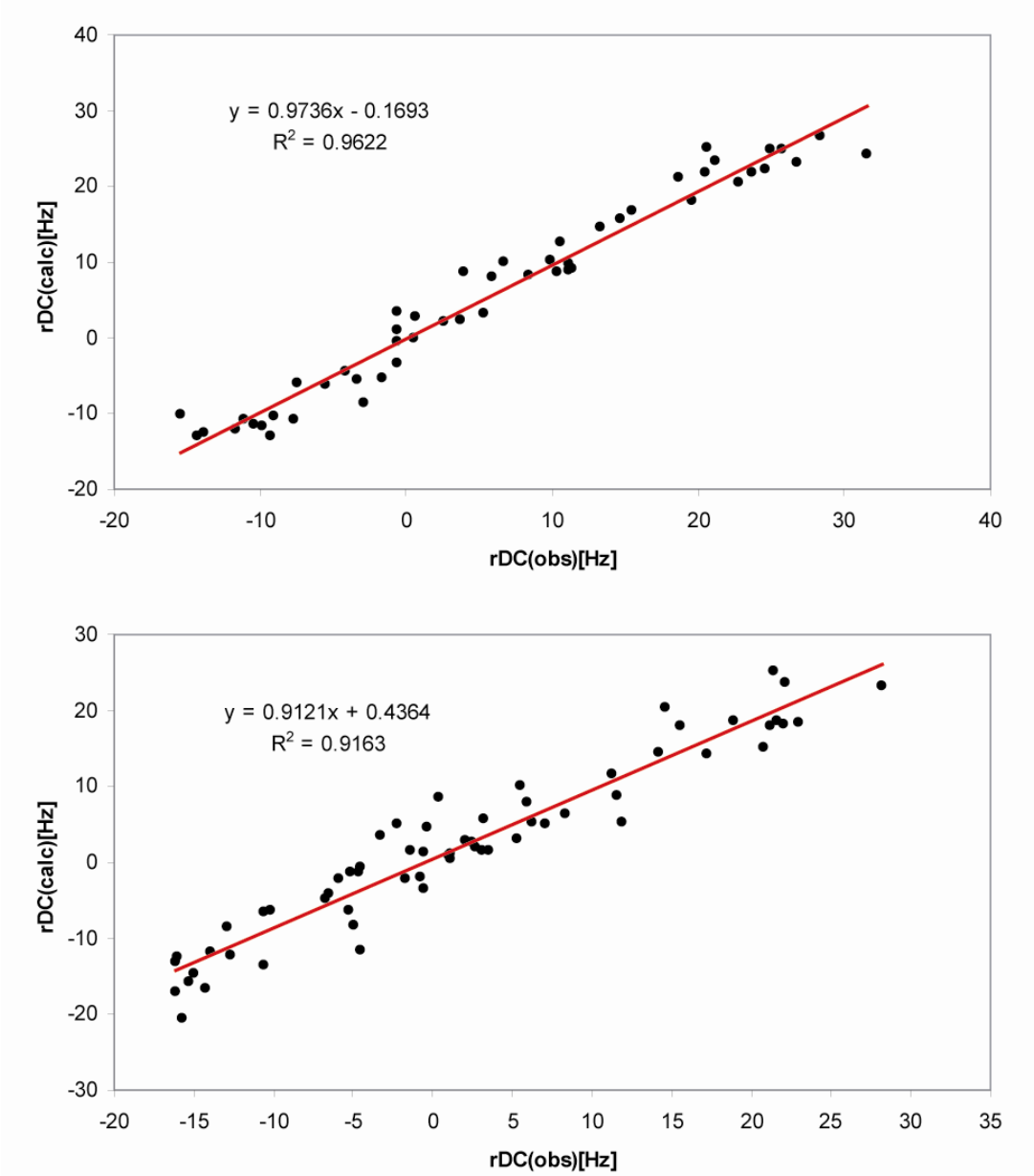

Figure 70. Correlation plots for the measured NH residual dipolar couplings of the ^{15}N CaM/Munc13-1(459-492) peptide complex aligned sterically with Pf1 cosolvent against back-calculated rDCs from free CaM NMR structure. Upper plot, N-terminal domain of CaM; lower plot, C-terminal domain of CaM.

Thus, this gave an experimental proof that this complex experiences inter-domain dynamics in the sub-millisecond time scale. However, it appeared to have lesser degrees of freedom than free CaM. This is intuitive, since the complex consists of a bipartite interaction, where the C-terminal domain of CaM binds to the amphiphilic α-helix of the peptide and the N-terminal domain of CaM binds to the C-terminal hydrophobic tail of the peptide.

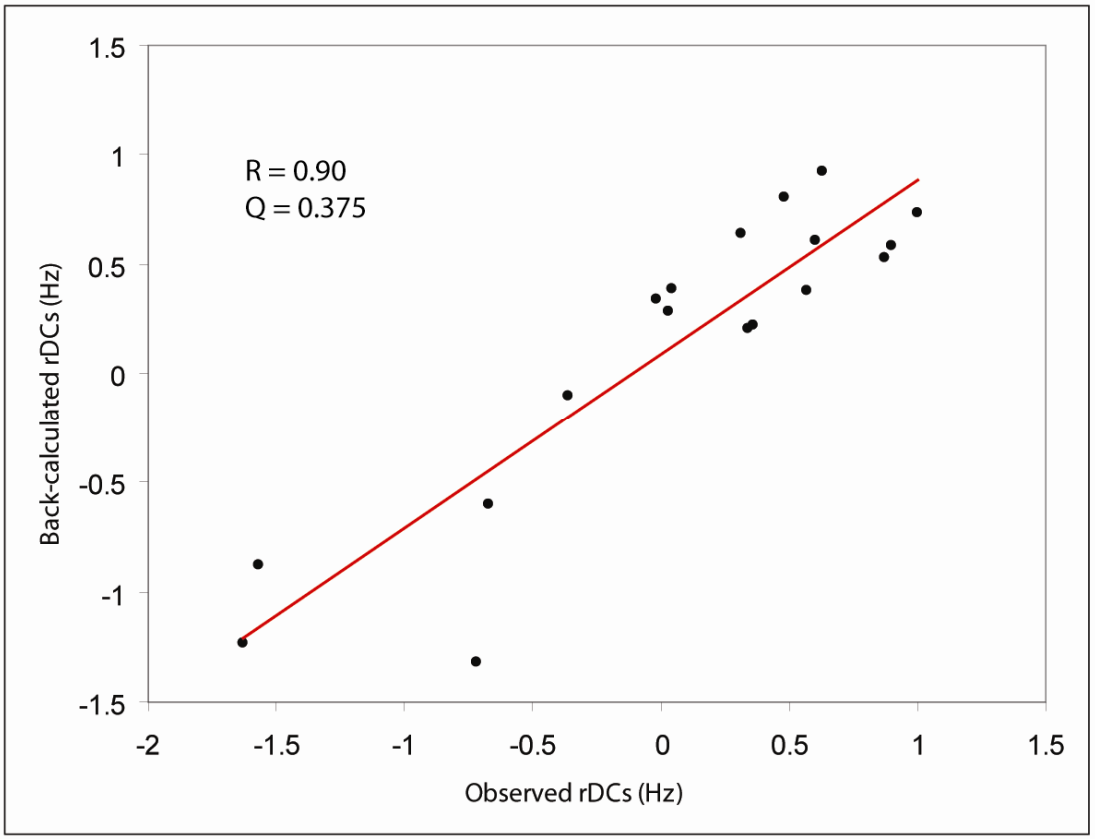

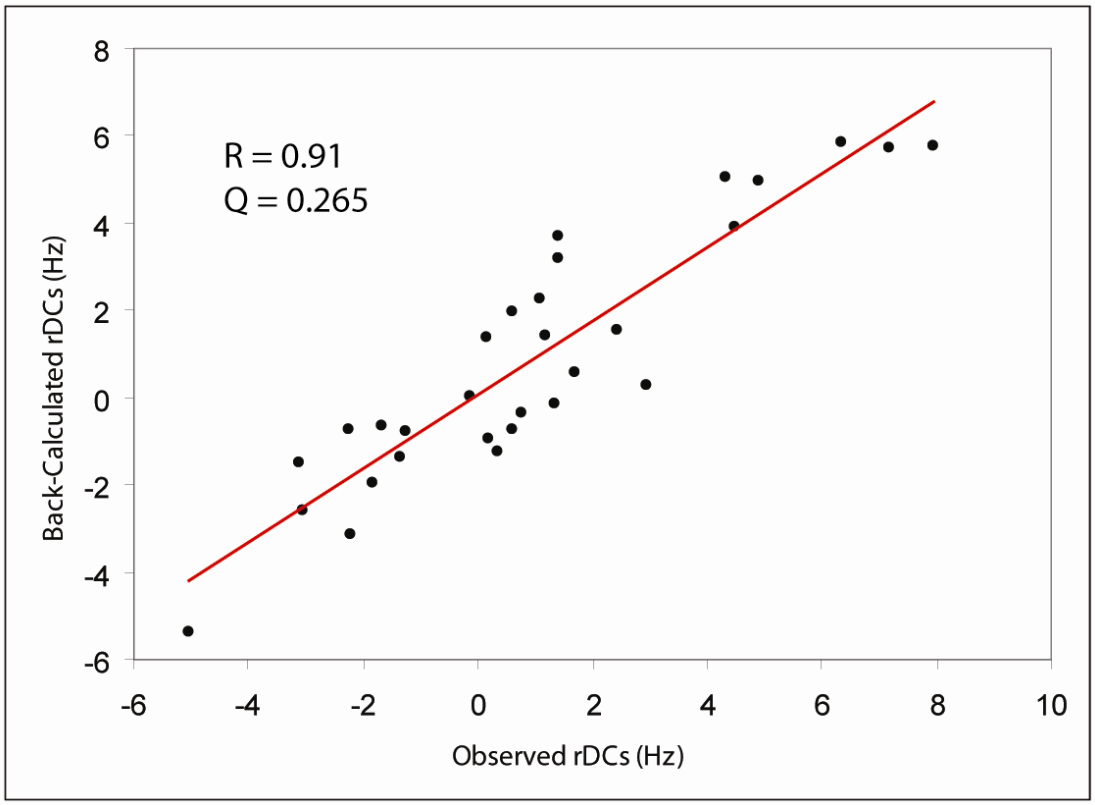

Figure 71. Paramagnetic alignment of the ^{15}N CaM/Munc13-1(459-492) peptide complex with an EDTA-based lanthanide binding tag attached to a cysteine mutant of CaM (T146C). Upper plot: Experimental rDCs correlated against the simulated rDCc from the NMR structure of the N-terminal domain of CaM; Lower plot: Experimental rDCs correlated against the simulated rDCc from the NMR structure of the C-terminal domain of CaM.

Since the chemical shift is sensitive to the environment of each nucleus, it was early recognized (Wishart and Sykes, 1994) that the nuclei in the different secondary structure elements experience environment effects that can be predicted. The difference of the observed chemical shifts for the Hα, Cα and C'resonances in the structured protein to the random-coil chemical shift values are known as secondary chemical shifts. The measured secondary chemical shifts for the $^{13}C,^{15}N$ CaM/ Munc13-1 (459-492) complex predicted very well the secondary structure elements of CaM (See Figure 72). All secondary structure elements of CaM were preserved upon peptide binding; this is in agreement with the rDC analysis discussed above.

For the CaM bound $^{13}C,^{15}N$ Munc13-1 (457-492) peptide, the secondary chemical shift plot (Figure 73) predicted a single α-helix in the N-terminal part of the peptide. This is in agreement with the amphiphilic α-helix binding model of CaM targets.

The total number of NOE constraints is shown in Figure 74 and the NOE contacts along the polypeptide sequence are summarized in Figure 75. The contact map gave a picture on the long-range contacts (*i.e.*, the tertiary structure) of this protein-peptide complex. From the diagram it was evident that both domains of CaM are independent and the Munc13-1 peptide had contacts mainly to the C-terminal domain of CaM. However there were also some contacts from the C-terminal part of the peptide to the N-terminal domain of CaM

Another representation of the NOE contacts consists of horizontal bars with different thickness (Figure 76), representing the cross-peak intensity, between single amino acid residues representing the proton-proton contacts within the secondary structure elements of the polypeptide.

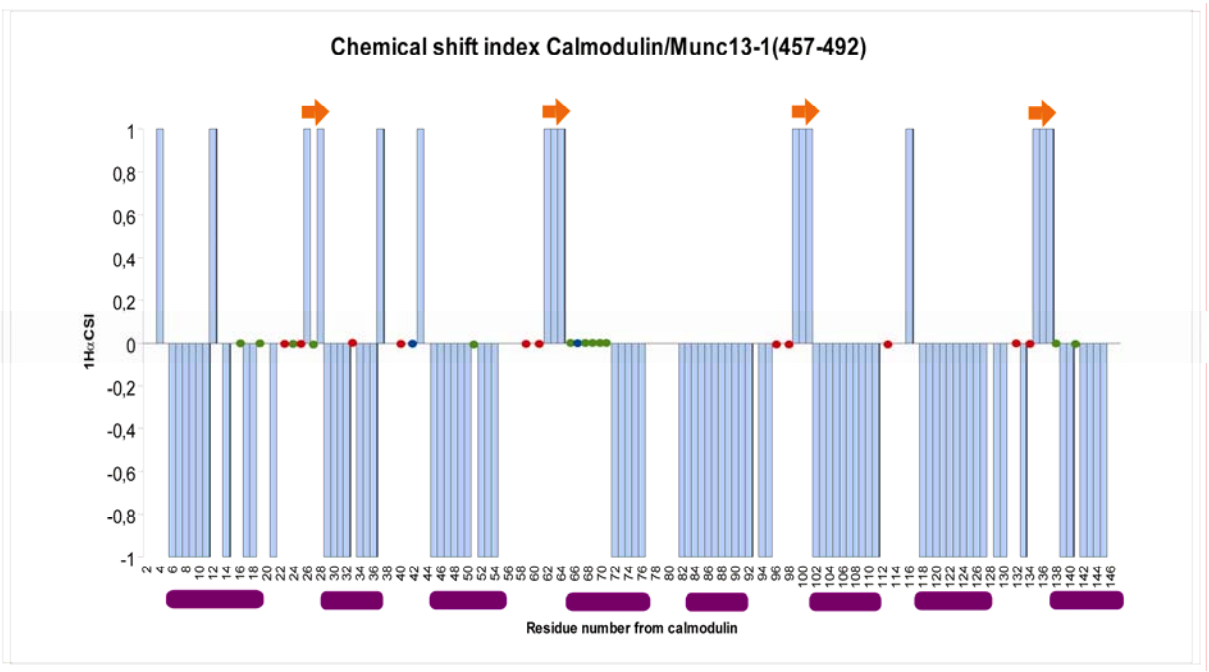

Figure 72. Secondary chemical shift for the Hα resonance of CaM in complex with the Munc13-1(459-492) peptide. The green dots are missing Hα assignments, the red dots are glycines and the blue dots are missing Hα in the residues preceding a proline. The α-helices in CaM are represented by purple bars and the β-sheets by orange arrows.

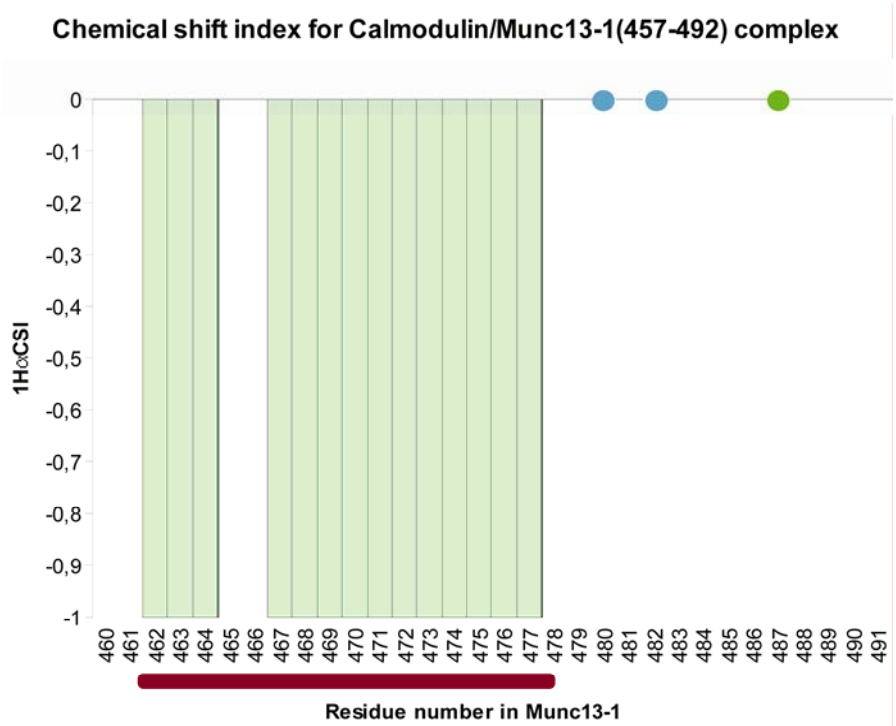

Figure 73. Secondary chemical shift for the Hα resonance of the ^{13}C,^{15}N Munc13-1(457-492) bound to CaM. The blue dots are glycines and the green dot is a missing Hα resonance. The α-helix is found between residues 462-477.

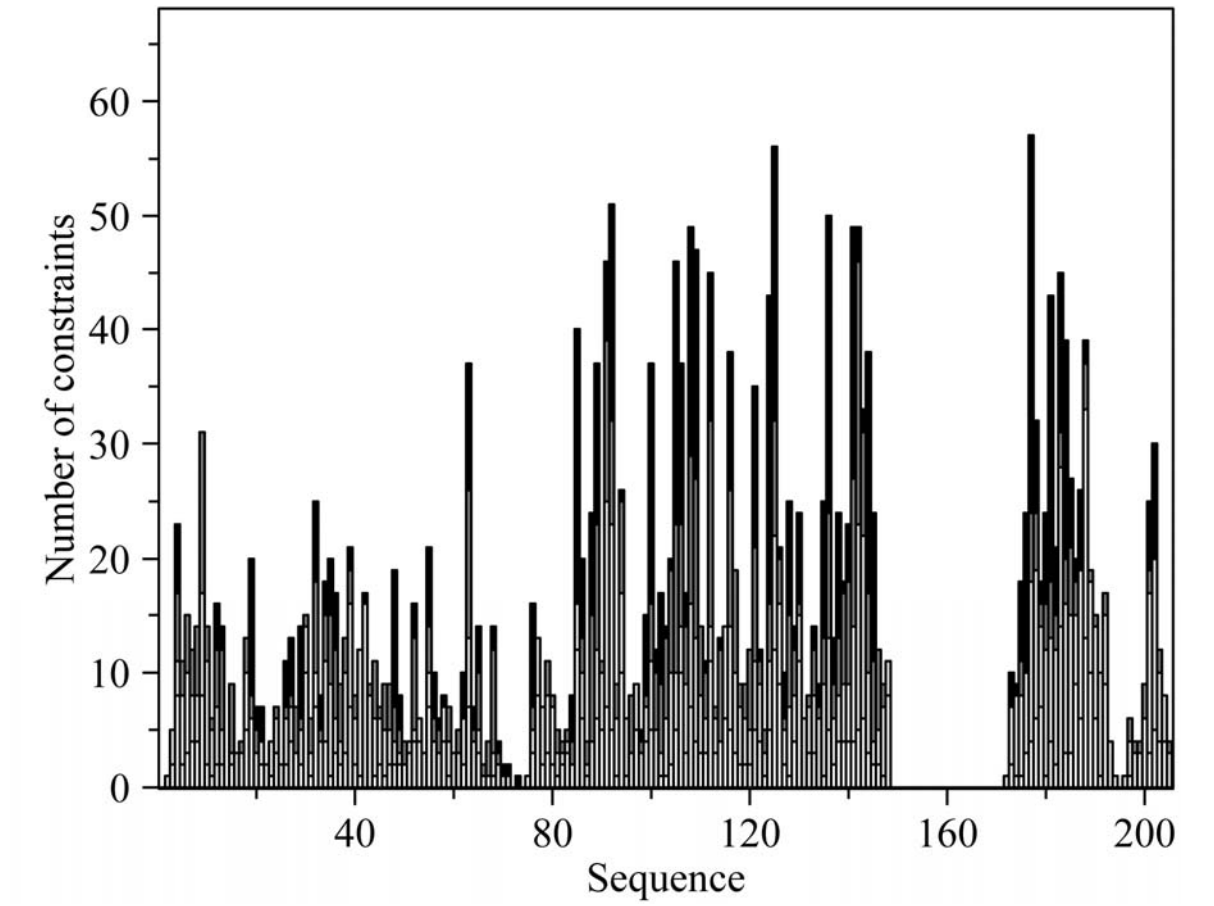

Figure 74. Number of NOE restraints per amino acid residue in CaM and the Munc13-1(457-492) peptide. The white bars represent intra-residue NOEs; the light grey bars, short-range NOEs; the dark grey bars medium-range NOEs; and the black bars long-range NOEs.

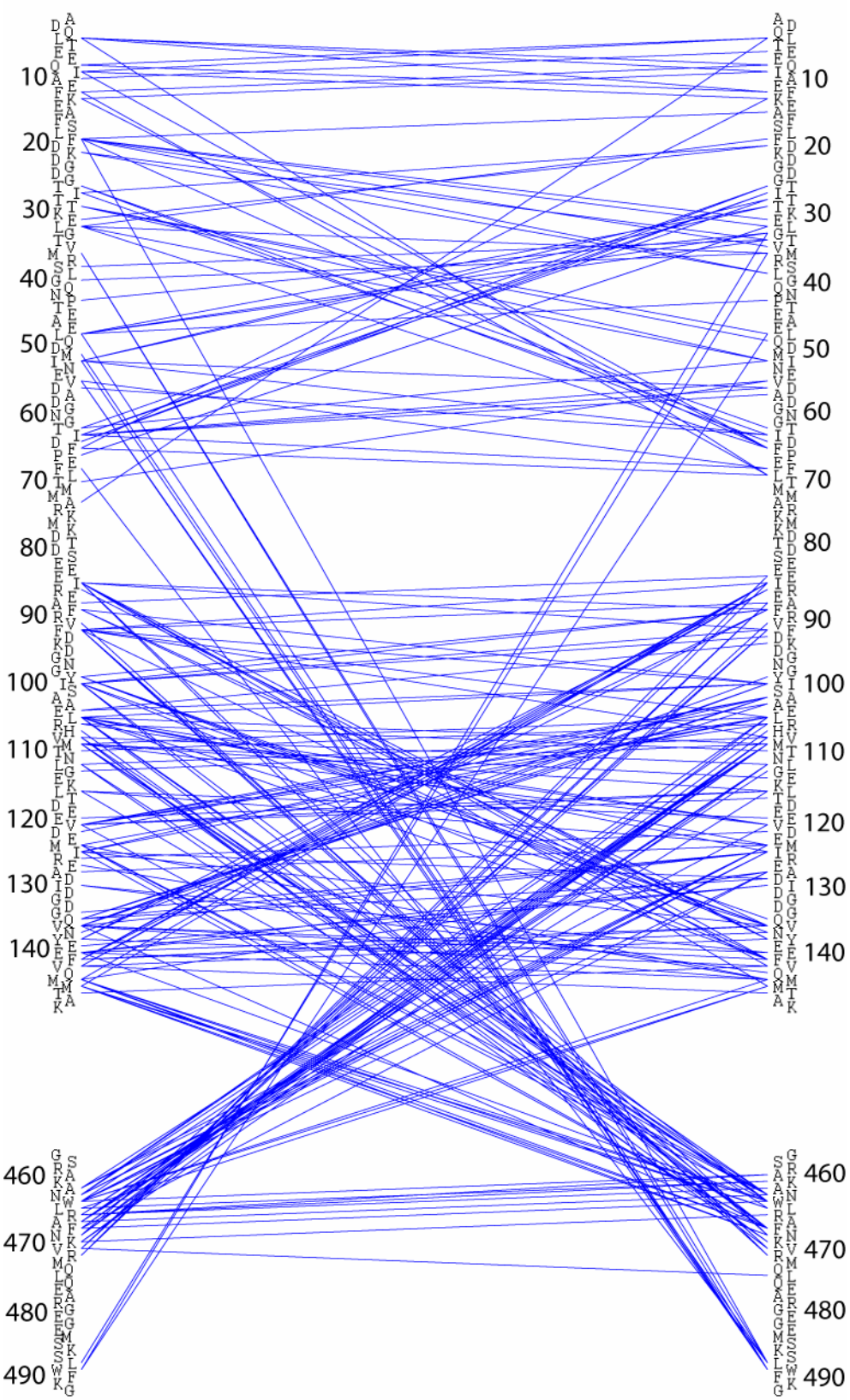

Figure 75. NOE contact map for the CaM/Munc13-1(457-492) peptide complex, these restraints were used for the NMR structure determination of the complex.

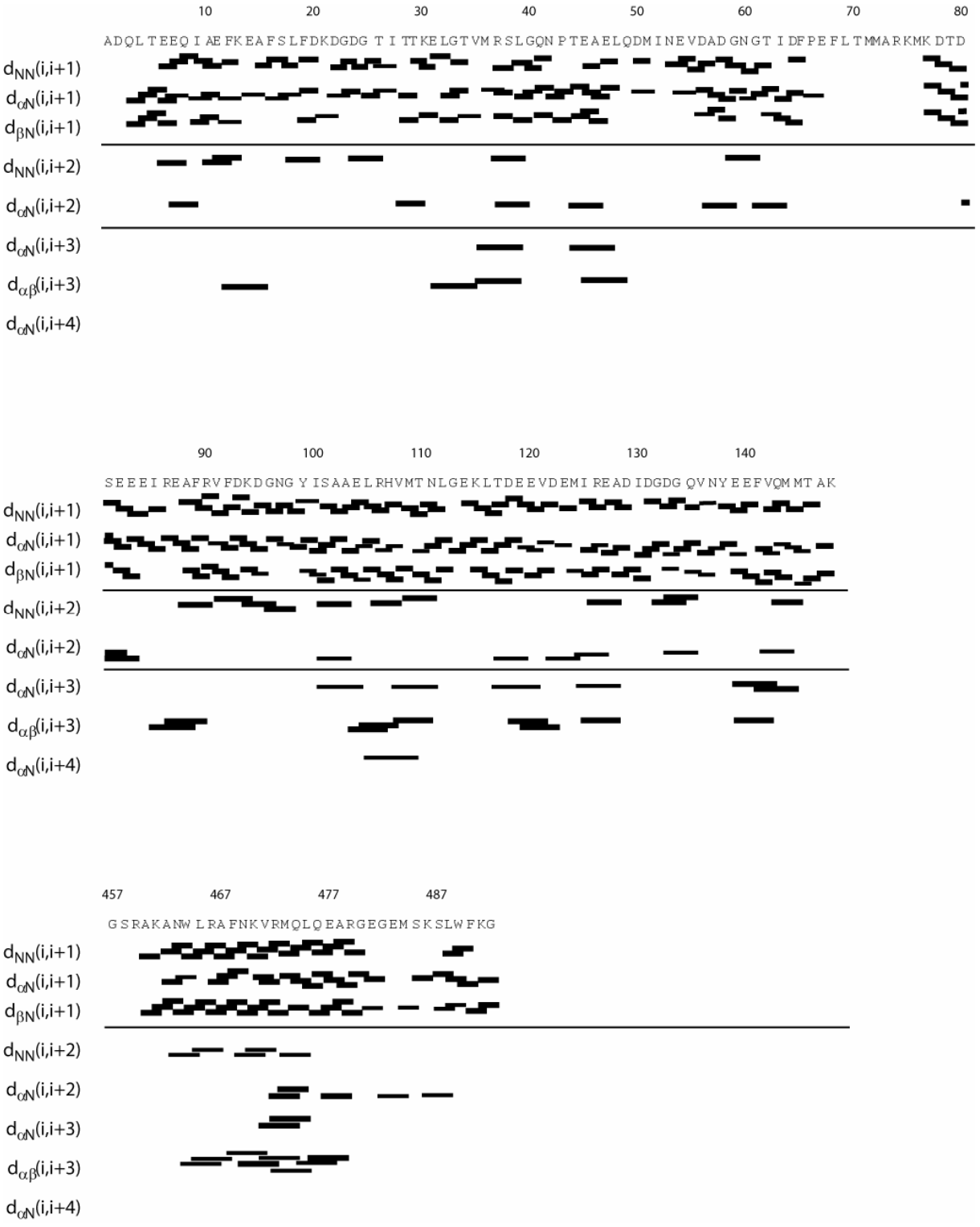

Figure 76. Survey of the sequential and medium range ^{1}H-^{1}H NOEs along the primary sequence of CaM (the first two panels) and the Munc13-1 peptide (457-492) (lowest panel) in the complex.

j. NMR structure determination of the CaM/Munc13-1 (457-492) peptide complex

The 3D structure of CaM has been extensively studied both by X-ray crystallography and NMR; there are numerous structures of the free protein as well as in complex with various interaction partners. The correlation of the NH residual dipolar couplings for the

individual domains of CaM in the complex was not very much perturbed, *i.e.* there is still a high correlation to the free CaM NMR structure. Therefore, the folded individual domains were a good starting point for a structure calculation.

In the literature, no high-resolution structural information on the Munc13-1 (457-492) region was found. Based on the knowledge of the various CaM – peptide interactions described and the studies by Junge *et al*., (2004), it was predicted that the Munc13-1 (457-492) could have an amphiphilic α-helix. In addition, several lines of evidence were found for the α-helical structure of the bound peptide: (a) the Hα secondary chemical shift predicted an α-helix between residues 462 and 477; (b) the phi and psi angles derived from the TALOS restraints also lied in the alpha helical part of the ramachandran plot; (c) the sequential NOEs for the NH and Hα have a α-helix pattern and the rDCs also agreed well with the α-helix model.

The next step was to generate various backbone conformation clusters for the Munc13-1 (457-492) peptide in order to use them for the docking with CaM(see Figure 77). The clusters were generated with the *Rosetta* program, based on the secondary structure prediction from PSI, the NH NOEs and the NH rDCs. In essence, all of the clusters predicted a α-helical structure; they differed just in the length of the α-helix. For the docking of the CaM/munc13-1(457-492) interaction based on intermolecular NOEs and rDCs, a cluster that consisted of a α-helix going from residue 461 to residue 478 and a random-coil C-terminal tail was selected. The side-chains were modelled in the program INSIGHT II (*Accelerys, Inc.*) and an energy minimization with the CHARMM force field (Brooks *et al*., 1983) was done in order to avoid steric clashes among the side-chains.

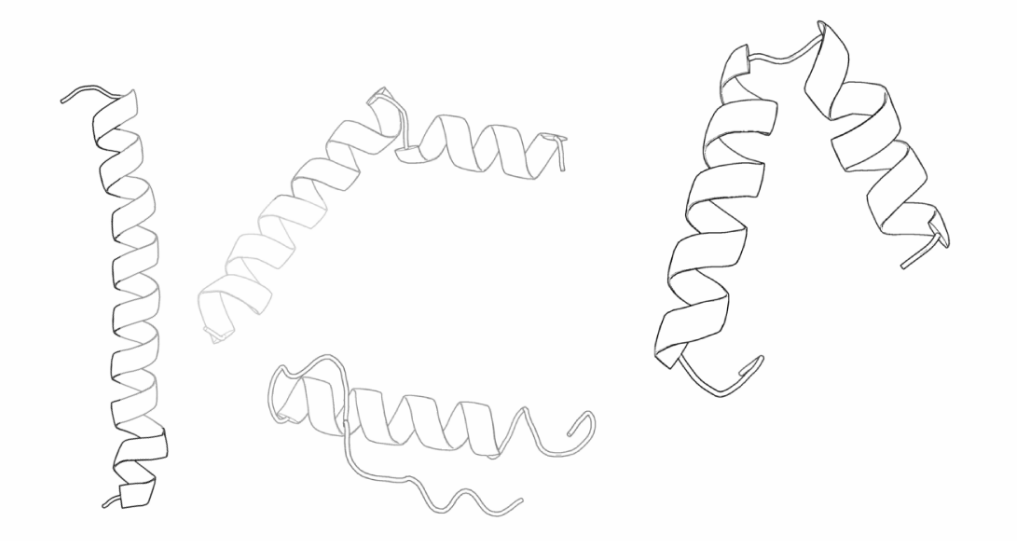

Figure 77. Different models for the backbone conformation of the Munc13-1(457-492) peptide based on NOE, NH residual dipolar couplings and chemical shift derived dihedral angles restraints from Rosetta program. The conformation on the lower part was used for the docking.

The docking protocol consisted of a rigid body minimization using a target function comprising only three terms, the experimental NOE-derived intermolecular interproton distances, the dipolar coupling restraints, and a simple intermolecular van der Waals repulsion potential (Clore, 2000). The restraints used were 35 intermolecular NOEs, and 31 NH rDCs for C-terminal domain of CaM and 14 rDCs for the bound Munc13-1 (457-492) peptide. The docking gave a first view of the complex between CaM and Munc13-1 (457-492) (Figure 78). This docked structure was used as a starting point for the structure calculation based on CYANA.

Automated NOESY assignment replaces the most time-consuming part of the interactive spectral analysis by a fast computational method and has thus significantly enhanced the overall efficiency of NMR structure determination (Jee and Güntert, 2003). A limiting factor for the application of these automated NOE assignment procedures is that they rely on the availability of an essentially complete list of chemical shifts from the preceding sequence-specific resonance assignment. For reliable automated NOESY assignment with the CANDID algorithm around 90% completeness of the chemical shift assignment is necessary, whereas the algorithm is remarkably tolerant with respect to incomplete NOESY peak picking. Another important pint is that the backbone root mean square deviation (RMSD) to the mean for the structure bundle of cycle 1 is below 3 Å.

Figure 78. Model of the CaM/Munc13-1 docked structure based on intermolecular NOEs and NH residual dipolar couplings. CaM is shown in green and the Munc13-1(457-492) peptide in blue.

Initially it was attempted to do a structure calculation with full length CaM and the full length Munc13-1 (457-492) peptide; however the results were suboptimal, especially for the N-terminal domain of CaM (see Figure 79). For this reason, further calculations were done with the two domains of CaM as separate modules interacting with different regions in the Munc13-1 peptide; this approach was also consistent with the bipartite interaction of this complex. An ensemble of structures is shown in Figure 80.

The C-terminal domain of CaM interacts with the amphiphilic α-helix of the Munc13-1 peptide and the hydrophobic anchors consist of the well studied motif 1-5-8 (W-F-V). A view into this hydrophobic pocket is shown in Figure 81.

For the N-terminal domain of CaM, the interaction with the C-terminal tail of the Munc13-1 peptide was found to be reduced to a hydrophobic motif L488 and W489 (see Figure 82). The interaction appeared to have a smaller surface area than in the case of the C-terminal domain of CaM.

After the structure calculation was optimized, the structures were refined with NH rDCs and their energy was minimized in explicit solvent. The ramachandran plot for the best structures is shown in Figure 83. In addition, the structure was analyzed by the PROCHECK-NMR program (Laskowski *et al*., 1996) and the structure statistics are shown in table 5.

The EF-hand domains in CaM show the ability to occupy different conformations depending on the environment, *i.e*., on the presence or absence of bound calcium ions and/or target proteins. As each EF-Hand motif as a helix-loop-helix structure, the interhelical angles have been proposed as structural parameters. All structural analyses on EF-Hand domains

suggest that a continuum of conformational states is occurring within the whole EF-Hand protein superfamily. In Table 6, the six-interhelical angles for the N- and C- terminal domains of the CaM/Munc13-1(457-492) peptide complex are compared with other ligated EF-hand states (taken from Babini *et al*., 2005). The model used for measuring the interhelical angles is shown in Figure 84.

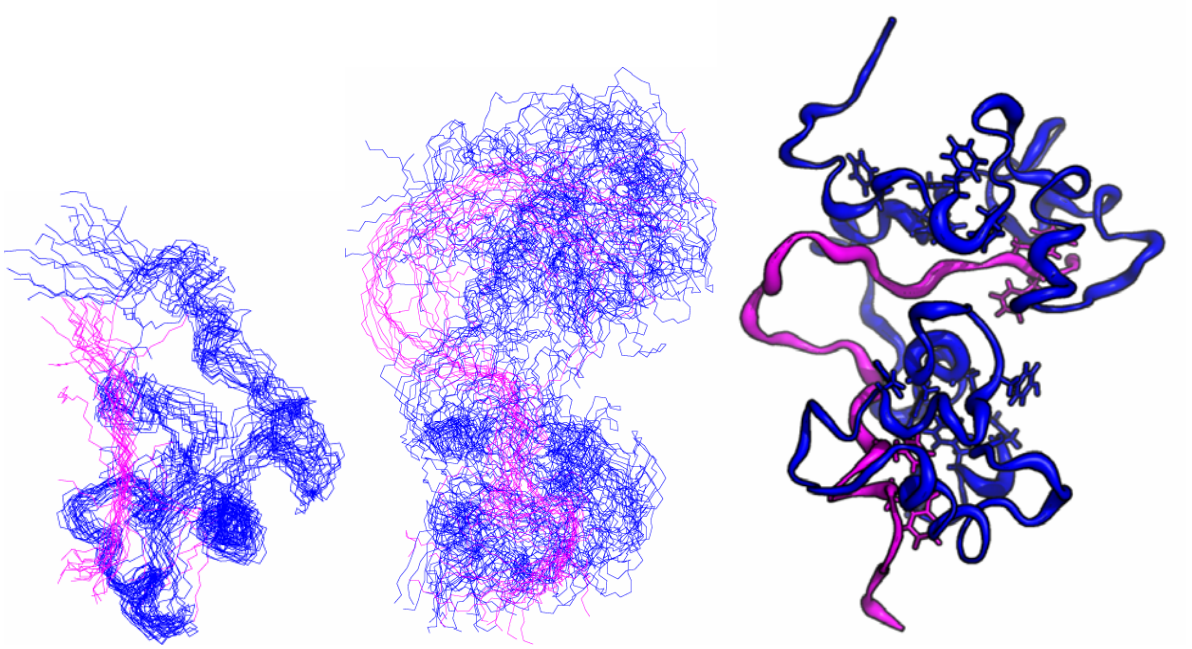

Figure 79. Ensemble of 20 structures for the CaM/Munc13-1(457-492) peptide complex calculated with CYANA using the full-length CaM and peptide restraints. On the left, the N-terminal domain was aligned. On the center, the whole complex is shown and on the right side a cartoon representation of the whole complex is shown, CaM (blue), peptide (magenta).

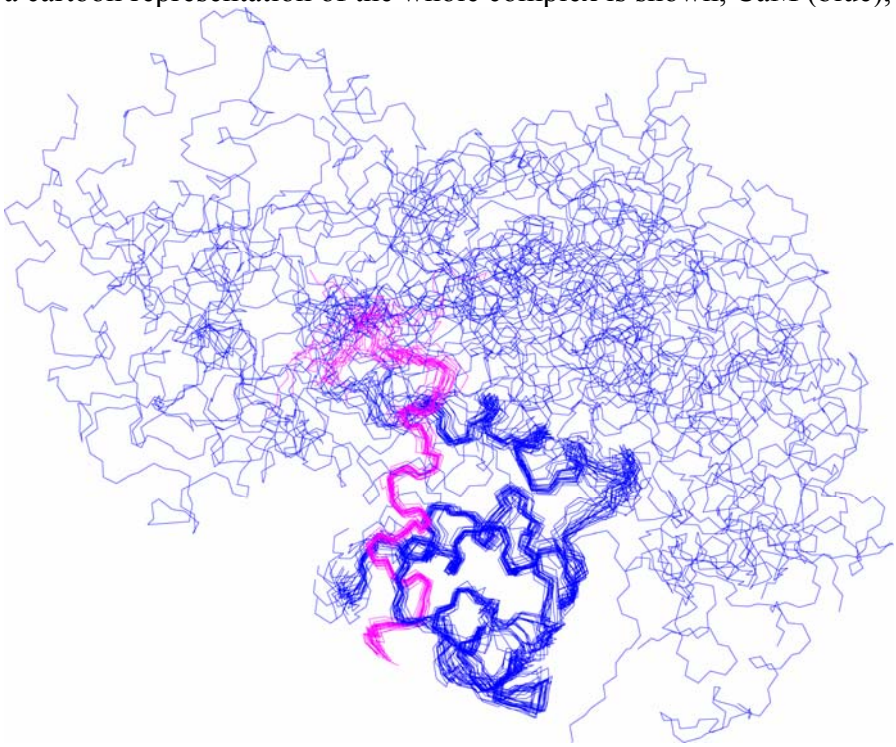

Figure 80. Ensemble of 20 structures of the CaM/Munc13-1 (457-492) peptide complex calculated with the C-terminal domain distance constraints for CaM and full-length distance constraints for the peptide in CYANA. CaM is shown in blue and the Munc13-1 (457-492) peptide is shown in magenta.

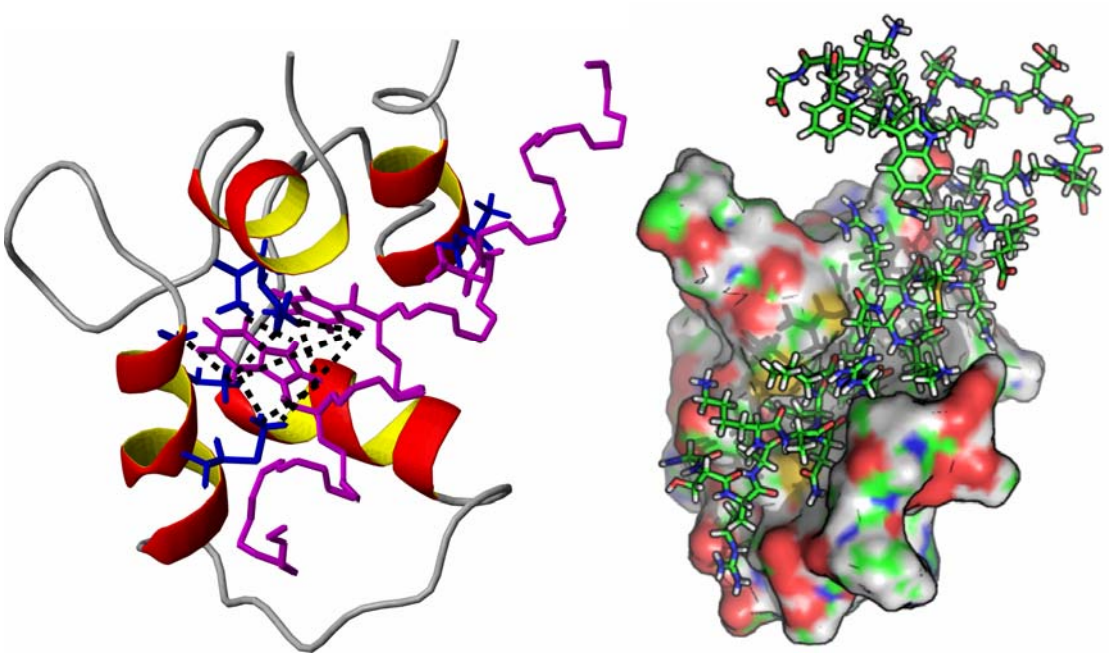

Figure 81. Ribbon (left) and surface (right) representation of the C-terminal domain of CaM bound to the N-terminal amphiphilic α-helix of the Munc13-1 (457-492) peptide in magenta. Some of the side-chain contacts derived from intermolecular NOEs between CaM and the hydrophobic anchors W464 and F468 of Munc13-1 are shown with dotted lines

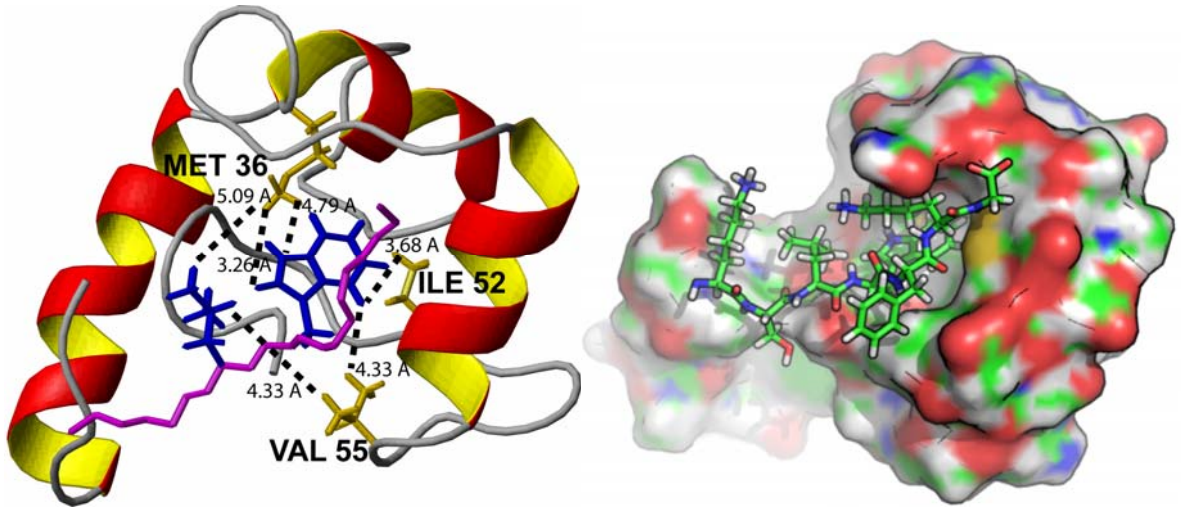

Figure 82. Ribbon (on the left) and surface (on the right) representations for the N-terminal domain of CaM bound to the C-terminal part of the Munc13-1 (457-492) peptide in magenta. Some of the side-chain contacts derived from intermolecular NOEs between CaM and the hydrophobic L488, W489 motif of Munc13-1 are shown with dotted lines and the distance in Å is also depicted.

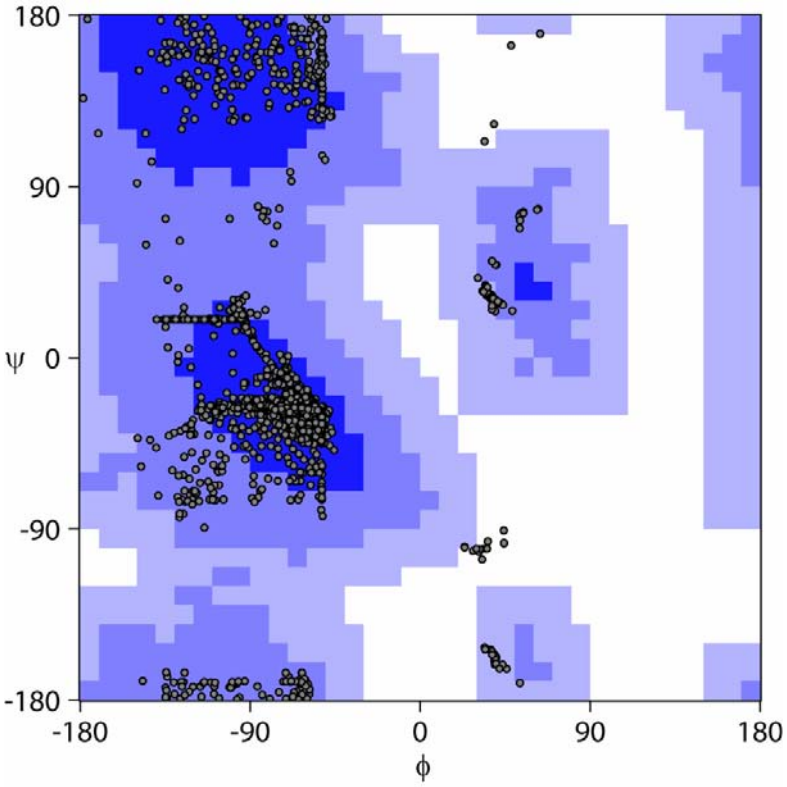

Figure 83. Ramachandran plot of the ensemble of 20 structures of the CaM/Munc13-1(457-492) peptide complex.

Table 5. Summary of the structure statistics for the NMR solution structure of the CaM/Munc13-1 (457-492) peptide complex.

Number of experimental restraints	2102 (11.4 restraints/residue)	
Distance restraints from NOEs	1758 (9.6 restraints/residue)	
CaM	1494	
M36	184	
CaM-M36	80	
Dihedral angle restraints (CaM)	168	
Hydrogen bond restraints	39	
CaM	30	
M36	9	
H-N residual dipolar couplings	137	
CaM	113	
M36	24	
Ramachandran analysis of CaM-M36		
Residues in favored regions (%)	89.4	
Residues in additional allowed regions (%)	9.05	
Residues in generously allowed regions (%)	1.55	
Residues in disallowed regions (%)	0.0	
Coordinate precision (Å)	**Backbone**	**All heavy-atoms**
CaM, residues 5-70, 84-146	0.52 ± 0.12	0.93 ± 0.12
M36, residues 4-21	0.41 ± 0.52	0.97 ± 0.51
CaM-M36, residues 5-70, 84-146, 4-21	0.46 ± 0.32	0.95 ± 0.32

Table 6. Comparison of the interhelical angles for the CaM/Munc13-1(457-492) peptide complex and previous high resolution CaM structures with different EF-hand states

EF-hand domain	I-II angle	I-III angle	I-IV angle	II-III angle	II-IV angle	III-IV angle
ApoCdom	124/135	65/77	140/160	140/150	30/50	125/140
ApoCdom +peptide	99	113	153	141	64	90
holoCdom	94/113	130/150	102/130	105/125	30/50	83/104
holoCdom +peptide	83/112	130/150	104/132	110/140	34/81	70/104
holoCdom +munc13-1	99	156	119	102	43	84
ApoNdom	132/145	75/89	124/132	117/130	50/60	128/145
ApoNdom +peptide	130/135	94/102	130/138	108/113	50/57	122/127
holoNdom	70/110	130/155	100/125	110/135	28/54	80/100
holoNdom +peptide	73/102	140/160	104/123	110/123	38/72	67/105
holoNdom +munc13-1	85	157	120	112	42	83

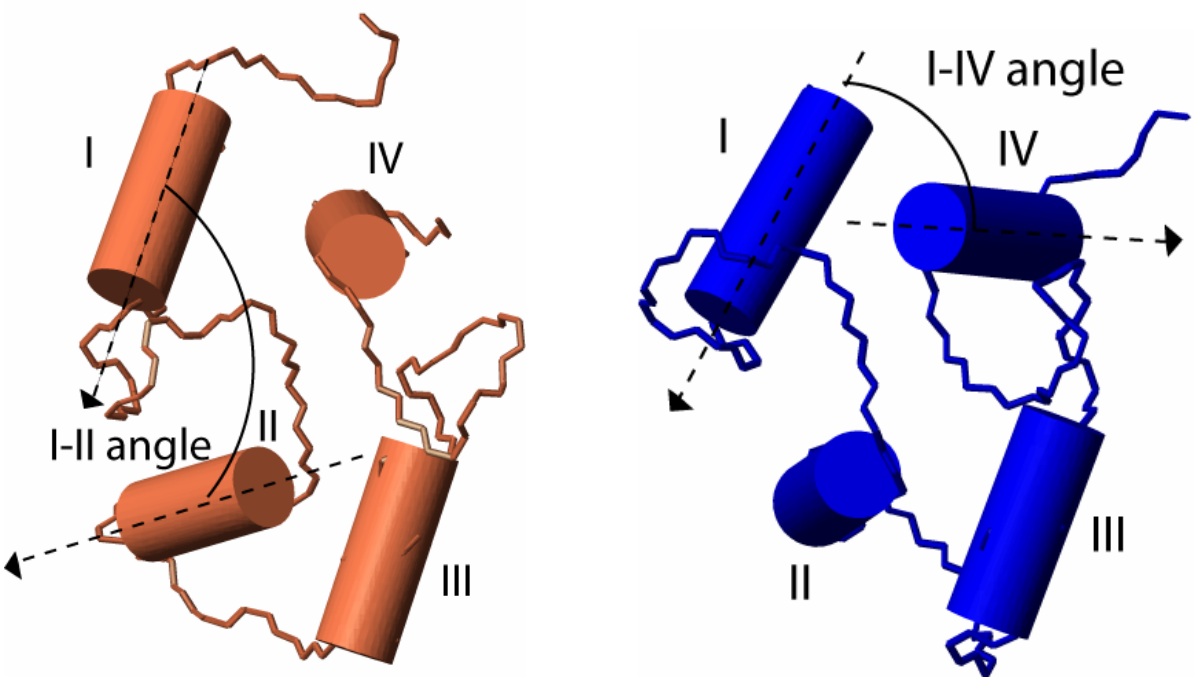

Figure 84. On the left is the N-terminal domain of CaM/Munc13-1 (457-492) peptide complex with its α-helices represented as cylinders for measuring the interhelical angles. On the right, the C-terminal domain of the complex is shown in blue.

The CaM/Munc13-1(457-492) peptide complex structure was overlaid with other high-resolution CaM structures in order to determine how well defined was the structure obtained. The backbone of the C-terminal domain region (84-146) was aligned to 10 different structures and the RMSD varied between 2.05 and 2.65 Å; two of the aligned structures are shown in Figure 85.

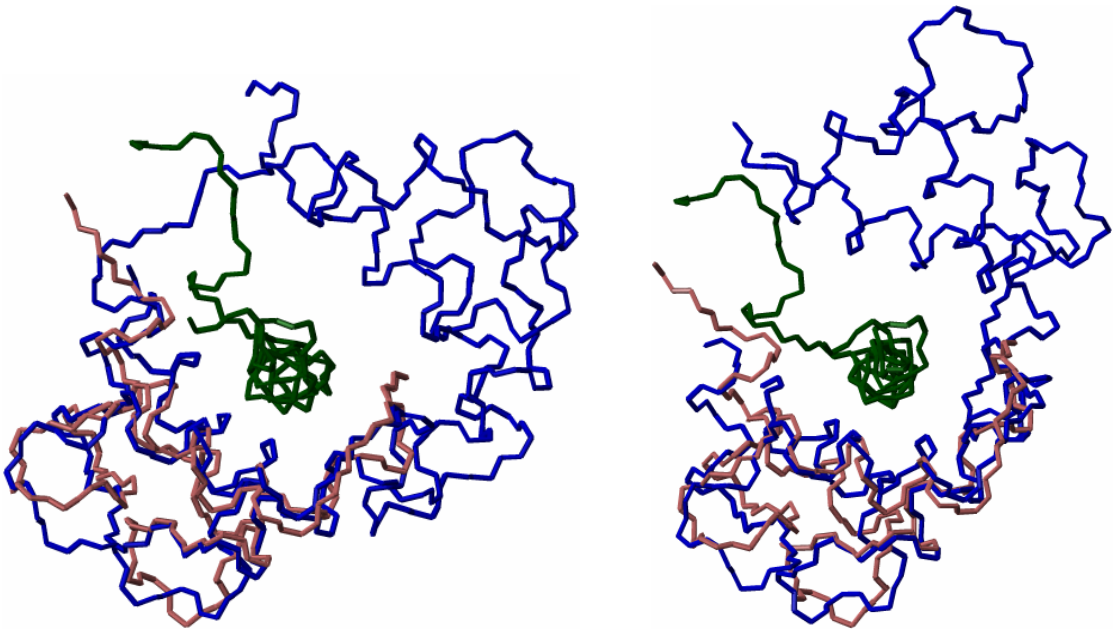

Figure 85. On the left is the overlaid C-terminal domain of CaM/Munc13-1(457-492) peptide complex structure with the CaM/smMLCK peptide complex (1CDL.pdb) and on the right with the CaM/CaMKII peptide complex (1CDM.pdb). The CaM C-domain in the CaM/Munc13-1 peptide complex is shown in light brown and the peptide in green. The full CaM backbone structure is shown for the other complexes in blue.

The backbone of the N-terminal domain region (4-70) was aligned to 9 different high-resolution CaM structures and the RMSD varied between 2.40 and 3.24 Å; two of the aligned structures are shown in Figure 86.

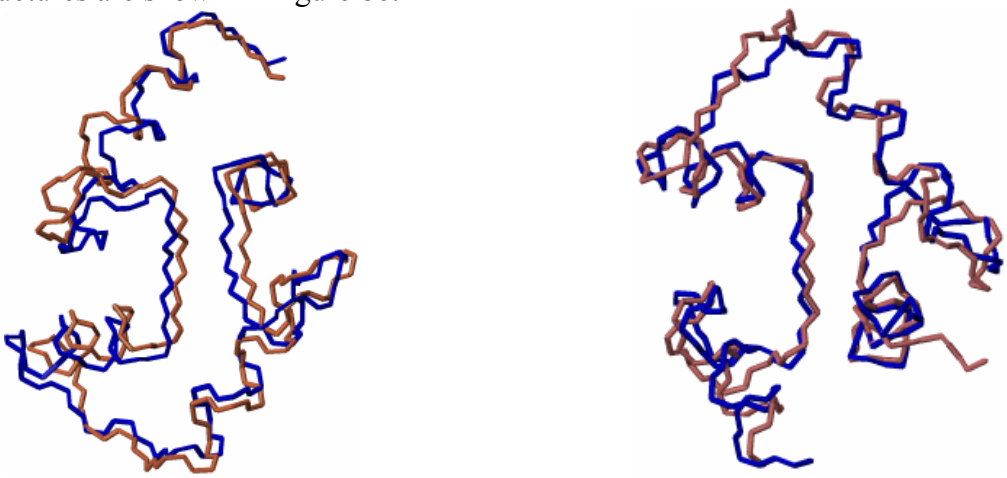

Figure 86. On the left is the overlaid N-terminal domain of the CaM/Munc13-1(457-492) peptide complex structure with the CaM/CaMKII (1CDM.pdb); and on the right overlaid with the free N-terminal domain NMR structure of CaM (1J7O.pdb). The CaM N-domain in the CaM/Munc13-1 peptide complex is shown in light brown and for the other models in blue.

k. Dynamic studies of CaM in its various activated states with paramagnetic alignment

CaM is a paradigm for multidomain proteins; it is well-recognized that interdomain orientation and dynamics play an important role in protein-protein interactions for multidomain proteins. Thus, the investigation of the interdomain dynamics at different activated states on this model system could shed light on different basic mechanisms governing macromolecular interactions of multidomain proteins.

The advantages of studying multidomain proteins with NMR in solution is the possibility to have access both to atomic resolution information as well as dynamic information in the time-averaged ensemble of molecules studied with this spectroscopic technique. In contrast, X-ray crystallography is a very robust method for obtaining atomic resolution models of a macromolecule within a crystalline lattice, but lacks large-time scale dynamic information like interdomain motions, which are from a mechanistically point of view, of essential importance in macromolecular interactions. Other spectroscopic techniques, like fluorescence spectroscopy, lack the atomic resolution that NMR possess.

Previous studies of CaM in its calcium-free (apo) state have revealed a more compact structure compared to its calcium bound (holo) state. The current model is that in average, the N- and C-terminal domains in apoCaM are closer to each other than in the calcium bound state. In this work, using paramagnetic alignment with an EDTA-based tag, it was possible to dissect the differences between the different activated states of CaM based on various paramagnetic restraints.

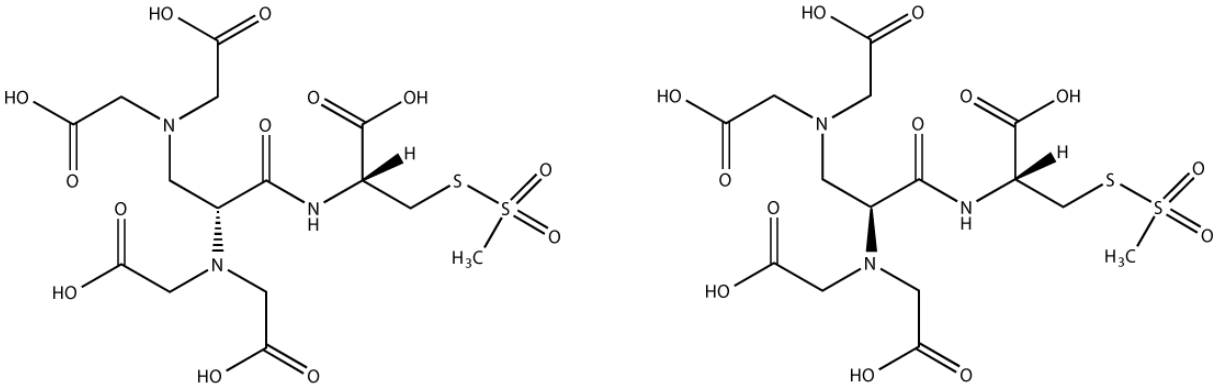

Figure 87. On the left is the tag pk1, N-[(R)-2,3-Bis[di(carboxymethyl)amino]propionyl]-S-mesyl-(R)-cysteine; on the right is the tag pk2, N-[(S)-2,3-Bis[di(carboxymethyl)amino] propionyl]-S-mesyl-(R)-cysteine.

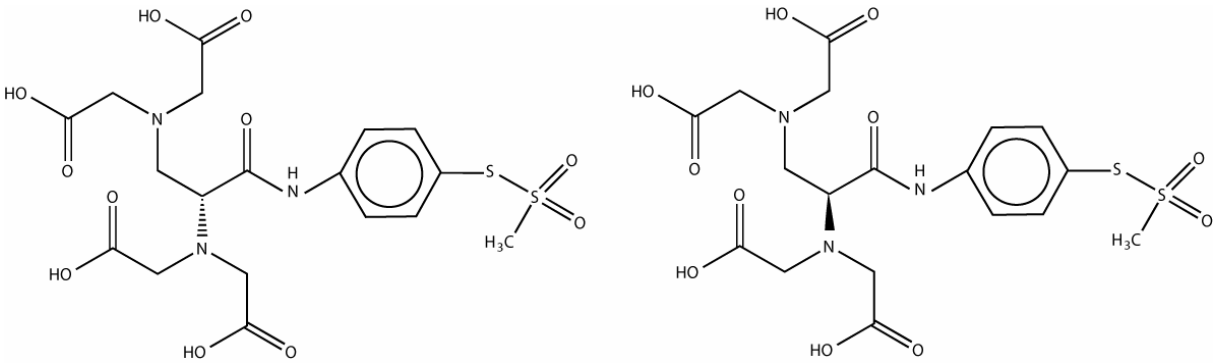

Figure 88. On the left side is the tag t43L, S-[4-[(R)-2,3-bis[di(*tert*-butoxycarbonylmehyl) amino]propionylamino]phenyl]ester; on the right side is the tag t43D, S-[4-[(S)-2,3-bis[di (*tert*-butoxycarbonylmehyl)amino]propionylamino]phenyl]ester.

The molecular structures of the EDTA-based paramagnetic tags used in this study are shown in Figures 87 and 88. They contain a mesyl- moiety which is a good leaving group; therefore they react readily with the thiol group of solvent accessible cysteines in the target protein.

CaM does not have any cysteine residues in its primary sequence; therefore it has to be introduced by site-directed mutagenesis. It is preferable to substitute an amino acid with similar properties like serine or threonine to minimize the risk of changing the folding or properties of CaM.

The studies on apoCaM were done on the S17C mutant. The N-terminal domain was paramagnetically aligned titrating Tb^{3+} (Figure 89) and the effects on the C-terminal domain were analyzed; however as discussed below the alignment tensor could not be measured.

The axial component of the alignment tensor of the N-terminal domain of apoCaM had a magnitude of 3.2 Hz at the 900 MHz spectrometer for the alignment with t43L (see Table 7 for the tensor information on the other alignments). The alignment tensor was well defined (see Figure 90). The measured rDCs on the C-terminal domain were rather small and therefore noisy. For this reason no correlation was found between the experimental data and the simulated data based on the refined NMR structure of apoCaM. However, pseudocontact shift measurements are more precise, establishing a difference between apo- and holo-CaM based on these paramagnetic restraints (See Figure 91).

Table 7. Axial (Da-HN) and Rhombic(Rhomb.) components (apoCaMS17C) of the alignment tensors and angles between them achieved for the four paramagnetic tags bound to Terbium.

Tag1/Tag2	Deg angle	tag	Hz Da-HN	Rhomb.
Pk1/pk2	61	Pk1	6.2	0.5
Pk1/t43L	92	Pk2	2.1	0.43
Pk1/t43D	112	T43D	3.4	0.32
Pk2/t43L	115	T43L	3.2	0.48
Pk2/t43D	106			
T43D/t43L	26			

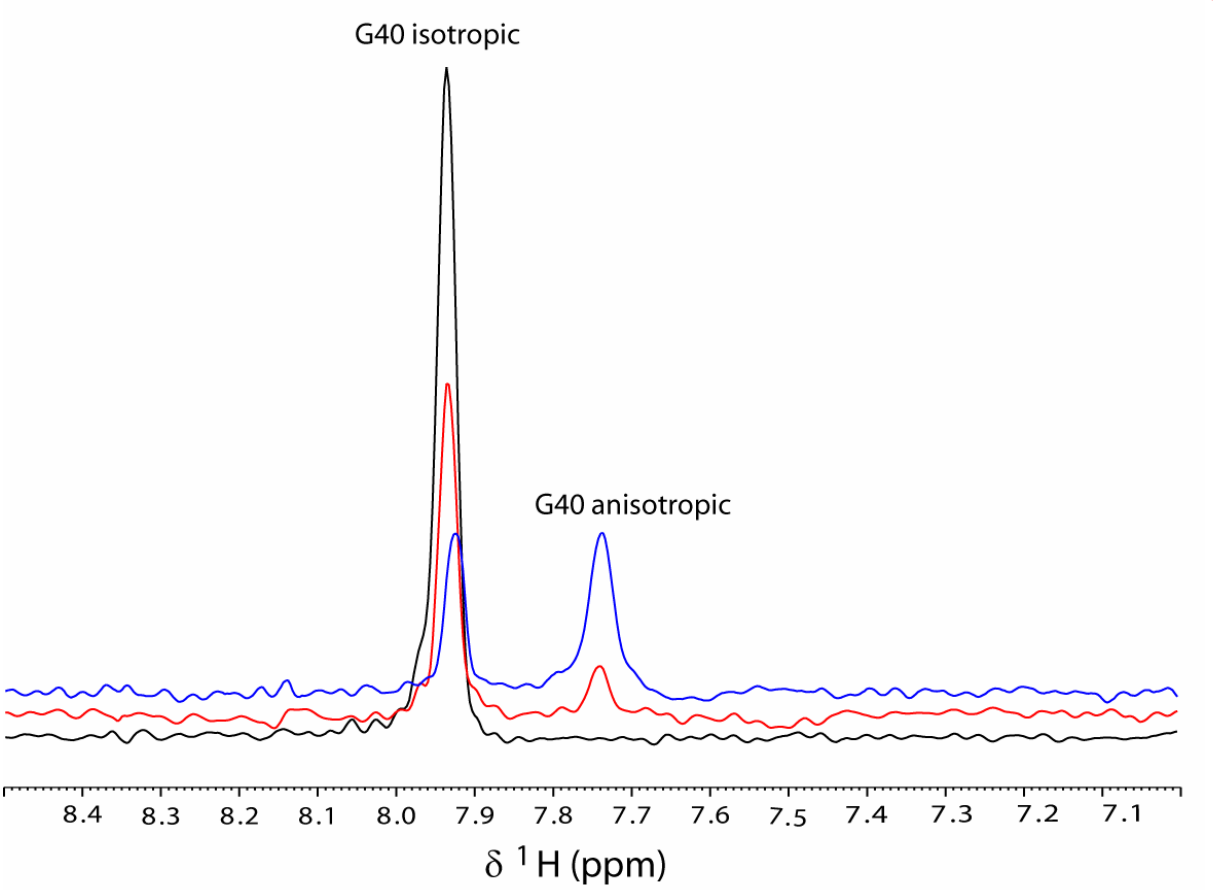

Figure 89. Titration of the apoCaMS17C-t43D with Tb^{3+}. In black is the isotropic spectrum in the absence of lanthanide ion; in red is the protein titrated with 20 % of lanthanide ion and in blue is the protein with 60 % of lanthanide ion.

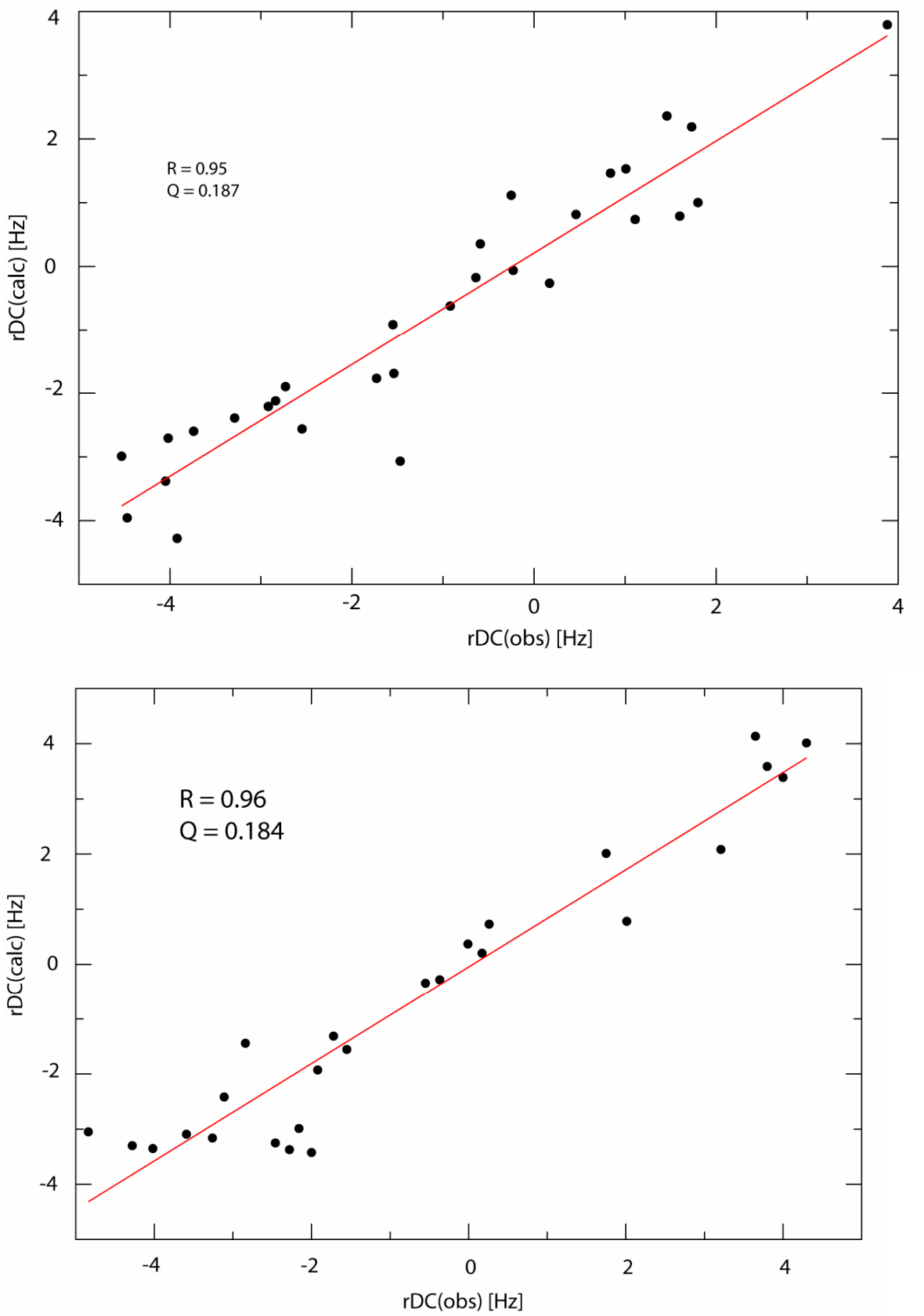

Figure 90. Correlation plot of the measured rDCs for the N-terminal domain of apoCaMS17C-T43D-Tb^{3+} (upper plot) and apoCaMS17C-T43L-Tb^{3+} (lower plot) against the back-calculated rDCs based on the refined NMR structure of apoCaM.

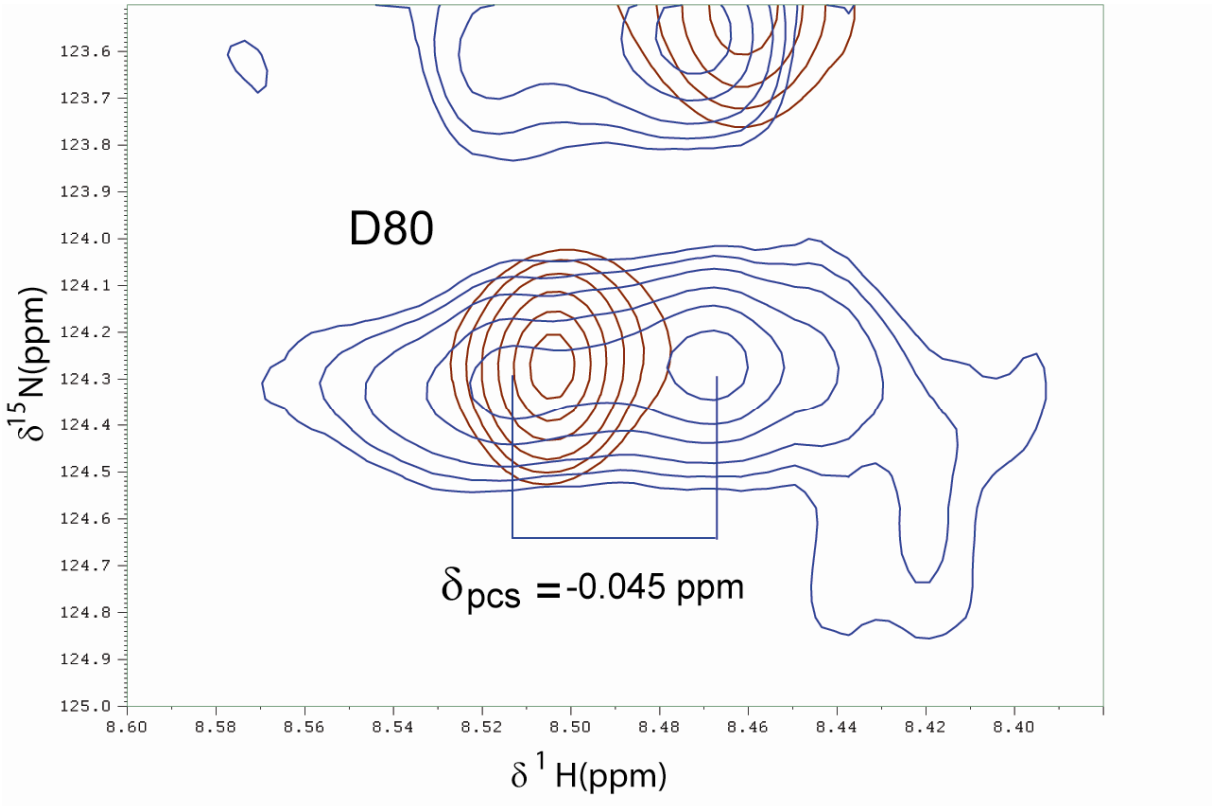

Figure 91. .Overlaid ^{15}N-^{1}H-HSQC spectra for ^{15}N apoCaMS17C-t43L in brown and ^{15}N apoCaM S17C-t43L-Tb^{3+} in blue. In the presence of the lanthanide ion, pseudocontact shifts were observed in the linker region (D80 NH cross-peak is shown) of apoCaM.

The pseudocontact shifts contain translational information (r^3 term) as well as information on orientation with respect to the magnetic field ($(3Cos^2\theta-1)$ term) for the vector between the unpaired electron of the lanthanide ion and the NH bond vector in this case. Thus, the coordinates of the metal ion in the molecular frame of apoCaM (Kubinowa *et al.*, 1995) could be located. The correlation plots between the measured PCS and the back-calculated PCS based on the NMR srtructure of apoCaM for three different tags are shown in Figures 92 and 93. The location of the metal relative to apoCaM is shown in Figure 94.

In Figure 95, the relationship between the metal-amide distances and the measured PCS were analyzed; a power (r^3) function was fitted to the data an upper bound r^3 function was constructed minimizing the values for the angular values in the PCS expression. This analysis allowed the qualitative description of a partial averaging of the PCS residues in the linker region of apoCaM; providing evidence of the existence of interdomain motions in apoCaM in the sub-millisecond time scale.

The interdomain dynamics of holoCaM have been previously studied by T_1 relaxation measurements of NH resonances at different temperatures (Chang *et al.*, 2003); this study provided a model of a cone motion of one domain of CaM relative to the other domain. However, T_1 relaxation measurements have the limitation that they just sense the dynamics on ps to ns time-scale. Therefore it would be interesting to compare these results with interdomain dynamics probed by residual dipolar couplings, which sense motions up to the sub-millisecond time scale. Bertini *et al.*, 2004 reported the paramagnetic alignment of the N-terminal domain of CaM and found a reduction of ~ 10 fold in the axial component of the alignment tensor for the C-terminal domain of CaM, they derived a model in which the C-terminal domain of CaM describes a cone motion with a semiangle of 20°.

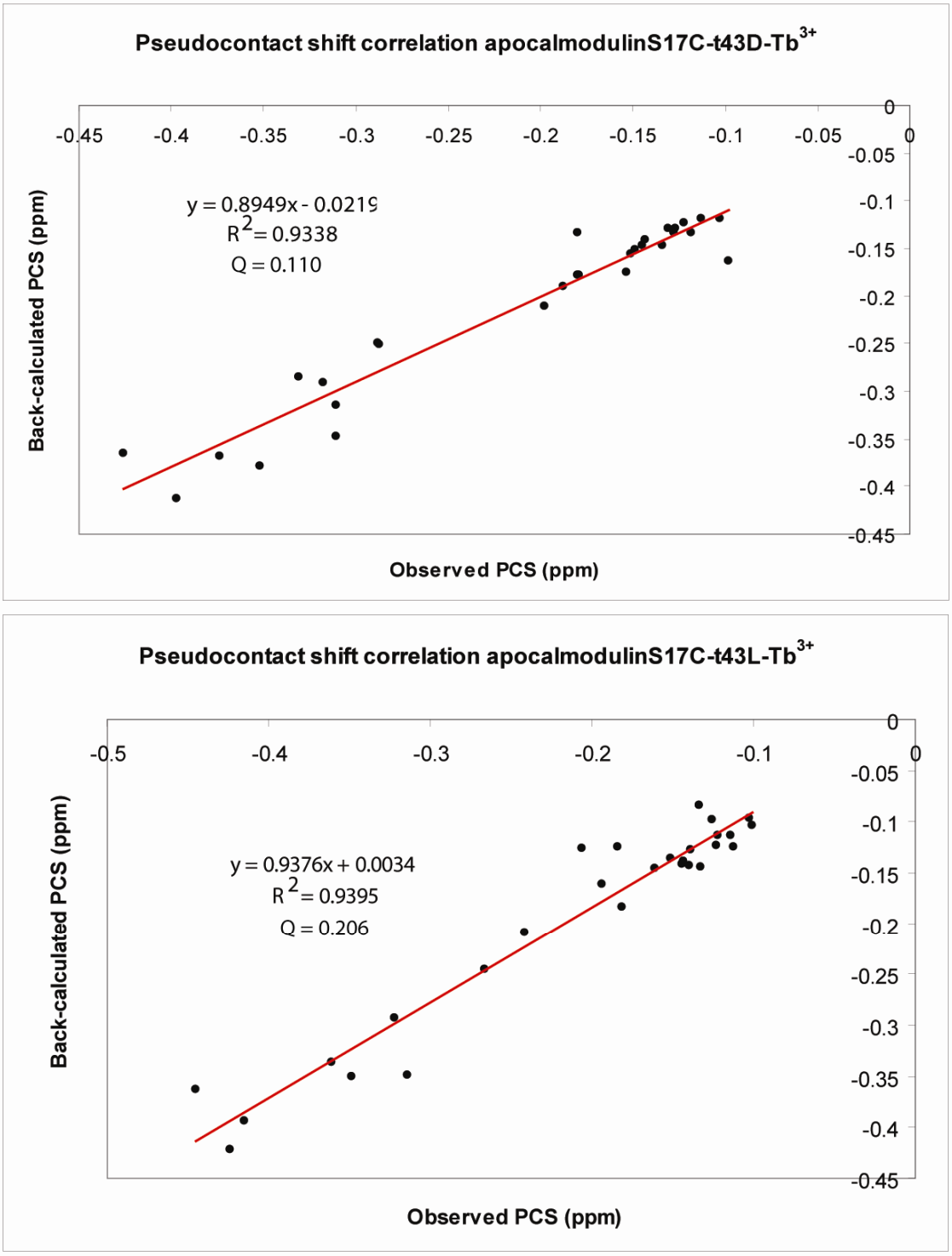

Figure 92. Correlation plot between the measured PCS for apoCaMS17C-t43D-Tb^{3+} (upper plot) and apoCaMS17C-t43L-Tb^{3+} (lower plot) against the back-calculated PCS based on the NMR structure of the N-terminal domain of apoCaM.

In this thesis, it was possible to establish a difference in the interdomain dynamics between holoCaM and the CaM/C20W peptide complex from the plasma membrane calcium channel based on paramagnetic derived rDCs. A previous study based on small angle X-ray scattering measurements established a significant difference in the radius of gyration of holoCaM and the CaM/C20W complex (Kataoka *et al.*, 1991).

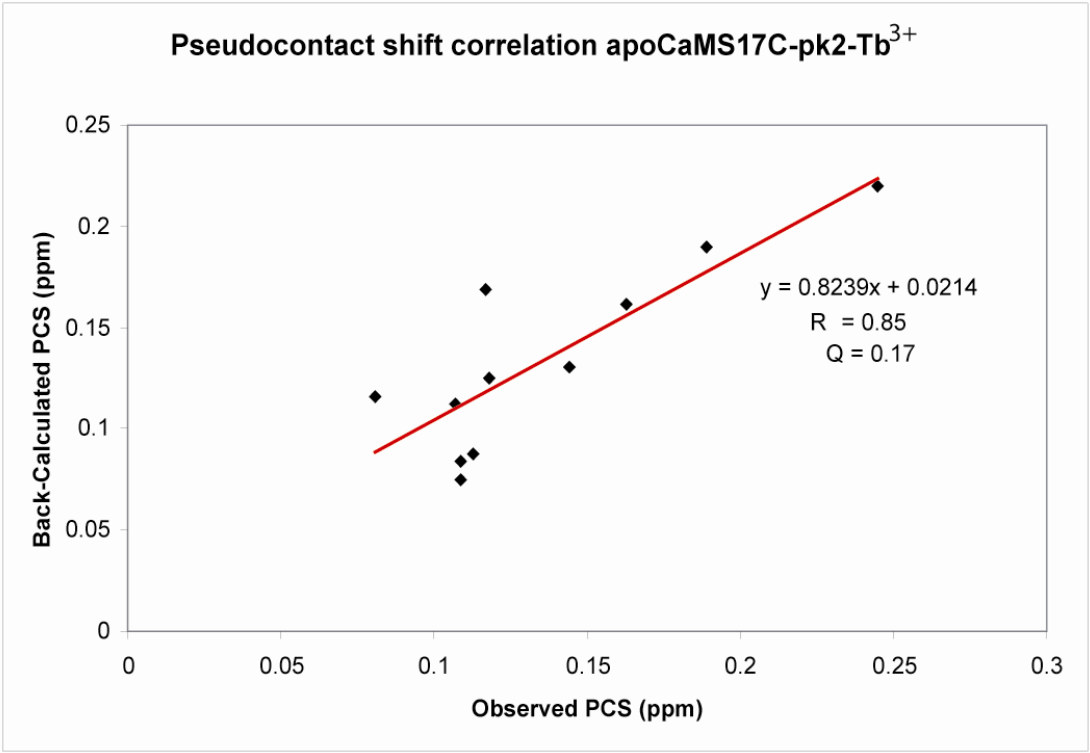

Figure 93. Correlation plot between the measured PCS for apoCaMS17C-pk2-Tb^{3+} and the back-calculated PCS from the NMR structure of the N-terminal domain of apoCaM.

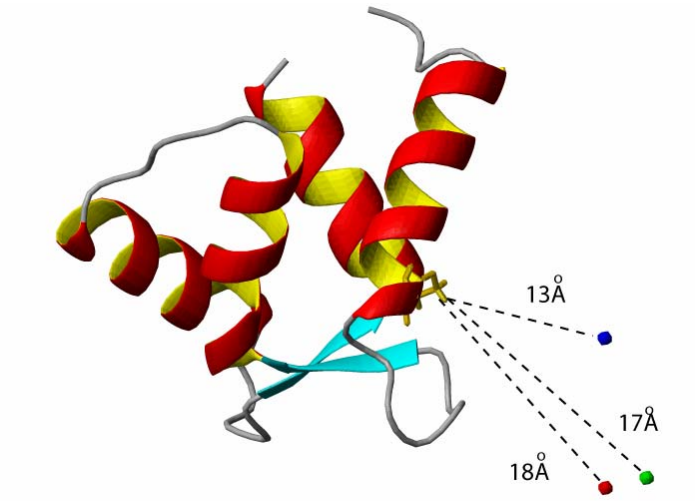

Figure 94. Location of the metal ion (Tb^{3+}) based on the pseudocontact shift restraints for the N-terminal domain of apoCaMS17C-t43D in red, apoCaMS17C-t43L in green and apoCaMS17C-pk2 in blue. The distance of the longest axis from the Oxygen atom of the serine in the *wt* protein to the metal ion is also given.

In principle, it is possible to derive the elements of the alignment tensor (d_{zz}, d_{yy} and d_{xx}) from the histogram analysis of the rDCs (Figures 96 and 97). However, since the NMR structure of the N- and C-terminal domain of CaM has been refined against numerous rDCs (Chou *et al.*, 2001), it was preferred to derive the tensor values with the singular value decomposition (SVD) algorithm from PALES (Zweckstetter and Bax, 2000). In this manner, the experimental values can be tested against the reference structural model and a correlation plot of the experimental values to the back-calculated rDCs is obtained. In addition, several other parameters are obtained, which provide an extended view of the error in the data.

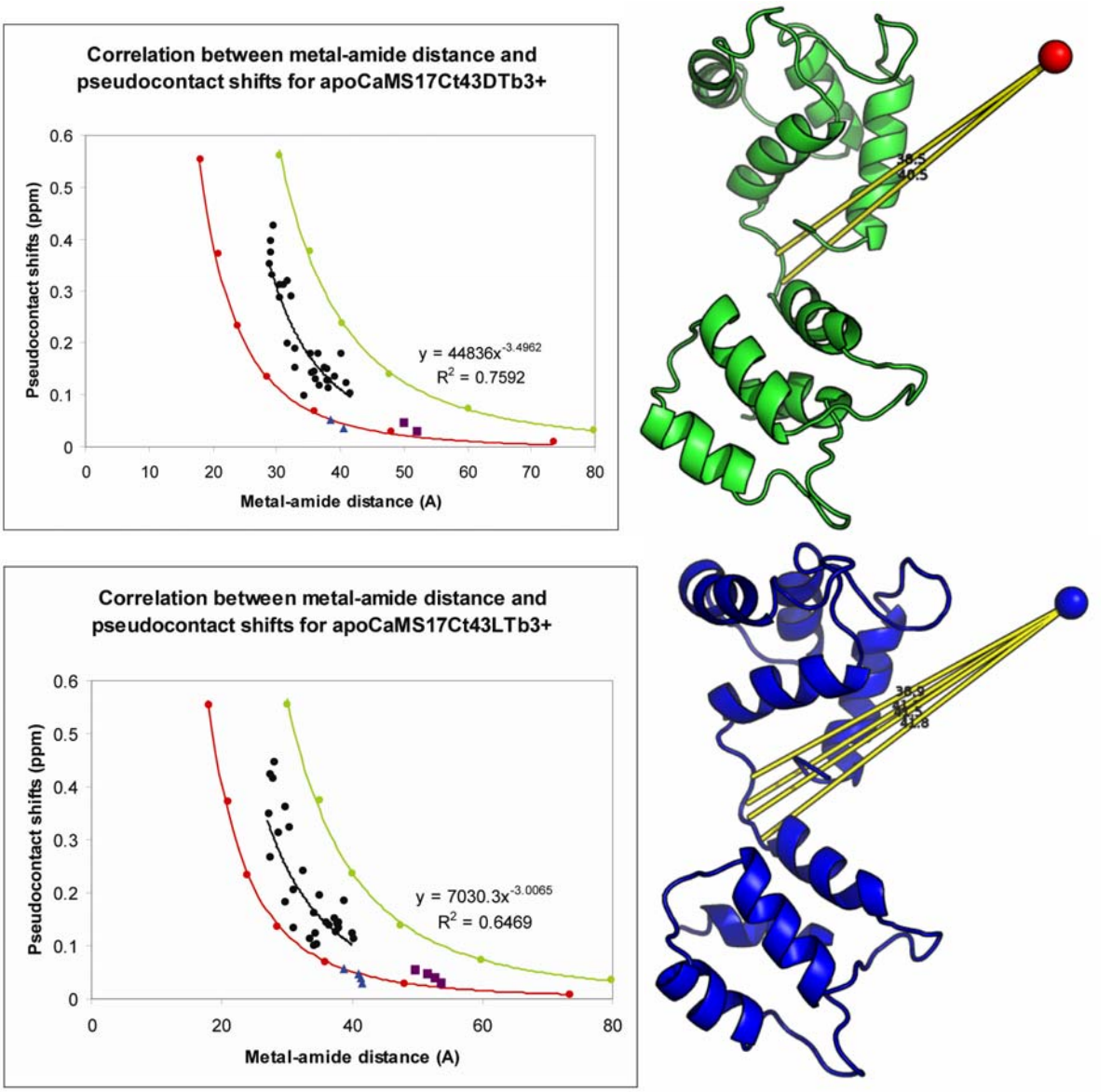

Figure 95. Relationship of the measured distances between the lanthanide ion and each amide proton and the observed PCS for apoCaMS17Ct43D-Tb^{3+}. An upper bound r^3 plot is shown in red and a lower-bound r^3 plot is shown in green. The blue triangles are the measured metal-amide distances for the linker residues T79 and D80 in the NMR structure of apoCaM. The purple squares are the predicted distances based on the r^3 function. On the right, the distances from the lanthanide ion (red) to the two amides in the linker are illustrated. The lower panel shows the same plot for apoCaMS17Ct43L-Tb^{3+}. The blue triangles and purple squares have the same meaning and represent the T79, D80, S81 and E82 in the linker region.

Table 8. Axial (Da-HN) and Rhombic(Rhomb.) components of the alignment tensors and angles between them achieved for the holoCaM samples aligned with Terbium.

Mutant	Tag1/tag2	Deg	tag	Hz Da-HN	Rhomb.
holoCaMS17C (N-domain tensor)	pk1/t43L	126	Pk1	2.2	0.32
			T43L	2.3	0.15
holoCaMT146C (C-domain tensor)			Pk2	3.0	0.58
			Pk1	3.9	0.22
			T43L	3.23	0.18
			T43L	2.47	0.23

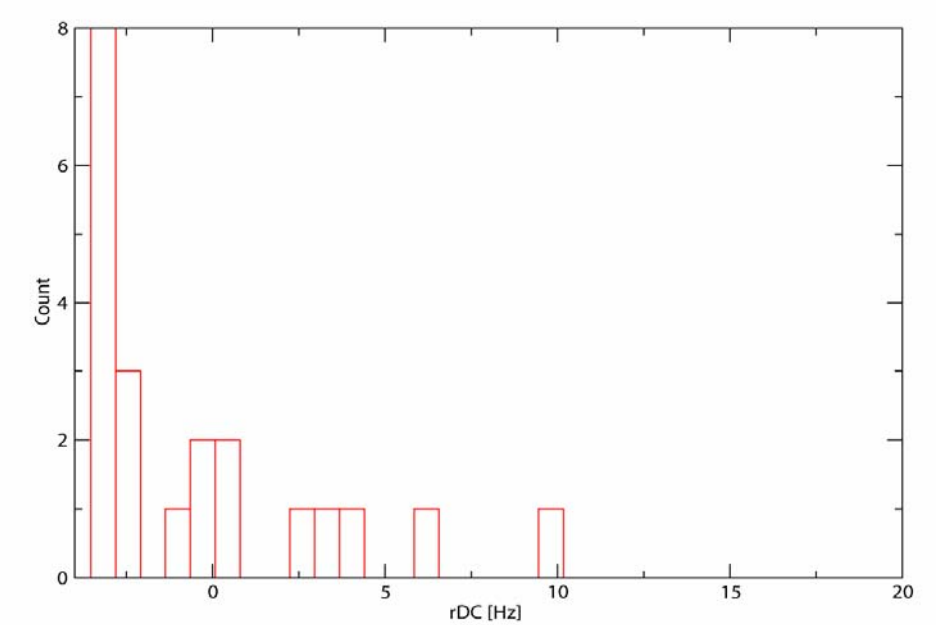

Figure 96. Histogram for the measured residual dipolar couplings of the C-terminal domain of the CaMT146C-pk2-Tb^{3+}/C20W peptide complex. From the histogram it is evident the anisotropic distribution of these couplings.

Based on numerous rDC analyses for the CaM/C20W peptide complex see Table 9, it was possible to establish residual interdomain motions in this complex. Moreover, it appears that the motions are more restricted than in the case of holoCaM. The experiments were done with the CaM T146C mutant. Thus, the C-terminal domain was paramgnetically aligned in the static magnetic field, $B_{0,}$ and the effects on the N-terminal domain were measured (See Figure 98). In average, a reduction in the magnitude of the axial component of the alignment tensor of a factor of 4 was found between the two domains.

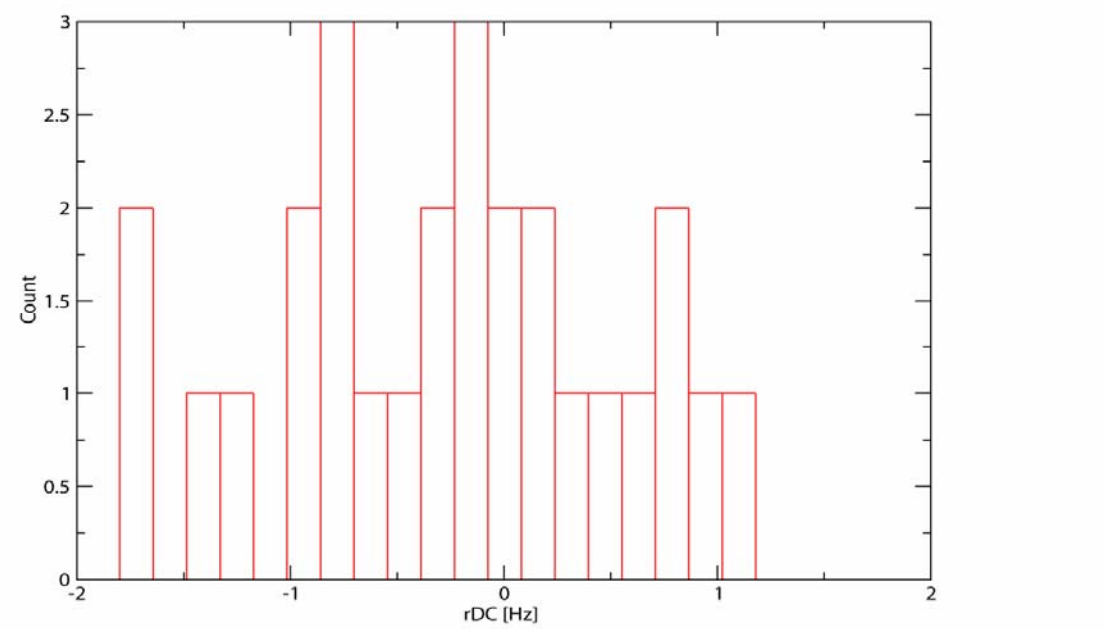

Figure 97. Histogram for the measured residual dipolar couplings of the N-terminal domain of the CaMT146C-pk2-Tb^{3+}/C20W peptide complex. In contrast to the previous histogram, the distribution of these rDCs is isotropic.

Table 9. Axial (Da-HN) and Rhombic(Rhomb.) components of the alignment tensors and angles between them achieved the CaMT146C/C20W complex aligned with Terbium

Observed domain	Tag1/tag2	Deg angle	tag	Hz Da-HN	Rhomb.
C-domain Tensor	Pk2/t43L	26	Pk2	3.47	0.13
			T43L	3.42	0.43
			T43D	3.0	0.24
N-domain Tensor	Pk2/t43L	92	Pk2	0.8	0.48
	T43L/t43D	49	T43L	0.9	0.48
			T43D	1.0	0.39

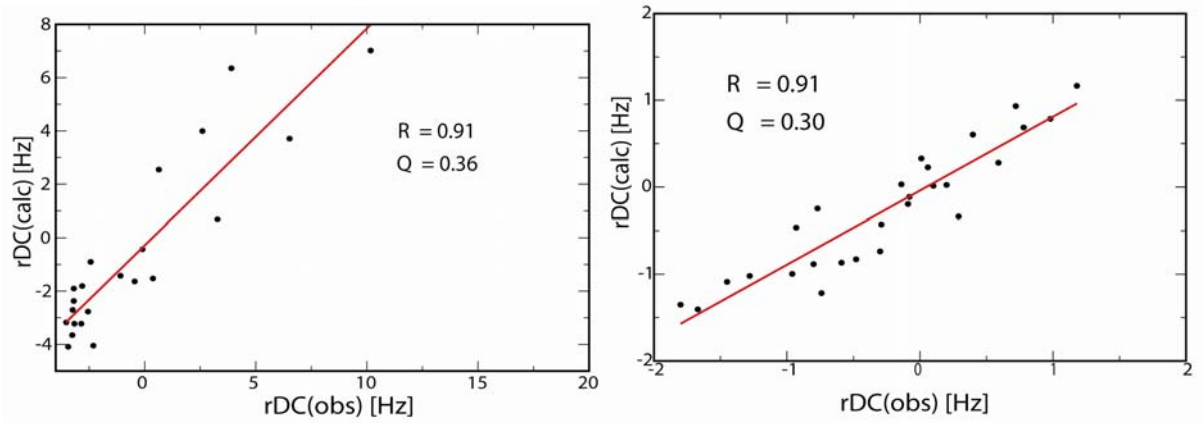

Figure 98. Correlation plots for the measured rDCs for the C-terminal domain (left side) and N-terminal domain (right side) of the CaMT146C-pk2-Tb^{3+}/C20W peptide complex

For holoCaMT146C it was not possible to measure the paramagnetic restraints on the N-terminal domain, since the measurement error was on the same order of magnitude than for the expected rDCs based on the results obtained by Bertini *et al*., 2004. In order to measure the alignment tensor of the N-terminal domain of CaM, a paramagnetic tag with a stronger alignment would be needed. However the tensor values were obtained for the C-terminal domain (Figure 100).

For rDC data analysis it is important to obtain various data sets with different orientation with respect to the magnetic field; the reason for this is that the rDCs suffer from orientational degeneracy, which can be resolved measuring several independent data sets. For the paramagnetic tags used in this study, this was possible by the different enantiomers of the tag. Another possibility is to complex that tag with different lanthanide ions, with different magnetic susceptibility properties. Tb^{3+} and Dy^{3+} are both similar in their alignment properties, but Tm^{3+} provides an alignment with a different orientation, this is illustrated in Figure 99.

In order to be confident about the statistical significance of the observed difference among the two states of CaM, the SVD algorithm was repeated 1000 times within a Monte Carlo simulation procedure and it was possible to derive some statistics about the alignment tensors. First, the distribution of the axial component (Da) for the tensors showed that the N-terminal domain in the CaM/C20W peptide complex (Figure 101) has a definite value above the noise of the data (0.8 ± 0.2 Hz).

The distribution in the rhombic component of the alignment tensor was larger (Figure 102), however it could be established that the C-terminal domain of the CaM/C20W complex has a low rhombic value (0.13 ± 0.1) whereas the C-terminal domain of the free CaM has a large rhombic value (0.58 ± 0.15). On the other hand, the rhombic value for the tensor of the N-terminal domain of the CaM/C20W complex is axially symmetric (0.48 ± 0.15).

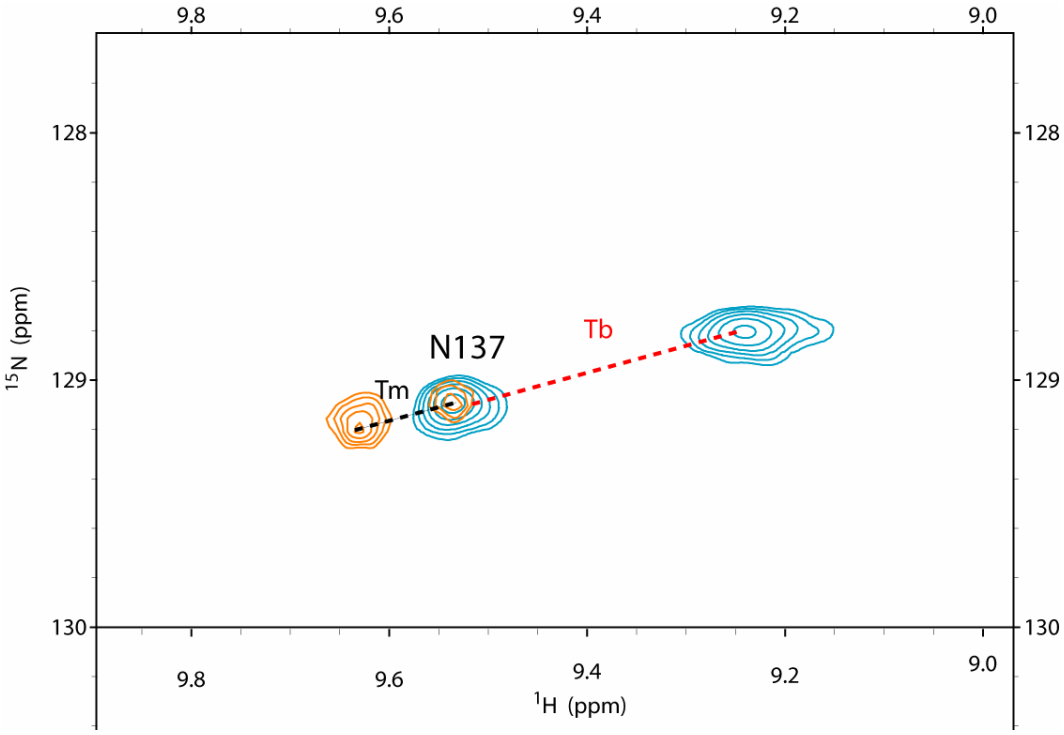

Figure 99. Overlaid ^{15}N-^{1}H HSQC spectra for the holoCaMT146C-t43D aligned with Tb^{3+} (blue) and with Tm^{3+} (orange). For the NH of N137 Tm^{3+} gives a positive PCS whereas Tb^{3+} a negative one, therefore these two data sets give also different alignment tensors in terms of orientation.

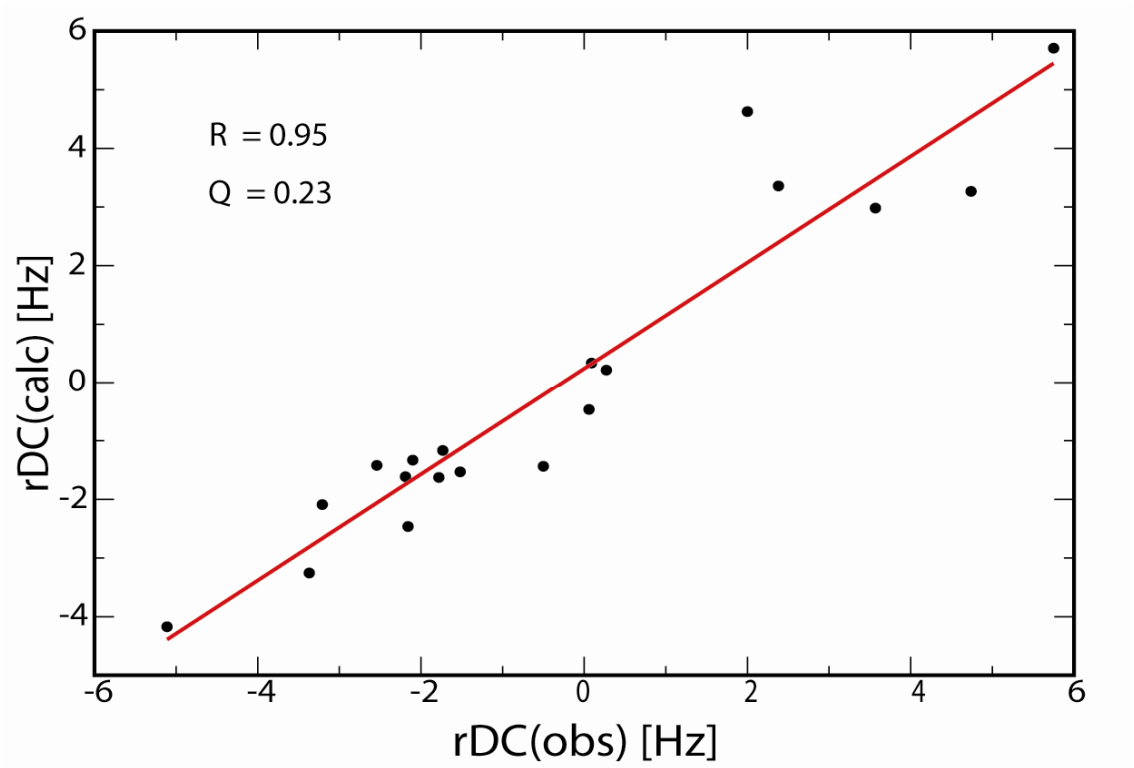

Figure 100. Correlation plot between the measured rDCs and back-calculated rDCs for the C-terminal domain of CaMT146C-pk2-Tb^{3+}.

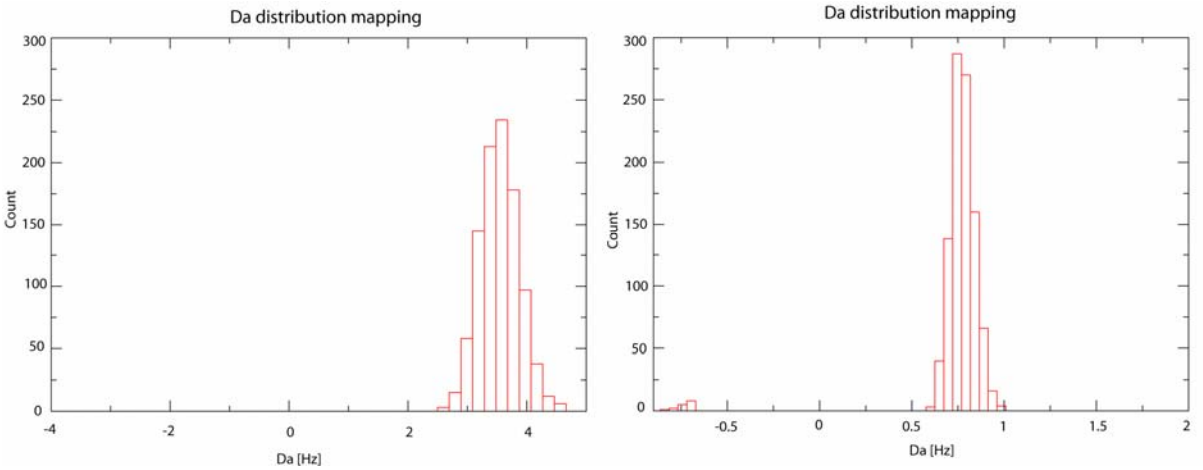

Figure 101. Distribution for the Axial component of the alignment tensor for the CaMT146C-pk2-Tb^{3+}/C20W peptide complex. On the left is the tensor for the C-terminal domain and on the right for the N-terminal domain.

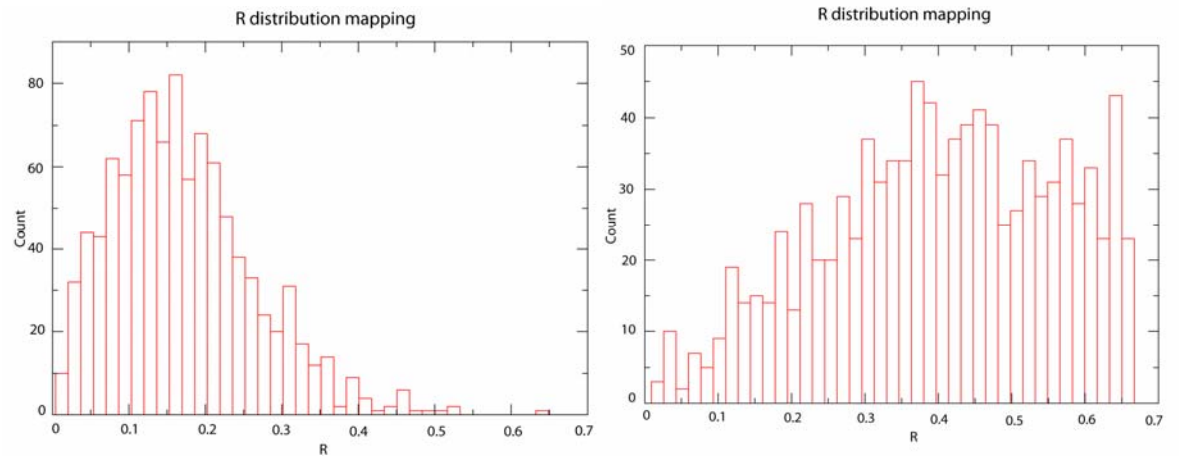

Figure 102. Distribution for the Rhombic component of the alignment tensor for the CaMT146C-pk2-Tb^{3+}/C20W peptide complex. On the left is the tensor for the C-terminal domain and on the right for the N-terminal domain.

The tensor distribution can also be visualized with the aid of a 3D plot. The plots of the tensor values for the C- and N- terminal domains of the CaM/C20W complex are shown in Figure 103. These plots show that both tensors are well defined and have a low spread around the average value.

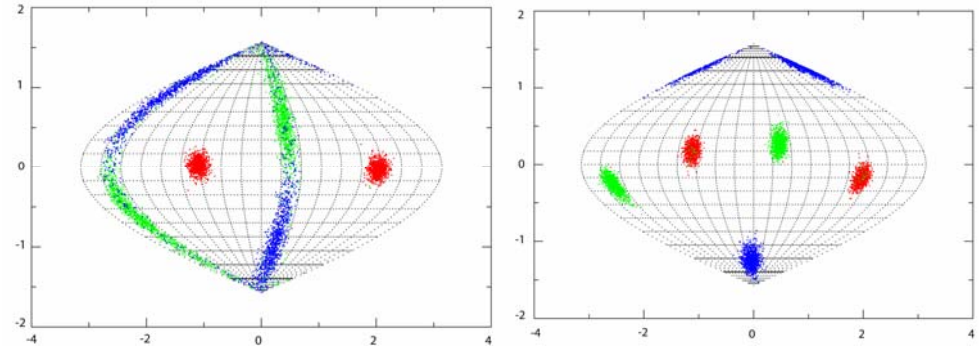

Figure 103. Mapping of the individual tensor values for the 1000 SVD calculations on a 3D plot for the CaMT146C-pk2-Tb^{3+}/C20W complex. On the left is the C-terminal domain and on the right is the N-terminal domain. The blue and green dots represent the d_{xx} and d_{yy} values and the red dots represent the d_{zz} values.

The distribution of the axial component (Da) for the tensors showed that the N-terminal domain in holoCaM is ambiguous. However the distribution of the axial component of the alignment tensor for the C-terminal domain gave a Da value of 3.1 ± 0.7 Hz (Figure 104).

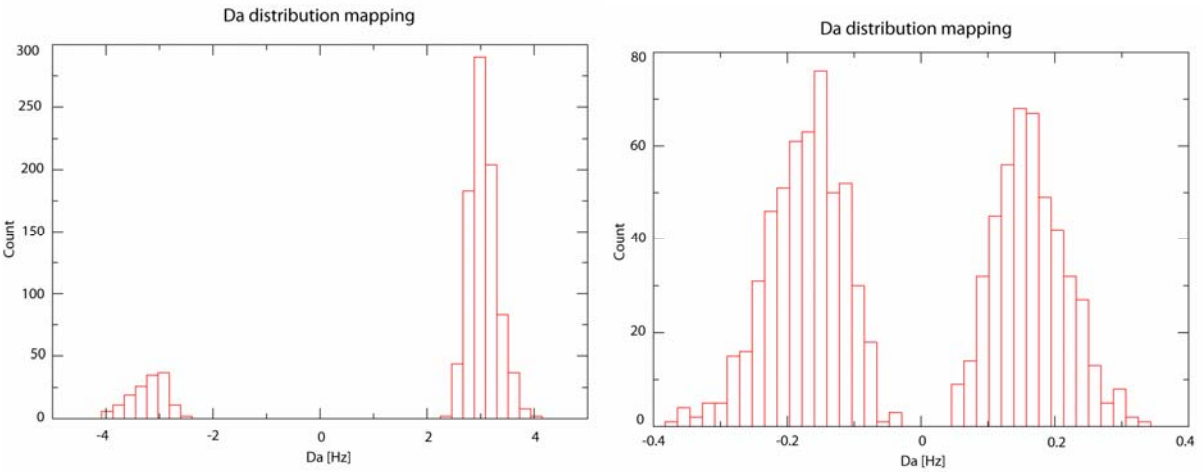

Figure 104. Distribution for the axial component (Da) of the alignment tensor for CaMT146C-pk2-Tb^{3+}. On the left is the tensor for the C-terminal domain and on the right for the N-terminal domain.

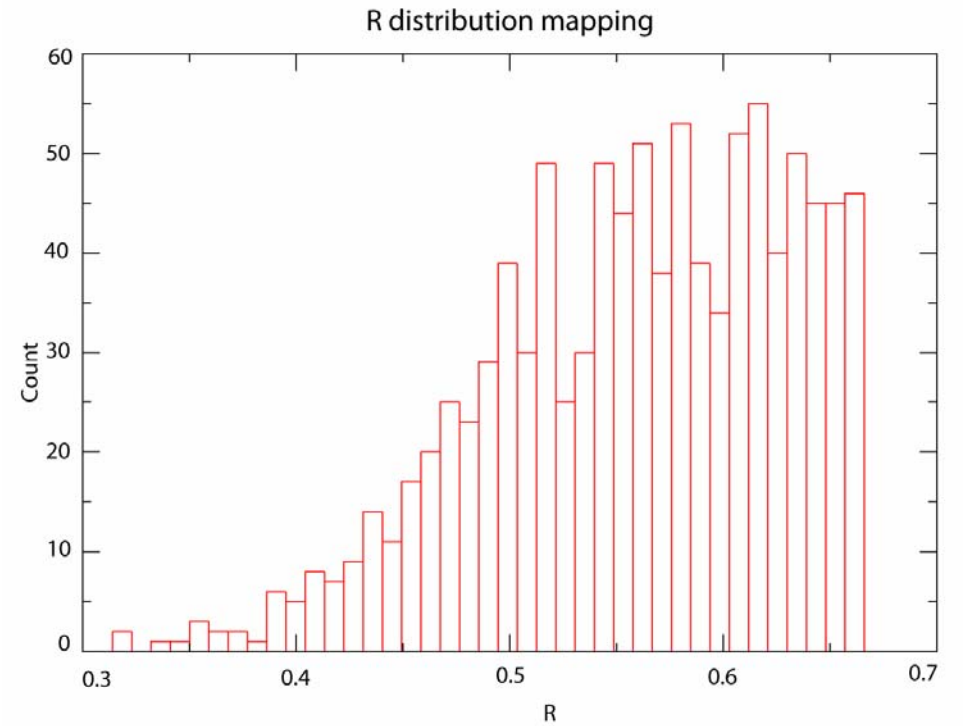

Figure 105. Distribution for the Rhombic component of the alignment tensor for the C-terminal domain of CaMT146C-pk2-Tb^{3+}.

The plots of the tensor values for the C- and N- terminal domains of CaM is shown in Figure 106; these plots show that just the alignment tensor of the C-terminal domain was well defined and had a low spread around the average value. In contrast, the alignment tensor for the N-terminal domain was randomized by the noise in the data.

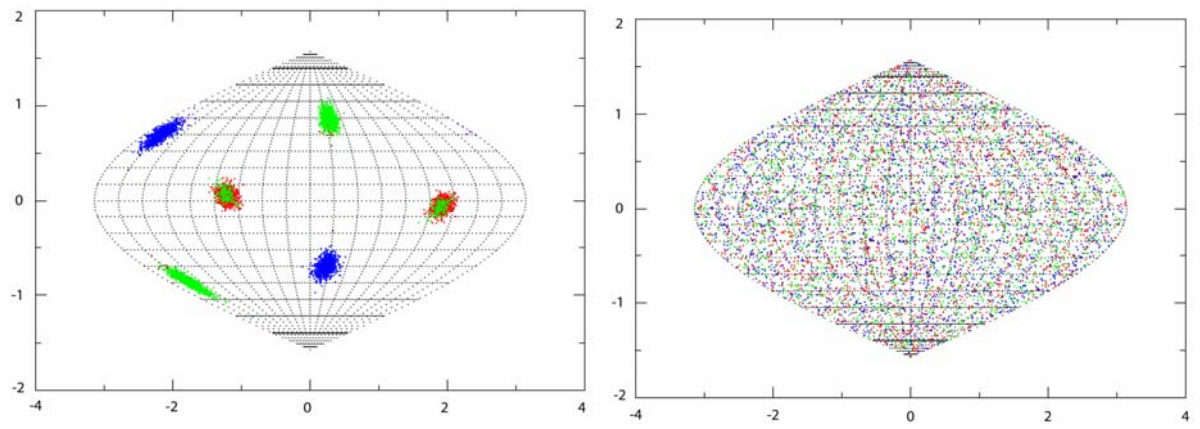

Figure 106. Mapping of the individual tensor values for the 1000 SVD calculations on a 3D plot for CaMT146C-pk2-Tb^{3+}. On the left is the C-terminal domain and on the right is the N-terminal domain.

The position of the metal was located based on the pseudocontact shift restraints (Figure 107). It was observed that the metal ion had a different position for holoCaMT146-pk2 and for the CaMT146C-pk2/C20W peptide complex. This suggested that the peptide might restrict the motion of the tag; this would also explain the larger anisotropy of the rDC distribution for this sample. In addition, the metal ion was found to be close to an acidic patch in helix E (Figure 108 and 109); it is possible that the coordination sphere of the lanthanide ion bound to the EDTA moiety could be completed by carboxylate side-chains of these residues. In a similar analysis done for apoCaM, the relationship between the metal-amide distances and the measured PCS was determined for the CaMT146C-pk2 and in its complex with C20W.

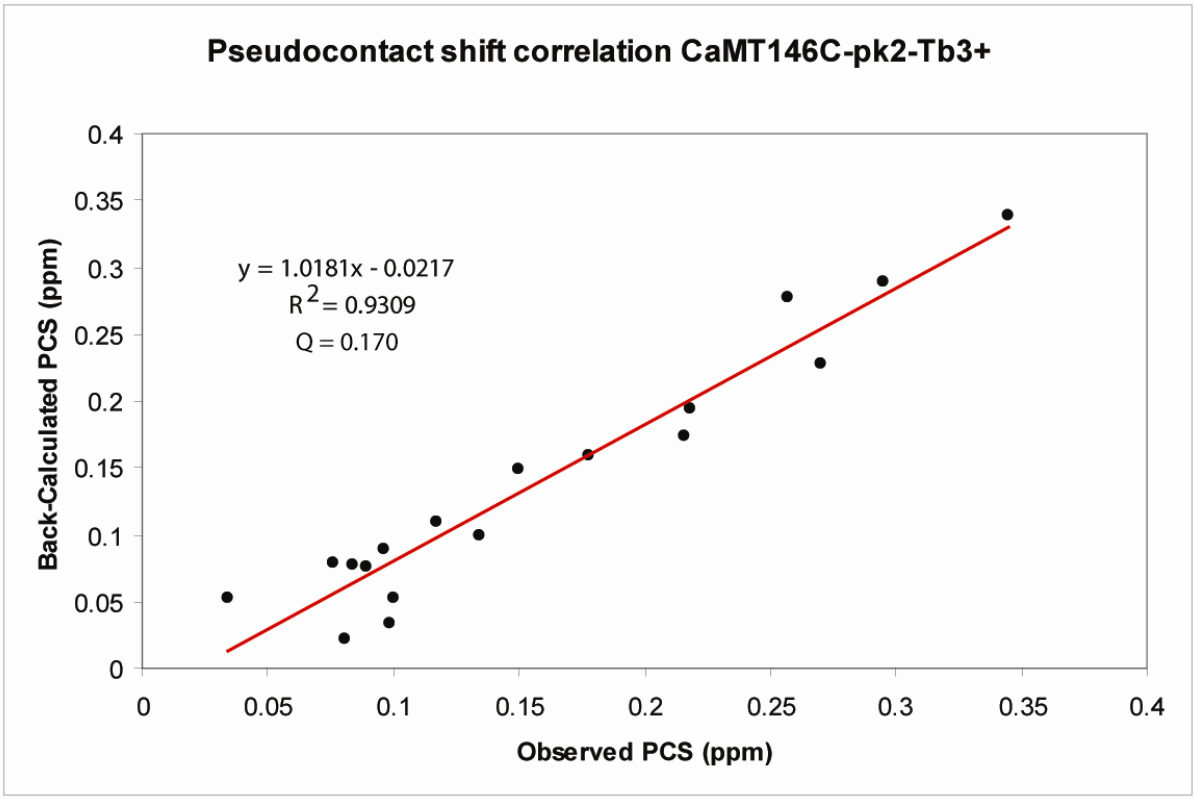

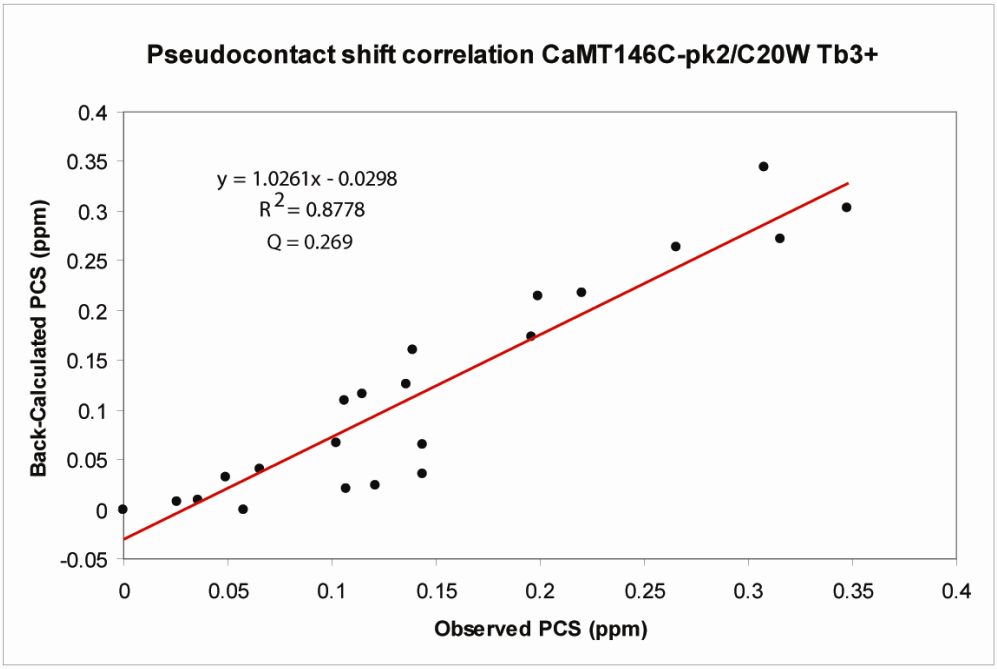

Figure 107. Correlation plot of the measured PCS for the C-terminal domain of CaMT146C-pk2-Tb^{3+} (upper plot) and CaMT146C-pk2-Tb^{3+}/C20W peptide complex (lower plot) against the back-calculated PCS based on the NMR structure of holoCaM.

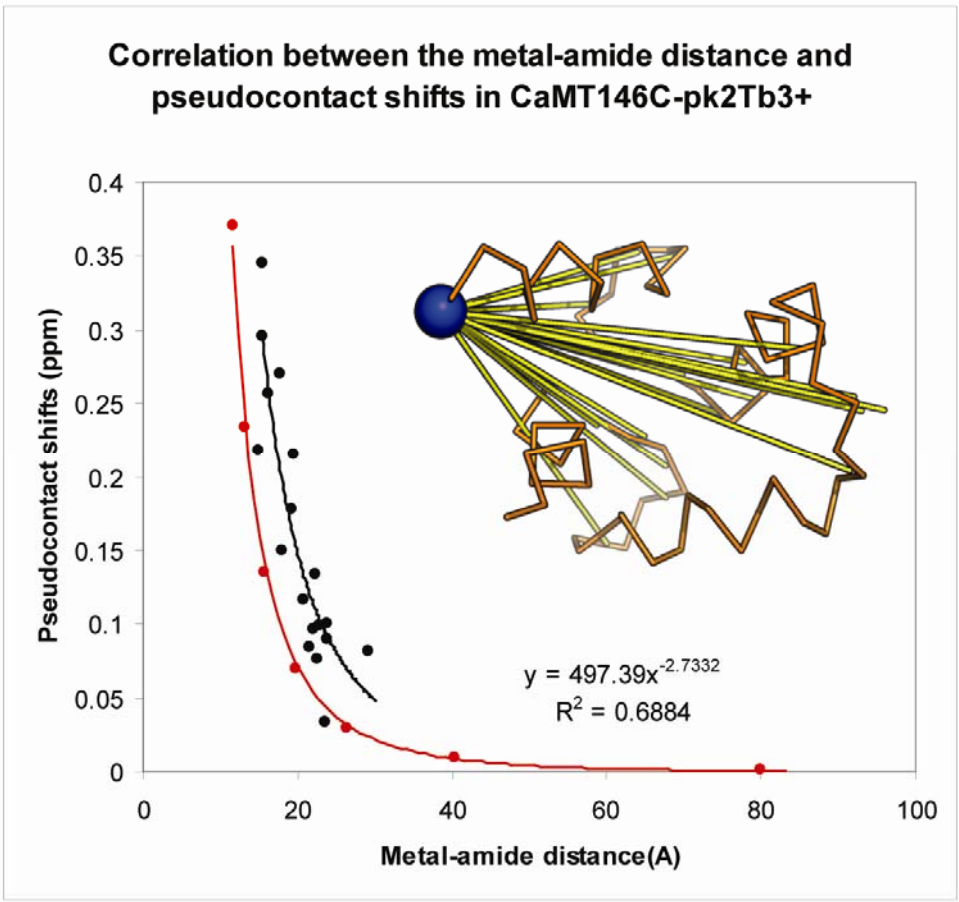

Figure 108. Correlation plot between the measured distances between the lanthanide ion and each amide proton and the observed pseudocontact shift for CaMT146C-pk2-Tb^{3+}. The curve was fit with a power function. An upper bound r^3 plot is shown in red.

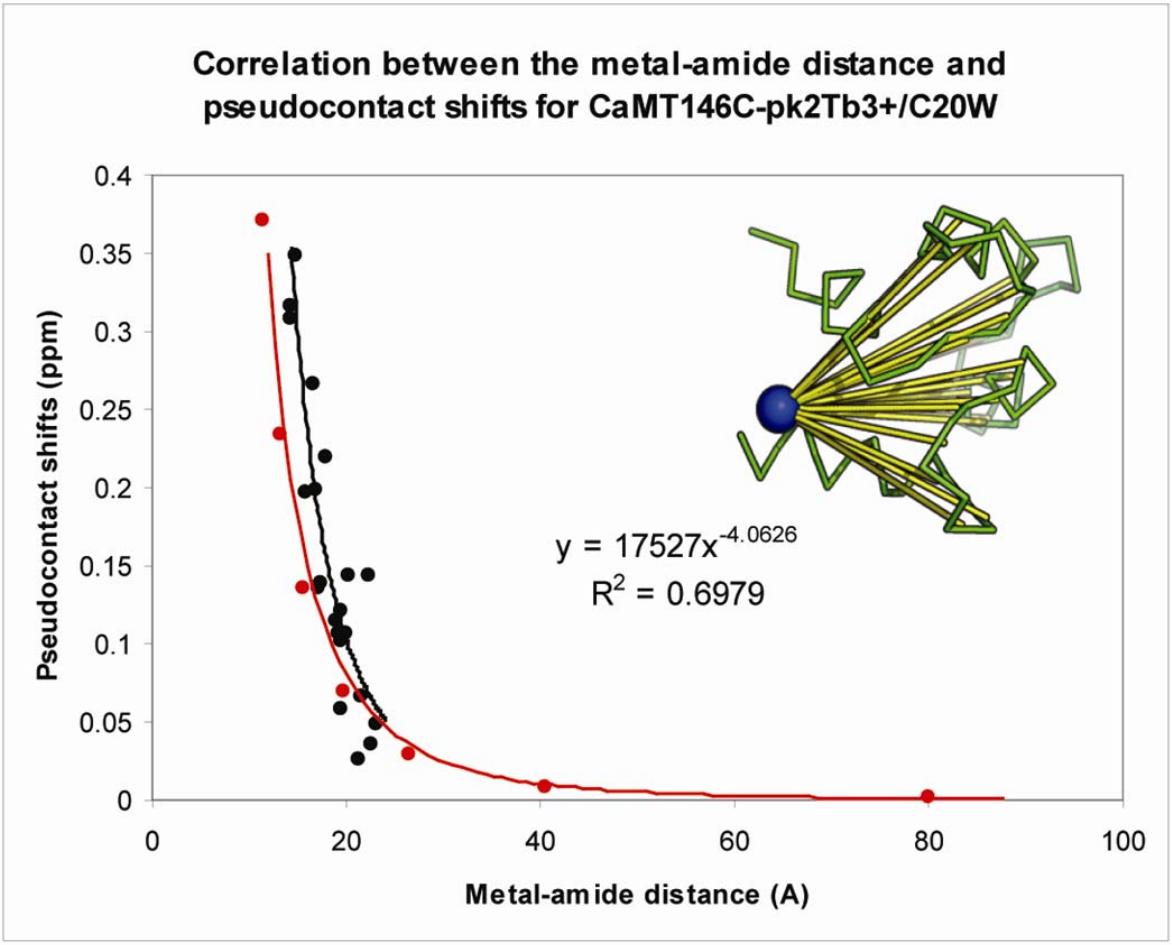

Figure 109. Correlation plot between the measured distances between the lanthanide ion and each amide proton and the observed pseudocontact shift for CaMT146C-pk2-Tb^{3+}/C20W peptide complex. The curve was fit with a power function. An upper bound r^3 plot is shown in red.

IV. DISCUSSION

1. Dynamic Studies on apoCaM

The paramagnetic alignment of the apoCaMS17C mutant with three different tags loaded with Terbium ion was successful. The alignment tensor parameters could be obtained and the coordinates of the metal could be located based on pseudocontact shift data for the three cases. However, the rDCs measured on the C-terminal domain were too small in magnitude and could not be measured with enough accuracy. Therefore the interdomain dynamic studies focused on the pseudocontact shifts measured on the linker region of apoCaM, for the alignments with t43D and t43L. In both cases, a PCS could be measured for the T79 and D80 amide cross-peaks and for the alignment with t43L the PCS for S81 and E82 were also obtained. In general, PCS data pose more difficulties in their analysis, since they are dependent both on the distance (r^3) and the orientation of the vector described by the unpaired electron of the metal ion and the spin under observation (amide in this case). In some cases, these two components can be disentangled with the aid of relaxation measurements using a high relaxing metal ion (like Gadolinium or Manganese) bound to the same paramagnetic tag; the relaxation enhancement provides upper bounds of the distance between the metal ion and the spin of interest with a r^6 dependency.

In this work, the apoCaMS17C-t43L sample was titrated with $MnCl_2$, but the effect on the line width broadening for the amides of interest in the linker region was very small (between 2 and 5 Hz), therefore, this approach was not successful. In order to obtain upper bounds for the PCS data, a r^3 function was constructed using the angles that maximized the $(3\cos^2\theta\text{-}1)$ and $(\sin^2\theta\cos 2\Omega)$ terms in the expression for the pseudocontact shift. This upper bound function was important in order to establish that the measured PCS in the linker region of apoCaM for both t43L and t43D samples deviated from the expected values based on the r^3 function. Thus, this gave experimental evidence that the residues in the liker region are not rigid and experience averaging in the submillisecond time scale due to interdomain dynamics and/or conformational exchange. It was apparent, that the averaging increases along the linker and PCS could not longer be observed in the C-terminal domain of apoCaM. Dynamic studies based on relaxation measurements on apoCaM have established that the C-terminal domain experiences conformational exchange in the μs time scale; it exchanges at least between a close conformation and a semi-open conformation (Tjandra *et al*., 1995). Chen and Hummer (2007) showed that the C-terminal domain of apoCaM populates three states in solution; a closed one, a partially unfolded one and an open one. In addition, molecular dynamic simulations have suggested that apoCaM experience large scale domain motions, and the center of mass of each domain varied from 29 to 39 Å (average distance 33 Å) during the simulation (Yang *et al*., 2003).

It is interesting to compare these results with those of holoCaM, since the same mutant (S17C) was also aligned with two paramagnetic tags. Although a defined tensor could be obtained for the N-terminal domain in both samples, the alignment tensor for the C-terminal domain could not be established. In addition, no PCS were observed in the linker region. This observation is in agreement with the knowledge that in average, the domains in holoCaM are further away from each other in comparison to apoCaM. The simulation done by Yang *et al*., 2004, gave an average value of 38 Å between the centers of mass for each domain in holoCaM and the variation was from 34 to 41 Å.

2. Dynamic Studies on holoCaM

The studies done on the paramagnetic alignment of the T146C mutant of holoCaM could not describe the interdomain dynamics on this system; since the alignment obtained was

too weak (rDCs up to 8 Hz) in order to obtain a reliable tensor for the N-terminal domain within the accuracy of the measurement of rDCs, based on the fact that Bertini *et al*., 2004 found a decrease by a factor of 10 in the axial component of the alignment tensor which did not contain the metal ion. Thus, the results obtained in this study are in nice agreement with these findings.

3. Dynamic Studies on the CaM/C20W peptide complex

The studies done on the paramagnetic alignment of the T146C mutant of CaM in complex with the C20W peptide showed that the mobility of this complex was more restricted than that one of holoCaM. The magnitude of the axial component for the tensor in the N-terminal domain for three different tags (pk2, t43L and t43D) complexed with Terbium got reduced in average by a factor of ~4 in comparison to that one of the paramagnetically aligned C-terminal domain. Tüchelman (1999) reported a reduced alignment tenor by a factor of two for the N-terminal domain of the CaM/C20W complex aligned with DTPA-Yb in the peptide. However, the magnitude of the dipolar couplings obtained in that work were too small to give an accurate value of the tensor parameters, however qualitatively the results are in agreement with the results presented in this thesis. In addition, these data agreed well with the SAXS studies reported by Kataoka *et al.* 1991, where it was established that the radius of gyration for the CaM/C20W peptide complex (57.5 Å) was significantly smaller than that one of CaM (62.5 Å) .

4. Structural studies on the CaM/Munc13-1 interaction

a. apoCaM interaction with Munc13-1 and ubMunc13-2

The observations done by Junge *et al*., 2004 based on intrinsic tryptophan emission fluorescence spectroscopy for the interaction of apoCaM with the Munc13-1(460-478) peptide were confirmed by recording a series of ^{15}N-^{1}H HSQC spectra adding increasing amounts of the synthetic peptide to ^{15}NapoCaM. The results clearly showed that the binding localizes to the C-terminal domain of apoCaM. The studies done on the ^{13}C,^{15}N labeled Munc13-1(457-492) peptide showed that upon binding to apoCaM, the peptide already adopts a α-helical conformation.

A similar HSQC-based titration experiment done for the ubMunc13-2 (382-402) synthetic peptide showed that this peptide also binds apoCaM with low affinity. The binding was also localized to the C-terminal domain of apoCaM, but it affected less NH cross peaks, suggesting that the interaction surface is smaller. Dimova *et al*., 2006 also probed the calcium sensitivity for the CaM/ubMunc13-2 interaction and established that the calcium concentration needed for the complex formation is between 20 and 30 nM.

b. [2Ca^{2+}]CaM interaction with Munc13-1

Upon EDTA addition to the ^{15}NCaM/Munc13-1(457-492) peptide complex it was possible to remove the two Ca^{2+} ions from the N-terminal domain of CaM, therefore the [2Ca^{2+}]-^{15}N CaM/ Munc13-1(457-492) peptide complex was completely populated and characterized with NMR spectroscopy. This complex state was referred as the half-activated state, since apparently, it is a high affinity (sub μM) interaction mediated solely by the C-terminal domain of CaM. Junge *et al.*, 2004 found in a two-hybrid yeast screen that some clones consisting solely of the C-terminal domain of CaM were selected as Munc13-1 interaction partners, therefore the [2Ca^{2+}]CaM state seemed to have a strong interaction with Munc13-1 *in vivo* as well. This half-activated state might be of physiological relevance, since

it would mean that at resting calcium concentrations in the neuron, the CaM/Munc13-1 interaction could be already present, increasing the kinetics of this protein-protein interaction upon full activation by eliminating the diffusion component of the reaction. Such a preformed complex has been already described in other CaM interactions like that one with the ryanodine receptor (Samsó and Wagenknecht, 2002) and with the voltage-gated Ca^{2+} channels (Erickson *et al*., 2001).

c. [4Ca^{2+}]CaM interaction with Munc13-1

The initial NMR studies on the CaM/Munc13-1(459-478) peptide complex showed that this complex had a (1:1) stoichiometry as was previously described by Junge *et al*., 2004. With the aid of NMR experiments it was evident that this small peptide did not perturb much the NH cross-peaks of the N-terminal domain of CaM. For this reason, the peptide was extended towards its C-terminus and the solution structure of the CaM/Munc13-1(457-492) peptide complex was determined.

d. Solution structure of the CaM/Munc13-1(457-492) peptide complex

The solution structure revealed a novel binding mode for CaM, where a bipartite interaction is established between the N-terminal amphiphilic α-helix of the Munc13-1 peptide and the C-terminal domain of CaM via a the classical (1-5-8) hydrophobic motif; and the N-terminal domain of CaM has contacts with a hydrophobic LW motif at the C-terminal tail of the peptide. Other singular properties of this novel CaM complex include: (a) submillisecond interdomain dynamics present in the complex determined with rDC analysis from paramagnetic alignment; (b) dimerization of the complex to give a (2:2) complex favored at higher salt concentrations (~300 mM KCl); and (c) heterogeneity of the W489 Nε-Hε side chain of the bound LW motif; one possible source of this heterogeneity could have arisen from an unbound (8.4%) and bound (91.6%) LW motif; another possible explanation could be different side chain χ-rotamer populations (8.4 % and 91.6 %) in slow exchange on the NMR time scale, giving rise to two resonances.

e. Accuracy of the solution structure of the CaM/Munc13-1(457-492) peptide complex

The total amount of NOE restraints (1758) were enough to obtain a well defined three-dimensional structure of this complex in solution. The backbone conformation converged to a RMSD of 0.56 Å for the C-terminal domain of CaM and to 0.74 Å for the N-terminal domain of CaM to the mean structure in the ensemble. The backbone atoms of each domain were overlaid to several high-resolution structures of CaM in various activated states, showing that the backbone conformation was not very much changed upon binding of the Munc13-1 peptide. An average backbone RMSD of 2.4 Å and 2.8 Å to the analyzed structures was found for the C- and N-terminal domains of CaM, respectively. This is consistent with the observation that the C-terminal domain had a larger number of NOE restraints per residue and resonance assignments than the N-terminal domain. Helix D in the N-terminal domain of CaM posed large difficulties in the resonance assignment, because of broad resonances, pointing towards conformational averaging. The solution structure of the protein-peptide complex revealed that CaM interacts with the Munc13-1 (457-492) peptide in an extended conformation. There are numerous previous reports in the literature for CaM interacting with its binding partner in an extended conformation: (a) the crystal structure of CaM with the CaM-binding domain of a Ca^{2+}-activated K^+ channel (Schumacher *et al*., 2001); (b) CaM complex with the Edema Factor of *Bacillus anthracis* (Drum *et al*., 2002); (c) the CaM complex with the C20W peptide of the plasma membrane Ca^{2+} pump (Elshorst *et al*., 1999);

(d) the CaM complex with a dimeric peptide from the basic helix-loop-helix transcription factor SEF2-1/EF2-2 (Larsson *et al*., 2001); (e) the CaM complex with two peptides of plant glutamate decarboxilase (Yap *et al*., 2003): and (f) the CaM interaction with the Microtubule-associated protein F-STOP (Bouvier *et al*., 2003). To our knowledge, this is the first report where an amphiphilic α helix motif (1-5-8) is bound to the C-terminal domain of CaM and a second hydrophobic anchor ($L^{488}W^{489}$) binds to the N-terminal domain of CaM. Therefore, the structure of the CaM/Munc13-1 (457-492) peptide complex supports the view of the studies done on the calcium-dependent inactivation mechanism of the CaM regulation of Voltage-gated calcium channels (van Petegem *et al*., 2005). In these studies, it has been established that the CaM-$Ca_V1.2$ IQ domain-CaM interaction has a bipartite nature, where the C-terminal and N-terminal domains of CaM bind distinct hydrophobic anchor residues in the target protein with different affinities. In the case of the Voltage-gated Ca^{2+} channels this differential interaction has relevance in the calcium-dependent facilitation regulation mechanism. The functional relevance for the bipartite interaction in the CaM/Munc13-1 peptide complex is not completely understood, but complementary studies done on the larger CaM/Munc13-1 (185aa) complex give hints to a switch mechanism as is discussed below.

f. NMR studies on the CaM/Munc13-1(185aa) monomeric (1:1) and dimeric (2:2) complexes

The NMR studies done on the CaM/Munc13-1(185aa) complex extended the understanding of this protein-protein interaction at a molecular level. First, the heterogeneity in the W489 Nε-Hε1 side chain described for the CaM/Munc13-1 peptide complex was also found in the NMR study of this larger complex and surprisingly, the W588 Nε-Hε1 side chain within the C_1 domain of Munc13-1 was also heterogeneous. Second, the (2:2) complex described for the CaM/Munc13-1 (459-479) peptide interaction was also present in the CaM/Munc13-1(185) interaction. In this larger complex, the dimerization appeared to be stronger and the two complex species could be separated and studied independently. Third, experiments done on the C_1 domain of Munc13-1 lacking the CaM binding site, gave a single resonance signal for the W588 Nε-Hε1 side-chain; therefore the heterogeneity observed in the larger CaM/Munc13-1(185aa) complex should be attributed either to its interaction with the N-terminal domain of CaM or to an intramolecular interaction upstream of the C_1 domain. Although the dimerization mechanism is not completely understood for this interaction, a picture starts to emerge: (a) The conformational exchange equilibrium between the N-terminal domain of CaM and the C_1 domain of Munc13-1 described in the CaM/Munc13-1(185aa) dimeric (2:2) complex species suggest that these two domains might be involved in the dimerization process. To add more evidence on this possible novel domain-domain interaction; it would be interesting to measure the exchange contribution to the relaxation of the NH cross-peaks in these two domains, in order to determine if the exchange occurs on the same time scale. (b) The activation of the C_1 domain of Munc13-1 in the CaM/Munc13-1 (185aa) dimeric (2:2) complex with its agonist, phorbol ester (PDBu), shifted the conformational exchange equilibrium towards the monomeric side of the reaction; since the line shape of the NH resonances improved significantly. In contrast, the same PDBu activation experiment done on the CaM/Munc13-1(185aa) monomeric (1:1) complex did not give rise to large changes in the HSQC spectrum, although clear ligand binding was observed. (c) Electrophysiology studies by Basu *et al*., 2007 proposed that in the basal state of Munc13-1, its C_1 domain appears to be inhibited by intramolecular interactions interfering with the C-terminal MUN catalytic domain. The activation with DAG/phorbol ester induces a conformational change disrupting the intramolecular interactions releasing the catalytic domain from its inhibited state; this open configuration of Munc13-1 is also mimicked by the H567K mutation that disrupts the C_1 domain fold removing one coordination site for the zinc

metal ion in this domain. (d) In line with the structural studies by Lu *et al*., 2006, it can be speculated that the basal state of Munc13-1 consists of a homodimer with an inhibited C-terminal MUN catalytic domain and upon the sequential or concerted action of the RIM zinc-finger domain, CaM, and PDBu activation, the homodimer is relieved and the catalytic MUN domain gets activated for acting on its down-stream targets like syntaxin-1 and Munc18. Additional experiments need to be done to better understand the modulation on the CaM/Munc13-1(185aa) complex dimer (2:2) to monomer (1:1) equilibrium by phorbol esters and/or calcium to gain a better understanding on the regulation of the presynaptic plasticity processes in neurons.

V. CONCLUSIONS

The contributions of this work to the understanding of CaM plasticity include:

1. The establishment of a difference in the dynamics of CaM in three distinct activated states based on paramagnetic restraints. Firstly, a difference between apoCaM and holoCaM dynamics could be described on the basis of pseudocontact shifts measured for the CaMS17C mutant aligned with various paramagnetic tags. Secondly a difference between holoCaM and the CaM/C20W peptide complex dynamics could be described on the basis of residual dipolar couplings measured for the CaMT146C mutant aligned with three different paramagnetic tags. In all of these three independent measurements, a residual alignment (around 25%) of the N-terminal domain of CaM was measured for the CaM/C20W peptide complex, whereas for the free holoCaM no residual alignment could be established.
2. The determination of the NMR solution structure of CaM complexed with the Munc13-1(458-492) peptide belonging to the diacylglycerol-binding protein Munc13-1, an essential priming factor in neurotransmitter release. The structure describes a new binding motif for CaM consisting in a bipartite interaction, where the C-terminal domain of CaM binds the N-terminal amphiphilic α-helix (1-5-8) hydrophobic motif in the peptide and the N-terminal domain of CaM binds to a C-terminal LW motif in the peptide. This bipartite binding mode parallels that one on the CaM/IQ motif interaction for the regulation of the voltage-gated Ca^{2+}-channels; however functional studies on Munc13-1 mutants should establish the physiological significance of this interaction mode.
3. The extension of the NMR studies of calmodulin with a larger fragment of Munc13-1 (447-631) consisting of its CaM-binding and diacylglycerol/phorbol ester C_1 binding domain suggests that the N-terminal domain of CaM switches between the LW motif found in the determined NMR structure of the CaM/Munc13-1 peptide complex and a second hydrophobic motif within the C_1 domain of Munc13-1. A definite experimental proof (long range distance NMR restraint provided by an intermolecular NOE or pseudocontact shift) is still needed to establish a direct interaction between the N-terminal domain of CaM and the C1 domain of Munc13-1, which would give a structural correlate to physiological studies suggesting interplay between these two modules in Munc13-1.
4. Strong evidence for the relevance of a dimerization mechanism on the CaM regulation of Munc13-1 could also be established, based on the NMR studies of the CaM/Munc13-1 (447-631) dimeric (2:2) complex and the binding to its agonist, the phorbol ester PDBu. Additional studies are needed to fully characterize this model.

VI. BIBLIOGRAPHY

Babu, Y.S., Bugg, C.E., Cook, W.J. (1988) Structure of calmodulin refined at 2.2 Å resolution. J. Mol. Biol. 204, 191-204.

Barbato, G., Ikura, M., Kay, L.E., Pastor, R.W., Bax, A. (1992) Backbone dynamics of calmodulin studied by ^{15}N relaxation using inverse detected two-dimensional NMR spectroscopy: The central helix is flexible. Biochemistry. 31, 5269-5278.

Basu, J., Betz, A., Brose, N., Rosenmund, C. (2007) Munc13-1 C1 domain activation lowers the energy barrier for synaptic vesicle fusion. J. Neurosci. 27, 1200-1210.

Basu, J., Shen, N., Dulubova, I., Lu, J., Guan, R., Guryev, O., Grishin, N.V., Rosenmund, C., Rizo, J. (2005) A minimal domain responsible for Munc13 activity. Nat. Struct. Mol. Biol. 12, 1017-1018.

Bax, A., Delaglio, F., Grzesiek, S., Vuister, G.W. (1994) Resonance assignment of methionine methyl groups and χ^3 angular information from long-range proton-carbon and carbon-carbon J correlation in a calmodulin-peptide complex. J. Biomol. NMR. 4, 787-797.

Bertini, I., Del Bianco, C., Gelis, I., Katsaros, N., Luchinat, C., Parigi, G., Peana, M., Provenzani, A., Zoroddu, M.A. (2004) Experimentally exploring the conformational space sampled by domain reorientation in calmodulin. Proc. Nat. Acad. Sci. 101, 6841-6846.

Bertini, I., Luchinat, C. (1996) "NMR of paramagnetic substances"Elsevier Science, S.A.

Bertini, I., Luchinat, C., Parigi, G. (2002) Magnetic susceptibility in paramagnetic NMR. Prog. NMR Spec. 40, 249-273.

Bonneau, R., Strauss, C.E., Rohl, C.A., Chivian, D., Bradley, P., Malmström, L., Robertson, T., Baker, D. (2002) De novo prediction of three-dimensional structures for major protein families. J. Mol. Biol. 322, 65-78.

Bouvier, D., Vanhaverbeke, C., Simorre, J-P., Arlaud, G.J., Bally, I., Forge, V., Margolis, R.L., Gans, P., Kleman, J-P. (2003) Unusual Ca^{2+}-calmodulin binding interactions of the microtubule-associated protein F-STOP. Biochemistry. 42, 11484-11493.

Brooks, B.R., Bruccoleri, R.E., Olafson, B.D., States, D.J, Swaminathan, S., Karplus, M. (1983) CHARMM: A program for macromolecular energy, minimization, and dynamics calculations. J. Comp. Chem. 4, 187-217.

Brose, N., Rosenmund, C., (2002) Move over protein kinase C, you've company: alternative cellular effectors of diacylglycerol and phorbol esters. J. Cell. Sci. 115, 4399-4411.

Brüschweiler, R. (1994) Measurements and theoretical models of structural dynamics of biopolymers in solution. In: Tycko, R. (ed.) Nuclear Magnetic Resonance Probes of Molecular Dynamics. Kluwer Acad. Publ. 301-334.

Cavanagh, J., Fairbrother, W.J., Palmer, A.G., Skelton, N.J. (1996) Protein NMR spectroscopy: Principles and Practice. Academic Press. San Diego. 587pp.

Chang, S-L., Szabo, A., Tjandra, N. (2003) Temperature dependence of domain motions of calmodulin probed by NMR relaxation at multiple fields. J. Am. Chem. Soc. 125, 11379-11384.

Chang, S-L., Tjandra, N. (2001) Analysis of NMR relaxation data of biomolecules with slow domain motions using wobble-in-a-cone approximation. J. Am. Chem. Soc. 123, 11484-11485.

Chen, Y-G., Hummer, G. (2007) Slow conformational dynamics and unfolding of the calmodulin C-terminal domain. J. Am. Chem. Soc. 129, 2414-2415.

Chou, J.J., Li, S., Bax, A. (2000) Study of conformational rearrangement and refinement of structural homology models by the use of heteronuclear dipolar couplings. J. Biomol. NMR. 18, 217-227.

Chou, J.J., Li, S., Klee, C.B., Bax, A. (2001) Solution structure of Ca^{2+}-calmodulin reveals flexible hand-like properties of its domains. Nature Struct. Biol. 8, 990-997.

Clore, G.M. (2000) Accurate and rapid docking of protein-protein complexes on the basis of intermolecular nuclear Overhauser enhancement data an dipolar couplings by rigid body minimization. Proc. Nat. Acad. Sci. 97, 9021-9025.

Cornilescu, G., Delaglio, F., Bax, A. (1999) Protein backbone angle restraints from searching a database for chemical shift and sequence homology. J. Biomol. NMR. 13, 289-302.

Delaglio, F., Grzesiek, S., Vuister, G.W., Zhu, G., Pfeifer, J., Bax, A. (1995) NMRPipe: a multidimensional spectral processing system based on UNIX pipes. J. Biomol. NMR. 6, 277-293.

Dimova, K., Kawabe, H., Betz, A., Brose, N., Jahn, O. (2006) Characterization of the Munc13-1-calmodulin interaction by photoaffinity labeling. Biochim. Biophys. Acta. 1763, 1256-1265.

Drum C.L., Yan, S-Z., Bard, J., Shen, Y-Q., Lu, D., Soelaiman, S., Grabarek, Z., Bohm, A., Tang, W-J. (2002) Structural basis for the activation of anthrax adenylyl cyclase exotoxin by calmodulin. Nature. 415, 396-402.

Dulubova, I., Lou, X., Lu, J., Huryeva, I., Alam, A., Schneggenburger, R., Südhof, T.C., Rizo, J. (2005) A Mucn13/RIM/Rab3 tripartite complex: from priming to plasticity? The EMBO J. 24, 2839-2850.

Elshorst, B., Hennig, M., Försterling, H., Diener, A., Maurer, M., Schulte, P., Schwalbe, H., Griesinger, C., Krebs, J., Schmid, H., Vorherr, T., Carafoli, E. (1999) NMR solution structure of a complex of calmodulin with a binding peptide of the Ca^{2+} pump. Biochemistry. 38, 12320-12332.

Erickson, M.G., Alseikhan, B.A., Peterson, B.Z., Yue, D.T. (2001) Preassociation of calmodulin with voltage-gated Ca^{2+} channels revealed by FRET in single living cells. Neuron. 31, 973-985.

Falke, J.J. (2002) Enzymology. A moving story. Science 295, 1480-1.

Fallon, J.L., Quiocho, F.A. (2003) A closed compact structure of native Ca^{2+}-calmodulin. Structure. 11, 1303-1307.

Florida State University (FSU). 1999. http://fajerpc.magnet.fsu.edu.

Gaponenko, V., Sarma, S.P., Altieri, A.S., Horita, D.A., Li, J., Byrd, A. (2004) Improving the accuracy of NMR structures of large proteins using pseudocontact shifts as long-range restraints. J. Biomol. NMR. 28, 205-212.

Goddard, T.D., Kneller, D.G. (1999) SPARKY 3. University of California, San Francisco.

Grzesiek, S., Anglister, J., Ren, H., Bax, A. (1993) Carbon-13 line narrowing by deuterium decoupling in deuterium/carbon-13/nitrogen-15 enriched proteins. Application to triple resonance 4D J connectivity of sequential amides. J. Am. Chem. Soc. 115, 4369-4370.

Groffen, A.J., Friedrich, R., Brian, E.C., Ashery, U., Verhage, M. (2006) DOC2A and DOC2B are sensors for neuronal activity with unique calcium-dependent and kinetic properties. J. Neurochem. 97, 818-833.

Güntert, P., Mumenthaler, C., Wüthrich, K. (1997) Torsion Angle Dynamics for NMR structure calculation with the new program DYANA. J. Mol. Biol. 273, 283-298.

Haberz, P., Rodríguez-Castañeda, F., Junker, J., Becker, S., Leonov, A., Griesinger, C. (2006) Two new chiral EDTA-Based metal chelates for weak alignment of proteins in solution. Org. Letters. 8, 1275-1278.

Heidorn, D.B., Trewhella, J. (1988) Comparison of the crystal and solution structures of calmodulin and troponin C. Biochemistry. 27, 909-915.

Herrmann, T., Güntert, P., Wüthrich, K. (2002) Protein NMR structure determination with automated NOE assignment using the new software CANDID and the Torsion Angle Dynamics Algorithm DYANA. J. Mol. Biol. 319, 209-227.

Hoeflich, K.P., Ikura, M. (2002). Calmodulin in action: diversity in target recognition and activation mechanisms. Cell. 108, 739-742.

Holthoff, K., Tsay, D. (2002) Calcium dynamics in spines: link to synaptic plasticity. Exp. Physiol. 87, 725-731.

Igumenova, T.I., Lee, A.L., Wand, A.J. (2005) Backbone and side chain dynamics of mutant calmodulin-peptide complexes. Biochemistry. 44, 12627-12639.

Ikegami, T., Verdier, L., Sakhaii, P., Grimme, S., Pescatore, B., Saxena, K., Fiebig, K.M., Griesinger, C. (2004) Novel techniques for weak alignment of proteins in solution using chemical tags coordinating lanthanide ions. J. Biomol. NMR. 29, 339-349.

Ikura, M., Ames, J.B. (2006) Genetic polymorphism and protein conformational plasticity in the calmodulin superfamily: Two ways to promote multifunctionality. Proc. Nat. Acad. Sci. 103, 1159-1164.

Ikura, M., Barbato, G., Klee, C.B., Bax, A. (1992) Solution structure of calmodulin and its complex with a myosin light chain kinase fragment. Cell Calcium. 13, 391-400.

Ikura, M., Clore, G.M., Gronenborn, A.M., Zhu, G., Klee, C.B., Bax, A. (1992) Solution structure of a calmodulin-target peptide complex by multidimensional NMR. Science. 256, 632-638.

Ikura, M., Kay, L.E., Bax, A. (1990) A novel approach for sequential assignment of 1H, 13C, and 15N spectra of proteins: heteronuclear triple-resonance three-dimensional NMR spectroscopy. Application to calmodulin. Biochemistry. 29, 4659-4667.

Jee, J.G., Güntert, P. (2003) Influence of the completeness of chemical shift assignments on NMR structures obtained with automated NOE assignment. J. Struct. Funct. Gen. 4, 179-189.

Johnson, C.K. (2006) Calmodulin, conformational states, and calcium signaling. A single-molecule perspective. Biochemistry. 45, 14233-14246.

Johnson, C.K., Osborn, K.D., Allen, M.W., Slaughter, B.D. (2005) Single-molecule fluorescence spectroscopy: New probes of protein function and dynamics. Physiology. 20, 10-14.

Junge, H.J., Rhee, J-S., Jahn, O., Varoqueaux, F., Spiess, J., Waxham, M.N., Rosenmund, C., Brose, N. (2004) Calmodulin and Munc13 form a Ca^{2+} sensor/effector complex that controls short-term synaptic plasticity. Cell. 118, 389-401.

Kalla, S., Stern, M., Basu, J., Varoqueaux, F., Reim, K., Rosenmund, C., Ziv, N.E., Brose, N. (2006) Molecular dynamics of a presynaptic active zone protein studied in Munc13-1-Enhanced Yellow Fluorescent Protein Knock-In mutant mice. J. Neurosci. 26, 13054-13066.

Kataoka, M., Head, J.F., Vorherr, T., Krebs, J., Carafoli, E. (1991) Small-angle X-ray scattering study of calmodulin bound to two peptides corresponding to parts of the calmodulin-binding domain of the plasma membrane Ca^{2+} pump. Biochemistry. 30, 6247-6251.

Kazanietz, M.G. (2002) Novel "Nonkinase" phorbol ester receptors: The C1 domain connection. Mol. Pharmacol. 61, 759-767.

Kazanietz, M.G., Barchi, J.J., Omichinski, J.G., Blumberg, P.M. (1995) Low affinity binding of phorbol esters to protein kinase C and its recombinant cysteine-rich region in the absence of phospholipids. J. Biol. Chem. 270, 14679-14684.

Kensal, E., van Holde, W., Johnson, C., Ho, P-S. (2006) Principles of physical biochemistry. 2nd. Ed. Prentice Hall. New Jersey, USA. 752pp.

Kubinowa, H., Tjandra, N., Grzesiek, S., Ren, H., Klee, C.B., Bax, A. (1995) Solution structure of calcium-free calmodulin. Nat. Struct. Biol. 2, 768-776.

Larsson, G., Schleucher, J., Onions, J., Hermann, S., Grundström, T., Wijmenga, S.S. (2001) A novel target recognition revealed by calmodulin in complex with the basic helix-loop-helix transcription factor SEF2-1/E2-2. Prot. Sci. 10, 169-186.

Larsson, G., Schleucher, J., Onions, J., Hermann, S., Grundström, T., Wijmenga, S.S. (2005) Backbone dynamics of a symmetric calmodulin dimer in complex with the calmodulin-binding domain of the basic-helix-loop-helix transcription factor SEF2-1/E2-2: A highly dynamic complex. Biophys. J. 89, 1214-1226.

Laskowski, R.A., Rullman, J.A.C., MacArthur, M.W., Kaptein, R., Thornton, J.M. (1996) AQUA and PROCHECK-NMR: Programs for checking the quality of protein structures solved by NMR. J. Biomol. NMR. 8, 477-486.

Leenders, A.G.M., Sheng, Z-H. (2005) Modulation of neurostransmitter release by the second messenger-activated protein kinases: implications for presynaptic plasticity. Pharmacol. Ther. 105, 69-84.

LeMaster, D.M. (1990) Deuterium labelling in NMR structural analysis of larger proteins. Q. Rev. Biophys. 23, 133-174.

Leonov, A., Voigt, B., Rodríguez-Castañeda, F., Sakhaii, P., Griesinger, C. (2005) Convenient syntheses of multifunctional EDTA-Based chiral metal chelates substituted with an S-mesylcysteine. Chem. Eur. J. 11, 1-8.

Li, L., Chin, L-S. (2003) The molecular machinery of synaptic vesicle exocytosis. CMLS, Cell. Mol. Life Sci. 60, 942-960.

Linge, J.P., Williams, M.A., Spronk, C.A.E.M., Bonvin, A.M.J.J., Nilges, M. (2003) Refinement of protein structures in explicit solvent. Proteins. 50, 496-506.

Lipari, G., Szabo, A. (1981) Nuclear magnetic resonance relaxation in nucleic acid fragments: models for internal motion. Biochemistry. 20, 6250-6256.

Lodish, H., Baltimore, D., Berk, A., Zipursky, S.L., Matsudaira, P., Darnell, J. (2000). Molecular Cell Biology. 4th. Ed. W.H. Freeman and Company. New York.

Lou, X., Scheuss, V., Schneggenburger, R. (2005) Allosteric modulation of the presynaptic Ca^{2+} sensor for vesicle fusion. Nature. 435, 497-501.

Lu, J., Machius, M., Dulubova, I., Dai, H., Südhof, T.C., Tomchick, D.R., Rizo, J. (2006) Structural basis for a Munc13-1 homodimer to munc13-1/RIM heterodimer switch. PLoS Biology. 4, e192.

Markley, J.L. and Kainosho, M. (1993) Stable isotope labeling and resonance assignments in larger proteins. In "NMR of macromolecules"edited by: Roberts, G.C.K. Oxford University Press. 399pp.

Meador, W.E., Means, A.R., Quiocho, F.A. (1993) Modulation of calmodulin plasticity in molecular recognition on the basis of X-ray structures. Science. 262, 1718-1721.

Mittermaier, A., Kay, L.E. (2006) New tools provide new insights in NMR studies of protein dynamics. Science. 312, 224-228.

Mülhardt, C. (2003) Experimentator: Molekularbiologie/Genomics. 4th. Ed. Spektrum Akademischer Verlag. 280pp.

Nofal, S., Becherer, U., Hof, D., Matti, U., Rettig, J. (2007) Primed vesicles can be distinguished from docked vesicles by analyzing their mobility. J. Neurosci. 27, 1386-1395.

Ottiger, M., Delaglio, F., Bax, A. (1998) Measurement of *J* and dipolar couplings from simplified two-dimensional NMR spectra. J. Magn. Res. 131, 373-378.

Panchal, S.C., Bhavesh, N.S., Hosur, R.V. (2001) Improved 3D triple resonance experiments, HNN and HN(C)N, for HN and 15N sequential correlations in (13C, 15N) labeled proteins: application to unfolded proteins. J. Biomol. NMR. 20, 135-147.

Prestegard, J.H., Al-Hashimi, H.M., Tolman, J.R. (2000) NMR structures of biomolecules using field oriented media and residual dipolar couplings. Quarterly Rev. Biophys. 33, 371-424.

Prestegard, J.H., Al-Hashimi, H.M., Tolman, J.R. (2000) NMR structures of biomolecules using field oriented media and residual dipolar couplings. Qarterly Reviews of Biophysics. 33, 371-424.

Rettig, J., Neher, E. (2002) Emerging roles of presynaptic proteins in Ca^{++}-triggered exocytosis. Science. 298, 781-785.

Rhee, J.S., Betz, A., Pyott, S., Reim, K., Varoqueaux, F., Augustin, I., Hesse, D., Südhof, T.C., Takahashi, M., Rosenmund, C., Brose, N. (2002) Beta phorbol ester- and diacylglycerol- induced augmentation of transmitter release is mediated by Munc13s and not by PKCs. Cell. 108, 121-133.

Richmond, J. (2005) Synaptic function, Wormbook, ed. The *C. elegans* Research Community, Wormbook, doi/10.1895/wormbook.1.69.1, http://www.wormbook.org.

Rodríguez-Castañeda, F., Haberz, P., Leonov, A., Griesinger, C. (2006) Paramagnetic tagging of diamagnetic proteins for solution NMR. Magn. Reson. Chem. 44, S10-S16.

Sambrook, J., Russell, D.W. (2001) Molcular Cloning: A Laboratory Manual. 3rd Ed. Cold Spring Harbor Laboratry Press. New York. 2344pp.

Samsó, M., Wagenknecht, T. (2002) Apocalmodulin and Ca^{2+}-Calmodulin bind to neighboring locations on the ryanodine receptor. J. Biol. Chem. 277, 1349-1353.

Sartor, M. (2003) Dynamic Light Scattering. University of California San Diego. USA.

Sattler, M., Schleucher, J., Griesinger, C. (1999) Heteronuclear multidimensional NMR experiments for the structure determination of proteins in solution. Prog. NMR Spec. 34, 93ß158.

Shen, N., Guryev, O., Rizo, J. (2005) Intramolecular occlusion of the diacylglycerol binding site in the C_1 domain of munc13-1. Biochemistry. 44, 1089-1096.

Schumacher, M.A., Rivard, A.F., Bächinger, H.P., Adelman, J.P. (2001) Structure of the gating domain of a Ca^{2+}-activated K^+ channel complexed with Ca^{2+}/calmodulin. Nature. 410, 1120-1124.

Shen, N., Guryev, O., Rizo, J. (2005) Intramolecular occlusion of the Diacylglycerol-binding site in the C1 domain of Munc13-1. Biochemistry. 44, 1089-1096.

Siivari, K., Zhang, M., Palmer III, A.G., Vogel, H.J. (1995) NMR studies of the methionine methyl groups in calmodulin. FEBS Letters. 366, 104-108.

Silinski, E.M., Searl, T.J. (2003) Phorbol esters and neurotransmitter release: more than just protein kinase C? British J. of Pharm. 138, 1191-1201.

Stevens, D.R., Wu, Z-X., Matti, U., Junge, H.J., Schirra, C., Becherer, U., Wojcik, S.M., Brose, N., Rettig, J. (2005) Identification of the minimal protein domain required for priming activity of Munc13-1. Curr. Biol. 15, 2243-2248.

Südhof, T.C. (2004) The synaptic vesicle cycle. Annu. Rev. Neurosci. 27, 509-547.

Tjandra, N., Bax, A. (1997) Direct measurement of distances and angles in biomolecules by NMR in a dilute liquid crystalline medium. Science. 278, 1111-1114.

Tjandra, N., Kuboniwa, H., Ren, H., Bax, A. (1995) Rotational dynamics of calcium-free calmodulin studied by ^{15}N-NMR relaxation measurements. Eur. J. Biochem. 230, 1014-1024.

Tüchelman, A. (1999) Synthese paramagnetischer Tags für Biomakromoleküle und applikation elektrischer felder zur gewinnung langreichweitiger NMR-Strukturinformation. Dissertation. Frankfurt am Main. 234 pp.

Van Petegem, F., Chatelain, F.C., Minor, D.L.Jr. (2005) Insights into voltage-gated calcium channel regulation from the structure of the CaV1.2 IQ domain-Ca^{2+}/calmodulin complex. Nat. Struct. Biol. 12, 1108-1115.

Velyvis, A., Yang, Y.R., Schachman, H.K., Kay, L.E. (2007) A solution NMR study showing that active site ligands and nucleotides directly perturb the allosteric equilibrium in aspartate transcarbamoylase. Proc. Nat. Acad. Sci. 104, 8815-8820.

Vetter, S.W., Leclerc, E. (2003) Novel aspects of calmodulin target recognition and activation. Eur. J. Biochem. 270, 404-414.

Vriend, G. (1990) WHAT IF: a molecular modeling and drug design program. J. Mol. Graph. 8, 52-56.

Wang, T., Frederick, K.K., Igumenova, T.I., Wand, A.J., Zuiderweg, E.R. (2005) Changes in calmodulin main-chain dynamics upon ligand binding revealed by cross-correlated NMR relaxation measurements. J. Am. Chem. Soc. 127, 828-829.

Wand, A.J. (2001) On the dynamics origins of allosteric activation. Science. 293, 1395.

Watterson, D.M., Sharief, F., Vanaman, T.C. (1980) The complete amino acid sequence of the Ca^{2+}-dependent modulator protein (calmodulin) of bovine brain. J. Biol. Chem. 255, 962-975.

Wishart, D.S., Sykes, B.D. (1994) The 13C chemical-shift index: A simple method for the identification of protein secondary structure using 13C chemical-shift data. J. Biomol. NMR. 4, 171-180.

Wolff, D.J., Huebner, J.A., Siegel, F.L. (1972) Calcium-binding phosphoprotein of pig brain: effects of cations on the calcium binding. J. Neurochem. 19, 2855-2862.

Wu, X.S., Wu, L.G. (2001) Protein kinase C increases the apparent affinity of the release machinery to Ca2+ by enhancing the release machinery downstream of the Ca2+ sensor. J. Neurosci. 21, 7928-7936.

Wühtrich, K. (1986) NMR of proteins and nucleic acids. John Wiley & Sons, Inc. 292pp.

Xia, Z., Storm, D.R. (2005) The role of calmodulin as a signal integrator for synaptic plasticity. Nature reviews neuroscience. 6, 267-275.

Xu, X-Z. S., Wes, P.D., Chen, H., Li, H-S., Yu, M., Morgan, S., Liu, Y., Montell, C. (1998) Retinal targets for calmodulin include proteins implicated in synaptic transmission. J. Biol. Chem. 273, 31297-31307.

Yang, C., Jas, G.S., Kuczera, K. (2003) Structure, dynamics and interaction with kinase targets: computer simulations of calmodulin. Biochim. Biophys. Acta. 1697, 289-300.

Yap, K.L., Yuan, T., Mal, T.K., Vogel, H.J., Ikura, M. (2003) Structural basis for simultaneous binding of two carboxy-terminal peptides of plant glutamate decarboxylase to calmodulin. J. Mol. Biol. 328, 193-204.

Zhang, G., Kazanietz, M.G., Blumberg, P.M., Hurley, J.H. (1995) Crystal structure of the Cys2 activator-binding domain of protein knase Cδ in complex with phorbol ester. Cell. 81, 917-924.

Zweckstetter, M., Bax, A. (2000) Prediction of sterically induced alignment in a dilute liquid crystalline phase: aid to protein structure determination by NMR. J. Am. Chem. Soc. 122, 3791-3792.

VII. APENDIX

1. *Magnetization pathways in the backbone nuclei of the polypeptide chain*

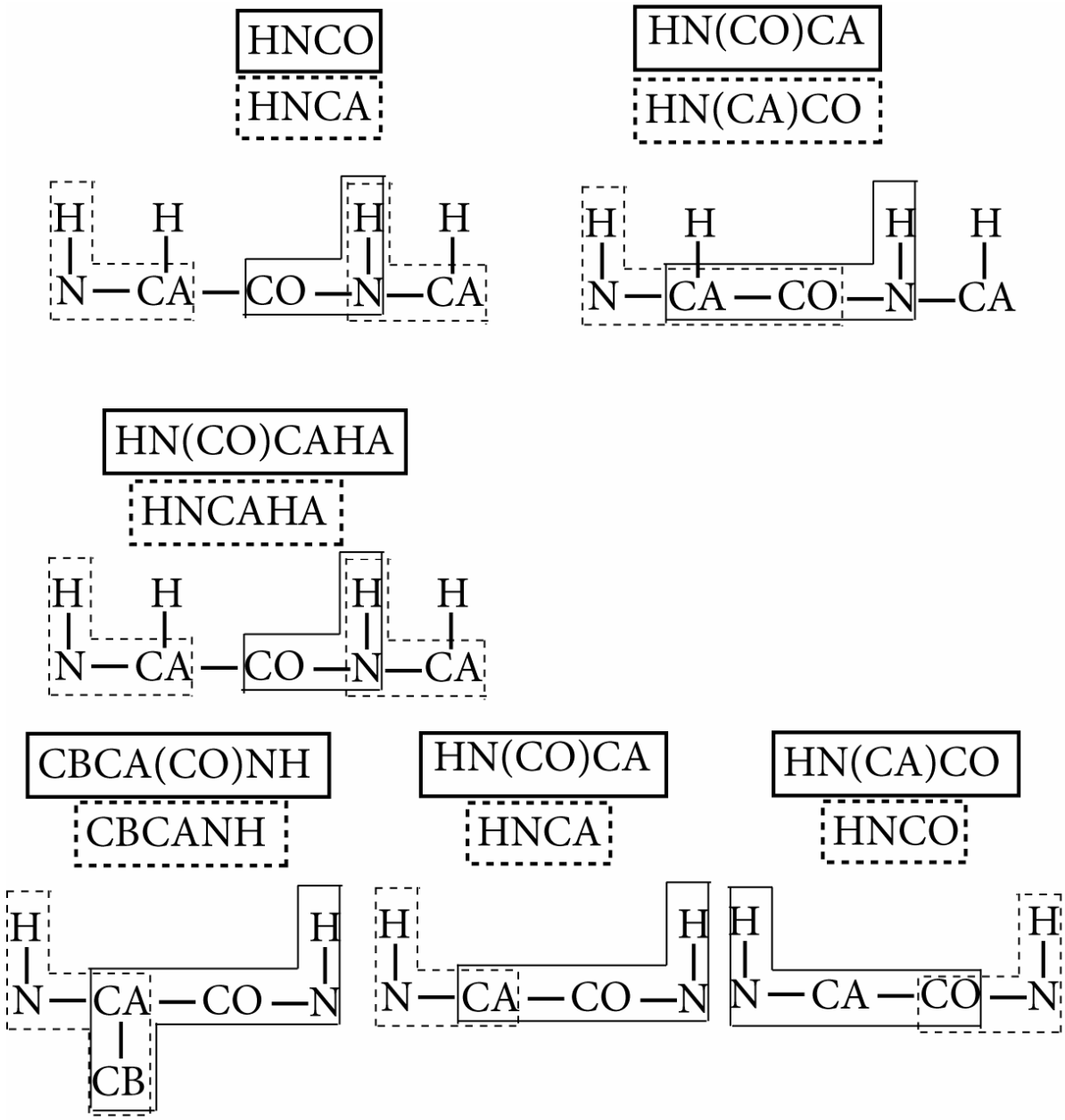

2. Pictorial view of the heteronuclear multidimensional NMR pulse sequences

a. Pulse sequence for atomatic side chain resonance assignment

(Hβ)Cβ(CγCδ)Hδ and (Hβ)Cβ(CγCδCε)Hε

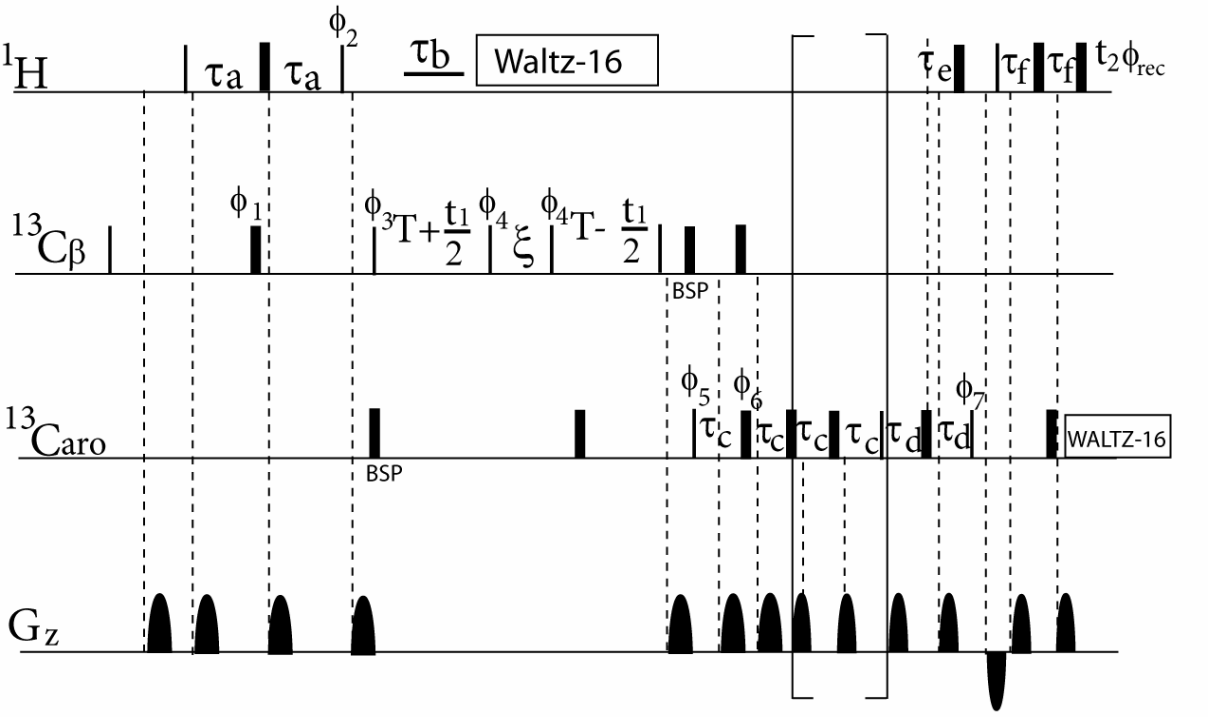

b. CBCA(CO)NH Pulse sequence for sequential backbone resonance assignment

3D CBCA(CO)NH Hβ,Hα -> Cβ,Cα(t_1) -> C′-> N(t_2) -> H^N(t_3)

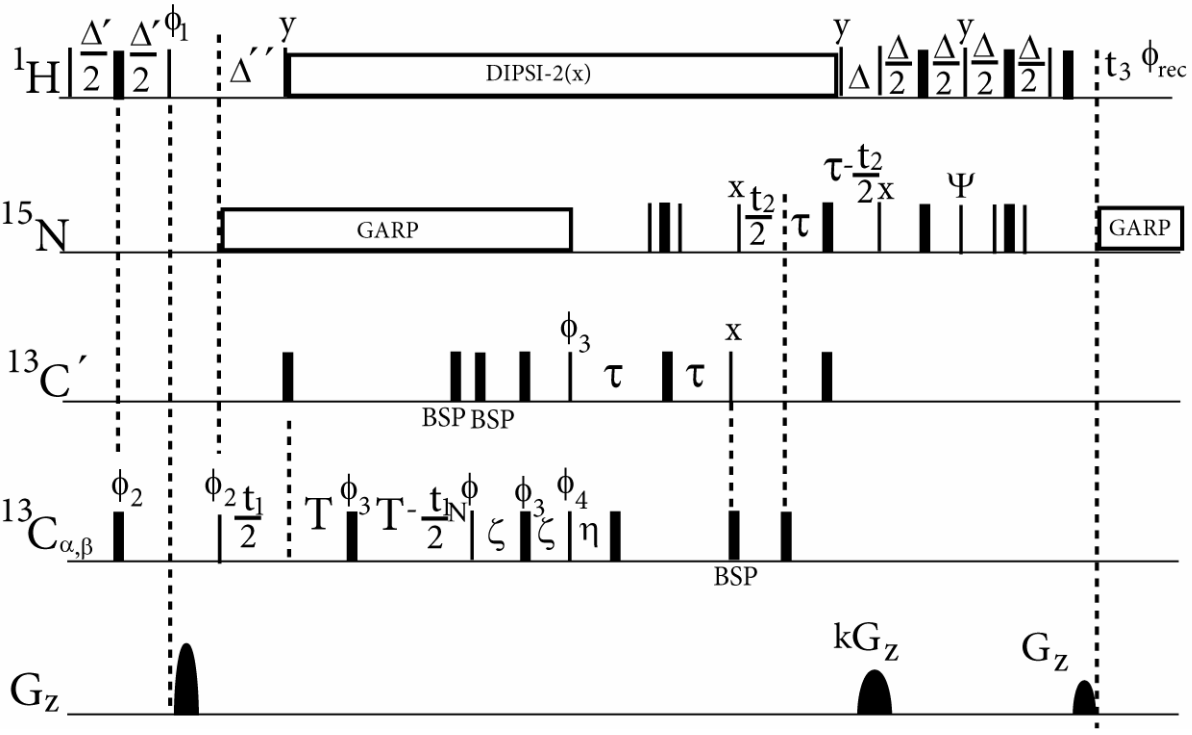

c. HNCA pulse sequence for sequential backbone resonance assignment

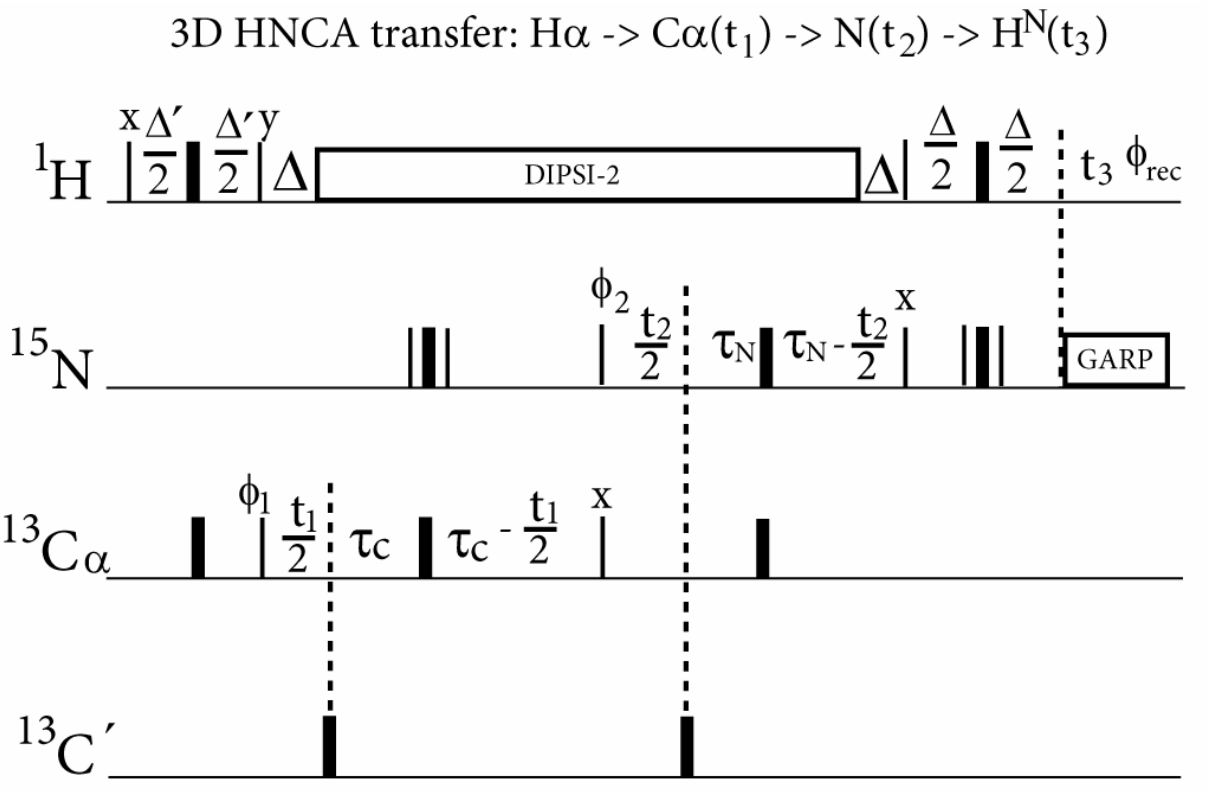

d. HNCACB pulse sequence for sequential backbone resonance assignment

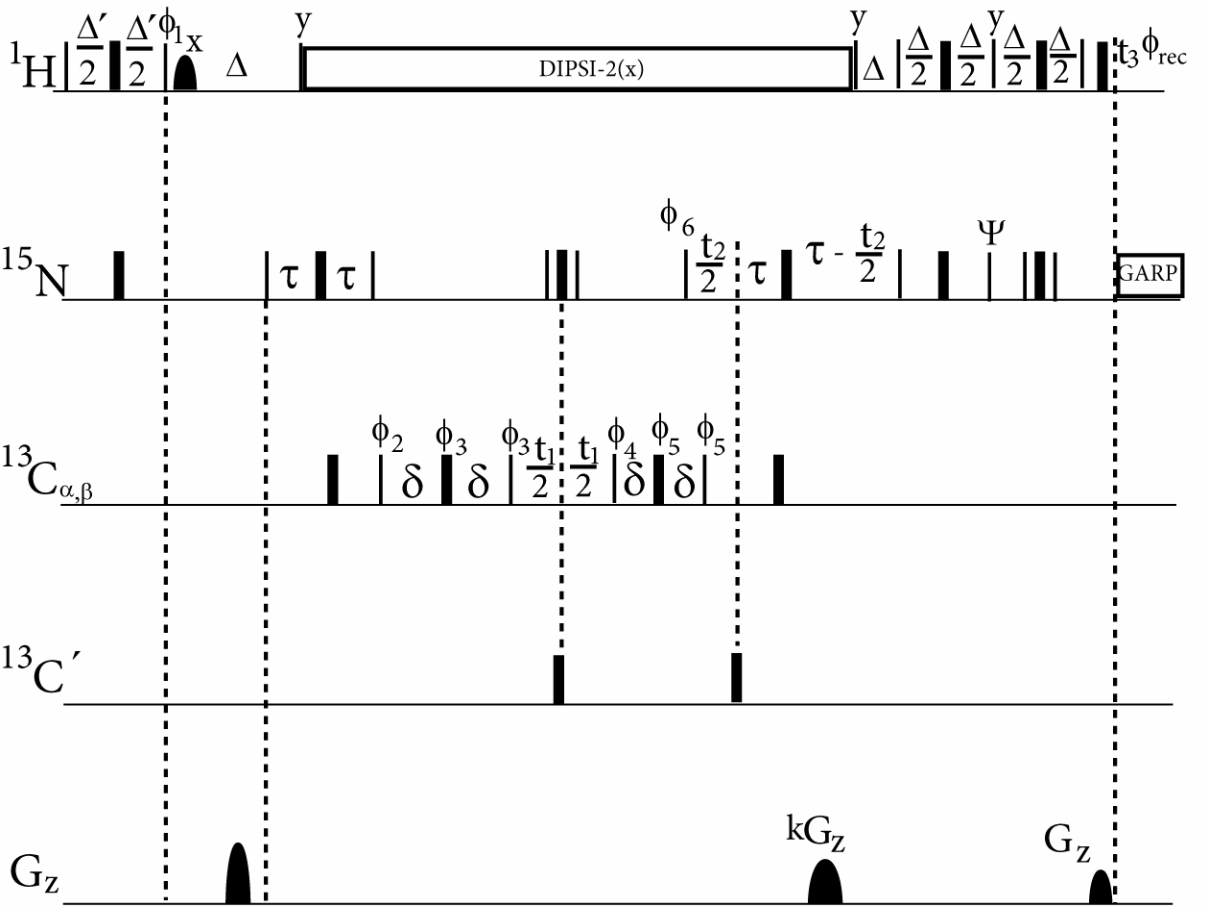

e. HNN pulse sequence for sequential backbone resonance assignment

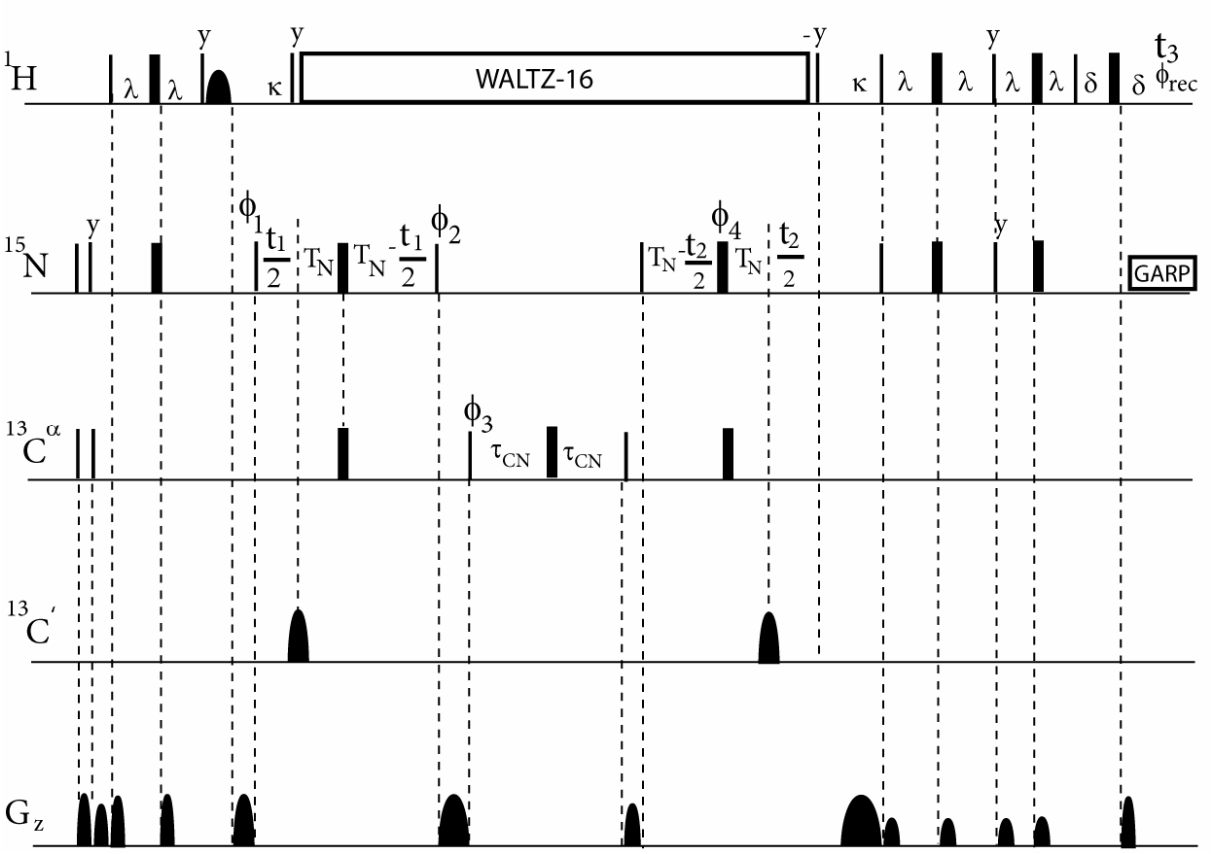

f. Pulse sequence for the resonance assignment of ε-methyl groups in methionines

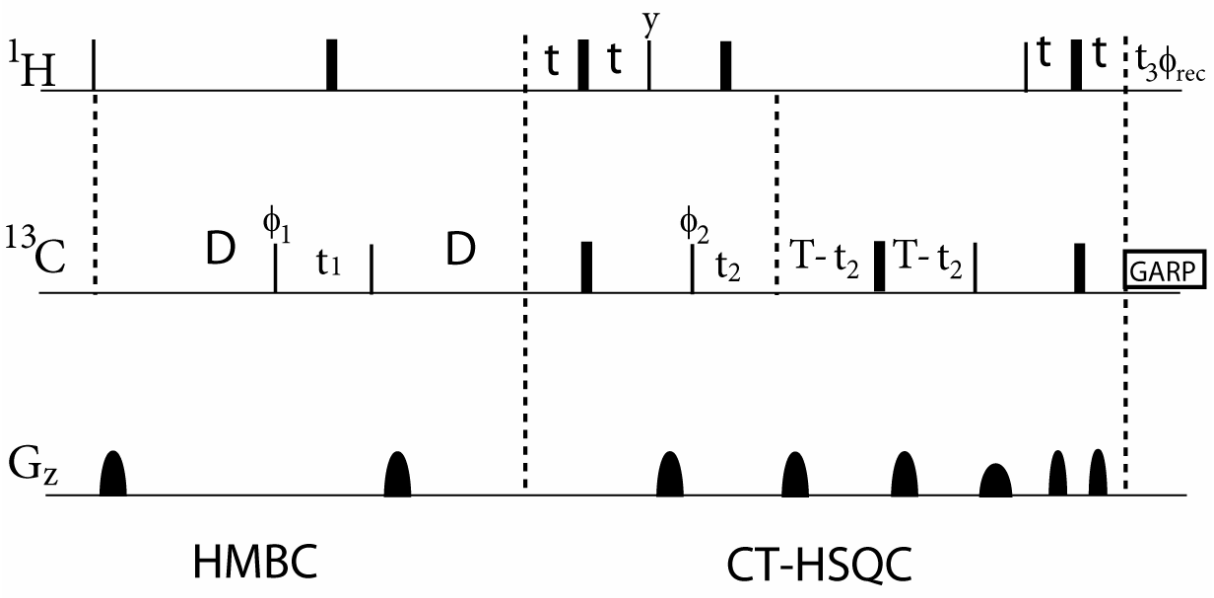

g. Pulse sequence of the 3D-^{15}N-edited-NOESY-HSQC

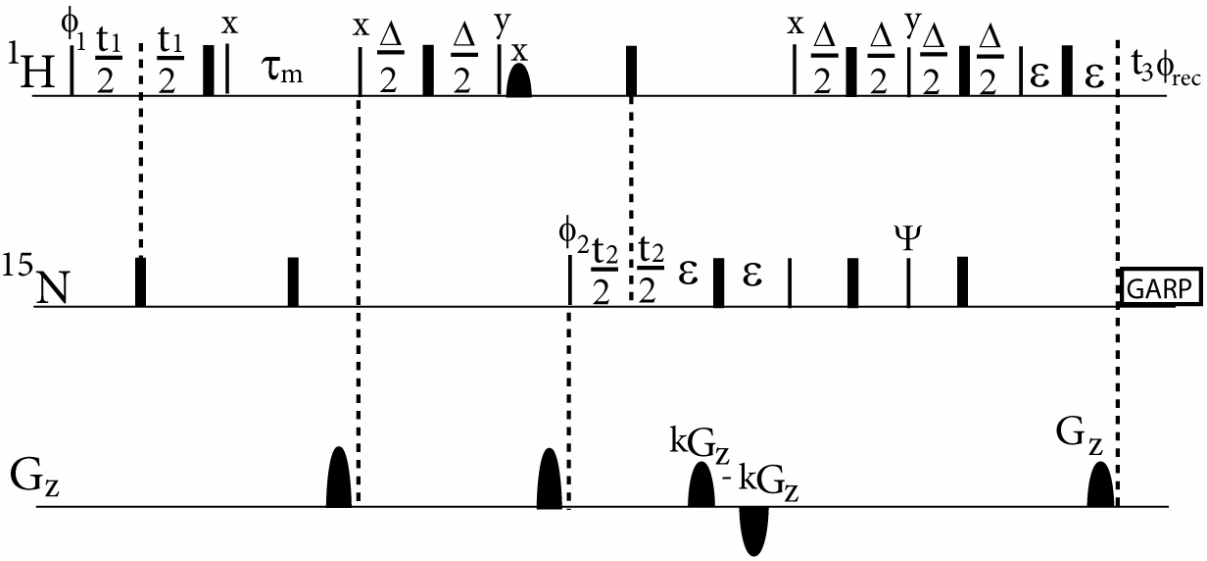

h. Pulse sequence of the isotope-filetered 3D-^{15}N-edited-NOESY-HSQC

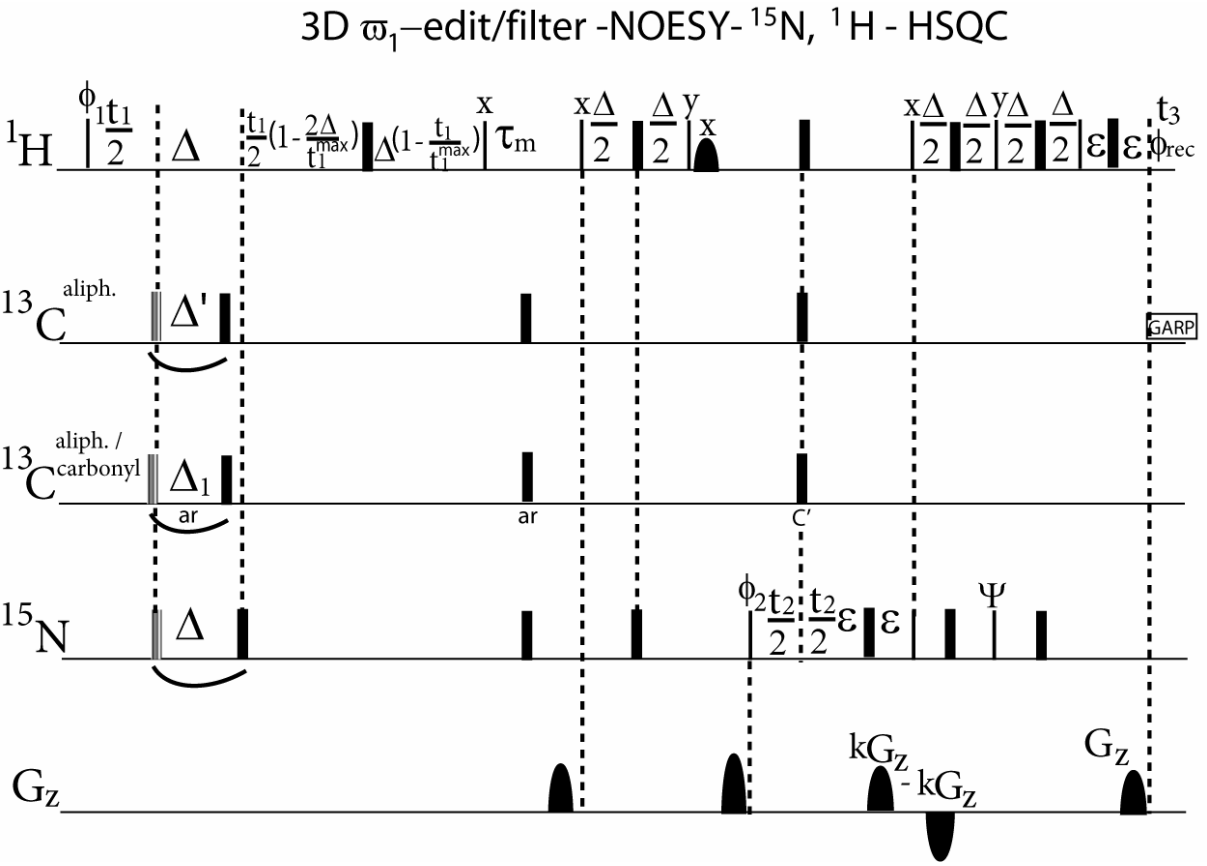

i. Pulse sequence of the IPAP-HSQC (S3E sequence)

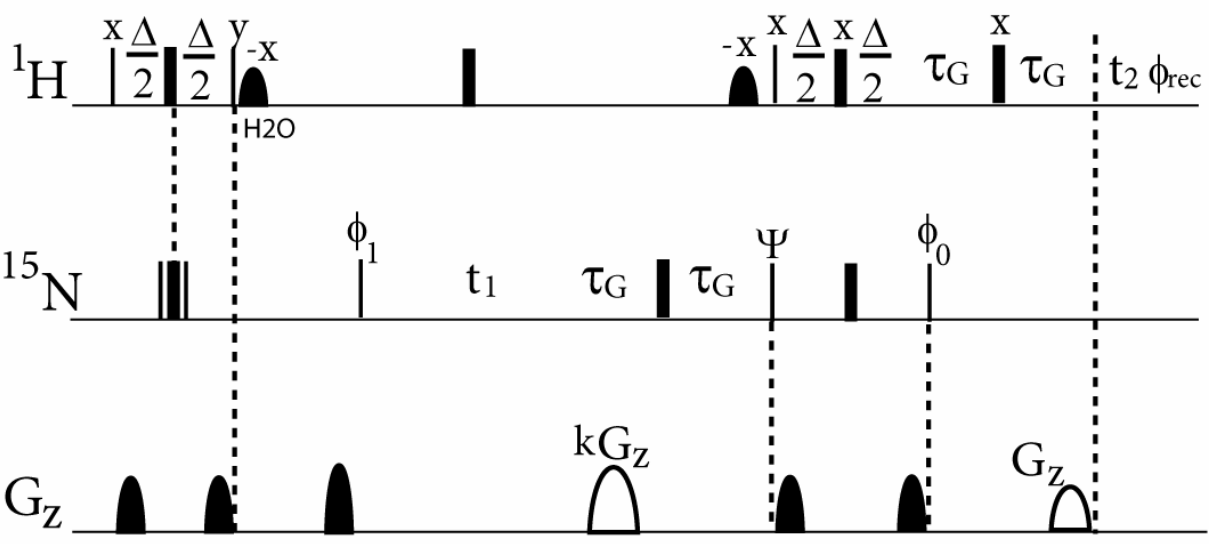

j. Pulse sequence of the TROSY-HSQC

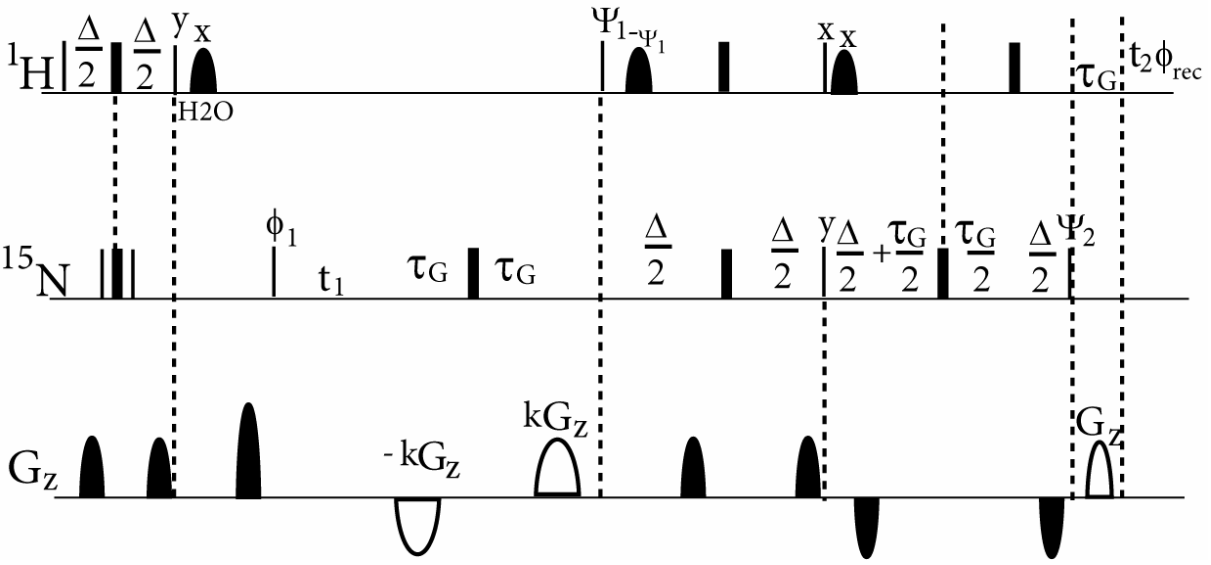

3. Chemical shift assignment list for the CaM/Munc13-1(457-492) peptide complex

Calmodulin

Atom #	Seq #	Res Type	Atom ID	Chem shift	error	Atom #	Seq #	Res Type	Atom ID	Chem shift	error
1	1	ALA	CB	19.353	0.4	58	7	GLU	HB2	2.112	0.05
2	1	ALA	HA	4.626	0.05	59	7	GLU	HB3	1.956	0.05
3	1	ALA	HB	1.510	0.05	60	7	GLU	N	118.929	0.4
4	2	ASP	C	172.776	0.4	61	7	GLU	HG2	2.348	0.05
5	2	ASP	CA	54.72	0.4	62	8	GLN	C	175.426	0.4
6	2	ASP	CB	41.41	0.4	63	8	GLN	CA	59.201	0.4
7	2	ASP	H	8.649	0.05	64	8	GLN	CB	29.297	0.4
8	2	ASP	HA	4.623	0.05	65	8	GLN	CG	34.994	0.4
9	2	ASP	HB2	2.657	0.05	66	8	GLN	H	7.726	0.05
10	2	ASP	HB3	2.577	0.05	67	8	GLN	HA	4.016	0.05
11	2	ASP	N	120.4	0.4	68	8	GLN	HB2	2.074	0.05
12	3	GLN	C	172.795	0.4	69	8	GLN	HB3	1.951	0.05
13	3	GLN	CA	55.508	0.4	70	8	GLN	N	119.631	0.4
14	3	GLN	CB	29.622	0.4	71	8	GLN	HG2	2.346	0.05
15	3	GLN	CG	33.763	0.4	72	9	ILE	C	174.972	0.4
16	3	GLN	H	8.348	0.05	73	9	ILE	CA	66.243	0.4
17	3	GLN	HA	4.371	0.05	74	9	ILE	CB	37.652	0.4
18	3	GLN	HB2	2.099	0.05	75	9	ILE	CG1	30.055	0.4
19	3	GLN	HB3	1.984	0.05	76	9	ILE	CG2	17.330	0.4
20	3	GLN	N	119.406	0.4	77	9	ILE	H	8.355	0.05
21	3	GLN	HG2	2.343	0.05	78	9	ILE	HA	3.667	0.05
22	4	LEU	C	174.846	0.4	79	9	ILE	HB	1.946	0.05
23	4	LEU	CA	54.428	0.4	80	9	ILE	HD1	0.869	0.05
24	4	LEU	CB	43.435	0.4	81	9	ILE	HG12	1.789	0.05
25	4	LEU	CD1	26.518	0.4	82	9	ILE	HG13	1.100	0.05
26	4	LEU	CD2	23.607	0.4	83	9	ILE	HG2	1.108	0.05
27	4	LEU	CG	26.711	0.4	84	9	ILE	N	119.286	0.4
28	4	LEU	H	8.275	0.05	85	10	ALA	C	178.227	0.4
29	4	LEU	HA	4.665	0.05	86	10	ALA	CA	55.338	0.4
30	4	LEU	HB2	1.719	0.05	87	10	ALA	CB	17.746	0.4
31	4	LEU	HB3	1.508	0.05	88	10	ALA	H	8.037	0.05
32	4	LEU	HD1	0.921	0.05	89	10	ALA	HA	4.114	0.05
33	4	LEU	HD2	0.913	0.05	90	10	ALA	HB	1.520	0.05
34	4	LEU	N	122.55	0.4	91	10	ALA	N	120.74	0.4
35	5	THR	C	172.634	0.4	92	11	GLU	C	177.704	0.4
36	5	THR	CA	60.493	0.4	93	11	GLU	CA	59.453	0.4
37	5	THR	CB	71.039	0.4	94	11	GLU	CB	28.33	0.4
38	5	THR	H	8.660	0.05	95	11	GLU	CG	35.588	0.4
39	5	THR	HA	4.457	0.05	96	11	GLU	H	7.847	0.05
40	5	THR	HB	4.742	0.05	97	11	GLU	HA	4.162	0.05
41	5	THR	HG2	1.334	0.05	98	11	GLU	HB2	2.097	0.05
42	5	THR	N	112.406	0.4	99	11	GLU	HB3	2.017	0.05
43	6	GLU	C	176.679	0.4	100	11	GLU	N	118.942	0.4
44	6	GLU	CA	60.113	0.4	101	11	GLU	HG2	2.0148	0.05
45	6	GLU	CB	28.877	0.4	102	12	PHE	C	175.906	0.4
46	6	GLU	CG	36.465	0.4	103	12	PHE	CA	58.9768	0.4
47	6	GLU	H	9.016	0.05	104	12	PHE	CB	37.4318	0.4
48	6	GLU	HA	3.988	0.05	105	12	PHE	CD1	128.343	0.4
49	6	GLU	N	120.053	0.4	106	12	PHE	CD2	128.343	0.4
50	6	GLU	HB2	2.069	0.05	107	12	PHE	H	8.6068	0.05
51	6	GLU	HG2	2.369	0.05	108	12	PHE	HA	5.0048	0.05
52	7	GLU	C	176.396	0.4	109	12	PHE	HB2	3.5338	0.05
53	7	GLU	CA	59.476	0.4	110	12	PHE	HB3	3.4618	0.05
54	7	GLU	CB	29.216	0.4	111	12	PHE	N	119.64	0.4
55	7	GLU	CG	36.573	0.4	112	12	PHE	HD1	7.1668	0.05
56	7	GLU	H	8.665	0.05	113	12	PHE	HD2	7.1668	0.05
57	7	GLU	HA	4.088	0.05	114	12	PHE	HE1	7.2128	0.05

115	12	PHE	HE2	7.2128	0.05	175	19	PHE	CA	59.102	0.4
116	12	PHE	HZ	6.7078	0.05	176	19	PHE	CB	40.413	0.4
117	13	LYS	C	176.515	0.4	177	19	PHE	N	114.926	0.4
118	13	LYS	CA	59.815	0.4	178	19	PHE	HA	3.8578	0.05
119	13	LYS	CB	31.056	0.4	179	19	PHE	HB2	2.631	0.05
120	13	LYS	H	9.2148	0.05	180	19	PHE	CB	41.4328	0.4
121	13	LYS	HA	4.0098	0.05	181	19	PHE	CD1	128.595	0.4
122	13	LYS	N	122.92	0.4	182	19	PHE	CD2	128.595	0.4
123	13	LYS	HB2	1.9098	0.05	183	19	PHE	H	7.0848	0.05
124	13	LYS	HG2	0.6978	0.05	184	19	PHE	HD1	7.3118	0.05
125	13	LYS	HD2	1.2578	0.05	185	19	PHE	HD2	7.3118	0.05
126	13	LYS	HD3	1.1078	0.05	186	19	PHE	HE1	7.2768	0.05
127	13	LYS	HE2	2.5478	0.05	187	19	PHE	HE2	7.2768	0.05
128	14	GLU	C	176.562	0.4	188	20	ASP	C	174.355	0.4
129	14	GLU	CA	58.722	0.4	189	20	ASP	CA	56.149	0.4
130	14	GLU	CB	28.825	0.4	190	20	ASP	CB	39.0518	0.4
131	14	GLU	H	7.7328	0.05	191	20	ASP	H	7.7588	0.05
132	14	GLU	N	119.254	0.4	192	20	ASP	HB2	2.4478	0.05
133	14	GLU	HA	3.8078	0.05	193	20	ASP	HA	4.5518	0.05
134	14	GLU	HB2	1.8978	0.05	194	20	ASP	N	116.333	0.4
135	14	GLU	HG2	2.0778	0.05	195	21	LYS	C	175.352	0.4
136	15	ALA	C	176.2	0.4	196	21	LYS	CA	58.4158	0.4
137	15	ALA	CA	55.2968	0.4	197	21	LYS	CB	32.6218	0.4
138	15	ALA	CB	18.4428	0.4	198	21	LYS	CD	28.1138	0.4
139	15	ALA	H	8.0278	0.05	199	21	LYS	CE	41.9438	0.4
140	15	ALA	HA	4.2028	0.05	200	21	LYS	CG	24.1018	0.4
141	15	ALA	HB	1.9258	0.05	201	21	LYS	H	7.6578	0.05
142	15	ALA	N	121.803	0.4	202	21	LYS	HA	3.9788	0.05
143	16	PHE	C	174.515	0.4	203	21	LYS	N	123.905	0.4
144	16	PHE	CA	61.9028	0.4	204	21	LYS	HB2	1.8628	0.05
145	16	PHE	CB	39.7248	0.4	205	21	LYS	HE2	2.9678	0.05
146	16	PHE	CE1	129.482	0.4	206	21	LYS	HG2	1.5388	0.05
147	16	PHE	CE2	129.482	0.4	207	21	LYS	HD2	1.8878	0.05
148	16	PHE	H	8.7548	0.05	208	22	ASP	C	174.872	0.4
149	16	PHE	HA	3.2708	0.05	209	22	ASP	CA	52.9928	0.4
150	16	PHE	N	118.544	0.4	210	22	ASP	CB	39.6798	0.4
151	16	PHE	HB2	2.9218	0.05	211	22	ASP	H	8.1708	0.05
152	16	PHE	HD1	6.5058	0.05	212	22	ASP	HA	4.5878	0.05
153	16	PHE	HD2	6.5058	0.05	213	22	ASP	HB2	2.7078	0.05
154	16	PHE	HE1	6.9738	0.05	214	22	ASP	HB3	2.2978	0.05
155	16	PHE	HE2	6.9738	0.05	215	22	ASP	N	113.617	0.4
156	17	SER	C	172.086	0.4	216	23	GLY	C	172.439	0.4
157	17	SER	CA	61.6608	0.4	217	23	GLY	CA	47.3378	0.4
158	17	SER	CB	63.2668	0.4	218	23	GLY	H	7.7238	0.05
159	17	SER	H	8.0948	0.05	219	23	GLY	HA2	3.8868	0.05
160	17	SER	HA	4.1188	0.05	220	23	GLY	HA3	3.8808	0.05
161	17	SER	HB2	4.1028	0.05	221	23	GLY	N	108.896	0.4
162	17	SER	N	112.66	0.4	222	24	ASP	C	174.627	0.4
163	18	LEU	C	174.982	0.4	223	24	ASP	CA	53.8208	0.4
164	18	LEU	CA	57.038	0.4	224	24	ASP	CB	40.4658	0.4
165	18	LEU	CB	41.4138	0.4	225	24	ASP	H	8.4838	0.05
166	18	LEU	H	7.4048	0.05	226	24	ASP	HA	4.4938	0.05
167	18	LEU	HA	3.9878	0.05	227	24	ASP	HB2	3.0608	0.05
168	18	LEU	HB2	1.6978	0.05	228	24	ASP	HB3	2.4508	0.05
169	18	LEU	HB3	1.4898	0.05	229	24	ASP	N	120.446	0.4
170	18	LEU	HD1	0.6838	0.05	230	25	GLY	C	170.854	0.4
171	18	LEU	HD2	0.8008	0.05	231	25	GLY	CA	45.2538	0.4
172	18	LEU	HG	1.3278	0.05	232	25	GLY	H	10.6268	0.05
173	18	LEU	N	120.184	0.4	233	25	GLY	HA2	4.3938	0.05
174	19	PHE	C	173.816	0.4	234	25	GLY	HA3	3.7288	0.05

235	25	GLY	N	112.712	0.4	296	32	LEU	CB	42.2968	0.4
236	26	THR	CA	60.71	0.4	297	32	LEU	CD1	25.8618	0.4
237	26	THR	C	170.112	0.4	298	32	LEU	CD2	23.5738	0.4
238	26	THR	CB	72.5468	0.4	299	32	LEU	CG	25.9618	0.4
239	26	THR	CG2	21.7198	0.4	300	32	LEU	H	8.6388	0.05
240	26	THR	H	8.2408	0.05	301	32	LEU	HA	4.0978	0.05
241	26	THR	HA	5.4288	0.05	302	32	LEU	HB2	1.8158	0.05
242	26	THR	HB	3.8598	0.05	303	32	LEU	HB3	1.3948	0.05
243	26	THR	HG2	1.0698	0.05	304	32	LEU	HD1	0.6208	0.05
244	26	THR	N	111.977	0.4	305	32	LEU	HD2	0.6018	0.05
245	27	ILE	H	9.9298	0.05	306	32	LEU	HG	0.5868	0.05
246	27	ILE	C	173.259	0.4	307	32	LEU	N	119.776	0.4
247	27	ILE	CA	60.675	0.4	308	33	GLY	C	172.329	0.4
248	27	ILE	CB	40.092	0.4	309	33	GLY	CA	48.2338	0.4
249	27	ILE	HA	4.8338	0.05	310	33	GLY	H	8.7038	0.05
250	27	ILE	HB	1.8038	0.05	311	33	GLY	HA2	3.9738	0.05
251	27	ILE	HG12	1.2588	0.05	312	33	GLY	HA3	3.5418	0.05
252	27	ILE	HG13	0.9878	0.05	313	33	GLY	N	105.213	0.4
253	27	ILE	HG2	0.3518	0.05	314	34	THR	CA	66.7648	0.4
254	27	ILE	N	126.544	0.4	315	34	THR	CB	68.6728	0.4
255	28	THR	C	173.729	0.4	316	34	THR	H	7.9948	0.05
256	28	THR	CA	59.1738	0.4	317	34	THR	HA	3.9408	0.05
257	28	THR	CB	72.1978	0.4	318	34	THR	HB	4.3668	0.05
258	28	THR	H	8.3888	0.05	319	34	THR	HG2	1.2878	0.05
259	28	THR	HA	4.8678	0.05	320	34	THR	N	117.782	0.4
260	28	THR	HB	4.8228	0.05	321	35	VAL	C	176.416	0.4
261	28	THR	HG2	1.2978	0.05	322	35	VAL	CA	66.5858	0.4
262	28	THR	N	115.935	0.4	323	35	VAL	CB	31.4628	0.4
263	29	THR	C	174.376	0.4	324	35	VAL	CG2	20.5538	0.4
264	29	THR	CA	66.4158	0.4	325	35	VAL	H	7.8458	0.05
265	29	THR	CB	68.1808	0.4	326	35	VAL	HA	3.6148	0.05
266	29	THR	CG2	23.4908	0.4	327	35	VAL	HB	2.0888	0.05
267	29	THR	H	9.1708	0.05	328	35	VAL	HG1	0.8688	0.05
268	29	THR	HA	3.7388	0.05	329	35	VAL	HG2	0.5318	0.05
269	29	THR	HB	4.1838	0.05	330	35	VAL	N	121.773	0.4
270	29	THR	HG2	1.1998	0.05	331	36	MET	C	176.427	0.4
271	29	THR	N	112.731	0.4	332	36	MET	CA	59.0398	0.4
272	30	LYS	C	177.096	0.4	333	36	MET	CB	30.484	0.4
273	30	LYS	CA	59.2648	0.4	334	36	MET	CE	17.4538	0.4
274	30	LYS	CB	32.4218	0.4	335	36	MET	CG	32.9598	0.4
275	30	LYS	CD	28.9608	0.4	336	36	MET	H	8.6078	0.05
276	30	LYS	CE	41.8798	0.4	337	36	MET	HA	4.1078	0.05
277	30	LYS	CG	24.6968	0.4	338	36	MET	HB2	1.6478	0.05
278	30	LYS	H	7.6038	0.05	339	36	MET	HE	1.8768	0.05
279	30	LYS	HA	4.1078	0.05	340	36	MET	N	117.819	0.4
280	30	LYS	N	120.172	0.4	341	36	MET	HG2	2.4908	0.05
281	30	LYS	HB2	1.8228	0.05	342	37	ARG	C	178.461	0.4
282	30	LYS	HD2	1.6858	0.05	343	37	ARG	CA	59.2508	0.4
283	30	LYS	HE2	2.9798	0.05	344	37	ARG	CB	29.5288	0.4
284	30	LYS	HG2	1.4218	0.05	345	37	ARG	CD	43.3388	0.4
285	31	GLU	C	176.336	0.4	346	37	ARG	HG2	1.8178	0.05
286	31	GLU	CA	59.5238	0.4	347	37	ARG	CG	29.3938	0.4
287	31	GLU	CB	28.886	0.4	348	37	ARG	H	8.5168	0.05
288	31	GLU	CG	38.8128	0.4	349	37	ARG	HA	4.7788	0.05
289	31	GLU	H	7.7168	0.05	350	37	ARG	HD2	3.2908	0.05
290	31	GLU	HA	4.1198	0.05	351	37	ARG	HD3	3.1358	0.05
291	31	GLU	N	121.065	0.4	352	37	ARG	N	118.513	0.4
292	31	GLU	HB2	2.7148	0.05	353	37	ARG	HB2	1.9028	0.05
293	31	GLU	HG2	2.4038	0.05	354	38	SER	C	172.053	0.4
294	32	LEU	C	176.129	0.4	355	38	SER	CA	61.2398	0.4
295	32	LEU	CA	57.7408	0.4	356	38	SER	CB	63.1948	0.4
357	38	SER	H	7.9658	0.05	408	43	PRO	HB2	1.9038	0.05

358	38	SER	HA	4.4128	0.05	418	45	GLU	C	176.176	0.4
359	38	SER	N	118.269	0.4	419	45	GLU	CA	59.9988	0.4
360	38	SER	HB2	4.0548	0.05	420	45	GLU	CB	29.4078	0.4
361	39	LEU	C	174.161	0.4	421	45	GLU	CG	36.3798	0.4
362	39	LEU	CA	54.5358	0.4	422	45	GLU	H	8.8228	0.05
363	39	LEU	CB	42.0178	0.4	423	45	GLU	HA	3.9828	0.05
364	39	LEU	CD1	25.6788	0.4	424	45	GLU	N	120.212	0.4
365	39	LEU	CD2	22.4138	0.4	425	45	GLU	HB2	1.4588	0.05
366	39	LEU	CG	25.9148	0.4	426	45	GLU	HG2	2.3548	0.05
367	39	LEU	H	7.4338	0.05	427	46	ALA	C	177.394	0.4
368	39	LEU	HA	4.4918	0.05	428	46	ALA	CA	55.0398	0.4
369	39	LEU	HD1	0.8268	0.05	429	46	ALA	CB	18.1898	0.4
370	39	LEU	HD2	0.8108	0.05	430	46	ALA	H	8.2698	0.05
371	39	LEU	HG	0.8018	0.05	431	46	ALA	HA	4.0878	0.05
372	39	LEU	N	120.296	0.4	432	46	ALA	HB	1.3958	0.05
373	39	LEU	HB2	1.8358	0.05	433	46	ALA	N	120.147	0.4
374	40	GLY	C	171.564	0.4	434	47	GLU	C	177.405	0.4
375	40	GLY	CA	45.4398	0.4	435	47	GLU	CA	58.9238	0.4
376	40	GLY	H	7.8938	0.05	436	47	GLU	CB	28.2468	0.4
377	40	GLY	HA2	4.2518	0.05	437	47	GLU	CG	33.9888	0.4
378	40	GLY	HA3	3.7918	0.05	438	47	GLU	H	7.6948	0.05
379	40	GLY	N	106.425	0.4	439	47	GLU	HA	3.9848	0.05
380	41	GLN	C	171.332	0.4	440	47	GLU	N	118.332	0.4
381	41	GLN	CA	54.4658	0.4	441	47	GLU	HB2	1.8868	0.05
382	41	GLN	CB	30.6968	0.4	442	47	GLU	HG2	2.4058	0.05
383	41	GLN	CG	33.5098	0.4	443	48	LEU	C	175.752	0.4
384	41	GLN	H	7.7978	0.05	444	48	LEU	CA	57.8508	0.4
385	41	GLN	HA	4.4858	0.05	445	48	LEU	CB	42.1988	0.4
386	41	GLN	HE21	7.4098	0.05	446	48	LEU	CG	25.8498	0.4
387	41	GLN	HE22	6.7788	0.05	447	48	LEU	H	8.1268	0.05
388	41	GLN	N	117.557	0.4	448	48	LEU	HA	4.0138	0.05
389	41	GLN	NE2	110.556	0.4	449	48	LEU	HD2	0.6978	0.05
390	41	GLN	HB2	1.6168	0.05	450	48	LEU	HG	1.0458	0.05
391	41	GLN	HG2	2.1668	0.05	451	48	LEU	N	119.439	0.4
392	41	GLN	HG3	2.1138	0.05	452	48	LEU	HB2	2.0508	0.05
393	42	ASN	CA	50.35	0.4	453	48	LEU	HD1	0.7938	0.05
394	42	ASN	CB	39.044	0.4	454	49	GLN	C	175.703	0.4
395	42	ASN	H	8.7018	0.05	455	49	GLN	CA	59.1438	0.4
396	42	ASN	HA	4.3298	0.05	456	49	GLN	CB	28.051	0.4
397	42	ASN	HD21	7.7668	0.05	457	49	GLN	CG	37.2758	0.4
398	42	ASN	HD22	6.9678	0.05	458	49	GLN	H	8.2468	0.05
399	42	ASN	N	116.151	0.4	459	49	GLN	HA	3.8418	0.05
400	42	ASN	ND2	114.422	0.4	460	49	GLN	HE21	7.5158	0.05
401	42	ASN	HB2	2.6418	0.05	461	49	GLN	HE22	6.9308	0.05
402	43	PRO	C	174.906	0.4	462	49	GLN	N	117.775	0.4
403	43	PRO	CA	61.9858	0.4	463	49	GLN	NE2	112.455	0.4
404	43	PRO	CB	31.9148	0.4	464	49	GLN	HB2	1.8108	0.05
405	43	PRO	HA	4.7228	0.05	465	49	GLN	HG2	2.4358	0.05
406	43	PRO	HD2	3.5758	0.05	466	50	ASP	CA	57.1128	0.4
407	43	PRO	HD3	3.2618	0.05	467	50	ASP	CB	40.0358	0.4
408	43	PRO	HB2	1.9038	0.05	468	50	ASP	H	8.1208	0.05
409	43	PRO	HG2	1.9418	0.05	469	50	ASP	HA	4.4378	0.05
410	44	THR	C	172.336	0.4	470	50	ASP	N	119.405	0.4
411	44	THR	CA	60.5658	0.4	471	50	ASP	HB2	2.8628	0.05
412	44	THR	CB	70.7718	0.4	472	51	MET	H	7.9218	0.05
413	44	THR	H	8.6648	0.05	473	51	MET	HA	4.0798	0.05
414	44	THR	HA	4.4338	0.05	474	51	MET	N	118.728	0.4
415	44	THR	HB	4.7188	0.05	475	51	MET	HB2	1.9378	0.05
416	44	THR	HG2	1.4328	0.05	476	51	MET	HB3	1.6278	0.05
417	44	THR	N	112.272	0.4	477	51	MET	HG2	2.4078	0.05

478	51	MET	HG3	2.1978	0.05	539	58	ASP	CB	39.7758	0.4
479	51	MET	HE	1.6978	0.05	540	58	ASP	H	8.2578	0.05
480	52	ILE	H	7.5878	0.05	541	58	ASP	HA	4.6198	0.05
481	52	ILE	N	117.735	0.4	542	58	ASP	HB2	3.0668	0.05
482	52	ILE	C	174.965	0.4	543	58	ASP	HB3	2.6918	0.05
483	52	ILE	CA	64.1228	0.4	544	58	ASP	N	113.496	0.4
484	52	ILE	CB	36.377	0.4	545	59	GLY	C	172.107	0.4
485	52	ILE	CD1	11.4728	0.4	546	59	GLY	CA	46.9268	0.4
486	52	ILE	CG2	16.2578	0.4	547	59	GLY	H	7.6128	0.05
487	52	ILE	HA	3.7538	0.05	548	59	GLY	HA2	3.8788	0.05
488	52	ILE	HB	2.0858	0.05	549	59	GLY	HA3	3.8278	0.05
489	52	ILE	HD1	0.6988	0.05	550	59	GLY	N	108.087	0.4
490	52	ILE	HG12	1.5958	0.05	551	60	ASN	C	174.007	0.4
491	52	ILE	HG13	1.2778	0.05	552	60	ASN	CA	52.273	0.4
492	52	ILE	HG2	0.7698	0.05	553	60	ASN	CB	37.6628	0.4
493	53	ASN	C	174.533	0.4	554	60	ASN	H	8.1948	0.05
494	53	ASN	CA	55.729	0.4	555	60	ASN	HA	4.6068	0.05
495	53	ASN	CB	37.9058	0.4	556	60	ASN	HB2	3.3368	0.05
496	53	ASN	H	8.7088	0.05	557	60	ASN	HB3	2.6538	0.05
497	53	ASN	HA	4.4348	0.05	558	60	ASN	N	118.324	0.4
498	53	ASN	HB2	2.9978	0.05	559	61	GLY	C	170.445	0.4
499	53	ASN	HB3	2.8708	0.05	560	61	GLY	CA	45.4348	0.4
500	53	ASN	HD21	7.8368	0.05	561	61	GLY	H	10.5728	0.05
501	53	ASN	HD22	6.9718	0.05	562	61	GLY	HA2	4.2558	0.05
502	53	ASN	N	117.691	0.4	563	61	GLY	HA3	3.4938	0.05
503	53	ASN	ND2	110.953	0.4	564	61	GLY	N	112.871	0.4
504	54	GLU	CA	58.6148	0.4	565	62	THR	C	170.378	0.4
505	54	GLU	CG	35.9758	0.4	566	62	THR	CA	59.213	0.4
506	54	GLU	H	7.6898	0.05	567	62	THR	CB	72.1128	0.4
507	54	GLU	HA	4.0438	0.05	568	62	THR	CG2	22.1088	0.4
508	54	GLU	N	115.838	0.4	569	62	THR	H	7.6938	0.05
509	54	GLU	HB2	1.8668	0.05	570	62	THR	HA	4.7958	0.05
510	54	GLU	HG2	2.3468	0.05	571	62	THR	HB	4.0208	0.05
511	55	VAL	C	172.915	0.4	572	62	THR	HG2	1.1598	0.05
512	55	VAL	CA	60.9138	0.4	573	62	THR	N	108.099	0.4
513	55	VAL	CB	39.549	0.4	574	63	ILE	C	172.687	0.4
514	55	VAL	CG1	22.5128	0.4	575	63	ILE	CA	58.9958	0.4
515	55	VAL	CG2	20.8048	0.4	576	63	ILE	CB	39.07	0.4
516	55	VAL	H	7.2148	0.05	577	63	ILE	CG1	27.365	0.4
517	55	VAL	HA	4.2588	0.05	578	63	ILE	CG2	18.3588	0.4
518	55	VAL	HB	2.1608	0.05	579	63	ILE	CD1	15.3698	0.4
519	55	VAL	HG1	0.8278	0.05	580	63	ILE	H	8.8238	0.05
520	55	VAL	HG2	0.8788	0.05	581	63	ILE	HA	5.2228	0.05
521	55	VAL	N	110.912	0.4	582	63	ILE	HB	2.1488	0.05
522	56	ASP	C	173.361	0.4	583	63	ILE	HD1	0.3718	0.05
523	56	ASP	CA	53.8648	0.4	584	63	ILE	HG13	0.9158	0.05
524	56	ASP	CB	40.1588	0.4	585	63	ILE	HG2	1.1978	0.05
525	56	ASP	H	7.7608	0.05	586	63	ILE	N	123.323	0.4
526	56	ASP	HA	4.5098	0.05	587	64	ASP	C	173.494	0.4
527	56	ASP	HB2	3.0068	0.05	588	64	ASP	CA	51.8118	0.4
528	56	ASP	HB3	2.7238	0.05	589	64	ASP	CB	42.2468	0.4
529	56	ASP	N	120.629	0.4	590	64	ASP	H	8.8928	0.05
530	57	ALA	C	175.842	0.4	591	64	ASP	HA	5.4908	0.05
531	57	ALA	CA	54.2908	0.4	592	64	ASP	HB2	3.1518	0.05
532	57	ALA	CB	19.4558	0.4	593	64	ASP	HB3	2.8708	0.05
533	57	ALA	H	8.2438	0.05	594	64	ASP	N	127.718	0.4
534	57	ALA	HA	4.2228	0.05	595	65	PHE	CA	63.193	0.4
535	57	ALA	HB	1.5318	0.05	596	65	PHE	CB	35.6308	0.4
536	57	ALA	N	131.226	0.4	597	65	PHE	CD1	129.971	0.4
537	58	ASP	C	175.471	0.4	598	65	PHE	CD2	129.971	0.4
538	58	ASP	CA	52.7878	0.4	599	65	PHE	CE1	128.531	0.4

600	65	PHE	CE2	128.531	0.4	661	72	MET	HB2	1.0678	0.05
601	65	PHE	H	8.9878	0.05	662	72	MET	HB3	0.9978	0.05
602	65	PHE	HA	3.7838	0.05	663	72	MET	HG2	1.4578	0.05
603	65	PHE	HB2	2.8208	0.05	664	72	MET	HG3	1.3778	0.05
604	65	PHE	HB3	2.0848	0.05	665	73	ALA	C	177.075	0.4
605	65	PHE	N	118.282	0.4	666	73	ALA	CA	54.504	0.4
606	65	PHE	HD1	6.7628	0.05	667	73	ALA	CB	18.2718	0.4
607	65	PHE	HD2	6.7628	0.05	668	73	ALA	H	7.8968	0.05
608	65	PHE	HE1	7.2108	0.05	669	73	ALA	HA	4.0248	0.05
609	65	PHE	HE2	7.2108	0.05	670	73	ALA	HB	1.3728	0.05
610	66	PRO	HA	3.8528	0.05	671	73	ALA	N	120.06	0.4
611	66	PRO	HB2	2.1578	0.05	672	74	ARG	C	175.04	0.4
612	66	PRO	HB3	1.8038	0.05	673	74	ARG	CA	58.032	0.4
613	66	PRO	HG2	1.3648	0.05	674	74	ARG	CB	29.32	0.4
614	66	PRO	HD2	3.7078	0.05	675	74	ARG	HA	3.7378	0.05
615	67	GLU	H	8.1738	0.05	651	71	MET	HA	3.4178	0.05
616	67	GLU	HA	4.4498	0.05	652	71	MET	HB2	1.7678	0.05
617	67	GLU	HB2	1.7678	0.05	653	71	MET	HG2	2.0978	0.05
618	67	GLU	HG2	2.6078	0.05	654	71	MET	HE	1.3978	0.05
619	67	GLU	HG3	2.2878	0.05	655	72	MET	HA	3.6478	0.05
620	67	GLU	N	116.98	0.4	656	72	MET	C	175.697	0.4
621	68	PHE	CD1	129.642	0.4	657	72	MET	CA	60.0268	0.4
622	68	PHE	CD2	129.642	0.4	658	72	MET	CG	31.9708	0.4
623	68	PHE	CE1	129.082	0.4	659	72	MET	H	8.1888	0.05
624	68	PHE	CE2	129.082	0.4	660	72	MET	N	115.879	0.4
625	68	PHE	H	8.6708	0.05	661	72	MET	HB2	1.0678	0.05
626	68	PHE	N	122.872	0.4	662	72	MET	HB3	0.9978	0.05
627	68	PHE	HA	3.6278	0.05	663	72	MET	HG2	1.4578	0.05
628	68	PHE	HB2	3.1278	0.05	665	73	ALA	C	177.075	0.4
629	68	PHE	HB3	2.8278	0.05	666	73	ALA	CA	54.504	0.4
630	68	PHE	HD1	6.9108	0.05	667	73	ALA	CB	18.2718	0.4
631	68	PHE	HD2	6.9108	0.05	668	73	ALA	H	7.8968	0.05
632	68	PHE	HE1	7.1818	0.05	669	73	ALA	HA	4.0248	0.05
633	68	PHE	HE2	7.1818	0.05	670	73	ALA	HB	1.3728	0.05
634	69	LEU	H	8.6748	0.05	671	73	ALA	N	120.06	0.4
635	69	LEU	N	119.155	0.4	672	74	ARG	C	175.04	0.4
636	69	LEU	CB	38.6428	0.4	673	74	ARG	CA	58.032	0.4
637	69	LEU	CD1	25.5958	0.4	674	74	ARG	CB	29.32	0.4
638	69	LEU	HA	3.9398	0.05	675	74	ARG	HA	3.7378	0.05
639	69	LEU	HD1	0.8388	0.05	676	74	ARG	HB2	1.4878	0.05
640	69	LEU	HD2	0.0638	0.05	677	74	ARG	HB3	1.3178	0.05
641	69	LEU	HB2	1.3058	0.05	678	74	ARG	HG2	1.0778	0.05
642	69	LEU	HG	0.6778	0.05	679	74	ARG	HD2	2.7378	0.05
643	70	THR	CB	67.8278	0.4	680	74	ARG	CD	43.7328	0.4
644	70	THR	H	7.5458	0.05	681	74	ARG	CG	27.3618	0.4
645	70	THR	HA	3.4478	0.05	682	74	ARG	H	7.4768	0.05
646	70	THR	HB	4.1948	0.05	683	74	ARG	N	116.115	0.4
647	70	THR	HG2	1.2488	0.05	684	75	LYS	C	174.877	0.4
648	70	THR	N	114.017	0.4	685	75	LYS	CA	57.313	0.4
649	71	MET	H	7.6178	0.05	686	75	LYS	CB	31.54	0.4
650	71	MET	N	119.16	0.4	687	75	LYS	CE	40.7878	0.4
651	71	MET	HA	3.4178	0.05	688	75	LYS	H	7.7728	0.05
652	71	MET	HB2	1.7678	0.05	689	75	LYS	HA	3.9348	0.05
653	71	MET	HG2	2.0978	0.05	690	75	LYS	N	118.389	0.4
654	71	MET	HE	1.3978	0.05	691	75	LYS	HB2	1.8288	0.05
655	72	MET	HA	3.6478	0.05	692	75	LYS	HE2	3.5488	0.05
656	72	MET	C	175.697	0.4	693	75	LYS	HG2	1.4908	0.05
657	72	MET	CA	60.0268	0.4	694	75	LYS	HD2	1.6878	0.05
658	72	MET	CG	31.9708	0.4	695	76	MET	C	173.683	0.4
659	72	MET	H	8.1888	0.05	696	76	MET	CA	56.4598	0.4
660	72	MET	N	115.879	0.4	697	76	MET	CB	28.262	0.4

698	76	MET	CE	17.0608	0.4	759	82	GLU	N	122.235	0.4
699	76	MET	CG	32.1808	0.4	760	82	GLU	HB2	2.1328	0.05
700	76	MET	H	7.9748	0.05	761	82	GLU	HG2	2.3588	0.05
701	76	MET	HA	4.3438	0.05	762	83	GLU	C	176.436	0.4
702	76	MET	HB2	2.1528	0.05	763	83	GLU	CA	59.2618	0.4
703	76	MET	HB3	2.1098	0.05	764	83	GLU	CB	29.5468	0.4
704	76	MET	HE	2.0868	0.05	765	83	GLU	CG	35.8858	0.4
705	76	MET	HG2	2.6608	0.05	766	83	GLU	H	8.2248	0.05
706	76	MET	HG3	2.6188	0.05	767	83	GLU	HA	4.1048	0.05
707	76	MET	N	117.535	0.4	768	83	GLU	N	119.203	0.4
708	77	LYS	C	173.704	0.4	769	83	GLU	HB2	2.0948	0.05
709	77	LYS	CA	56.8018	0.4	770	83	GLU	HG2	2.3658	0.05
710	77	LYS	CB	32.7798	0.4	771	84	GLU	C	177.343	0.4
711	77	LYS	CD	28.8688	0.4	772	84	GLU	CA	59.6828	0.4
712	77	LYS	CE	41.9038	0.4	773	84	GLU	CB	30.3448	0.4
713	77	LYS	CG	24.5088	0.4	774	84	GLU	CG	36.2148	0.4
714	77	LYS	H	7.7548	0.05	775	84	GLU	H	8.1158	0.05
715	77	LYS	HA	4.2988	0.05	776	84	GLU	HA	4.1448	0.05
716	77	LYS	HB2	1.8628	0.05	777	84	GLU	HG2	2.4798	0.05
717	77	LYS	HB3	1.8208	0.05	778	84	GLU	HG3	2.3118	0.05
718	77	LYS	N	119.562	0.4	779	84	GLU	N	117.902	0.4
719	77	LYS	HD2	1.6868	0.05	780	84	GLU	HB2	2.1508	0.05
720	77	LYS	HE2	2.9838	0.05	781	85	ILE	C	174.656	0.4
721	77	LYS	HG2	1.4828	0.05	782	85	ILE	CA	65.6048	0.4
722	78	ASP	CA	54.3988	0.4	783	85	ILE	CB	37.4178	0.4
723	78	ASP	C	173.716	0.4	784	85	ILE	CD1	13.3228	0.4
724	78	ASP	CB	40.8618	0.4	785	85	ILE	CG1	29.7868	0.4
725	78	ASP	H	8.1648	0.05	786	85	ILE	CG2	18.5638	0.4
726	78	ASP	HA	4.7048	0.05	787	85	ILE	H	8.0018	0.05
727	78	ASP	HB2	2.8028	0.05	788	85	ILE	HA	4.0898	0.05
728	78	ASP	HB3	2.7438	0.05	789	85	ILE	HB	2.2168	0.05
729	78	ASP	N	120.459	0.4	790	85	ILE	HD1	0.7028	0.05
730	79	THR	C	171.541	0.4	791	85	ILE	HG12	1.9488	0.05
731	79	THR	CA	62.1658	0.4	792	85	ILE	HG13	0.9628	0.05
732	79	THR	CB	69.7638	0.4	793	85	ILE	HG2	1.1078	0.05
733	79	THR	CG2	21.4248	0.4	794	85	ILE	N	119.58	0.4
734	79	THR	H	8.0398	0.05	795	86	ARG	CA	60.3318	0.4
735	79	THR	HA	4.3208	0.05	796	86	ARG	CB	29.9378	0.4
736	79	THR	HB	4.2538	0.05	797	86	ARG	CD	42.9598	0.4
737	79	THR	HG2	1.2238	0.05	798	86	ARG	CG	27.3348	0.4
738	79	THR	N	113.759	0.4	799	86	ARG	H	8.3748	0.05
739	80	ASP	C	173.897	0.4	800	86	ARG	HA	4.1548	0.05
740	80	ASP	CA	54.4298	0.4	801	86	ARG	HB2	2.0668	0.05
741	80	ASP	CB	40.9508	0.4	802	86	ARG	HB3	1.8628	0.05
742	80	ASP	H	8.4268	0.05	803	86	ARG	HG2	1.6538	0.05
743	80	ASP	HA	4.7098	0.05	804	86	ARG	HG3	1.5228	0.05
744	80	ASP	N	122.666	0.4	805	86	ARG	N	121.213	0.4
745	80	ASP	HB2	2.7928	0.05	806	86	ARG	HD2	2.9658	0.05
746	81	SER	C	172.788	0.4	807	87	GLU	CA	59.2028	0.4
747	81	SER	CA	59.4528	0.4	808	87	GLU	CB	29.6808	0.4
748	81	SER	CB	63.0578	0.4	809	87	GLU	CG	36.2078	0.4
749	81	SER	H	8.4558	0.05	810	87	GLU	H	8.3608	0.05
750	81	SER	HA	4.4138	0.05	811	87	GLU	HA	4.0938	0.05
751	81	SER	N	117.057	0.4	812	87	GLU	N	117.579	0.4
752	81	SER	HB2	3.9998	0.05	813	87	GLU	HB2	2.0958	0.05
753	82	GLU	C	175.133	0.4	814	87	GLU	HG2	2.3498	0.05
754	82	GLU	CA	58.6118	0.4	815	88	ALA	C	176.595	0.4
755	82	GLU	CB	29.7828	0.4	816	88	ALA	CA	54.9348	0.4
756	82	GLU	CG	36.6058	0.4	817	88	ALA	CB	18.5808	0.4
757	82	GLU	H	8.5098	0.05	818	88	ALA	H	8.3528	0.05
758	82	GLU	HA	4.1568	0.05	819	88	ALA	HA	4.1738	0.05

820	88	ALA	HB	1.9338	0.05	881	93	ASP	HB2	2.2178	0.05
821	88	ALA	N	120.095	0.4	882	94	LYS	C	175.567	0.4
822	89	PHE	C	173.566	0.4	883	94	LYS	CA	59.3298	0.4
823	89	PHE	CA	61.8048	0.4	884	94	LYS	CB	32.5108	0.4
824	89	PHE	CB	38.9878	0.4	885	94	LYS	CD	28.2778	0.4
825	89	PHE	H	8.8348	0.05	886	94	LYS	CE	41.5298	0.4
826	89	PHE	HA	3.3128	0.05	887	94	LYS	CG	23.7708	0.4
827	89	PHE	HZ	7.2848	0.05	888	94	LYS	H	7.4178	0.05
828	89	PHE	N	118.86	0.4	889	94	LYS	HA	3.8858	0.05
829	89	PHE	HB2	3.0008	0.05	890	94	LYS	HD2	1.6468	0.05
830	89	PHE	CE1	126.947	0.4	891	94	LYS	HD3	1.4968	0.05
831	89	PHE	CE2	126.947	0.4	892	94	LYS	HG2	1.5198	0.05
832	89	PHE	HD1	6.5598	0.05	893	94	LYS	HG3	1.4738	0.05
833	89	PHE	HD2	6.5598	0.05	894	94	LYS	N	124.29	0.4
834	89	PHE	HE1	7.0808	0.05	895	94	LYS	HB2	1.8608	0.05
835	89	PHE	HE2	7.0808	0.05	896	94	LYS	HE2	2.8508	0.05
836	90	ARG	C	174.665	0.4	897	95	ASP	CA	53.9748	0.4
837	90	ARG	CA	58.3618	0.4	898	95	ASP	C	175.057	0.4
838	90	ARG	CB	30.3938	0.4	899	95	ASP	CB	39.9358	0.4
839	90	ARG	CD	43.3538	0.4	900	95	ASP	H	8.4428	0.05
840	90	ARG	CG	27.8308	0.4	901	95	ASP	HA	4.5038	0.05
841	90	ARG	H	7.6278	0.05	902	95	ASP	HB2	2.6828	0.05
842	90	ARG	HA	3.9408	0.05	903	95	ASP	HB3	2.1948	0.05
843	90	ARG	HB2	1.9898	0.05	904	95	ASP	N	113.716	0.4
844	90	ARG	HB3	1.9528	0.05	905	96	GLY	C	172.324	0.4
845	90	ARG	HG2	1.9688	0.05	906	96	GLY	CA	46.9648	0.4
846	90	ARG	HG3	1.7988	0.05	907	96	GLY	H	7.9008	0.05
847	90	ARG	N	114.46	0.4	908	96	GLY	HA2	3.9218	0.05
848	90	ARG	HD2	3.2628	0.05	909	96	GLY	HA3	3.8578	0.05
849	91	VAL	C	174.176	0.4	910	96	GLY	N	109.038	0.4
850	91	VAL	CA	65.6048	0.4	911	97	ASN	C	173.111	0.4
851	91	VAL	CB	31.0978	0.4	912	97	ASN	CA	51.9718	0.4
852	91	VAL	CG1	22.5558	0.4	913	97	ASN	CB	37.3228	0.4
853	91	VAL	CG2	20.9048	0.4	914	97	ASN	H	8.4328	0.05
854	91	VAL	H	7.4118	0.05	915	97	ASN	HA	4.6208	0.05
855	91	VAL	HA	3.5488	0.05	916	97	ASN	HB2	3.3158	0.05
856	91	VAL	HB	2.2488	0.05	917	97	ASN	HB3	2.6908	0.05
857	91	VAL	HG1	1.0318	0.05	918	97	ASN	HD21	8.0918	0.05
858	91	VAL	HG2	0.7098	0.05	919	97	ASN	HD22	7.4058	0.05
859	91	VAL	N	117.632	0.4	920	97	ASN	N	119.49	0.4
860	92	PHE	C	173.432	0.4	921	97	ASN	ND2	116.123	0.4
861	92	PHE	CA	60.5698	0.4	922	98	GLY	C	169.922	0.4
862	92	PHE	CB	41.0488	0.4	923	98	GLY	CA	44.6868	0.4
863	92	PHE	CD1	130.697	0.4	924	98	GLY	H	10.7648	0.05
864	92	PHE	CD2	130.697	0.4	925	98	GLY	HA2	4.0968	0.05
865	92	PHE	CE1	129.847	0.4	926	98	GLY	HA3	3.4538	0.05
866	92	PHE	CE2	129.847	0.4	927	98	GLY	N	112.415	0.4
867	92	PHE	H	7.2058	0.05	928	99	TYR	C	171.883	0.4
868	92	PHE	HA	4.1938	0.05	929	99	TYR	CA	55.7868	0.4
869	92	PHE	N	114.928	0.4	930	99	TYR	CB	42.7778	0.4
870	92	PHE	HB2	2.7418	0.05	931	99	TYR	CD1	131.47	0.4
871	92	PHE	HD1	7.5308	0.05	932	99	TYR	CD2	131.47	0.4
872	92	PHE	HD2	7.5308	0.05	933	99	TYR	CE1	116.395	0.4
873	92	PHE	HE1	7.2868	0.05	934	99	TYR	CE2	116.395	0.4
874	92	PHE	HE2	7.2868	0.05	935	99	TYR	H	7.6948	0.05
875	93	ASP	C	174.487	0.4	936	99	TYR	HA	5.0578	0.05
876	93	ASP	CA	52.4208	0.4	937	99	TYR	HB2	2.5608	0.05
877	93	ASP	CB	38.8108	0.4	938	99	TYR	HB3	2.5378	0.05
878	93	ASP	H	7.8908	0.05	939	99	TYR	N	115.788	0.4
879	93	ASP	HA	4.5588	0.05	940	99	TYR	HD1	6.7708	0.05
880	93	ASP	N	114.746	0.4	941	99	TYR	HD2	6.7708	0.05

942	99	TYR	HE1	6.9438	0.05	1002	106	ARG	CA	59.8628	0.4
943	99	TYR	HE2	6.9438	0.05	1003	106	ARG	CB	30.0268	0.4
944	100	ILE	C	172.814	0.4	1004	106	ARG	CD	43.4158	0.4
945	100	ILE	CA	61.4788	0.4	1005	106	ARG	CG	27.4768	0.4
946	100	ILE	CB	39.6218	0.4	1006	106	ARG	H	8.7128	0.05
947	100	ILE	CD1	16.1228	0.4	1007	106	ARG	HA	3.8018	0.05
948	100	ILE	CG1	26.7908	0.4	1008	106	ARG	HB2	1.9498	0.05
949	100	ILE	CG2	17.5398	0.4	1009	106	ARG	HB3	1.7308	0.05
950	100	ILE	H	10.2758	0.05	1010	106	ARG	HD2	3.2588	0.05
951	100	ILE	HA	4.7148	0.05	1011	106	ARG	HD3	3.1358	0.05
952	100	ILE	HB	1.9998	0.05	1012	106	ARG	N	117.74	0.4
953	100	ILE	HD1	0.6218	0.05	1013	106	ARG	HG2	1.6418	0.05
954	100	ILE	HG12	1.5078	0.05	1014	107	HIS	C	175.029	0.4
955	100	ILE	HG13	0.6148	0.05	1015	107	HIS	CA	59.0188	0.4
956	100	ILE	HG2	1.1548	0.05	1016	107	HIS	CB	28.6158	0.4
957	100	ILE	N	126.892	0.4	1017	107	HIS	CD2	118.538	0.4
958	101	SER	C	172.611	0.4	1018	107	HIS	CE1	134.929	0.4
959	101	SER	CA	55.3568	0.4	1019	107	HIS	H	7.8868	0.05
960	101	SER	CB	66.6608	0.4	1020	107	HIS	HA	4.3998	0.05
961	101	SER	H	8.9958	0.05	1021	107	HIS	HB2	3.4228	0.05
962	101	SER	HA	5.0128	0.05	1022	107	HIS	HB3	3.3728	0.05
963	101	SER	N	123.234	0.4	1023	107	HIS	HD2	7.2578	0.05
964	101	SER	HB2	4.0118	0.05	1024	107	HIS	HE1	8.5098	0.05
965	102	ALA	C	176.445	0.4	1025	107	HIS	N	117.72	0.4
966	102	ALA	CA	55.9148	0.4	1026	108	VAL	C	175.248	0.4
967	102	ALA	CB	17.7798	0.4	1027	108	VAL	CA	66.5638	0.4
968	102	ALA	H	9.3348	0.05	1028	108	VAL	CB	31.5708	0.4
969	102	ALA	HA	3.9268	0.05	1029	108	VAL	CG1	23.7288	0.4
970	102	ALA	HB	1.5048	0.05	1030	108	VAL	CG2	20.5588	0.4
971	102	ALA	N	122.755	0.4	1031	108	VAL	H	8.4398	0.05
972	103	ALA	C	178.77	0.4	1032	108	VAL	HA	3.5928	0.05
973	103	ALA	CA	54.8718	0.4	1033	108	VAL	HG1	1.0148	0.05
974	103	ALA	CB	18.3008	0.4	1034	108	VAL	HG2	0.4988	0.05
975	103	ALA	H	8.3158	0.05	1035	108	VAL	N	119.959	0.4
976	103	ALA	HA	4.0298	0.05	1036	108	VAL	HB	2.0938	0.05
977	103	ALA	HB	1.4298	0.05	1037	109	MET	C	176.437	0.4
978	103	ALA	N	118.198	0.4	1038	109	MET	CA	57.3908	0.4
979	104	GLU	C	176.136	0.4	1039	109	MET	CB	29.5328	0.4
980	104	GLU	CA	59.0858	0.4	1040	109	MET	CE	16.9208	0.4
981	104	GLU	CB	28.889	0.4	1041	109	MET	CG	32.3898	0.4
982	104	GLU	CG	37.9988	0.4	1042	109	MET	H	8.4358	0.05
983	104	GLU	H	7.9448	0.05	1043	109	MET	HA	4.2358	0.05
984	104	GLU	HA	4.0258	0.05	1044	109	MET	HE	1.8318	0.05
985	104	GLU	N	119.337	0.4	1045	109	MET	HG2	2.7948	0.05
986	104	GLU	HB2	1.8718	0.05	1046	109	MET	HG3	2.3318	0.05
987	104	GLU	HG2	2.6128	0.05	1047	109	MET	N	115.295	0.4
988	105	LEU	C	175.538	0.4	1048	109	MET	HB2	2.3128	0.05
989	105	LEU	CA	57.9358	0.4	1049	110	THR	C	175.497	0.4
990	105	LEU	CB	42.1528	0.4	1050	110	THR	CA	66.5808	0.4
991	105	LEU	CD1	26.475	0.4	1051	110	THR	CB	68.5218	0.4
992	105	LEU	CD2	23.777	0.4	1052	110	THR	CG2	21.3928	0.4
993	105	LEU	CG	26.6848	0.4	1044	109	MET	HE	1.8318	0.05
994	105	LEU	H	8.6268	0.05	1045	109	MET	HG2	2.7948	0.05
995	105	LEU	HA	4.1598	0.05	1046	109	MET	HG3	2.3318	0.05
996	105	LEU	HD1	0.7698	0.05	1047	109	MET	N	115.295	0.4
997	105	LEU	HD2	0.7538	0.05	1048	109	MET	HB2	2.3128	0.05
998	105	LEU	HG	1.5638	0.05	1049	110	THR	C	175.497	0.4
999	105	LEU	N	120.144	0.4	1050	110	THR	CA	66.5808	0.4
1000	105	LEU	HB2	1.9418	0.05	1051	110	THR	CB	68.5218	0.4
1001	106	ARG	C	175.898	0.4	1052	110	THR	CG2	21.3928	0.4

1053	110	THR	H	8.1258	0.05	1113	116	LEU	CB	44.1758	0.4
1054	110	THR	HA	4.0568	0.05	1114	116	LEU	CD1	24.0658	0.4
1055	110	THR	HB	4.2578	0.05	1115	116	LEU	CD2	23.7548	0.4
1056	110	THR	HG2	1.2748	0.05	1116	116	LEU	CG	26.9828	0.4
1057	110	THR	N	115.318	0.4	1117	116	LEU	H	8.0528	0.05
1058	111	ASN	CA	55.8368	0.4	1118	116	LEU	HA	4.6688	0.05
1059	111	ASN	CB	37.9678	0.4	1119	116	LEU	HB2	1.5498	0.05
1060	111	ASN	H	7.9988	0.05	1120	116	LEU	HB3	1.3748	0.05
1061	111	ASN	HA	4.4508	0.05	1121	116	LEU	HD1	0.6908	0.05
1062	111	ASN	HD21	7.5168	0.05	1122	116	LEU	HD2	0.6898	0.05
1063	111	ASN	HD22	6.7198	0.05	1123	116	LEU	HG	0.6798	0.05
1064	111	ASN	N	122.63	0.4	1124	116	LEU	N	124.274	0.4
1065	111	ASN	ND2	111.625	0.4	1125	117	THR	CA	60.9128	0.4
1066	111	ASN	HB2	2.7928	0.05	1126	117	THR	CB	70.9388	0.4
1067	112	LEU	C	174.584	0.4	1127	117	THR	CG2	21.5258	0.4
1068	112	LEU	CA	54.8318	0.4	1128	117	THR	H	9.1258	0.05
1069	112	LEU	CB	42.5438	0.4	1129	117	THR	HA	4.4238	0.05
1070	112	LEU	CD1	25.9018	0.4	1130	117	THR	HB	4.7248	0.05
1071	112	LEU	CD2	22.0388	0.4	1131	117	THR	HG2	1.3388	0.05
1072	112	LEU	CG	26.2718	0.4	1132	117	THR	N	113.635	0.4
1073	112	LEU	H	7.9058	0.05	1133	118	ASP	C	175.917	0.4
1074	112	LEU	HA	4.3308	0.05	1134	118	ASP	CA	57.6808	0.4
1075	112	LEU	HB2	1.9378	0.05	1135	118	ASP	CB	39.5228	0.4
1076	112	LEU	HB3	1.6348	0.05	1136	118	ASP	H	8.9128	0.05
1077	112	LEU	HD1	0.8158	0.05	1137	118	ASP	HA	4.2238	0.05
1078	112	LEU	HD2	0.7718	0.05	1138	118	ASP	HB2	3.0378	0.05
1079	112	LEU	HG	1.6608	0.05	1139	118	ASP	HB3	2.6168	0.05
1080	112	LEU	N	117.455	0.4	1140	118	ASP	N	120.87	0.4
1081	113	GLY	C	171.823	0.4	1141	119	GLU	C	176.438	0.4
1082	113	GLY	CA	45.5118	0.4	1142	119	GLU	CA	59.7978	0.4
1083	113	GLY	H	7.9138	0.05	1143	119	GLU	CB	28.7848	0.4
1084	113	GLY	HA2	4.1398	0.05	1144	119	GLU	CG	35.8818	0.4
1085	113	GLY	HA3	3.7798	0.05	1145	119	GLU	H	8.6268	0.05
1086	113	GLY	N	107.043	0.4	1146	119	GLU	HA	4.1258	0.05
1087	114	GLU	C	172.814	0.4	1147	119	GLU	HB2	2.3388	0.05
1088	114	GLU	CA	55.1648	0.4	1148	119	GLU	HB3	2.0548	0.05
1089	114	GLU	CB	30.5298	0.4	1149	119	GLU	N	118.815	0.4
1090	114	GLU	CG	35.2058	0.4	1150	119	GLU	HG2	2.3498	0.05
1091	114	GLU	H	7.8588	0.05	1151	120	GLU	C	176.259	0.4
1092	114	GLU	HA	4.3238	0.05	1152	120	GLU	CA	59.5158	0.4
1093	114	GLU	HG2	2.1188	0.05	1153	120	GLU	CB	30.8308	0.4
1094	114	GLU	HG3	1.9848	0.05	1154	120	GLU	CG	38.2848	0.4
1095	114	GLU	N	119.028	0.4	1155	120	GLU	H	7.7748	0.05
1096	114	GLU	HB2	1.7328	0.05	1156	120	GLU	HA	3.9208	0.05
1097	115	LYS	C	172.455	0.4	1157	120	GLU	N	120.193	0.4
1098	115	LYS	CA	55.2348	0.4	1158	120	GLU	HB2	2.1208	0.05
1099	115	LYS	CB	31.7618	0.4	1159	120	GLU	HG2	2.3668	0.05
1100	115	LYS	CD	28.8418	0.4	1160	121	VAL	C	175.276	0.4
1101	115	LYS	CE	41.4828	0.4	1161	121	VAL	CA	66.8298	0.4
1102	115	LYS	CG	24.3778	0.4	1162	121	VAL	CB	31.1878	0.4
1103	115	LYS	H	8.6538	0.05	1163	121	VAL	CG1	23.3228	0.4
1104	115	LYS	HA	4.3778	0.05	1164	121	VAL	CG2	21.8348	0.4
1105	115	LYS	HB2	1.7448	0.05	1165	121	VAL	H	8.0268	0.05
1106	115	LYS	HB3	1.6408	0.05	1166	121	VAL	HA	3.5098	0.05
1107	115	LYS	N	123.982	0.4	1167	121	VAL	HB	2.1848	0.05
1108	115	LYS	HD2	1.6378	0.05	1168	121	VAL	HG1	0.8808	0.05
1109	115	LYS	HE2	2.9508	0.05	1169	121	VAL	HG2	0.9418	0.05
1110	115	LYS	HG2	1.2958	0.05	1170	121	VAL	N	121.619	0.4
1111	116	LEU	C	175.378	0.4	1171	122	ASP	C	176.327	0.4
1112	116	LEU	CA	54.1328	0.4	1172	122	ASP	CA	57.5188	0.4

1173	122	ASP	CB	40.0848	0.4	1233	128	ALA	C	174.788	0.4
1174	122	ASP	H	8.1848	0.05	1234	128	ALA	CA	51.6648	0.4
1175	122	ASP	HA	4.3648	0.05	1235	128	ALA	CB	20.8668	0.4
1176	122	ASP	HB2	2.7908	0.05	1236	128	ALA	H	7.2248	0.05
1177	122	ASP	HB3	2.6998	0.05	1237	128	ALA	HA	4.3508	0.05
1178	122	ASP	N	119.587	0.4	1238	128	ALA	HB	1.2118	0.05
1179	123	GLU	C	175.641	0.4	1239	128	ALA	N	116.627	0.4
1180	123	GLU	CA	59.3828	0.4	1240	129	ASN	C	172.792	0.4
1181	123	GLU	CB	30.1128	0.4	1241	129	ASN	CA	54.3598	0.4
1182	123	GLU	CG	36.4218	0.4	1242	129	ASN	CB	40.3068	0.4
1183	123	GLU	H	8.1898	0.05	1243	129	ASN	H	7.8978	0.05
1184	123	GLU	HA	3.9668	0.05	1244	129	ASN	HA	4.4838	0.05
1185	123	GLU	N	119.238	0.4	1245	129	ASN	HB2	2.8958	0.05
1186	123	GLU	HB2	2.2938	0.05	1246	129	ASN	HB3	2.5088	0.05
1187	123	GLU	HG2	2.4258	0.05	1247	129	ASN	N	117.321	0.4
1188	124	MET	C	177.098	0.4	1248	130	ILE	C	175.157	0.4
1189	124	MET	CA	60.6858	0.4	1249	130	ILE	CA	63.2378	0.4
1190	124	MET	CB	29.557	0.4	1250	130	ILE	CB	38.5768	0.4
1191	124	MET	CG	33.3538	0.4	1251	130	ILE	CD1	12.3058	0.4
1192	124	MET	CE	14.9908	0.4	1252	130	ILE	CG1	27.6178	0.4
1193	124	MET	H	7.7708	0.05	1253	130	ILE	CG2	17.2438	0.4
1194	124	MET	HA	3.9128	0.05	1254	130	ILE	H	8.2758	0.05
1195	124	MET	HE	0.6608	0.05	1255	130	ILE	HA	3.8998	0.05
1196	124	MET	N	118.205	0.4	1256	130	ILE	HB	1.9548	0.05
1197	124	MET	HB2	1.8458	0.05	1257	130	ILE	HD1	0.8608	0.05
1198	124	MET	HG2	2.7888	0.05	1258	130	ILE	HG12	1.6528	0.05
1199	125	ILE	CA	63.0148	0.4	1259	130	ILE	HG13	1.2608	0.05
1200	125	ILE	CB	35.5488	0.4	1260	130	ILE	HG2	0.9198	0.05
1201	125	ILE	CD1	9.4738	0.4	1261	130	ILE	N	127.388	0.4
1202	125	ILE	CG1	26.9728	0.4	1262	131	ASP	C	175.047	0.4
1203	125	ILE	CG2	16.4428	0.4	1263	131	ASP	CA	54.0058	0.4
1204	125	ILE	H	7.8768	0.05	1264	131	ASP	CB	40.0758	0.4
1205	125	ILE	HA	3.8498	0.05	1265	131	ASP	H	8.4118	0.05
1206	125	ILE	HB	2.3988	0.05	1266	131	ASP	HA	4.5008	0.05
1207	125	ILE	HD1	0.8248	0.05	1267	131	ASP	HB2	3.0488	0.05
1208	125	ILE	HG12	1.7318	0.05	1268	131	ASP	HB3	2.6358	0.05
1209	125	ILE	HG13	1.4938	0.05	1269	131	ASP	N	116.226	0.4
1210	125	ILE	HG2	0.8108	0.05	1270	132	GLY	C	172.439	0.4
1211	125	ILE	N	119.224	0.4	1271	132	GLY	CA	47.2278	0.4
1212	126	ARG	C	176.484	0.4	1272	132	GLY	H	7.6768	0.05
1213	126	ARG	CA	59.5788	0.4	1273	132	GLY	HA2	3.9908	0.05
1214	126	ARG	CB	30.2498	0.4	1274	132	GLY	HA3	3.8608	0.05
1215	126	ARG	CD	43.4668	0.4	1275	132	GLY	N	108.352	0.4
1216	126	ARG	CG	27.9058	0.4	1276	133	ASP	C	174.74	0.4
1217	126	ARG	H	8.5118	0.05	1277	133	ASP	CA	53.9868	0.4
1218	126	ARG	HA	4.0908	0.05	1278	133	ASP	CB	39.9928	0.4
1219	126	ARG	HG2	1.8238	0.05	1279	133	ASP	H	8.4278	0.05
1220	126	ARG	HG3	1.6708	0.05	1280	133	ASP	HA	4.4988	0.05
1221	126	ARG	N	117.057	0.4	1281	133	ASP	HB2	2.9688	0.05
1222	126	ARG	HB2	1.8898	0.05	1282	133	ASP	HB3	2.5268	0.05
1223	126	ARG	HD2	3.2478	0.05	1283	133	ASP	N	120.564	0.4
1224	127	GLU	C	174.423	0.4	1284	134	GLY	C	169.86	0.4
1225	127	GLU	CA	58.8898	0.4	1285	134	GLY	CA	45.5158	0.4
1226	127	GLU	CB	30.1128	0.4	1286	134	GLY	H	10.3178	0.05
1227	127	GLU	CG	36.6448	0.4	1287	134	GLY	HA2	4.0688	0.05
1228	127	GLU	H	8.2808	0.05	1288	134	GLY	HA3	3.4518	0.05
1229	127	GLU	HA	4.0608	0.05	1289	134	GLY	N	112.342	0.4
1230	127	GLU	N	115.021	0.4	1290	135	GLN	C	172.149	0.4
1231	127	GLU	HB2	2.3078	0.05	1291	135	GLN	CA	53.2138	0.4
1232	127	GLU	HG2	2.4958	0.05	1292	135	GLN	CB	32.3578	0.4

1293	135	GLN	CG	33.0208	0.4	1353	140	GLU	CG	37.4508	0.4
1294	135	GLN	H	7.9788	0.05	1354	140	GLU	H	8.7048	0.05
1295	135	GLN	HA	4.9768	0.05	1355	140	GLU	HA	3.8288	0.05
1296	135	GLN	HE21	6.5038	0.05	1356	140	GLU	HB2	2.1588	0.05
1297	135	GLN	HE22	5.9758	0.05	1357	140	GLU	HB3	1.9918	0.05
1298	135	GLN	HG2	2.0118	0.05	1358	140	GLU	HG2	2.8448	0.05
1299	135	GLN	HG3	1.6658	0.05	1359	140	GLU	HG3	2.3648	0.05
1300	135	GLN	N	114.483	0.4	1360	140	GLU	N	119.391	0.4
1301	135	GLN	NE2	108.133	0.4	1361	141	PHE	C	173.478	0.4
1302	135	GLN	HB2	1.7268	0.05	1362	141	PHE	CA	61.5828	0.4
1303	136	VAL	C	172.968	0.4	1363	141	PHE	CB	39.8728	0.4
1304	136	VAL	CA	61.6478	0.4	1364	141	PHE	CD1	129.982	0.4
1305	136	VAL	CB	33.494	0.4	1365	141	PHE	CD2	129.982	0.4
1306	136	VAL	CG1	23.0538	0.4	1366	141	PHE	CE1	129.459	0.4
1307	136	VAL	CG2	21.0718	0.4	1367	141	PHE	CE2	129.466	0.4
1308	136	VAL	H	9.1448	0.05	1368	141	PHE	H	8.4738	0.05
1309	136	VAL	HA	5.2068	0.05	1369	141	PHE	HA	3.3988	0.05
1310	136	VAL	HB	2.3778	0.05	1370	141	PHE	HB2	3.2698	0.05
1311	136	VAL	HG1	1.1408	0.05	1371	141	PHE	HB3	2.8878	0.05
1312	136	VAL	HG2	1.0668	0.05	1372	141	PHE	HZ	8.5208	0.05
1313	136	VAL	N	124.979	0.4	1373	141	PHE	N	123.444	0.4
1314	137	ASN	C	171.857	0.4	1374	141	PHE	HD1	6.6488	0.05
1315	137	ASN	CA	50.7558	0.4	1375	141	PHE	HD2	6.6488	0.05
1316	137	ASN	CB	38.3368	0.4	1376	141	PHE	HE1	7.0578	0.05
1317	137	ASN	H	9.6288	0.05	1377	141	PHE	HE2	7.0578	0.05
1318	137	ASN	HA	5.3468	0.05	1378	142	VAL	C	176.735	0.4
1319	137	ASN	HD21	7.5038	0.05	1379	142	VAL	CA	66.8108	0.4
1320	137	ASN	HD22	7.3288	0.05	1380	142	VAL	CB	31.3188	0.4
1321	137	ASN	N	128.916	0.4	1381	142	VAL	CG1	21.1198	0.4
1322	137	ASN	ND2	111.858	0.4	1382	142	VAL	CG2	22.8868	0.4
1323	137	ASN	HB2	3.1808	0.05	1383	142	VAL	H	8.6118	0.05
1324	138	TYR	C	173.214	0.4	1384	142	VAL	HA	2.9608	0.05
1325	138	TYR	CA	62.0288	0.4	1385	142	VAL	HB	1.7098	0.05
1326	138	TYR	CB	37.5368	0.4	1386	142	VAL	HG1	0.6598	0.05
1327	138	TYR	CD1	130.347	0.4	1387	142	VAL	HG2	0.4038	0.05
1328	138	TYR	CD2	130.347	0.4	1388	142	VAL	N	118.366	0.4
1329	138	TYR	CE1	116.007	0.4	1389	143	GLN	CA	58.7918	0.4
1330	138	TYR	CE2	116.007	0.4	1390	143	GLN	CB	27.9958	0.4
1331	138	TYR	H	8.3428	0.05	1391	143	GLN	CG	33.7228	0.4
1332	138	TYR	HA	3.2258	0.05	1392	143	GLN	H	7.8028	0.05
1333	138	TYR	HB2	2.3428	0.05	1393	143	GLN	HA	3.7798	0.05
1334	138	TYR	HB3	2.0148	0.05	1394	143	GLN	HE21	7.3518	0.05
1335	138	TYR	N	118.187	0.4	1395	143	GLN	HE22	6.7088	0.05
1336	138	TYR	HD1	6.2598	0.05	1396	143	GLN	N	119.002	0.4
1337	138	TYR	HD2	6.2598	0.05	1397	143	GLN	NE2	111.126	0.4
1338	138	TYR	HE1	6.4808	0.05	1398	143	GLN	HB2	2.0018	0.05
1339	138	TYR	HE2	6.4808	0.05	1399	143	GLN	HG2	2.3288	0.05
1340	139	GLU	C	177.373	0.4	1400	144	MET	C	173.938	0.4
1341	139	GLU	CA	59.7578	0.4	1401	144	MET	CA	56.4348	0.4
1342	139	GLU	CB	29.275	0.4	1402	144	MET	CB	29.669	0.4
1343	139	GLU	CG	35.8908	0.4	1403	144	MET	CE	16.0918	0.4
1344	139	GLU	H	8.0338	0.05	1404	144	MET	CG	30.6068	0.4
1345	139	GLU	HA	3.5918	0.05	1405	144	MET	H	7.3888	0.05
1346	139	GLU	HG2	2.3258	0.05	1406	144	MET	HA	4.1898	0.05
1347	139	GLU	HG3	2.2958	0.05	1407	144	MET	HE	1.6808	0.05
1348	139	GLU	N	117.957	0.4	1408	144	MET	N	116.678	0.4
1349	139	GLU	HB2	2.0058	0.05	1409	144	MET	HB2	1.4298	0.05
1350	140	GLU	C	176.476	0.4	1410	144	MET	HG2	1.6998	0.05
1351	140	GLU	CA	58.5078	0.4	1411	145	MET	C	174.791	0.4
1352	140	GLU	CB	28.8998	0.4	1412	145	MET	CA	55.0798	0.4

1413	145	MET	CB	30.904	0.4	1433	147	ALA	C	174.107	0.4
1414	145	MET	CE	18.1958	0.4	1434	147	ALA	CA	52.4268	0.4
1415	145	MET	CG	32.2298	0.4	1435	147	ALA	CB	19.0508	0.4
1416	145	MET	H	7.3048	0.05	1436	147	ALA	H	7.8608	0.05
1417	145	MET	HA	4.0238	0.05	1437	147	ALA	HA	4.3328	0.05
1418	145	MET	HB2	1.4938	0.05	1438	147	ALA	HB	1.3908	0.05
1419	145	MET	HB3	1.1088	0.05	1439	147	ALA	N	126.675	0.4
1420	145	MET	HE	1.1438	0.05	1440	148	LYS	CA	57.6978	0.4
1421	145	MET	HG2	1.4608	0.05	1441	148	LYS	CB	33.241	0.4
1422	145	MET	HG3	1.3398	0.05	1442	148	LYS	CD	28.8568	0.4
1423	145	MET	N	112.325	0.4	1443	148	LYS	CE	41.6988	0.4
1424	146	THR	C	171.522	0.4	1444	148	LYS	CG	24.7878	0.4
1425	146	THR	CA	61.8998	0.4	1445	148	LYS	H	8.0078	0.05
1426	146	THR	CB	70.5428	0.4	1446	148	LYS	HA	4.0798	0.05
1427	146	THR	CG2	21.1358	0.4	1447	148	LYS	HB2	1.7998	0.05
1428	146	THR	H	7.4728	0.05	1448	148	LYS	HB3	1.7308	0.05
1429	146	THR	HA	4.2518	0.05	1449	148	LYS	N	126.4	0.4
1430	146	THR	HB	4.1468	0.05	1450	148	LYS	HD2	1.6478	0.05
1431	146	THR	HG2	1.0658	0.05	1451	148	LYS	HE2	2.9868	0.05
1432	146	THR	N	108.155	0.4	1452	148	LYS	HG2	1.3938	0.05

Munc13-1(457-492)

Atom #	Seq #	Res Type	Atom ID	Chem shift	error	Atom #	Seq #	Res Type	Atom ID	Chem shift	error
1	458	SER	CA	55.709	0.5	38	463	ASN	CA	53.033	0.5
2	458	SER	CB	61.137	0.5	39	463	ASN	CB	35.5	0.5
3	458	SER	C	175.368	0.5	40	463	ASN	H	8.372	0.05
4	458	SER	H	8.193	0.05	41	463	ASN	HA	4.459	0.05
5	458	SER	HB2	3.879	0.05	42	463	ASN	HB2	2.858	0.05
6	458	SER	N	120.637	0.5	43	463	ASN	HB3	2.683	0.05
7	459	ARG	C	173.718	0.5	44	463	ASN	N	118.243	0.5
8	459	ARG	CA	55.993	0.5	45	464	TRP	C	172.698	0.5
9	459	ARG	CB	27.411	0.5	46	464	TRP	CA	58.19	0.5
10	459	ARG	CG	23.675	0.5	47	464	TRP	CB	26.538	0.5
11	459	ARG	H	8.654	0.05	48	464	TRP	CD1	128.771	0.5
12	459	ARG	HA	3.838	0.05	49	464	TRP	H	8.533	0.05
13	459	ARG	HG2	1.546	0.05	50	464	TRP	HA	4.203	0.05
14	459	ARG	N	125.365	0.5	51	464	TRP	HB2	3.382	0.05
15	460	ALA	C	171.624	0.5	52	464	TRP	HB3	2.867	0.05
16	460	ALA	CA	52.358	0.5	53	464	TRP	HD1	7.313	0.05
17	460	ALA	CB	15.958	0.5	54	464	TRP	HE1	10.381	0.05
18	460	ALA	H	8.193	0.05	55	464	TRP	HZ2	7.128	0.05
19	460	ALA	HA	4.164	0.05	56	464	TRP	HH2	6.987	0.05
20	460	ALA	HB	1.353	0.05	57	464	TRP	N	121.805	0.5
21	460	ALA	N	120.862	0.5	58	464	TRP	NE1	129.285	0.5
22	461	LYS	C	173.138	0.5	59	465	LEU	C	171.618	0.5
23	461	LYS	CA	56.959	0.5	60	465	LEU	CA	55.499	0.5
24	461	LYS	CB	28.819	0.5	61	465	LEU	CB	38.641	0.5
25	461	LYS	CD	26.742	0.5	62	465	LEU	CD1	22.725	0.5
26	461	LYS	H	7.9	0.05	63	465	LEU	CG	23.208	0.5
27	461	LYS	HA	4.185	0.05	64	465	LEU	H	8.264	0.05
28	461	LYS	HB2	1.895	0.05	65	465	LEU	HA	4.172	0.05
29	461	LYS	HB3	1.863	0.05	66	465	LEU	HB2	1.841	0.05
30	461	LYS	N	118.064	0.5	67	465	LEU	HB3	1.6	0.05
31	462	ALA	CA	52.15	0.5	68	465	LEU	HD1	0.881	0.05
32	462	ALA	CB	14.865	0.5	69	465	LEU	HD2	0.886	0.05
33	462	ALA	H	7.778	0.05	70	465	LEU	HG	1.785	0.05
34	462	ALA	HA	4.06	0.05	71	465	LEU	N	118.722	0.5
35	462	ALA	HB	1.444	0.05	72	466	ARG	C	172.228	0.5
36	462	ALA	N	120.253	0.5	73	466	ARG	CA	56.888	0.5
37	463	ASN	C	173.138	0.5	74	466	ARG	CB	27.368	0.5

75	466	ARG	H	8.264	0.05	137	472	ARG	CA	56.805	0.5
76	466	ARG	HA	4.128	0.05	138	472	ARG	CB	26.506	0.5
77	466	ARG	HG2	0.882	0.05	139	472	ARG	CD	40.184	0.5
78	466	ARG	N	120.684	0.5	140	472	ARG	CG	22.439	0.5
79	466	ARG	HB2	1.927	0.05	141	472	ARG	H	8.639	0.05
80	466	ARG	HD2	3.251	0.05	142	472	ARG	HA	3.763	0.05
81	467	ALA	C	172.178	0.5	143	472	ARG	HD2	3.333	0.05
82	467	ALA	CA	52.558	0.5	144	472	ARG	HD3	2.98	0.05
83	467	ALA	CB	16.041	0.5	145	472	ARG	HG2	1.335	0.05
84	467	ALA	H	8.067	0.05	146	472	ARG	HG3	1.207	0.05
85	467	ALA	HA	3.978	0.05	147	472	ARG	N	119.209	0.5
86	467	ALA	HB	1.584	0.05	148	472	ARG	HB2	1.565	0.05
87	467	ALA	N	121.482	0.5	149	473	MET	C	172.688	0.5
88	468	PHE	C	174.298	0.5	150	473	MET	CA	55.673	0.5
89	468	PHE	CA	58.326	0.5	151	473	MET	CB	29.324	0.5
90	468	PHE	CB	37.668	0.5	152	473	MET	CE	14.99	0.5
91	468	PHE	CE1	129.841	0.5	153	473	MET	H	7.701	0.05
92	468	PHE	CE2	129.841	0.5	154	473	MET	HA	4.105	0.05
93	468	PHE	H	9.052	0.05	155	473	MET	HB2	2.115	0.05
94	468	PHE	HA	4.35	0.05	156	473	MET	HB3	2.1	0.05
95	468	PHE	HB2	3.418	0.05	157	473	MET	HE	2.509	0.05
96	468	PHE	HB3	3.354	0.05	158	473	MET	N	117.427	0.5
97	468	PHE	N	117.615	0.5	159	473	MET	HG2	2.186	0.05
98	468	PHE	HD1	7.082	0.05	160	474	GLN	C	172.068	0.5
99	468	PHE	HD2	7.082	0.05	161	474	GLN	CA	55.976	0.5
100	468	PHE	HE1	7.157	0.05	162	474	GLN	CB	24.407	0.5
101	468	PHE	HE2	7.157	0.05	163	474	GLN	CG	31.276	0.5
102	469	ASN	C	173.128	0.5	164	474	GLN	H	7.733	0.05
103	469	ASN	CA	53.709	0.5	165	474	GLN	HA	4.049	0.05
104	469	ASN	CB	35.325	0.5	166	474	GLN	HB2	2.142	0.05
105	469	ASN	H	8.602	0.05	167	474	GLN	HB3	2.084	0.05
106	469	ASN	HA	4.166	0.05	168	474	GLN	HG2	2.438	0.05
107	469	ASN	HB2	2.95	0.05	169	474	GLN	HG3	2.262	0.05
108	469	ASN	HB3	2.703	0.05	170	474	GLN	N	119.752	0.5
109	469	ASN	N	116.425	0.5	171	475	LEU	C	171.858	0.5
110	470	LYS	C	171.718	0.5	172	475	LEU	CA	54.386	0.5
111	470	LYS	CA	57.174	0.5	173	475	LEU	CB	39.047	0.5
112	470	LYS	CB	30.526	0.5	174	475	LEU	CD1	24.762	0.5
113	470	LYS	CD	26.002	0.5	175	475	LEU	CD2	20.787	0.5
114	470	LYS	CG	22.045	0.5	176	475	LEU	CG	25.779	0.5
115	470	LYS	H	8.076	0.05	177	475	LEU	H	8.151	0.05
116	470	LYS	HA	4.045	0.05	178	475	LEU	HA	4.013	0.05
117	470	LYS	HB2	2.01	0.05	179	475	LEU	HB2	1.871	0.05
118	470	LYS	HB3	1.839	0.05	180	475	LEU	HB3	1.371	0.05
119	470	LYS	HD2	1.681	0.05	181	475	LEU	HD1	0.733	0.05
120	470	LYS	HD3	1.617	0.05	182	475	LEU	HD2	0.718	0.05
121	470	LYS	HG2	1.681	0.05	183	475	LEU	N	120.063	0.5
122	470	LYS	HG3	1.4	0.05	184	475	LEU	HG	1.78	0.05
123	470	LYS	HE2	2.928	0.05	185	476	GLN	C	172.968	0.5
124	470	LYS	N	119.958	0.5	186	476	GLN	CA	55.365	0.5
125	471	VAL	C	173.222	0.5	187	476	GLN	CB	25.474	0.5
126	471	VAL	CA	64.19	0.5	188	476	GLN	CG	31.233	0.5
127	471	VAL	CB	28.483	0.5	189	476	GLN	H	7.911	0.05
128	471	VAL	CG1	21.475	0.5	190	476	GLN	HA	3.98	0.05
129	471	VAL	CG2	18.862	0.5	191	476	GLN	HB2	2.33	0.05
130	471	VAL	H	8.41	0.05	192	476	GLN	HB3	2.078	0.05
131	471	VAL	HA	3.532	0.05	193	476	GLN	HG2	2.412	0.05
132	471	VAL	HG1	0.938	0.05	194	476	GLN	HG3	2.337	0.05
133	471	VAL	HG2	0.839	0.05	195	476	GLN	N	118.054	0.5
134	471	VAL	N	121.488	0.5	196	477	GLU	C	173.278	0.5
135	471	VAL	HB	2.218	0.05	197	477	GLU	CA	55.49	0.5
136	472	ARG	C	172.261	0.5	198	477	GLU	CB	26.666	0.5

199	477	GLU	CG	34.168	0.5	261	484	MET	CG	33.966	0.5
200	477	GLU	H	7.975	0.05	262	484	MET	H	8.348	0.05
201	477	GLU	HA	4.016	0.05	263	484	MET	HA	4.175	0.05
202	477	GLU	HG2	2.31	0.05	264	484	MET	HB2	2.022	0.05
203	477	GLU	HG3	2.184	0.05	265	484	MET	HB3	1.948	0.05
204	477	GLU	N	119.803	0.5	266	484	MET	HE	2.052	0.05
205	477	GLU	HB2	2.012	0.05	267	484	MET	N	120.436	0.5
206	478	ALA	C	172.778	0.5	268	484	MET	HG3	2.176	0.05
207	478	ALA	CA	50.517	0.5	269	485	SER	C	176.328	0.5
208	478	ALA	CB	15.961	0.5	270	485	SER	CA	56.067	0.5
209	478	ALA	H	7.726	0.05	271	485	SER	CB	60.603	0.5
210	478	ALA	HA	4.19	0.05	272	485	SER	H	8.125	0.05
211	478	ALA	HB	1.385	0.05	273	485	SER	HA	4.338	0.05
212	478	ALA	N	121.648	0.5	274	485	SER	HB2	4.12	0.05
213	479	ARG	C	173.978	0.5	275	485	SER	HB3	3.842	0.05
214	479	ARG	CA	53.836	0.5	276	485	SER	N	115.589	0.5
215	479	ARG	CB	27.401	0.5	277	486	LYS	C	174.458	0.5
216	479	ARG	CD	40.823	0.5	278	486	LYS	CA	53.958	0.5
217	479	ARG	CG	24.527	0.5	279	486	LYS	CB	30.005	0.5
218	479	ARG	H	7.645	0.05	280	486	LYS	CD	26.823	0.5
219	479	ARG	HA	4.211	0.05	281	486	LYS	CE	39.61	0.5
220	479	ARG	HG2	1.678	0.05	282	486	LYS	CG	22.144	0.5
221	479	ARG	HG3	1.617	0.05	283	486	LYS	H	7.986	0.05
222	479	ARG	N	117.484	0.5	284	486	LYS	HA	4.22	0.05
223	479	ARG	HB2	1.834	0.05	285	486	LYS	HB2	1.706	0.05
224	479	ARG	HD2	3.135	0.05	286	486	LYS	HB3	1.596	0.05
225	480	GLY	C	176.758	0.5	287	486	LYS	HE2	2.837	0.05
226	480	GLY	CA	42.457	0.5	288	486	LYS	HG2	1.275	0.05
227	480	GLY	H	7.961	0.05	289	486	LYS	N	122.255	0.5
228	480	GLY	N	107.622	0.5	290	487	SER	C	176.458	0.5
229	480	GLY	HA2	3.909	0.05	291	487	SER	CA	55.826	0.5
230	480	GLY	HA3	3.909	0.05	292	487	SER	CB	61.064	0.5
231	481	GLU	C	174.088	0.5	293	487	SER	H	7.972	0.05
232	481	GLU	CA	53.78	0.5	294	487	SER	HA	3.676	0.05
233	481	GLU	CB	27.272	0.5	295	487	SER	HB2	3.806	0.05
234	481	GLU	CG	33.333	0.5	296	487	SER	HB3	3.744	0.05
235	481	GLU	H	8.163	0.05	297	487	SER	N	114.856	0.5
236	481	GLU	HA	4.269	0.05	298	488	LEU	C	174.198	0.5
237	481	GLU	HB2	2.049	0.05	299	488	LEU	CA	53.057	0.5
238	481	GLU	HB3	1.889	0.05	300	488	LEU	CB	39.082	0.5
239	481	GLU	N	120.497	0.5	301	488	LEU	CD1	20.626	0.5
240	481	GLU	HG2	2.202	0.05	302	488	LEU	CD2	18.346	0.5
241	482	GLY	C	176.808	0.5	303	488	LEU	H	8.017	0.05
242	482	GLY	CA	42.485	0.5	304	488	LEU	HA	4.3	0.05
243	482	GLY	H	8.35	0.05	305	488	LEU	HB2	1.427	0.05
244	482	GLY	N	108.85	0.5	306	488	LEU	HB3	1.272	0.05
245	482	GLY	HA2	3.902	0.05	307	488	LEU	HD1	0.733	0.05
246	482	GLY	HA3	3.902	0.05	308	488	LEU	HD2	0.689	0.05
247	483	GLU	C	174.108	0.5	309	488	LEU	HG	1.426	0.05
248	483	GLU	CA	54.039	0.5	310	488	LEU	N	123.172	0.5
249	483	GLU	CB	27.066	0.5	311	489	TRP	C	175.518	0.5
250	483	GLU	CG	33.267	0.5	312	489	TRP	CA	53.958	0.5
251	483	GLU	H	8.142	0.05	313	489	TRP	CB	26.283	0.5
252	483	GLU	HA	4.132	0.05	314	489	TRP	CD1	129.291	0.5
253	483	GLU	HB2	2.027	0.05	315	489	TRP	H	7.636	0.05
254	483	GLU	HB3	1.911	0.05	316	489	TRP	HA	4.124	0.05
255	483	GLU	N	120.369	0.5	317	489	TRP	HB2	2.964	0.05
256	483	GLU	HG2	2.201	0.05	318	489	TRP	HB3	2.925	0.05
257	484	MET	C	174.538	0.5	319	489	TRP	HD1	7.073	0.05
258	484	MET	CA	53.324	0.5	320	489	TRP	HE1	9.797	0.05
259	484	MET	CB	29.849	0.5	321	489	TRP	HZ2	7.204	0.05
260	484	MET	CE	14.43	0.5	322	489	TRP	HH2	7.075	0.05

323	489	TRP	N	117.409	0.5	341	491	LYS	CB	30.222	0.5
324	489	TRP	NE1	130.113	0.5	342	491	LYS	CD	26.208	0.5
325	490	PHE	C	176.158	0.5	343	491	LYS	CE	39.534	0.5
326	490	PHE	CA	55.014	0.5	344	491	LYS	CG	20.917	0.5
327	490	PHE	CB	36.68	0.5	345	491	LYS	H	7.864	0.05
328	490	PHE	CE1	129.98	0.5	346	491	LYS	HA	4.195	0.05
329	490	PHE	CE2	129.98	0.5	347	491	LYS	HB2	1.759	0.05
330	490	PHE	H	7.377	0.05	348	491	LYS	HB3	1.595	0.05
331	490	PHE	HA	4.325	0.05	349	491	LYS	N	123.484	0.5
332	490	PHE	HZ	7.242	0.05	350	491	LYS	HD2	1.611	0.05
333	490	PHE	N	119.308	0.5	351	491	LYS	HE2	2.902	0.05
334	490	PHE	HB2	2.844	0.05	352	491	LYS	HG2	1.297	0.05
335	490	PHE	HD1	7.05	0.05	353	492	GLY	CA	43.436	0.5
336	490	PHE	HD2	7.05	0.05	354	492	GLY	H	7.381	0.05
337	490	PHE	HE1	6.986	0.05	355	492	GLY	N	115.197	0.5
338	490	PHE	HE2	6.986	0.05	356	492	GLY	HA2	3.647	0.05
339	491	LYS	C	175.708	0.5	357	492	GLY	HA3	3.647	0.05
340	491	LYS	CA	53.521	0.5						

Curriculum Vitae

Personal data

Name: Fernando Rodríguez Castañeda

Birth date: 23.08.1978

Place of Birth: Guatemala City, Guatemala

Education

1986-1991 Primary school “Liceo Javier”

1992-1994 Secondary school “Liceo Javier”

1995-1996 High school “Liceo Javier”

1997-2002 Biochemistry studies at the “Universidad del Valle de Guatemala”

07/2001: Bachelor of Science degree (Major in biochemistry)

04/2002: “Licenciatura” degree in biochemistry (*Cum laude*)

2003-2007 M.Sc./Ph.D. studies in Molecular Biology at Georg August Universität Göttingen.

03/2004: M.Sc. degree in molecular biology

Working experience

June-July 1999: Summer internship at the pharmaceutical company Frycia Centro America, S.A.
February-August 2002: Quality control laboratory assistant at the pharmaceutical company Frycia Centro America, S.A.

Research projects

January –may 1999: Organic chemistry 3 research project entitled “Organic synthesis of a NADH analogue and its redox potential”
June-July 2000: Enzymology research project entitled “Over expression and purification of the recombinant protein Taq DNA polymerase”
August-November 2000: Natural products chemistry research project entitled “Phytochemical screening of the fruits, leaves and flowers of the elderberry (Caprifoliaceae: *Sambucus mexicana*)”
October 2000 – October 2001: Licenciatura degree thesis entitled “Genetic population of the malaria vector, the mosquito *Anopheles albimanus*, based on microsatellite DNA in Central America and the Caribbean”
January –march 2003: Laboratory rotation in the department of molecular genetics of the Max Planck Institute for Biophysical Chemistry. “Study of deletion mutants of the human deoxycytidine kinase”.
March –may 2003: Laboratory rotation in the department of biochemistry, medical faculty University of Goettingen. “Characterization of the formylglycine formation in the *Caulobacter crescentus* arylsulfatase”

May – July 2003: Laboratory rotation in the department of NMR based structural biology of the Max Planck Institute for Biophysical Chemistry. “Alignment of protein induced by a chemical coordinating lanthanide ion tag”.
October 2003-March 2004: M.Sc. thesis in the department of NMR based structural biology of the Max Planck Institute for Biophysical Chemistry. “Study of the denatured state of ubiquitin by NMR”
Since April 2004: Ph.D. thesis entitled “Study of protein dynamics by NMR”

Publications

Molina-Cruz, A., de Merida, AM., Mills, K., Rodriguez, F., Schoua, C., Yurrita, M.M., Molina, E., Palmieri, M and Black, W.C.4th. 2004. Gene flow among *Anopheles albimanus* populations in Central America, South America and the Caribbean assessed by microsatellites and mitochondrial DNA. *Am. J. Trop. Med. Hyg.,* **71(3)**: 350-9.

Leonov, A., Voigt, B., Rodriguez-Castaneda, F., Sakhaii, P. and Griesinger, C. 2005. Convenient syntheses of multifunctional EDTA-based chiral metal chelates substituted with an S-mesylcysteine. *Chem. Eur. J.,* **11:** 1-8.

Haberz, P., Rodriguez-Castaneda, F., Junker, J., Becker, S., Leonov, A. and Griesinger, C. 2006. Two new chiral EDTA-based metal chelates for weak alignment of proteins in solution. *Organic Letters,* **8(7):** 1275-1278.

Rodríguez-Castañeda, F., Haberz, P., Leonov, A. and Griesinger, C. 2006. Paramagnetic tagging of diamagnetic proteins for solution NMR. *Magnetic resonance in chemistry,* **44:** S10-S16.

Rodríguez-Castañeda, F., Brose, N., Carlomagno, T., Griesinger, C. Resonance assignment of the calmodulin-Munc13-1 peptide complex. J. Biomol. Assignments. To be submitted.